DOE/ER/01388-509

annual report 1979

nuclear physics laboratory
··niversity of washington

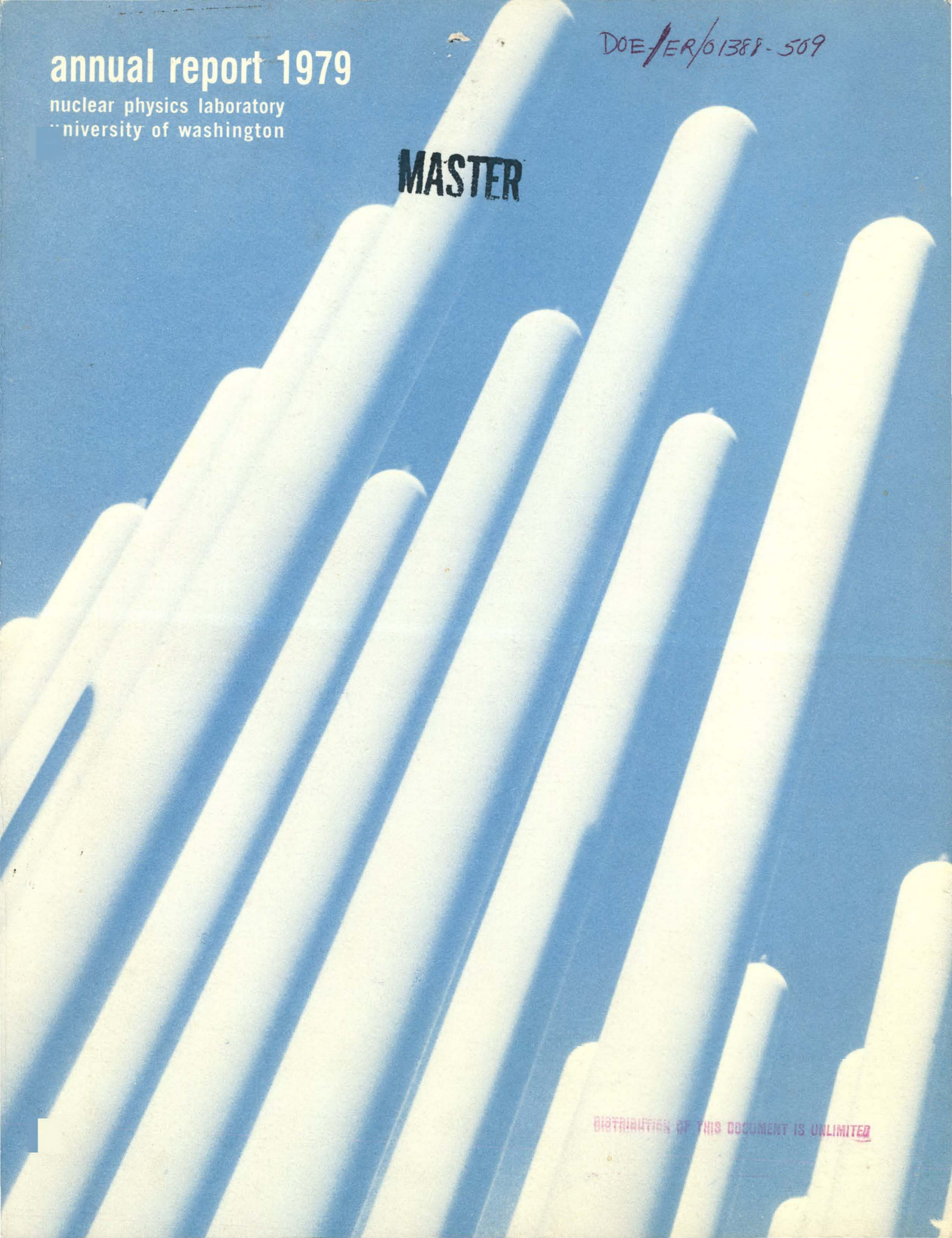

DISCLAIMER

DOE/ER/01388--509

ANNUAL REPORT

Nuclear Physics Laboratory
University of Washington
July, 1979

Supported in part by the United States Department of Energy under contract EY-76-C-06-1388 Program A.

INTRODUCTION

This annual report covers the period from April 1978 to April 1979. The past year has seen the beginning and growth of a number of large and time consuming new projects. We developed a proposal for a major new accelerator facility—a 20 MV folded tandem with a high current polarized ion source. This machine would be a very powerful instrument; we believe its capabilities would be a real asset to the nuclear physics community. Our new PDP 11/60 computer is now operational although work on interfacing and especially on data acquisition programs remains to be done. We have also decided to acquire a VAX 780 for the off-line analysis computer, and funds for this machine have been approved. These two new computers should provide us with an excellent facility for some years to come. We have, in collaboration with Prof. Harold Enge designed a new type of magnetic spectrometer—its large solid angle, isochronous properties and wide range make it ideally suited to coincidence experiments. A strong effort was devoted to building the apparatus for the hydrogen atom parity mixing experiment. Major progress has been made on the magnets, Rf cavities, ultrahigh vacuum system, detectors and electronics required for the measurements. In spite of these large projects which consumed a sizable share of the lab resources, the last year has been a productive one in other areas as well; for example, the discovery that the radiative capture of polarized protons can be used to identify M1 resonances and the exploration of the technique to locate previously unseen M1 strength in ^{16}O. In next year's progress report I expect one will find other interesting applications of this technique. The lower limit on charge nonconserving decays of nucleons has been improved by a factor of 25 and another improvement by an order of magnitude is expected using a different technique.

The dependence of the magnitude and alignment of the angular momentum transfer on inelasticity in collisions between heavy ions has been determined over a wide range of energy losses. The alignment is small for small energy losses and increases to large values as the energy loss increases. This dependence can be understood simply in terms of a mechanism involving nucleon exchange. The alignment is small for small energy losses because the randomly oriented component of the angular momentum arising from the Fermi notion is larger than the aligned component from the relative motion of the nuclei. With more nucleon transfers the coherent sum of the aligned components grows faster than the sum of the random components from the Fermi notion, and a large final alignment can be achieved.

An upper limit of $24 \pm 29 \times 10^{-4}$ has been placed on the parity—violating circular polarization of the 2.7 MeV γ-ray on ^{21}Ne. This is considerably smaller than theoretical estimates and probably indicates that the calculated weak N-N potential is not correct.

This year we have a number of new faces in the Lab. We are very pleased that we were able to attract Derek W. Storm from Columbia back to Seattle. He is currently working with characteristic energy on the new magnetic detector, on ion sources and beam optics. Our new postdoctoral associates Eric Norman and Albert Lazzarini have already made large contributions to our research in astrophysics and heavy ions respectively. We are delighted to have Hubert Doubre visiting us from Orsay. George Farwell has returned to the Lab and is now working

on problems of radiochronology using the tandem accelerator. Ying Halpern will be returning this summer from a sabbatical year at Saclay.

The tandem again runs very well after a tube replacement (one of the old tube sections had run for 77,000 hrs) and the polarized ion source has continued to improve. However we are still not satisfied with the performance of the sputter source and are working on a new version.

As in the past we welcome applications from scientists at other institutions who may wish to use our facilities. At present outside users are active on both the tandem and the cyclotron. The salient characteristics of these machines are listed on the following page. Anyone interested in using the facilities should consult with a potential collaborator from the University of Washington or Dr. William Weitkamp, Technical Director, Nuclear Physics Laboratory GL-10, University of Washington, Seattle, WA 98195 or telephone (206) 543-4080.

Let me close by reminding the reader that the articles in this report describe work in progress and are not to be regarded as publications nor quoted without permission of the investigators. The names of the investigators on each article have been listed alphabetically but where appropriate the name of the person primarily responsible for the report has been underlined.

Eric Adelberger

Eric G. Adelberger
Editor, 1979 Annual Report

THREE STAGE TANDEM VAN DE GRAAFF ACCELERATOR

(A High Voltage Engineering Corp. Model FN)

Completed: 1967
Funding: Purchasing with NSF funds; maintained by ERDA funds and some funds from the State of Washington.

Beams currently available: (See also W.G. Weitkamp and F.H. Schmidt "The University of Washington Three Stage Van de Graaff Accelerator" Nucl. Instrum. Methods 122, 65 (1974).

Ion	Max. Current 2 stage (μA)	Max. Practical Energy 2 Stage (MeV)	Typ. Current 3 stage (μA)	Max. Practical Energy 3 Stage (MeV)
p,d	20	18	10	25
polarized p,d	0.1	18	----	---
^{3,4}He	3	27	----	---
^{6,7}Li	0.5	36	----	---
C	2	63	1	70
N	2	72	1	79
O	10	81	3	88
Si	0.2	90	----	---
Cl	0.2	117	0.2	124
Ni	0.5	117		
Br	0.1	125		
Ag	0.01	125		

CYCLOTRON

(A 60-inch fixed energy machine)

Completed: 1952
Funding: Constructed primarily with State funds and subsequently supported by AEC funds. Now sustained by funds from outside users.

Beams currently available:

Ion	Typical Current (μA)	Maximum Practical Energy (MeV)
p	100	11
d	150	22
^{4}He	30	42

TABLE OF CONTENTS

1. ASTROPHYSICS AND COSMOLOGY

1.1 Nucleosynthesis of ^{26}Al

E. B. Norman

A. ^{26}Al Production via the $^{25}Mg(p,\gamma)$ Reaction

There has been much recent astrophysical interest in the nuclide ^{26}Al. Lee *et al.*[1] discovered excess abundances of ^{26}Mg compared with ^{24}Mg and ^{25}Mg in inclusions from the Allende meteorite which seemed to correlate with the Al/Mg elemental abundance ratios. This was interpreted to indicate that ^{26}Al was present at the time of formation of the inclusions and later decayed in situ to produce the observed ^{26}Mg abundance excess. The relatively short half-life of ^{26}Al (7.2×10^5 years) implies that the nucleosynthetic event which produced this ^{26}Al must have occurred no more than a few million years prior to the formation of these inclusions.

The ^{26}Al 5^+ ground state, $^{26}Al^g$, has a half-life of 7.2×10^5 years. However, as can be seen in Fig. 1.1-1, there exists a nearly 0^+ level, $^{26}Al^m$, which β^+ decays to ^{26}Mg with a half-life of 6.345 seconds and does not decay to the ^{26}Al ground state. Thus any ^{26}Al formed in this isomeric state will not survive long enough to become incorporated into a meteoritic inclusion as ^{26}Al.

One of the major ^{26}Al production mechanisms is thought to be the $^{25}Mg(p,\gamma)$ reaction.[2] This reaction has been studied experimentally by de Neijs *et al.*[3] Fifty-two resonances were observed in the astrophysically interesting energy range E_p = 0.3 - 1.7 MeV. By following the γ-cascade from each

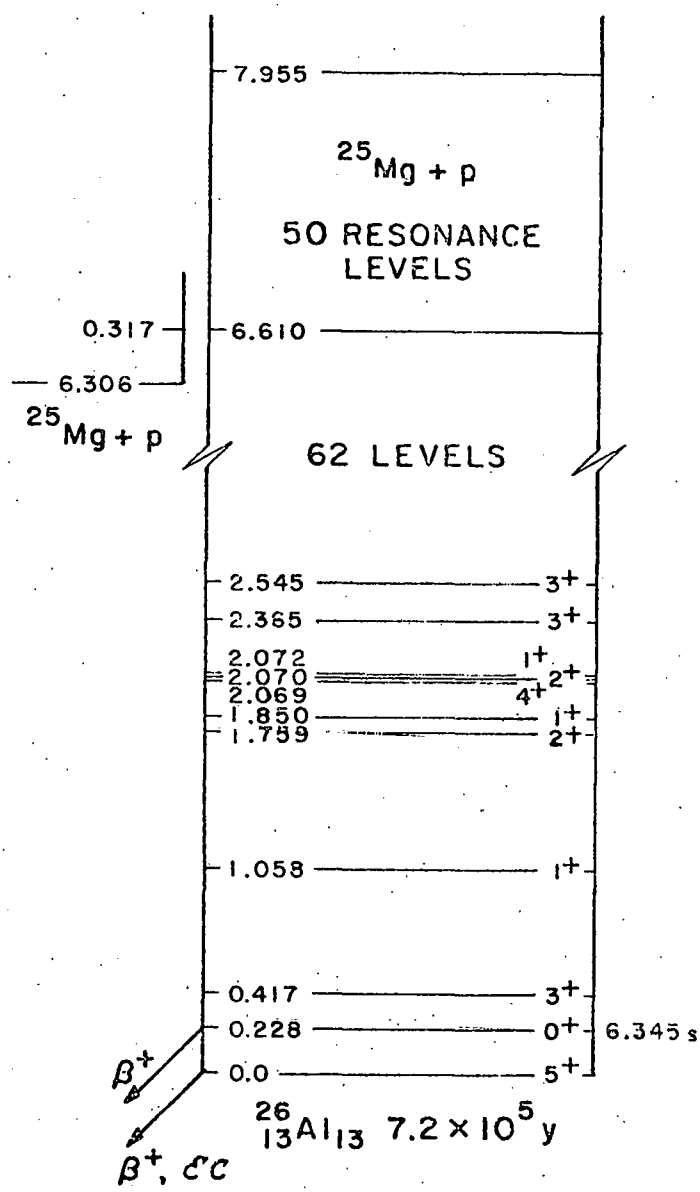

Fig. 1.1-1. Level Scheme of ^{26}Al

of the observed resonances, the reaction strength from each resonance that eventually ends up in the isomer and that which ends up in the ground state has been determined. Combining this data with a Maxwell-Boltzmann distribution of proton energies for temperatures appropriate for stellar interiors, one finds that the relative yields of $^{26}Al^m$ and $^{26}Al^g$ are in the approximate ratio 1/3. Thus, previous estimates for the rate of the $^{25}Mg(p,\gamma)$ reaction overestimated the net $^{26}Al^g$ production rate by roughly 25%.

B. ^{26}Al Production via the $^{23}Na(\alpha,n)$ Reaction

Another possibly important ^{26}Al production mechanism is the $^{23}Na(\alpha,n)$ reaction. At present, however, the cross sections for this reaction are not known. As a result, we have begun a series of experiments to measure the $^{26}Al^g$ production cross section. Thick Na_2CO_3 targets are bombarded with α-particles. Following activation, the $^{26}Al^g$ cross section is determined by measuring the yield of 1.806 MeV γ-rays emitted following the β-decay of $^{26}Al^g$. It is hoped that it will be possible to measure an excitation function for this reaction over the energy range E_α = 5 - 25 MeV.

C. Destruction of $^{26}Al^g$ via Photoexcitation to $^{26}Al^m$

Under the conditions of extremely high temperatures and pressures that exist in stellar interiors, $^{26}Al^g$ may be destroyed via thermal excitation of the isomeric level followed by β^+ decay or other nuclear reactions. Though $^{26}Al^g$ and $^{26}Al^m$ do not directly "communicate" with each other, photoexcitation and inelastic scattering reactions to higher lying states may allow the isomer and ground state to reach their thermal equilibrium abundance ratio. Thus the net yield of $^{26}Al^g$ may be further reduced. Calculations of the rate of equilibration are currently in progress.

---

1. T. Lee, D.A. Papanastassiou, and G.J. Wasserburg, Astrophys. J. 211, L107 (1977).
2. W.D. Arnett and J.P. Wefel, Astrophys. J. 224, L139 (1978).
3. E.O. de Neijs *et al.*, Nucl. Phys. A230 (1974), 490.

1.2 The Half-Life of ^{176}Lu

E.B. Norman

During the past forty years, the half-life of ^{176}Lu has been measured a number of times with widely scattered results. Published values for the half-life range from 2.1×10^{10} years[1] to 7.3×10^{10} years,[2] with the more recently published values clustered in the range $(3.5\text{-}4.0) \times 10^{10}$ years.[3] Recently, McCulloch *et al.*[4] have used ^{176}Lu as a chronometer to determine the age of the universe. The result obtained by such a method depends on the value taken for the ^{176}Lu half-life.

As a result, it was decided that a new experiment should be performed to measure the ^{176}Lu half-life. ^{176}Lu β^- decays approximately 99% of the time to the 6^+ state at 597 keV in ^{176}Hf. This decay is followed by a cascade of γ-rays with energies of 307, 202, and 88 keV. The present experiment consisted of measuring the yields of these gamma rays during a specified counting interval from a known quantity of ^{176}Lu.

A 217 mg sample of natural lutetium metal (containing 2.6% ^{176}Lu) in the form of a thin foil was placed on the front of a well shielded 79-cm^3 Ge(Li) detector. The sample was counted for about 44 hours yielding approximately 10^5 counts in both the 202- and 307-keV photopeaks. Background measurements were performed for approximately 11 hours. Photopeak and total detector efficiencies were determined using accurately calibrated (3-5% uncertainties) standard γ-ray sources. Corrections for summing effects, attenuation in the sample, and internal conversion are currently being evaluated. Preliminary analysis indicates that the ^{176}Lu half-life is approximately 3.7×10^{10} years.

---

1. J.R. Arnold, Phys. Rev. 93, 743 (1954).
2. W.F. Libby, Phys. Rev. 56, 21 (1939).
3. D.J. Horen and B. Harmatz, Nucl. Data Sheets 19, 383 (1976).
4. M.T. McCulloch, J.R. deLaeter, and K.J.R. Rosman, Earth Planet. Sci. Letters 28 308 (1976).

1.3 Production of ^{176}Lu^m and ^{180}Ta^m Via Coulomb Scattering

E.B. Norman

It is now becoming apparent that long-lived isomeric states may play important roles in several types of nucleosynthesis processes.[1,2] In some cases, these isomers β-decay to neighboring isobars rather than electromagnetically decaying to the parent ground state. This has the effect of decreasing the net production yield of the parent nucleus. In other cases, the isomeric levels may undergo various nuclear reactions with rates quite different than those for the nuclear ground state. The effect that this may have on the net yield depends on the particular nucleus.

Questions exist as to whether these isomeric levels can achieve their equilibrium abundances on time scales short compared to the nucleosynthesis time scale. Photoexcitation of the ground state to the isomer is one possible equilibration mechanism, and its rate can be calculated reasonably accurately. Contributions from other inelastic scattering processes are harder to estimate. Thus it was decided that an attempt should be made to measure the production cross sections for some isomeric levels from Coulomb scattering. There has recently been astrophysical interest in the nucleosynthesis of ^{176}Lu[3] and ^{180}Ta[4], and thus it was decided to begin this project by attempting to measure the production cross sections of ^{176}Lu^m and ^{180}Ta^m from Coulomb scattering.

Thick targets of natural Lu (2.6% ^{176}Lu) and natural Ta (0.012% ^{180}Ta) were bombarded with both protons and alpha particles. The projectile energies were kept below the thresholds for any transfer reactions that could produce the sought for isomeric levels. Following activation, the targets were placed in front of a Ge(Li) detector, and a search was made for γ-rays produced by the decays of the isomers. Because of the low isotopic percentages of ^{176}Lu and ^{180}Ta in the natural elements, the expected counting rates are quite low. To date, only upper limits on the order of 1 mb have been established for the production of both $^{176}Lu^{m}$ and $^{180}Ta^{m}$ from the Coulomb scattering of 5-MeV protons and 7.5-MeV alpha particles. Future investigations with protons and alphas will be made using higher beam currents. Also, investigations will be made using heavier projectiles such as ^{12}C and ^{16}O.

---

1. R.A. Ward, Astrophys. J. 216, 540 (1977).
2. See Section 1.1 of this report.
3. M.T. McCulloch, J.R. deLaeter, and K.J.R. Rosman, Earth Planet. Sci. Letters 28, 308 (1976).
4. E.B. Norman and T.R. Renner, to be published.

1.4 Cross Sections Relevant to Gamma Ray Astronomy

D. Bodansky, P. Dyer,† D.R. Maxon,†† and A.G. Seamster

Analysis has continued on data obtained in measurements of gamma-ray yields for proton and alpha-particle reactions with nuclei of relatively high cosmic abundance: ^{12}C, ^{14}N, ^{16}O, ^{20}Ne, ^{24}Mg, ^{28}Si, and ^{56}Fe. As discussed in previous reports,[1] gamma-ray excitation functions can provide information necessary to the interpretation of astronomical gamma-ray line spectra in terms of the abundances, energy spectra, and, possibly, directions of the interacting nuclei.

The determination of the proton excitation functions for prominent lines is nearing completion. The cross sections can be averaged over hypothesized cosmic proton energy spectra to give average cross sections. We have followed the conventional, if somewhat arbitrary, procedure of assuming a power law spectrum in proton kinetic energy, of the form: $\emptyset(E) \propto E^{-S}$, $E \geq E_c$ and $\emptyset(E) = 0$, $E < E_c$. For illustrative purposes, average cross sections for this spectral shape are presented in Table 1.4-1, for one specific choice for the exponent s and the cutoff energy, E_c. (The present data extends to about 23 MeV, and extrapolated cross sections, based when possible on measurements in the literature, were used above 23 MeV. For the (p,p') and (p,n) reactions virtually all the yield arises from interactions below 23 MeV, and the extrapolation introduces negligible error. For the remaining reactions, the extrapolation is more significant and the results are correspondingly more uncertain.)

The strong lines seen in (p,p') reactions can in most cases also be produced via (p,n) reactions followed by β^{+} decay. Except for A = 14 and A = 56, the lifetimes are too short or the decay yield to excited states are too small, or both, to make a distinction between these two components relevant, and both

Table 1.4-1. Average cross sections for prominent gamma ray lines. A power law spectrum in proton kinetic energy is assumed, with s = 3 and E_c = 5 MeV. (Uncertainties in these cross sections typically are in the neighborhood of 10%; the results remain subject to further small corrections.)

Target Nucleus	Residual Nucleus	Energy (MeV)	$\bar{\sigma}$ (mb)	Comments
^{12}C	^{12}C	4.439	143	
^{14}N	^{14}N	2.313	53	Includes ^{14}O decay
^{16}O	^{16}O	6.130	39	
^{16}O	^{12}C	4.439	10	
^{20}Ne	^{20}Ne	1.634	338	
^{20}Ne	^{16}O	6.130	8	
^{24}Mg	^{24}Mg	1.369	398	
^{24}Mg	^{20}Ne	1.634	10	
^{28}Si	^{28}Si	1.779	272	
^{56}Fe	^{56}Fe	0.847	296	From (p,p') only
^{56}Fe	^{56}Fe	0.847	147[a]	From ^{56}Co decay
^{56}Fe	^{56}Fe	1.238	60	From (p,p') only
^{56}Fe	^{56}Fe	1.238	98[a]	From ^{56}Co decay
^{56}Fe	^{56}Fe	1.811	31	From (p,p') only
^{56}Fe	^{56}Co	0.812	42	
^{56}Fe	^{55}Fe	0.931	19	Includes ^{55}Co decay

[a]Based on activation measurement for $^{56}Fe(p,n)^{56}Co$

are included together. For the 71-second decay of ^{14}O, it was necessary to make a separate determination of the $^{14}N(p,n)^{14}O$ cross section to correct for errors introduced by the relatively short time of individual p + ^{14}N bombardments. We find this cross section to be about a factor ten lower than previously reported.[2] The ^{14}N results presented in Table 1.4-1 include both components. For the 79-day decay of ^{56}Co, the distinction between the two groups becomes of considerable potential interest, depending upon the astronomical scenario, and the cross sections are presented separately.

The presence of numerous prominent lines from ^{56}Fe offers the hope that a comparison of iron line yields could shed light on the actual proton spectral

shape. Specifically, the cross section for the 0.931-MeV line from $^{56}Fe(p,pn)^{55}Fe$, which is unimportant below about 15 MeV, rises above that of all the other iron lines at 21 MeV. Thus the relative prominence of this line could provide a direct indication of the hardness of the proton spectrum.

After completion of the analysis of the proton excitation functions, we plan to extract the excitation functions for the alpha-particle induced reactions, and study the Doppler broadened line shapes for both sets of data. Details of the line shape and the location of the central energy in principle offer the possibility of providing information on the direction of the particle fluxes and possibly on their energy spectra, as well as of distinguishing between proton and alpha particle produced yields. The reality of this prospect depends upon the intensity of the yet-to-be-observed gamma ray lines from astronomical sources.

---

† Present address: Cyclotron Laboratory, Michigan State University, East Lansing, Michigan 48824.

†† Permanent address: Brown University, Providence, Rhode Island 02912.

1. Nuclear Physics Laboratory Annual Report, University of Washington (1976), p. 51; *ibid* (1977), p. 1; *ibid* (1978), p. 1.

2. H. Kuan and J.R. Risser, Nucl. Phys. 51, 518 (1964).

1.5 Liquid Xenon Gamma Ray Detectors

J.G. Cramer, C.R. Gruhn,† and R.A. Loveman

The effectiveness with which one can make observational measurements of gamma rays is presently very limited. Sodium iodide detectors have relatively poor energy resolution and serious problems with activation by charged particle bombardment. Germanium detectors have good energy resolution, but have the problems of low efficiency, small detection volumes, and radiation damage. We are starting development of another kind of detector which promises advantages over both germanium and sodium iodide detectors. This new detector is the liquid inert gas ionization chamber (LIGIC).

Preliminary work on high resolution LIGIC devices has been done by C.R. Gruhn† and his group at Los Alamos. They have found that the key to high resolution is purification down to the parts-per-billion level. It is particularly important to remove such electron scavangers as oxygen, nitrogen, and sulfur hexafluoride. Using a chamber filled with super-pure argon Gruhn and Edmiston were able to obtain a resolution of 34 keV for 1 MeV conversion electrons.[1]

LIGIC devices are similar to gaseous ionization chambers. They have the same flexibility in design, and have the greatly increased densities necessay for high energy particle and gamma detection. In particular liquid xenon detectors look very promising. As of now another group has made preliminary measurements[2] of gamma spectra, and while the results are not as good as might be expected, it is believed design changes could result in substantial improvements in energy resolution.

In addition to serving as high resolution gamma detectors we are looking into LIGIC devices as gamma ray polarimeters. There are two possibilities we are looking at. Both are based on the fact that a large amount of the gamma ray polarization is transferred to the momentum of a photo-electron. The two methods we are looking at involve pulse shape discrimination, similar to that tried by Sanford, Cruise, and Calhane[3] and pulse height discrimination with varying electric field and charge collection configurations. The problem seems to be the degree to which a beta moves in a diffusive path compared with the degree with which it moves in a straight line. A Monte-Carlo type program has been written to calculate the energy deposition relative to the original line of motion, and preliminary results suggest that there is directional information in the pulse shape. Further results are necessary in order to determine where and when pulse shape discrimination could be used.

Aside from making preliminary calculations, we are starting to assemble the apparatus necessary for a simple LIGIC device. It is our hope to participate in experiments and development of LIGIC devices both here and at LBL. One such experiment has already been started at Berkeley. We measured the ionization yield from alpha particles in liquid argon, doped with liquid xenon and compared that yield with the yield of pure liquid argon. The yield showed a substantial decrease. This is very different from a similar experiment with conversion electrons in which a ten percent yield increase was observed by Nakamoto *et al.*[2] We attribute this difference to the effect of xenon on the alpha track structure. We are repeating the measurement to check the results.

---

† Lawrence Berkeley Lab.

1. M.D. Edmiston and C.R. Gruhn, IEEE Transactions on Nuclear Science, Vol. NS-25, No. 1, 352 (1978).
2. A. Nakamoto, S. Kubota, T. Doke, K. Masuda, Y. Hoshi, A. Hitachi, T. Takahashi, and E. Shibamura, Preprint, Dept. of Physics, Rikkyo University.
3. P.W. Sanford, A.M. Cruise and J.A. Culhane, NonSolar X and γ-ray Astronomy, I.A.U. Symposium No. 37, 35 (1970).

1.6 Absorber Theory Experiment

J.G. Cramer, E.B. Norman, and A.G. Seamster

In previous Annual Reports[1,2] we have described an experiment designed to provide a test of the Wheeler-Feynman Absorber Theory[3] as it applies to the emission of neutrinos. The basic measurement which is performed is a spatial asymmetry measurement of the beta particles emitted from a pure Fermi or pure Gamow-Teller beta decay, exploiting the good beta-neutrino angular correlation present in such decays to search for possible inhibition of neutrino emission in certain spatial directions. Such an inhibition would arise, according to W-F Absorber Theory, if the integral probability of neutrino absorption in a given direction were less than unity.

In beginning "production" runs with the apparatus in the past year, we discovered that the plastic scintillators had "crazed," presumably due to a manufacturing defect. This was producing unacceptably large instrumental asymmetries. It was therefore necessary to obtain new scintillators of the same design.

After the new scintillators were installed, we had a cyclotron run in which a quantity of ^{66}Ga was produced, and this was used for a preliminary run lasting approximately 4 days, during which about 100 right-left spectra were accumulated in the ND2400 analyzed at 30 minute intervals and recorded on magnetic tape.

A program for the PDP 11/60 for analyzing these data has been written and is now being tested. We anticipate that it will require several more cyclotron runs, producing ^{66}Ga and other sources, before any definitive statement can be made about possible spatial asymmetries in neutrino emission.

---

1. Nuclear Physics Laboratory Annual Report, University of Washington (1978), p. 6.
2. Nuclear Physics Laboratory Annual Report, University of Washington (1977), p. 3.
3. J.A. Wheeler and R.P. Feynman, Rev. Mod. Physics 17, 425 (1949).

---

2. FUNDAMENTAL SYMMETRIES

2.1 An Improved Test of Nucleon Charge Conservation

E.B. Norman and A.G. Seamster

Experimental searches for charge non-conserving decays of electrons have set lower limits on the lifetimes for such decays on the order of 10^{22} years.[1] As pointed out recently by Bahcall,[2] however, limits on charge non-conserving decays involving nucleons are much less stringent. The only experimental test of charge conservation involving nucleons of which we are aware is that of Sunyar and Goldhaber.[3] They searched for a charge non-conserving decay of the type

$$n \rightarrow p + \text{neutrals} \qquad (1)$$

using the nuclei ^{87}Rb and ^{87}Sr. As can be seen in Fig. 2.1-1, ^{87}Rb normally β^- decays to the ^{87}Sr ground state with a half-life of 4.8×10^{10} years and a decay energy of 273 keV. Thus, it is not energetically possible for ^{87}Rb to decay to the 2.8-hr isomeric level, $^{87}Sr^m$, via a normal β^- decay. However, if a decay of the type (1) occurred in which the neutral particles were photons and/or neutrinos, then ^{87}Rb could decay to $^{87}Sr^m$ with a decay energy of 396 keV.

Sunyar and Goldhaber searched for such charge non-conserving decays using a 30 gram sample of RbF. They chemically separated the Sr fraction and then searched for the electromagnetic decay of $^{87}Sr^m$ using a NaI detector. No such decays were observed, and a lower limit on the lifetime of 1.8×10^{16} years was established.

We have devised a new experiment involving the same pair of nuclei which will have a sensitivity at least one hundred times greater than the previous experiment. As in the previous experiment, we chemically separate the Sr fraction from a Rb sample. The separation procedure utilizes the insolubility of $SrCo_3$ in H_2O. A 400 gram sample of Rb_2CO_3 was dissolved in 200 ml of H_2O. A known amount of Sr^{++} carrier is then added to the solution. The non-radioactive Sr and any $^{87}Sr^m$, if present, precipitate as $SrCO_3$ and are filtered out of solution using the apparatus shown in Fig. 2.1-2. The $SrCO_3$ precipitate is then placed on the front of a well shielded Ge(Li) detector and a search is made for the 388.4-keV γ-ray that is produced by the decay of the 2.8 hour $^{87}Sr^m$.

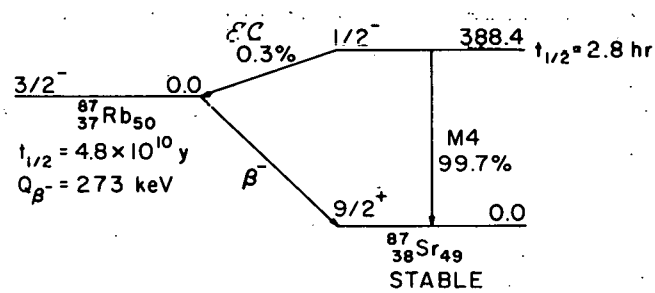

Fig. 2.1-1. $^{87}Sr^m$ Decay Scheme

A check of the separation procedure was made using ^{85}Sr and ^{86}Rb radiotracers that were produced at the University of Washington's nuclear reactor. Known amounts of ^{85}Sr and ^{86}Rb were introduced into a 100 gram sample of Rb_2CO_3 in H_2O. Following separation, the recovered $SrCo_3$ was counted using a Ge(Li) detector. This test showed that the level of Rb in the separated $SrCO_3$ was less than 0.1% of the amount in the original sample and that the Sr recovery efficiency was the 80-90% range.

To date the separation procedure has been repeated six times using the same 400 gram Rb_2CO_3 sample. The Sr recovery efficiency from each separation was determined by using a known amount of Sr carrier and weighing the separated $SrCO_3$. No excess of counts above background was observed in the region around 388.4 keV. From these measurements we have determined that at the 2σ confidence level the lifetime for this charge non-conserving decay is

$$\tau_{CNC} \geq 4 \times 10^{17} \text{ years}$$

The experiment is presently being revised in an attempt to increase our sensitivity by another factor of ten. Instead of searching for the γ-rays emitted in the decay of $^{87}Sr^{m}$, we plan to look for the conversion electrons which are also emitted. By using silicon surface-barrier detectors, we should be able to reduce the background and increase our detection efficiency, thus increasing the experimental sensitivity.

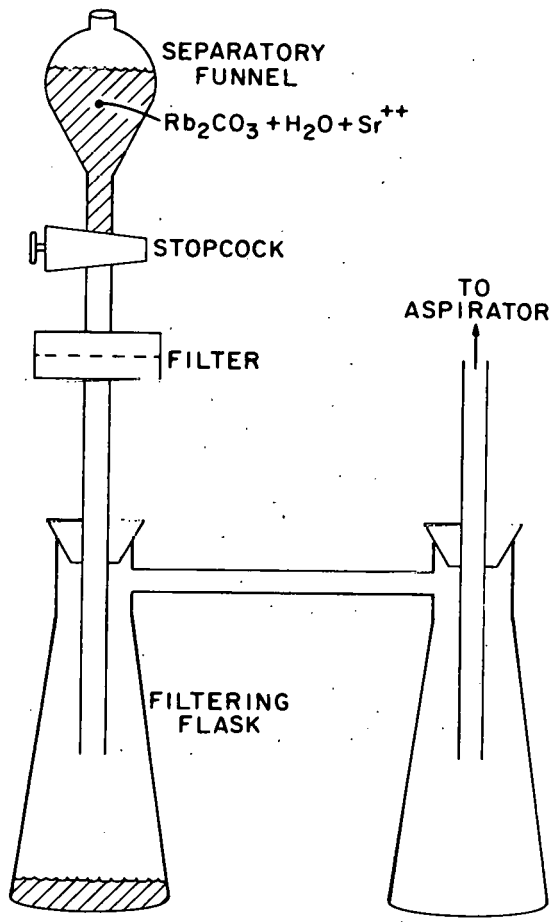

Fig. 2.1-2. Apparatus used to separate Sr fraction from Rb sample

1. M.K. Moe and F. Reines, Phys. Rev. 140, 992 (1965).
2. J.N. Bahcall, Rev. Mod. Phys. 50, 881 (1970).
3. A.W. Sunyar and M. Goldhaber, Phys. Rev. 120, 871 (1960).

2.2 Parity Mixing in the J=1/2 Doublet of ^{19}F

E.G. Adelberger, T.A. Trainor, H.E. Swanson and R. VonLintig

Our data from the Mark II version of the ^{19}F experiment discussed in last year's annual report[1] showed a statistically significant parity violating asymmetry in the 110 keV γ-ray. The simultaneously measured asymmetry in the 74 keV γ-ray from the decay of a 0^+ state in ^{22}Na was zero within statistics. This is expected since a J=0 state must decay isotropically. However, the 74 keV asymmetry showed a curious behavior that was not observed for the 110 keV γ-ray—namely a significant difference between results taken with the Wein precessor NORMAL and REVERSED. This indicated a dependence on the transverse field in the spin flip region (T-coil)[2] rather than on the beam polarization. Of course our experiment was designed to correct for just such effects since we always ran for essentially equal charges in both Wein precessor states. However it is hard to see what physical process would affect the 74 keV γ-ray in this fashion and not also produce something similar in the 110 keV γ-ray.

During the last year we investigated this problem further. We made an additional 1 week run with the two Ge(Li) detectors interchanged. The 110 keV γ-ray results were typical; the 74 keV asymmetry did not display a significant dependence on T-coil state. The accumulated results of the Mark II experiment are shown in Figs. 2.2-1 and 2.2-2. In Fig. 2.2-1 the results for each Wein precessor state are plotted separately. There is a clear difference in the 74 keV asymmetry in the two Wein precessor states—when the two precessor states are averaged this effect is cancelled and the resultant (false) asymmetry is very small $\delta_{74} = (0 \pm 13) \times 10^{-6}$. On the other hand there is no significant difference in the 110 keV asymmetries in the two precessor states. If we assume that the "74 keV effect" is due to some unexplained misalignment of the ion source or detection system then one would expect that the "74 keV effect" would average to zero on a week-by-week basis. It appears to do so as shown in Fig.

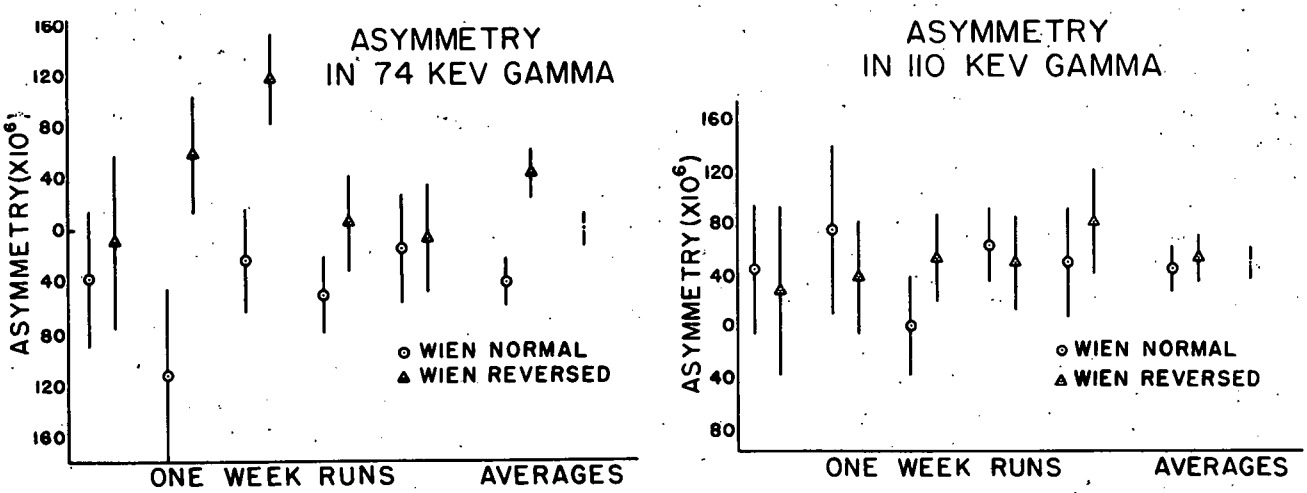

Fig. 2.2-1. Asymmetries $A = \frac{1}{4}\left(\frac{L^+ R^-}{L^- R^+} - 1\right)$ of the 110 keV and 74 keV photopeaks. Results in two Wein precessor states are plotted separately.

2.2.2 where the two precessor states have been averaged for each one week run. The results are quite consistent with the spread in the one week runs being due only to counting statistics.

$$\delta_{74} = (0 \pm 13) \times 10^{-6} \qquad \chi^2/\nu = 6.75/4 \qquad P_{\chi^2} = 0.16$$

$$K\delta_{110} = (49 \pm 13) \times 10^{-6} \qquad \chi^2/\nu = 1.12/4 \qquad P_{\chi^2} = 0.88$$

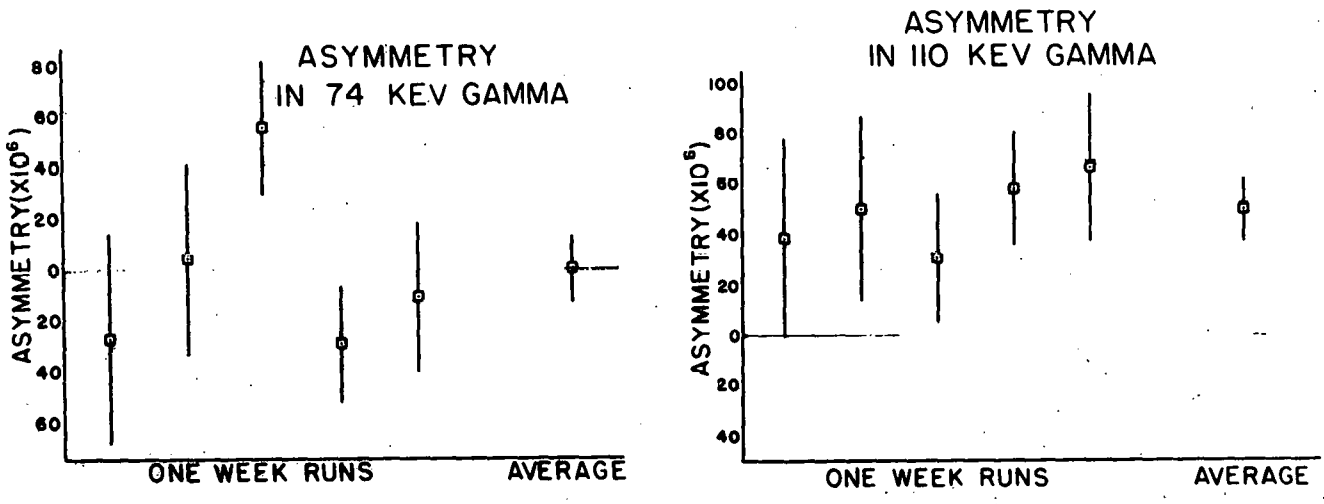

Fig. 2.2-2. Asymmetries of the 110 keV and 74 keV photopeaks. Data taken in the two Wein precessor states have been averaged.

One possible explanation for the unexplained behavior of the 74 keV asymmetry could be that an unresolved group lies underneath the peak from the 74 keV photon and that this unresolved group is responsible for the anomaly. We ruled this out by taking data at E_p = 4.5 MeV, just below the threshold for the 74 keV γ-ray. No peaks were observed in the location of the 74 keV photopeak and in addition the asymmetry of the background in the "74 keV" window was much too small to account for the effect.

We also made measurements of the spin correlated modulation of the position and angle of the beam on target using the beam-correlation analyzer.[3] We did not find any modulations large enough to explain the "74 keV effect."

At present we interpret our results as follows. When the 74 keV and 110 keV results are both processed as we had always intended to do (combining both Wein precessor states to cancel any T-coil dependent effects)—there is no apparent asymmetry in the 74 keV γ-ray. This demonstrates that our errors are indeed dominated by counting statistics. The asymmetry in the 110 keV photon shows a parity violating angular distribution asymmetry.

$$\delta_{110} = \frac{K\delta_{110}}{K} = \frac{(49 \pm 13) \times 10^{-6}}{(-0.55 \pm 0.07)} = -(90 \pm 26) \times 10^{-6}$$

1. Nuclear Physics Laboratory Annual Report, University of Washington, 1978. p. 8.
2. Nuclear Physics Laboratory Annual Report, University of Washington, 1977, p. 157.
3. H.E. Swanson, Ph.D. thesis, University of Washington (unpublished), 1974.

2.3 Parity Mixing in the J=1/2 Doublet of ^{21}Ne

E.G. Adelberger, C.A. Barnes, E.D. Earle, A.B. McDonald, K.A. Snover, H.E. Swanson, T.A. Trainor, and R.D. VonLintig

A. Introduction

The 2.8 MeV J=1/2 doublet in ^{21}Ne is an exceedingly interesting system for probing the parity nonconserving (PNC) N-N force. ^{21}Ne is the only odd-N, even-Z nucleus where a PNC matrix element connecting two levels has been inferred directly from a measurement of a pseudoscalar observable (via the two-state mixing approximation). When the effects in ^{21}Ne are combined with those in even-N, odd-Z nuclei, such as ^{19}F, one can hope to distinguish the relative roles of the $\Delta I=0$ and $\Delta I=1$ PNC N-N forces. One can see this for a highly simplified model, in which the $J=1/2^-$ level in ^{19}F consists of a proton hole in the ^{20}Ne(T=0) core, while the $1/2^-$ level in ^{21}Ne consists of a nucleon hole in the A=22 (T=1) core. Then simple considerations predict that the $\Delta I=1/\Delta I=0$ mixing in Ne will be -1/3 that in ^{19}F. A realistic calculation by Millener[1] gives -1/1.7 for this ratio. In addition ^{21}Ne is an exquisitely sensitive system since the splitting of the J=1/2 doublet is only 7.6 keV and the regular E1 transition from the $J^\pi=1/2^-$ level is highly retarded: $\tau_{\gamma_0} = 696 \pm 51$ ps so that[1] $|P_\gamma(2.789)| = |(9.5 \times 10^{-2}\ eV^{-1})| < + |H_{PNC}| - >|$. We populate the 2.789 MeV level of ^{21}Ne in the ^{21}Ne(p,p') reaction at $E_p = 4.08$ MeV, near the peak of a 30 keV wide resonance. This reaction provides a more favorable ratio of 2.789 MeV/2.796 MeV γ's than any other reaction known to us, has no neutron channels open, and is suitable for high beam current experiments.

The circular polarization of the 2.789 MeV γ-ray was measured in a pair of transmission Compton polarimeter developed for our measurement of parity mixing in ^{19}F.[2] The polarimeters were modified to accept 3" x 3" NaI detectors rather than the Ge(Li) detectors used in the ^{18}F measurement (See Fig. 2.3-1 for the geometry of the experiment). The ^{21}Ne activity was produced by bombarding a cell containing 1.3 atmospheres of neon gas enriched to 95% in ^{21}Ne. The cell had a 0.0025 mm Mo entrance window and a watercooled Pt beam stop. A thin C "fuzzer" foil located ahead of the cell diffused the beam spot on the target cell.

The data acquisition system is depicted in Fig. 2.3.2 and is essentially that developed for the ^{19}F parity violation experiment.[3] The polarized source magnet switching controller reverses the polarimeter magnetic fields and routes signals (beam current integration, time, detector pulses) to the proper scalers and groups in the multichannel analyzer. The four resulting spectra (2 detectors

X 2 magnet polarities) are then analyzed in a manner previously described.[4] Peak areas are generated and four-fold peak area ratios in which beam current fluctuations and many instrumental asymmetries automatically cancel, are calculated. The ratios are related to the helicity of the gammas by:

$$\delta = \left(\frac{\sqrt{\frac{L^+ R^-}{R^+ L^-}} - 1}{\sqrt{\frac{L^+ R^-}{R^+ L^-}} + 1} \right) = \eta f P_\gamma$$

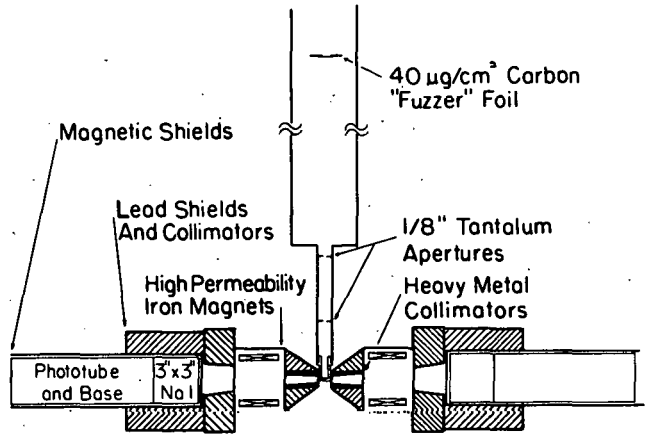

Fig. 2.3-1. The arrangement of detectors, polarimeters, gas cell and beam collimator in the ^{21}Ne parity violation experiment.

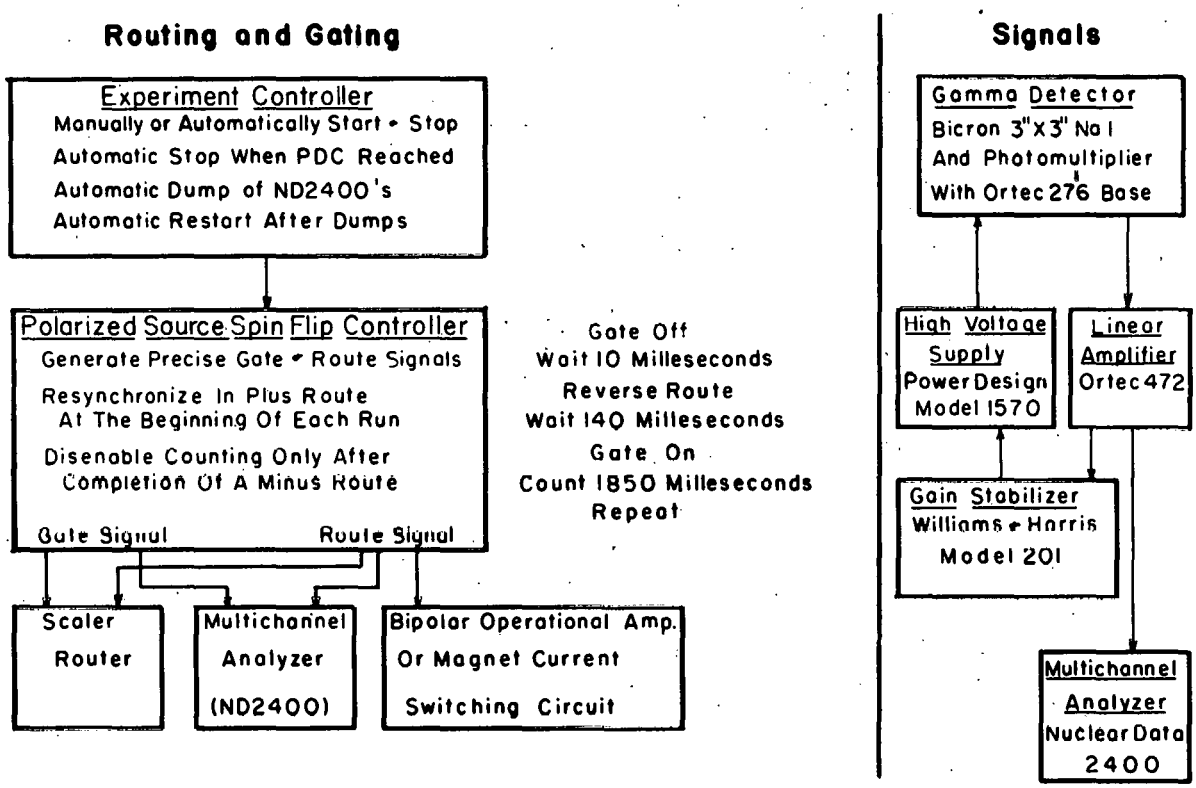

Fig. 2.3-2. Sketch showing routing logic and signal electronics.

where L(R) = Peak area from left (right) detector
+(-) = Peak area is accumulated while magnetic fields face left (right)
δ = Peak area asymmetry
Circular Polarization (P_γ) = $\delta/\eta f$
η = Polarimeter efficiency = -0.034
f = 2.789 MeV peak area "dilution" factor

B. Results of the Circular Polarization Measurement

Data were accumulated in two runs, each of about 2 weeks duration. The results of our first run, with 7 μA on target, yielded[5] $P_\gamma(1.789) = (+9 \pm 51) \times 10^{-4}$. Since these results have already been published[6] they will not be discussed further in this report.

For the second run several improvements were made to the experiment. These included increased beam intensity, improved outgassing procedures to reduce oxidation of the molybdenum foil under bombardment, and installation of better magnetic shields for the photomultiplier tubes. Realignment of the beam-shaping electrodes in the direct extraction source and experimentation with the source parameters, including aperture position, produced a 32 μA beam at the low energy cup. Several brief development runs proved that oxygen impurity in the gas cell was responsible for the failure of molybdenum foils during the previous data run.[4] Special care in outgassing the system and introduction of small amounts of hydrogen into the target gas ensured adequate foil lifetime. Substitution of commercially prepared magnetic shields with welded (instead of simply juxtaposed) end caps, reduced the average gain shift between magnetic field states by a factor of 10 to 0.005 percent. In addition, an electronically isolated, water-cooled beam collimation system was installed which allowed the current on the beam-defining aperture to be monitored. These improvements permitted us to run the experiment for 13 consecutive days at 14 μA target current with only four brief interruptions—three times to replace gradually failing molybdenum foils and once to switch filaments in the ion source.

The area asymmetries, δ, of both the 2.44 MeV and 2.79 MeV photopeaks for each 12-hours data collection period of the second run are displayed in Fig. 2.3-3. These values are obtained off-line using a computer program, PARITY, described previously,[4] which ensures that an exactly consistent basis for peak areas (including corrections for the slight gain shifts) is used for all four spectra. The phase of the polarimeter magnetic fields relative to the routing of scalers and multichannel analyzers was reversed typically after each 12-hour counting period as a precaution against instrumental asymmetries. The signs of those asymmetries obtained with the phase reversed have been changed in the figure and in compiling the overall results. It is readily apparent that there are no significant differences in the results for the two modes of data collection.

The average asymmetries obtained for the second data run were:

δ(2.79 MeV) = $(-122 \pm 56) \times 10^{-6}$ ~~± 16~~ 53

δ(2.44 MeV) = $(-\ 4 \pm 27) \times 10^{-6}$

δ(Background) = $(\ 45 \pm 52) \times 10^{-6}$

Based on next page

16 is absolutely wrong and I think -122 is also wrong. I don't know where these numbers came from.

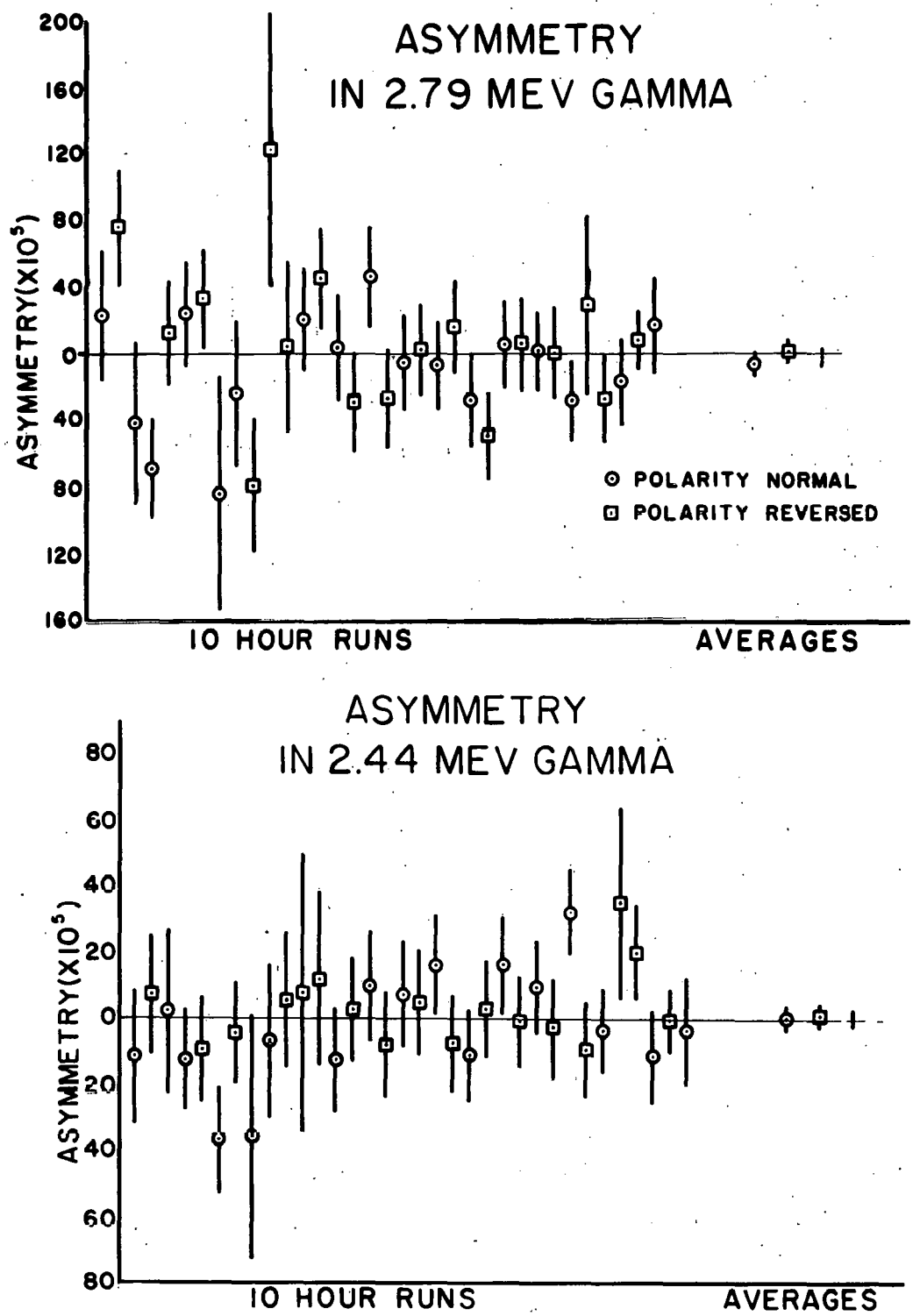

Fig. 2.3-3. Run by run record of asymmetries measured for the 2.79 MeV gamma ray (top) expected to exhibit parity violation and the 2.44 MeV gamma expected to exhibit no parity violation.

The 2.44 MeV photopeak, as discussed previously,[6] is expected to exhibit a negligible asymmetry since the regular transition is a healthy E2 transition. That it and the background asymmetry are easily consistent with zero confirms the absence of instrumental symmetries in the system at this level.

The ratio of 2.780 MeV to 2.796 MeV γ's was slightly less favorable in the second run than in the first because the somewhat thicker Mo foils were used, which slightly "washed out" the (p,p') resonance used to populate the 1/2 level. As a result the "dilution" factor accounting for the reduction in the asymmetry by the presence of unresolved and unpolarized 2.796 MeV gammas in the 2.79 MeV photopeak is slightly less favorable for this run, ~0.46 compared to 0.52 obtained previously. The preliminary circular polarization obtained from the second data run is

$$P_\gamma = 0.36 \pm 0.34 \text{ percent}$$

Combining this with the value $P_\gamma = -0.10 \pm 0.56$ percent from the first run gives an overall preliminary result of

$$P_\gamma = 0.24 \pm 0.29 \text{ percent}$$

The theoretical predictions for $P_\gamma(2.789)$ are not yet in a completely satisfactory state. Millener[1] predicts a $|P_\gamma|$ of ~1% and 0.2% from the ΔI=0 and ΔI=1 matrix elements respectively. Brandenberg, et al. predicts values from 0.2 to 1.9% for the ΔI=0 matrix element depending on various models of the nuclear structure. Before our ^{21}Ne measurements can be interpreted in a decisive fashion it is clear that the "theoretical error bars" due to nuclear structure uncertainties will have to be reduced. We are pleased to acknowledge the theoretical and experimental efforts the Brookhaven group of Warburton, Millener and collaborators are continuing to devote to delineating the structure of ^{21}Ne. At this point however, it does seem as if the measured effect in ^{21}Ne is rather smaller than expected.

C. Measurement of the Circular Polarimeter Efficiency

E.G. Adelberger, K.A. Snover, H.E. Swanson, T.A. Trainor and R. Von Lintig

We have measured the efficiency of the circular polarimeters used in the ^{21}Ne parity violation experiment[6] for gamma rays of nearly the same energy as the 2.789 MeV gammas observed in that experiment. ^{24}Na sources up to 20 mC in strength were used to produce a reasonable count rate of the 2.756 MeV ^{24}Mg gamma. Each ^{24}Na source was produced by irradiating 1.6 grams of sodium fluoride powder in the University of Washington reactor. The sources had a geometrical extent very similar to the beam spot size used in the ^{21}Ne parity mixing experiment. The gamma rays, collimated by a series of lead apertures, passed through both polarimeter magnets mounted in tandem and were detected in a NaI detector. The magnetization of one of the magnets was reversed every 2 seconds (as in the main experiment) to produce a slightly polarized (about 3 percent) beam of photons with alternately positive and negative helicity. The other magnet, with constant

magnetization, then preferentially either transmitted or scattered the slightly polarized beam depending upon the relative polarity of the two magnets. The apparatus is displayed in Fig. 2.3-4.

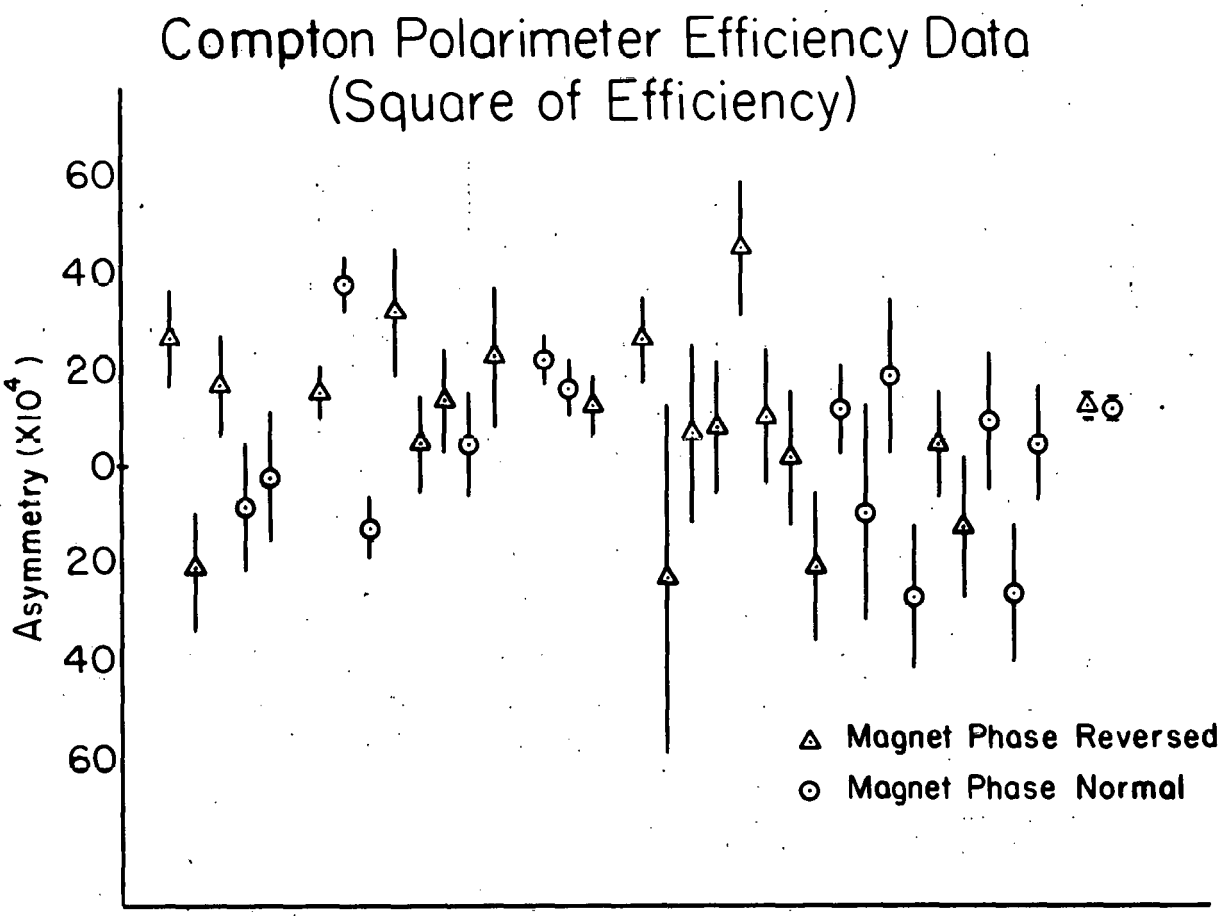

Fig. 2.3-4. Arrangement of polarimeters for the efficiency measurement

The measured effect in this experiment is the square of the efficiency or analyzing power of the polarimeters, and it was expected to be about 0.001 based upon a simple calculation and upon earlier measurements using ^{60}Co γ-rays at Caltech.[7] The measured effect is extracted from the full energy peak areas using the following expression:

$$\eta = [(N+/N-) - 1]2$$

N+ = Peak area with magnets parallel

N- = Peak area with magnets anti-parallel

The results are displayed in Fig. 2.3-5. Small but significant "dead time" corrections have been applied to the data. The corrections were based on a "pseudo-random" pulser which was counted simultaneously with the γ-rays. Although dead time was a small effect in this measurement (because of the low count rate and because only the difference in dead time for the two magnet polarities is important) the corrections affected our value for η by about 10%.

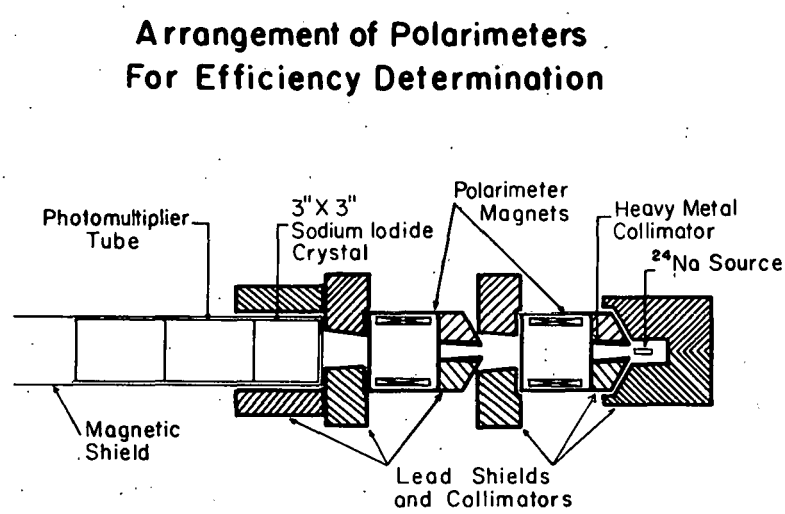

Fig. 2.3-5. Asymmetry measurements run by run for the polarimeter efficiency determination. The displayed quantity is the square of the polarimeter efficiency.

Combining all of the displayed runs gives the overall result:

$$\eta^2 = (11.99 \pm 1.63) \times 10^{-4}$$

$$\eta = (3.46 \pm 0.23) \times 10^{-2}$$

Without dead time correction the results were as follows:

$$\eta^2 = (9.34 \pm 1.63) \times 10^{-4}$$

$$\eta = (3.04 \pm 0.27) \times 10^{-2}$$

The data are displayed run by run in Fig. 2.3-5. In order to reduce possible systematic errors data were accumulated with either the upstream magnet or the downstream magnet flipping and with both possible senses of the multichannel analyzer routing. No significant dependence on the configuration was observed.

The value $(3.41 \pm 0.10) \times 10^{-2}$ we had been using (see Section 2.3B, p. 17 of this report) for the efficiency of the polarimeters at 2.789 MeV based on the Caltech efficiency measurement[2,7] is in excellent agreement with the value of $(3.46 \pm 0.23) \times 10^{-2}$ obtained in the present determination.

D. A Measurement of Polarization Transfer in ^{21}Ne($\vec{p}$,p') at E_p = 4.185 MeV

Our current upper limit for the parity-violating circular polarization (CP) of the 2.789 MeV γ decay in ^{21}Ne (see Section 2.3.6) is the result of nearly 4 weeks of running. A significant reduction of this uncertainty, even with improved apparatus, would require an unreasonable amount of machine time. We therefore decided to determine whether the parity mixing could be measured

more effectively by using a polarized beam to produce polarized ^{21}Ne's and then measuring the parity violating asymmetry in the angular distribution of gamma rays. This method eliminates the attenuation of gamma quanta and the low analyzing efficiency inherent in a Compton polarimeter, and it allows the detectors to be placed much closer to the gas cell. But these advantages are substantially offset by the smaller polarized beam (50 nA versus 15 μA) and by the inefficient transfer of polarization from the protons to the excited ^{21}Ne nuclei.

We measured the polarization transfer by measuring the parity-allowed CP of the $1/2^- \rightarrow 5/2^+$ 2.44 MeV γ-transition following inelastic scattering with a polarized incoming proton beam. The $1/2^- \rightarrow 5/2^+$ branch was chosen because this is the dominant decay of the $1/2^-$ level and because its multipole mixing ratio is known[1] (it was measured for this purpose). Equations (10) and (11a) of ref. 1 along with the E3/M2 mixing ratio reported in ref. 1 lead to

$$CP(2.44\ MeV) = -(0.55 \pm 0.06)P_w(1/2)\cos\theta$$

where $P_w(1/2$ is the polarization of the $1/2^-$ level and θ is the angle between the γ-ray and the $1/2^-$ polarization direction.

Work done at Chalk River in preparation for the circular polarization measurement discussed previously indicated that only near E_p = 4.18 MeV in the ^{21}Ne(p,p') reaction did one populate the $1/2^-$(2.789 MeV) level in ^{21}Ne with a reasonably large cross section, low background and favorable $1/2^-/1/2^+$ population ratio (the $1/2^- \rightarrow$ g.s. and $1/2^+ \rightarrow$ g.s. γ-decays cannot be resolved in a NaI detector). Hence our measurements of polarization transfer were limited to the same beam energy and target gas pressure and foil thickness as was found to be optimum for the CP measurement (Section 2.3.A). The gas cell and polarimeter geometry was as described in Section 2.3.A. The 4-counter polarimeter[7] developed for the ^{19}F parity mixing experiment was used upstream of the gas cell to continuously monitor the beam polarization which had an average value P = 0.76, with a beam current on target of about 45 nA. The routing of the NaI detectors and the flipping of the γ-ray polarimeter fields was as described in Section 2.3.A with the exception that here the magnetic fields in the 2 γ-ray polarimeters were always anti-parallel, and the sense of the routing electronics with respect to the polarimeter fields was not reversed. Beam polarization was in the reaction plane along the axis of the γ-ray polarimeters, and its direction was reversed several times during the course of the experiment. Measured asymmetries δ(2.44 MeV) (divided by beam polarization P) versus run number are shown in Fig. 2.3-6. These results were accumulated over 5 continuous days of running. The average value of $\delta(2.44)/P$ is $(1.59 \pm 0.92) \times 10^{-3}$, corresponding to an average circular polarization $CP \simeq \overline{[\delta(2.44\ MeV)/P]} \times P/\eta = (3.55 \pm 1.83\%)$, where

$\eta \simeq 0.34$ and $P = 0.76$ as given above. The polarization transfer is then given by $\Delta P = CP/(-0.55)P = 0.085 \pm 0.044$.

For a polarization transfer of this magnitude the detection of a parity violating asymmetry could be competitive (within a factor of 2) with the circular polarizations technique. However, 2 factors weigh strongly against pursuing this technique:

1) In order to interpret a parity-violating asymmetry in terms of a parity mixing amplitude, one must know the M2/E1 mixing ratio for the $1/2^- \rightarrow 3/2^+$ (g.s.) decay, since the asymmetry is quite sensitive to this mixing ratio[1] (the circular polarization is not). The required measurement would be to observe CP (2.789 MeV) with polarized beam. Here the 2.789 and 2.796 MeV γ-rays must be resolved, and hence this would be an extremely difficult measurement.

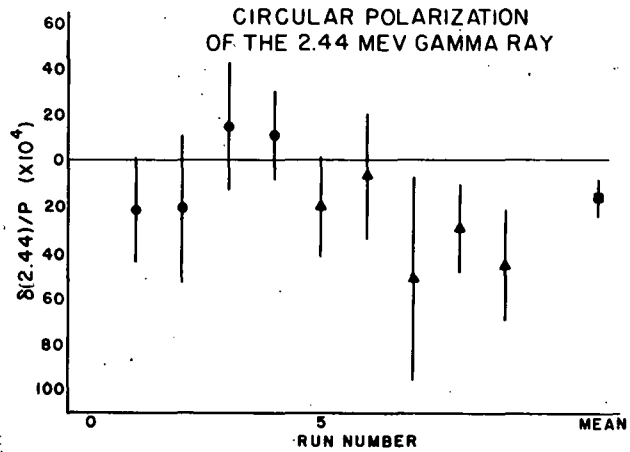

Fig. 2.3-6. Measured asymmetry divided by beam polarization $\delta(2.44\ \text{MeV})/P$ versus run number, the solid dots correspond to data obtained with positive beam polarization and the triangles to negative beam polarization.

2) A much bigger effort would have to go into an improved polarization transfer measurement with a small enough uncertainty to be useful in interpreting an asymmetry measurement.

Thus, all things considered, we needed to find a much bigger polarization transfer in order that the asymmetry technique be attractive to us. Further, the circular polarization experiment can be improved using more polarimeters (e.g., four positioned symmetrically about the beam axis) and larger detectors (e.g., 5" by 5" instead of 3" by 3" sodium iodide crystals). Such polarimeters are being designed and constructed at Chalk River Nuclear Laboratories.

---

† Kellogg Laboratory, Caltech, Pasadena, CA 91125.

†† Chalk River Nuclear Laboratories, ASCL Chalk River, Ontario KOJIJO, Canada.

1. D.J. Millener, E.K. Warburton, K.A. Snover, P.G. Ikossi and R.D. VonLintig, Phys. Rev. C 18, 1878 (1978). See also Nuclear Physics Laboratory Annual Report, University of Washington (1978), p. 23.
2. C.A. Barnes *et al.*, Phys. Rev. Lett. 40, 840 (1978).
3. Nuclear Physics Laboratory Annual Report, University of Washington (1977), p. 157.
4. Nuclear Physics Laboratory Annual Report, University of Washington (1978), p. 132.
5. In Ref. 6 a small mistake was made in computing the error in the circular polarization. The correct value is $(+9 \pm 56) \times 10^{-4}$.
6. K.A. Snover *et al.*, Phys. Rev. Lett. 41, 145 (1978).
7. M.M. Lowry, Ph.D. Thesis, Caltech, 1979.

8. Nuclear Physics Laboratory Annual Report, University of Washington (1976), p. 36.
9. R.A. Brandenburg, B.H.J. McKellar and I. Morrison, Phys. Rev. Lett. 41 (1978), 618.

2.4 Parity Mixing of the $2s_{1/2}$-$2p_{1/2}$ States in Hydrogen Atoms

A. Introduction

E.G. Adelberger

One of the important problems in weak interactions involves the e-N neutral current interaction. In this interaction there are 4 fundamental parity violating (pv) terms, which are denoted[1] as follows:

$$C_1^p = g_A^e g_V^p \qquad C_2^p = g_V^e g_A^p$$

$$C^n = g_A^e g_V^n \qquad C_2^n = g_V^e g_A^n$$

Experiments in heavy atoms[2,3,4] are sensitive primarily to $ZC_1^p + NC_1^n$. The SLAC experiment with longitudinally polarized electrons[5] also is primarily sensitive to the C_1 coefficients since the electron, rather than the nucleon spin is flipped (C_2 terms do enter through the y-dependence of the asymmetry, but it is difficult to measure this accurately).

On the other hand experiments in hydrogen and deuterium atoms can, in principle, determine all 4 of the C's.[1] We have begun a program to study the $2s_{1/2}$-$2p_{1/2}$ parity mixing in hydrogenic atoms. We intend first to measure C_2^p since this coupling is not well determined by any other experiments. We will then study deuterium to obtain $C_2^p + C_2^n$. The apparatus has been designed to make possible, at a later date, measurements of the C_1 coefficients as well.

The basic principles behind our experiment have already been presented[6] so we will only present a sketchy discussion here.

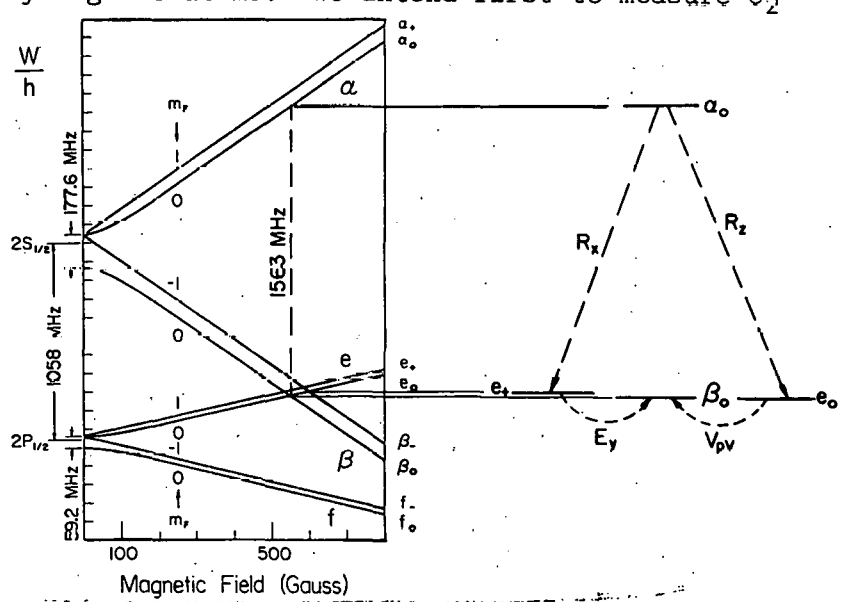

Fig. 2.4-1. left) Breit Rabi diagram for the n=2 $J^{1/2}$ states of hydrogen; right) transitions involved in the parity mixing experiment.

We try to drive E1 transitions between two of the hyperfine components of the $2s_{1/2}$ state ($\alpha \rightarrow \beta$ see Fig. 2.4-1). These proceed via $2p_{1/2}$ admixtures in the $2s_{1/2}$ state. The experiment is performed at ∿570 gauss where a $2p_{1/2}$ state (e) and a $2s_{1/2}$ (β) state cross. This enhances the parity admixture of the β_o and e_o levels. The $\alpha_o \xrightarrow{E1} e_o \xrightarrow{pv} \beta_o$ transition is interfered with an $\alpha_o \xrightarrow{E1} e_+ \xrightarrow{E} \beta_o$ transition where the p state impurity is induced by an external $\vec{E}$ field (Stark mixing). The parity violation is measured by changing the relative sign of the pv and Stark amplitudes, for example by changing the sign of the external $\vec{E}$ field.

During the last year a major effort was concentrated on building the apparatus. All major components are now constructed and installed and we have begun preliminary data taking with emphasis on understanding the line shapes and backgrounds. Our report on the experiment is broken down into sections in which some of the larger sub-projects in this experiment are described in more detail.

B. Theoretical Analysis of Atomic Transition Rates in the Experimental Apparatus

T.E. Chupp, M.Z. Iqbal and T.A. Trainor

In last year's annual report, we described calculations of the atomic transition rates of importance to the hydrogen atom parity mixing experiment. These calculations were based on the exact, analytical solution to the Schrödinger equation for the four level problem. It was necessarily assumed that the external static and oscillating fields in the rest frame of the atom turn on abruptly, remain constant and turn off abruptly. In a realistic situation these fields will rise and fall gradually; we have therefore developed a numerical integration routine to study the problem with arbitrary field profiles.

The computer code developed for these calculations grew from a program written during development of a spin filter polarized hydrogen, deuterium tritium source.[7] The original program was set up to calculate the populations of the four n = 2 levels of interest as a function of time. Our program calculates these populations as a function of axial magnetic field for a variety of electric field strengths. We consider six levels connected by oscillating and static electric fields and the possible parity violating interaction.

The Schrödinger equation is

$$i\hbar \frac{\partial}{\partial t} |\psi> = H|\psi> \text{ where } H = H_o + e\vec{E}\cdot\vec{r} + V_{pv}$$

H_o is the Hamiltonian for the atom in a constant magnetic field
$\vec{E}$ is the applied electric field
V_{pv} is the parity violating weak Hamiltonian.
The state $|\psi>$ may be written

$$|\psi> = \sum_{i=1}^{n} a_i(t) e^{-iw_i t} |i>$$

where the i are eigenstates of H_o and $n = 4$ (4-level problem) for each of the four important processes considered at the axial magnetic field strength 570 gauss. The Schrödinger equation then becomes

$$\frac{\partial}{\partial t} a_j(t) = \frac{1}{i\hbar} \sum_{i=1}^{4} \langle j | e\vec{E}\cdot\vec{r} + V_{pv} | i \rangle a_i(t) e^{-iw_{ij}t}$$

with $w_{ij} = w_i - w_j$.

Thus
$$|\alpha^+ \rangle = \phi_{2s} \, |m_j = 1/2 \; m_I = 1/2 \rangle$$
$$|\alpha^o \rangle = \phi_{2s} \, (\cos\theta_B \, | 1/2, -1/2 \rangle + \sin\theta_B \, | -1/2, \; 1/2 \rangle)$$
$$|\beta^o \rangle = \phi_{2s} \, (\cos\theta_B \, | -1/2, 1/2 \rangle - \sin\theta_B \, | 1/2, -1/2 \rangle)$$
$$|\beta^- \rangle = \phi_{2s} \, | -1/2, -1/2 \rangle$$
$$|e^+ \rangle = \phi_{2p} \, | 1/2 \; 1/2 \rangle$$
$$|e^o \rangle = \phi_{2p} \, (\cos\theta_B \, | 1/2, -1/2 \rangle + \sin\theta_B \, | -1/2, 1/2 \rangle)$$

The hyperfine mixing angle θ_B is given by $\tan 2\theta_B = \Delta W / 2\mu_o B$; ΔW is the hyperfine splitting for the 2s state and μ_o = Bohr magneton.

Selection rules require that these states are connected in the four level problems as follows:

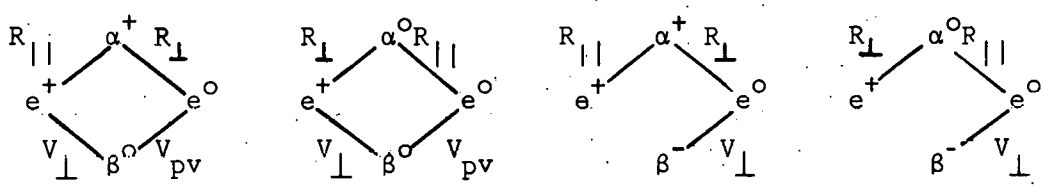

where $R_{||} = E_z^1 \cos wt$ is an axial Rf electric field

$R_\perp = (E_x^2 + iE_y^2) \cos wt$ is a transverse Rf electric field

$V_\perp = (E_x^3 + iE_y^3)$ is a transverse static electric field

The validity of four level instead of six level calculations was discussed in last year's annual report. In addition, numerical calculations of the six level problem using straightforward, fixed step size integration shows that the four level and six level problems give similar results for the population of the β states. Six level numerical calculations will be carried out with the more sophisticated integration techniques described below.

The fundamental advantage of this numerical technique is that the profiles in time of the electric fields can be controlled. For the exact calculation fields, necessarily rise and fall abruptly. The fundamental disadvantages are the limited accuracy estimated to be 1% and the long calculational times on the laboratory's PDP 1160. For the purposes of analyzing experimental results, the 1% accuracy presents no problem.

Each of the four processes are calculated separately and the total population of the β states is given by straightforward addition of the four independent probabilities:

$$|\beta|^2 = |\beta_o^I|^2 + |\beta_-^{II}|^2 + |\beta_-^{III}|^2 + |\beta_-^{IV}|^2$$

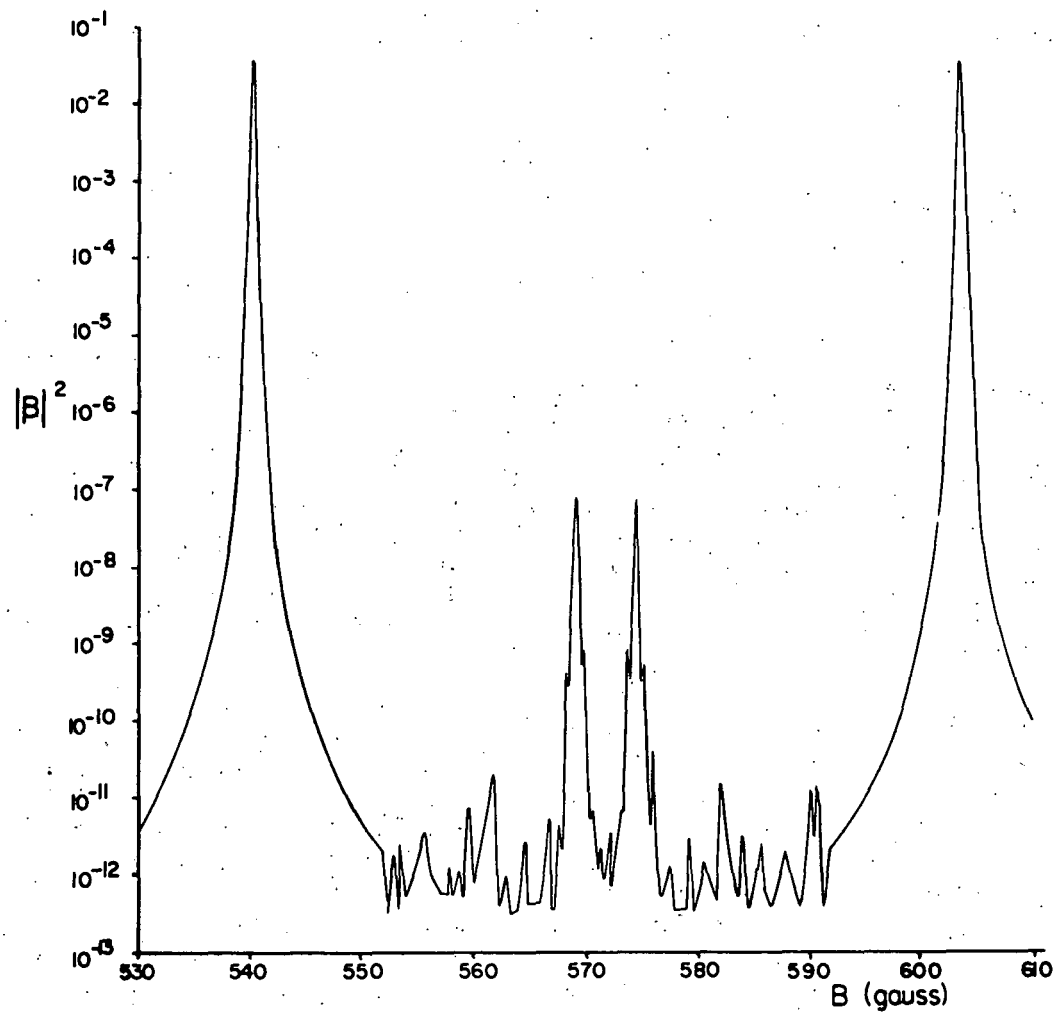

Fig. 2.4-2. Calculation of β state transmission as a function of axial magnetic field at 1608 MHz.

Where I refers to process (I), etc. The 4 coupled first order (in time) differential equations are integrated using a 4^{th} order Adams-predictor corrector algorithm. The first derivatives $\partial/\partial t\, a_j(t)$ are calculated for each t with the step size variable. Since these first derivatives depend on $\vec{E}$, the value of the perturbing field is calculated for each t as well.

Figure 2.4-2 shows the results of a typical calculation. The field strengths are close to the optimum calculated with the exact calculation. The profile in time of the perturbing fields consists of gaussian rise and fall with varying half-widths, and a flat region between. The rise and fall times are typical of bead pulls for the Rf fields and electrostatic tank measurements for the static fields. The total integration time of 1.6 μsec was taken in about 10^4 steps with a maximum error of 10^{-4} per step. As expected, the most striking difference between results of this calculation and the earlier exact calculation is the much lower background and enhanced peak to valley ratio due to the smoother turning on of the perturbation. This is confirmed in our measurements with the apparatus and predicts much more favorable experimental conditions than the exact calculations.

C. Apparatus Development

i. Introduction

E.G. Adelberger and T.A. Trainor

We have completed and installed all of the hardware systems required for our initial hydrogen-PV experiment design. Studies of prototypes for our large solenoid and main rf cavity as well as computer simulations of several other systems were reported in last year's annual report.[8] Final designs based on these studies have been arrived at and construction is completed on all major items. During the prototype studies we have developed a number of novel construction techniques and introduced locally several technologies not ordinarily found in a nuclear physics laboratory. In this introduction we briefly discuss the main items of apparatus, which are described in greater detail in separate articles below.

Main Solenoid — This solenoid is 1400 turns of #4 square copper wire, 125 cm long and about 32 cm diameter. The solenoid was lathe-wound and potted with high thermal conductivity epoxy. The flux return is 1004 low-carbon steel plates welded into an octagonal shell. The total mass is about 800 kG. The maximum magnetic field is 1200G at 100 amps. The solenoid liner is an electropolished stainless steel tube with a 26 cm ID. Flanges mounted at either end of this tube with aluminum O-rings form the bulk of the ultra-high-vacuum system. The electropolishing was performed with a solution of hypophosphoric acid, glycerin, and water at 110°C. The heated tube was rotated during polishing while a current of 200 amps was passed through the solution for two hours.

Main Rf Cavity — This cavity is 50 cm long and has a square cross section. It resonates in the TM_{110} mode at 1608 MHz. It is fabricated of copper and gold-plated stainless steel. Isolated sections of the side plates are ter-

minated in $\lambda/4$ slots to maintain a high Q ($\sim$5000).[9] These isolated panels were carefully designed, via electrolytic tank measurements and computer simulation, to generate the required static electric field shape along the beam axis.

Cryopumps — These are two helium expander modules driven by an 8 watt compressor unit. The cryopanels were developed by us to be mechanically compatible with our complex apparatus and to have large pumping speeds for hydrogen, our principle gas load. The final panels are nickel-plated OFHC copper. Hydrogen pumping is provided by activated charcoal granules fixed to the inner 20°K panels by sodium silicate adhesive. Total pumping speed for hydrogen is about 10,000 ℓ/s.

Sublimation Pump — The potential gas load in our UHV system is dominated by the beam itself. To insure the required vacuum we "dump" the beam inside a titanium sublimation pump of our own design after it has passed through the solenoid. The solenoid and pump are separated by a differential pumping tube.

Helmholtz Coils — These are four coil assemblies contained in welded stainless steel cans inside the UHV system. The coils are attached to the Rf cavity exterior and provide a transverse magnetic field whose magnitude along the beam axis matches the shape of the static electric field generated inside the cavity. The final coil design was arrived at via prototypes and computer simulations concurrently with the cavity design work.

Lyman-α Detectors — We are using proportional gas counters with NO gas fill and MgF_2 windows. We have observed that these counters lose efficiency after a period of use in high fluxes of L-α radiation. We find that the efficiency is fully restored by refilling with purified NO gas. We have developed a fractional distillation system for the purification process. We have observed efficiencies after refilling of $\sim$80% (compared with $\sim$63% factory specification). These detectors are used with a spherical mirror system designed by us and produced commercially. The mirror surface is evaporated aluminum covered by a MgF_2 layer to prevent oxidation. The reflectivity is 70-80% depending on incidence angle.

Computer Interface — We will use a microprocessor to control automatic variation and sampling of experiment parameters. This processor communicates with our PDP 11/03 and various peripherals via an IEEE 488 Bus. A compiler has been written and the processor has been used for simple voltage sampling tasks during some of our preliminary runs.

An overall view of the apparatus is shown in Fig. 2.4-3. The frame is two 4" x 8" aluminum I-beams resting on two aluminum towers. Three of the four major sections of the device are mounted on wheeled carts for easy access. Wheels on one side are on a V-groove and typical runout is ± 0.13 mm.

More detailed descriptions of some of the apparatus as well as results of various metastable beam studies with this complete apparatus are discussed below.

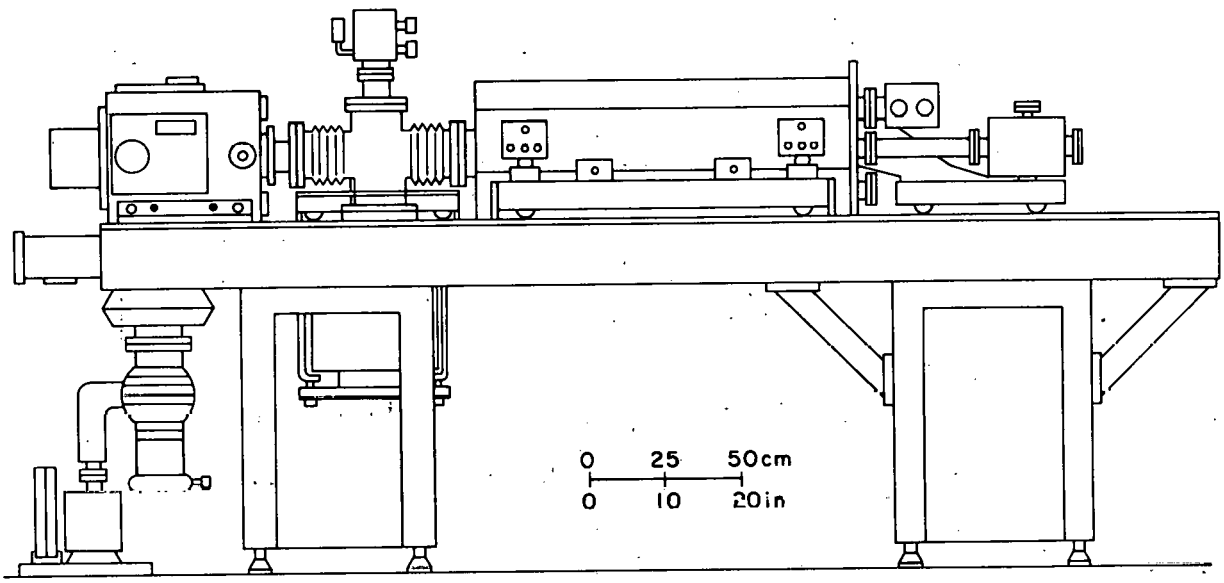

Fig. 2.4-3. Elevation view of parity violation experiment.

ii. Construction and Testing of the Large Solenoid for the Hydrogen Atom Parity Mixing Experiment

T.E. Chupp, W.B. Ingalls and T.A. Trainor

The large solenoid which provides the 570 gauss B_z for the hydrogen atom parity mixing experiment, has been operational since October, 1978. In the last year the following work was completed: final design and construction of the iron flux return; construction of the ultra high vacuum vessel; winding of the solenoid and final trimming of the magnetic field profile; and construction of the freon cooling system and associated interlocks.

The availability of very soft steel for the construction of precise electromagnets for research purposes has been drastically reduced since ARMCO has discontinued its production of what used to be the standard material. We therefore decided to use an ASTM 1004 grade steel, available only in sheets. The flux return was therefore redesigned with an octagonal cross section instead of the originally conceived cylindrical shape. The octagon is 18 cm on each side and the entire flux return is 135 cm long. A net magnetic moment initially present after construction of the solenoid was reduced by degaussing with high currents at 60 cycles flowing through a spiral of cable wrapped around the solenoid.

The flux return is incorporated into the ultra high vacuum system as shown in Fig. 2.4-4. Innermost is a stainless steel tube of 26 cm ID. This has been welded to the iron of the flux return at the downstream end and mates to commercial conflat flanges at the upstream end. The solenoid itself surrounds this innermost tube with space provided for freon flow. The entire assembly of vacuum vessel, solenoid and flux return weighs 900 kg.

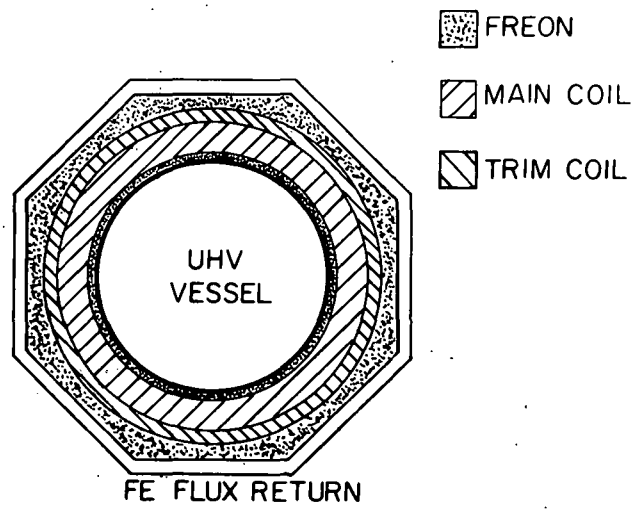

Fig. 2.4-4. Cross section of solenoid

The main coil of the solenoid was wound in a single day (September 21, 1978). The coil was wound of (1400) turns in 8 layers of square cross-sectional, insulated magnet wire (0.202" x 0.202"). The entire solenoid is held together with heat conducting, electrically insulating epoxy. The profile of B_z vs. z was measured and a computer code was employed, first to match the magnetic effects of the flux return and then to predict the positions and configurations of the trim coils which would produce the desired field profile. The goal of uniformity of 0.1 gauss over 50 cm has been achieved with the combination of coils shown in Table 2.4-1. The resultant profile of B_z is shown in Fig. 2.4-5.

Table 2.4-1. Main Magnet Configuration

	Number of Turns	Shunt
Main coil	1400 (6 x 233)	none
Upstream trim coil	28 (4 x 7)	0.08Ω
Downstream trim coil	20 (4 x 5)	0.03Ω
Upstream single turn	1	3-1/2 #16 copper wire
Downstream single turn	1	4" #16 copper wire

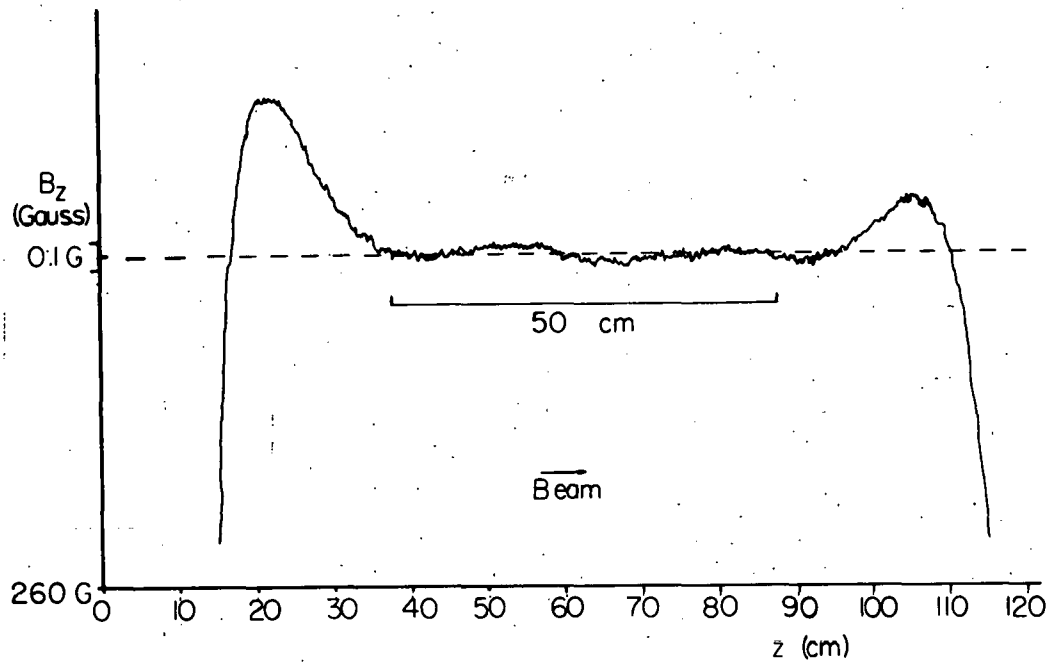

Fig. 2.4-5. Profile of axial magnetic field

The total power dissipated by the solenoid at 1100 gauss will be 6.5 kw. A freon cooling system with 30 ℓ/sec capacity has been constructed to cool both the solenoid and the smaller helmholz coil.

The large power supplies are interlocked to this cooling system such that the solenoid will not operate without cooling. The interlocks may, however, be overridden so that the solenoid coil can be employed as a bakeout heater for the ultra high vacuum system.

iii. H-Atom Helmholz Coils

E.G. Adelberger, C.D. Hoyle, and T.A. Trainor

Helmholtz coils, to produce a magnetic field perpendicular to the field of the main solenoid (beam axis), were designed and constructed. The criteria for the magnetic field produced by these coils was that the field have the same form factor as the static electric field in the RF cavity and a maximum value of 50 gauss. The form factors are required to be the same so that the motional magnetic field seen by the hydrogen atoms moving through the static electric field can be cancelled by the field of the coils.

Given the well known form of a static electric field in a box (RF cavity) with one side at +V, the opposite side at -V, and other sides grounded, the obvious solution was to mount rectangular coils on the outside of the grounded sides of the cavity that are parallel to the beam axis. However there were two problems with the simple solution. First, since the coils by necessity were further away from the beam axis that the sides of the RF cavity, the magnetic field fell off more slowly than the static electric field. Second, the magnetic field due to a single coil changes sign as one passes the end of the coil whereas the static electric field does not change sign but simply goes to zero. The first problem of an electric field that fell too fast was solved by introducing a set of ground wires in the cavity to make the field fall more slowly. The second problem of the negative undershoot of the magnetic field was solved by adding small rectangular trim coils at the ends of the main Helmholtz coil which were wound in the opposite sense cancelling the undershoot.

Five main Holmholtz coils and ten trim coils were wound; each main coil is 15-3/4" x 3-5/8" x 13/16" and consists of 225 turns of 5 amp #16 wire. Ten trim coils were wound; each trim coil is 3-3/4 x 1-1/4 x 13/16" and consists of 75 turns in series with the main coil. At present these coils are being installed in stainless steel, freon cooled, vacuum containers. One of the units will be mounted on each of the four sides of the RF cavity with the fifth unit held in reserve as a spare. A coil is mounted on each side of the RF cavity so that the field can be rotated in an arbitrary azimuthal angle, and can be reversed without ever going through zero.

iv. Ultra High Vacuum System for Hydrogen Parity Experiment

E.G. Adelberger, M.Z. Iqbal and T.A. Trainor

For the hydrogen parity mixing experiment a very good vacuum is required to minimize the background from β states produced by collision with residual gas. This report describes the design and construction, and testing of two cryopumps for use inside the solenoid to attain ultra high vacuum. The pumps are designed to pump hydrogen predominantly since the main residual gas is hydrogen from the neutral hydrogen beam.

Description of refrigerator: Two Air Products Corp. DE 202 expander modules with gas supplied from a separate compressor are used to cool the cryopanels. The first stage of each expander operates at about 35°K with no heat load and at 77°K with a heat load of 7 watts. The second stage operates below 10K with no heat load and at 20k with 2 watts.

In designing the cryopump the following points were considered:

1) The vapour pressure of hydrogen is a strong function of temperature at very low temperatures. So, a smaller surface area at a low temperature is better for pumping than a larger surface area at somewhat higher temperature.

2) Other than the heat of adsorption of hydrogen the main heat load on the cryopanels is from radiation, and the size of the pump is restricted by this.

The cryopanels must be shielded from thermal radiation. The system should be clean and cooled down in a good vacuum so that it is free from significant amounts of water. The cryodeposit of water can increase the emissivity by one order of magnitude and cool down may be unusually lengthy or impossible.

3) To pump hydrogen at about ∿10°K one needs adsorbent, activated coconut charcoal grains of about 0.85-1.7 mm (10/20 mesh) size which are found to be a very good adsorber. The charcoal is bonded by sodium silicate on the cold surface. Sodium silicate is inorganic with a low vapor pressure and makes a very thin layer keeping most of the charcoal grain surface exposed.

4) The surface of a cryopanel with charcoal should always face a black surface inside the heat shield. A commercial product of graphite suspended in alcohol is very convenient to paint black the inner surface.

5) There should be sufficiently large holes in shield for pumping. One needs to reach the optimization between heat load and pumping speed of the cryopump.

All cryopanels are made of nickel plated OFHC copper. Indium is used at each joint for good conduction of heat. The cryopumps as installed in the apparatus are shown in Fig. 2.4.6.

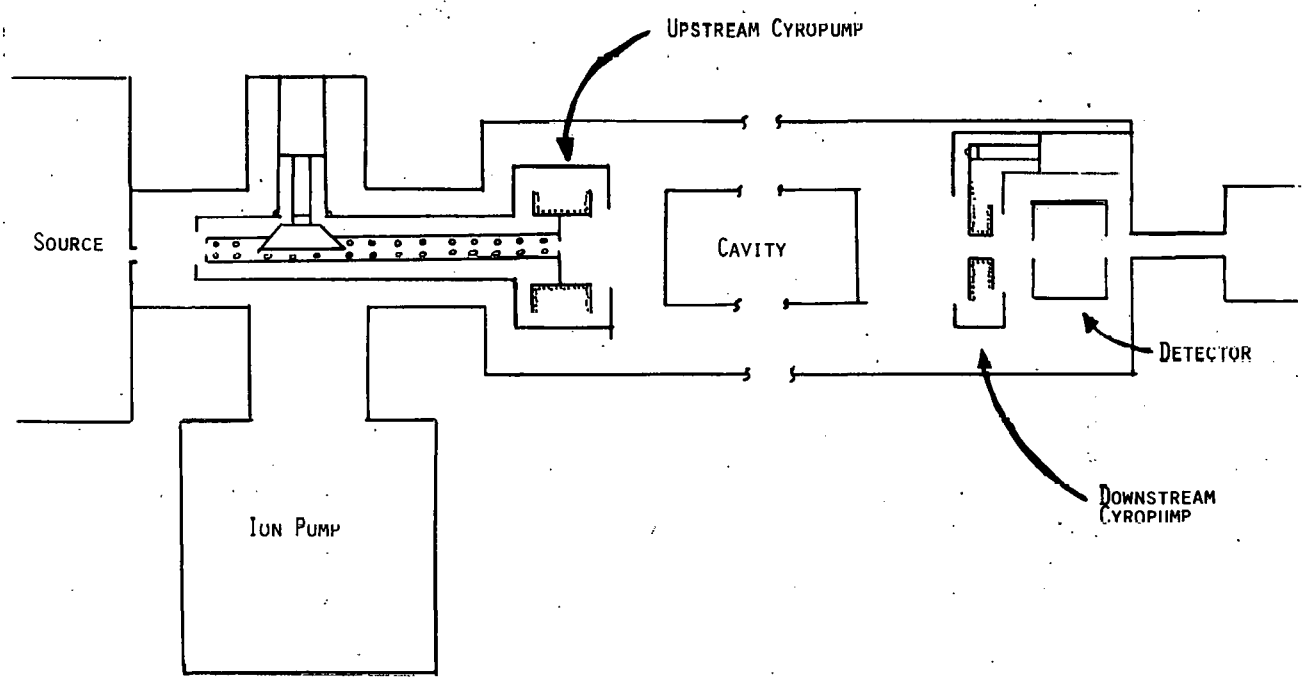

Fig. 2.4-6. The cryopumps as installed in the apparatus

Measurements of pumping speeds for hydrogen and nitrogen were made using a six-inch diameter copper plate (with and without charcoal) as cryopanel. Three two-inch diameter holes were made for pumping. The test chamber used had a diffusion pump but the base pressure was never better than 10^{-5} and always had significant amounts of water vapor on it. This restricted some of the measurements.

To measure the pumping speed a continuous flow of gas $\frac{\Delta v}{\Delta t}$ at atmospheric pressure P_o was let in and the change in base pressure ΔP inside the test box was noted. The pumping speed S is given by

$$S = \frac{P_o}{\Delta P}\left(\frac{dv}{dt}\right)$$

The test results are shown in Figs. 2.4-7 and 2.4-8. The pumping speeds are shown in Table 2.4-2.

Table 2.4-2. Measured Pumping Speed (1000 liters/sec)

Gas	Diff Pump	6" copper plate as cryopump with charcoal	6" copper plate without charcoal	Downstream cryopump
Nitrogen	0.382	1.21	1.00	2.77
Hydrogen	1.67	1.95	0	3.09

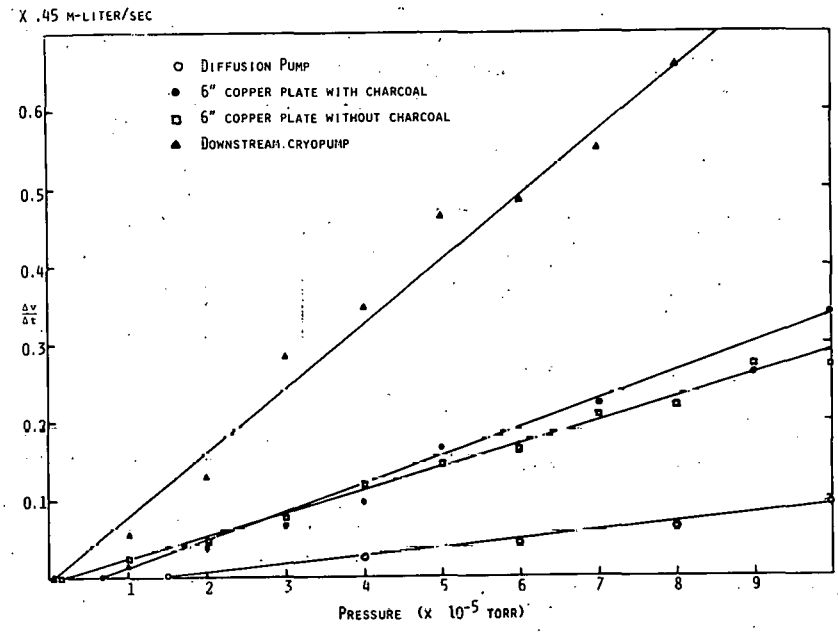

Fig. 2.4-7. The rate at which a volume of gas in atmospheric pressure is pumped, is plotted against the equilibrium pressure of the system. The slope is proportion to the pumping speed of nitrogen.

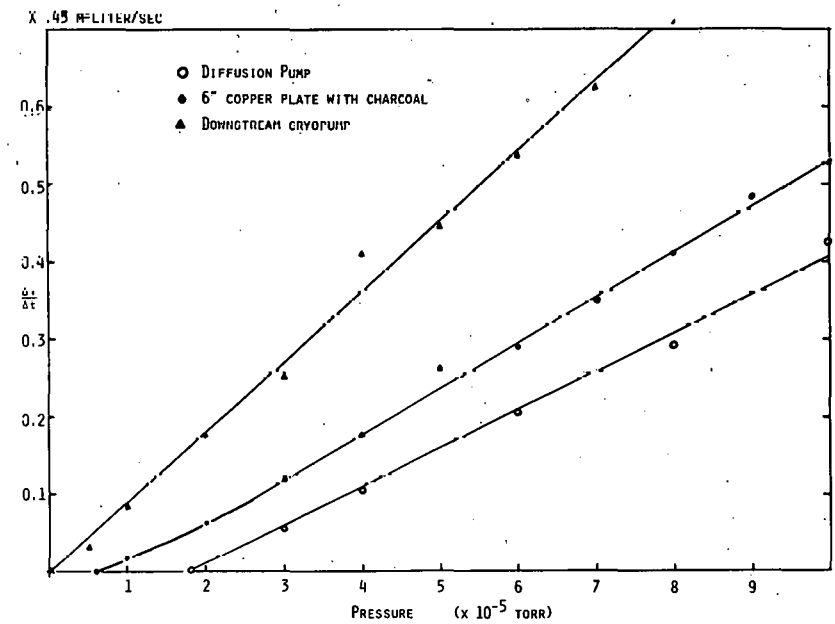

Fig. 2.4-8. The rate at which a volume of gas in atmospheric pressure is pumped, is plotted against the equilibrium pressure of the system. The slope is proportional to the pumping speed of hydrogen.

v. RF Cavities

E.G. Adelberger, T.E. Chupp, D. Holmgren and T.A. Trainor

The electric fields which drive transitions among the n = 2 states of hydrogen and deuterium for the hydrogen atom parity mixing experiment are produced in a resonant cavity described in last year's Annual Report. Both static and oscillating (at 1608 MHz) fields are required in the transition region; the static fields are perpendicular to and the RF fields are parallel to the axis defined by the atomic beam.

The RF fields are produced within the cavity which is 13.9 cm x 13.9 cm x 50 cm long. The TM_{110} mode is excited by a magnetically coupled loop at the middle of the 50 cm side. Another magnetically coupled, but smaller loop is located opposite this drive loop to monitor the power level within the cavity. A feedback signal from the pickup loop is used to maintain a constant power level in the cavity. The ratio of the energy stored in the cavity per cycle to the energy used to drive the cavity per cycle or the "Q" should be about 5,000 to insure stability of the power and to reject spurious, orthogonal modes. We have found that in order to achieve this Q and to reject unwanted modes, the cavity must come close to being a solid box with solid electrical contact throughout (though slots parallel to the beam axis do not have drastic effects). This box is therefore made up of four sides with triangular end pieces soldered to them. These sides are suspended from a superstructure which also supports the Helmholz coils.

Working cavities have been constructed in which the static electric fields are produced by two different schemes. In one scheme, parallel plates insulated from the grounded cavity end caps overlap the end caps to form a 1/4 wave choke. This scheme has worked well providing a Q of 5740. The investigations described in Section 2.4.c-ix were carried out with this scheme. An alternate scheme of producing static fields with parallel grids of parallel wire has been investigated for two reasons: 1) if the cavity sides are to be solid static fields which fall off slowly cannot be produced by simply biasing the cavity sides; and 2) the static field can be tailored to the desired profile which will match the profile of the magnetic field produced by the Helmholz coils. Measurements of electric field profile were carried out in a tank of electrolyte on a mockup cavity and grid scheme. The grids were biased with 10 V ac and a lock in amplifier wave used to measure the potential difference produced across a probe. By varying the spacing of wires in the grids, we have been able to match $V_{\perp}$ and $B_{\perp}$ as shown in Fig. 2.4-9.

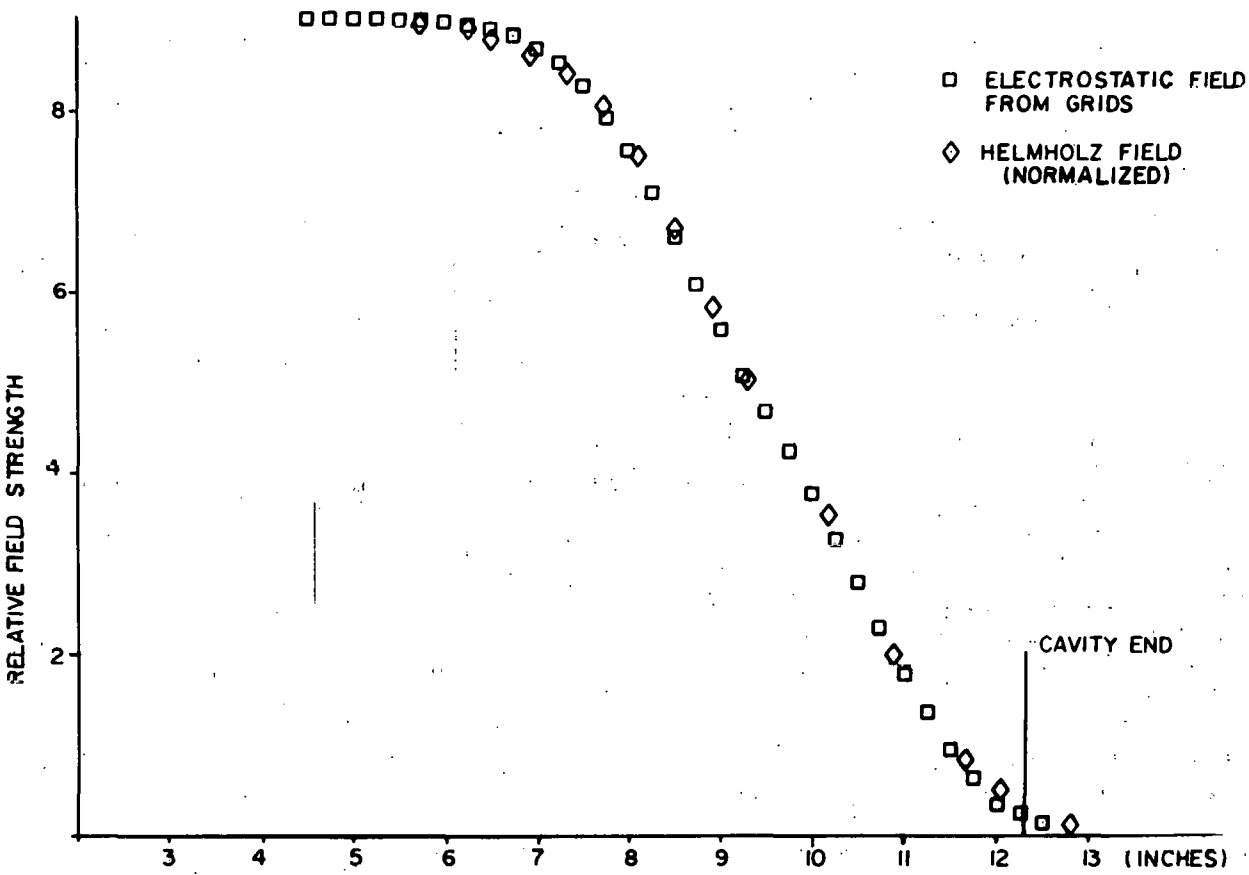

Fig. 2.4-9. Normalized field profiles of B_1 and V_1.

vi. β-State Quenching and Lyman-α Detection

E.G. Adelberger, K.J. Davis, E.N. Fortson and T.A. Trainor

The efficiency for detection of Lyman-α radiation produced by β-state quenching in the hydrogen parity experiment can be enhanced by the use of mirrors which focus the light onto two detectors. The ideal geometry for such an application involves two ellipsoidal mirrors, as discussed in our previous Annual Report (1978, p. 20). The principal drawback of an ellipsoidal geometry is the difficulty of fabrication. Consequently, we investigated the geometrical efficiency of a spherical approximation to an elliptical surface using a code for computer modeling of elliptical mirrors.[10] The detector geometry is shown in Fig. 2.4-10. It was found that a spherical geometry is acceptable though it reduces the size of the region in which the quenching must be accomplished. It was found also that the detector position can be varied to optimize the efficiency. A plot of optimum efficiency versus point sources position is given in Fig. 2.4-11. Roughly speaking, there is a cylindrical region 0.4 in. in diameter and 0.35 in. long for which the geometrical efficiency is approximately 95%. This region may be thought of as the "target" from the point of quenching.

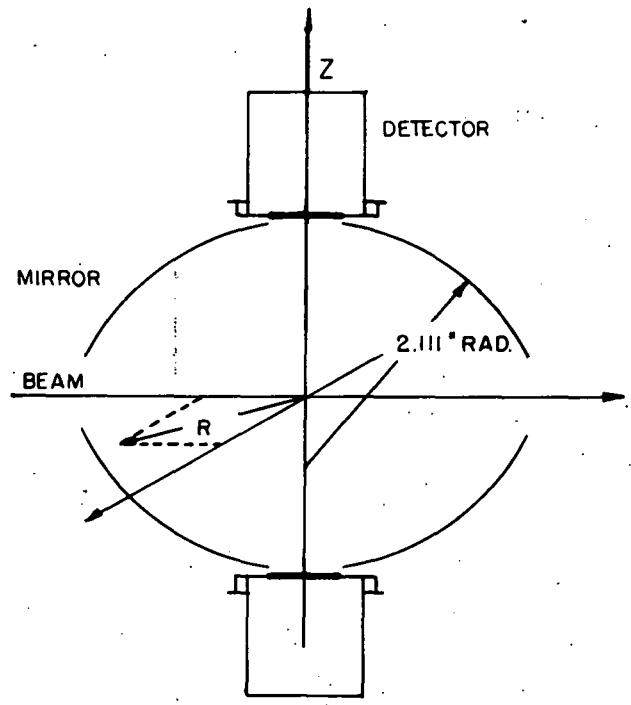

Fig. 2.4-10. A cross section of the detector arrangement consisting of two spherical mirrors and two detectors.

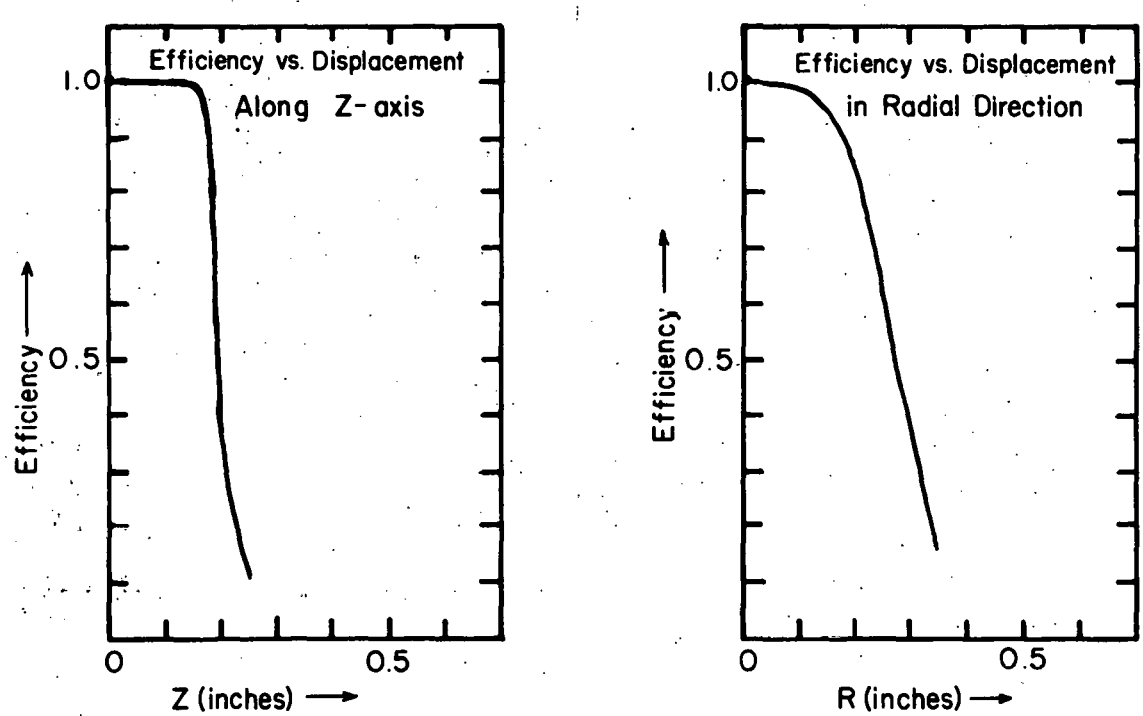

Fig. 2.4-11. Computed efficiencies of the system for point sources displaced from the origin in (a) the Z-direction and (b) the radial direction for the spherical mirror geometry with 5/8 in. diameter detector windows

The mirror surface must be carefully prepared to optimize reflection at 1216 Å. The mirrors are constructed from aluminum, Kanigen coated and polished so as to have a low scatter ultraviolet finish. Aluminum is then evaporated onto this surface and immediately followed by a 250 Å layer of MgF_2 which is relatively transparent at 1216 Å and protects the aluminum surface from oxidation and contamination. A reflectivity of ∿83% for normal incidence can be achieved by using these techniques.[11] Difficulties in obtaining a uniform MgF_2 coating may result in a reflectivity of only 70% at the edges of the mirrors. The fabrication, Kanigen coating and polishing is being done currently by the Muffaletto Optical Co. (Baltimore, Maryland) and the aluminum and MgF_2 coatings will be performed by Acton Research Corporation (Acton, Massachusetts).

The gas gain detectors from Artech Corp. (Falls Church, Virginia) are being specially made with a MgF_2 window 5/8" diameter, are fabricated entirely from non-magnetic material and are capable of being baked to 200°C.

A framework which attaches to the end plate of the main coil has already been constructed to hold the mirrors, detectors and quenching apparatus.

Quenching is achieved by a static electric field perpendicular to the quantization (beam) axis. In order to quench the beam within the target region the electric field must rise over as small a region as possible. The necessary field will be produced by two parallel oppositely biased wires near the center of the mirrors on each side of and perpendicular to the beam. This provides an approximately Lorentzian perpendicular field on axis. To make the field rise faster the beam travels through a grounded high transparency mesh tube before emerging between the wires. This configuration was mocked up at 4X scale and measured in an electrolytic tank. An on-axis scan of the electric field is shown in Fig. 2.4-12 after appropriate scaling. This represents a worst case since the field rises faster and to a higher value off-axis.

In the same figure, the calculated β-light distribution corresponding to the measured electric field is shown. 99.5% of the beam is quenched and most of it is in the target region. (NOTE: The beam diameter is ∿0.4 inch.)

Taking into account the various losses of β-light and including the detector efficiency of 66% an overall efficiency of ∿40% should be achievable.

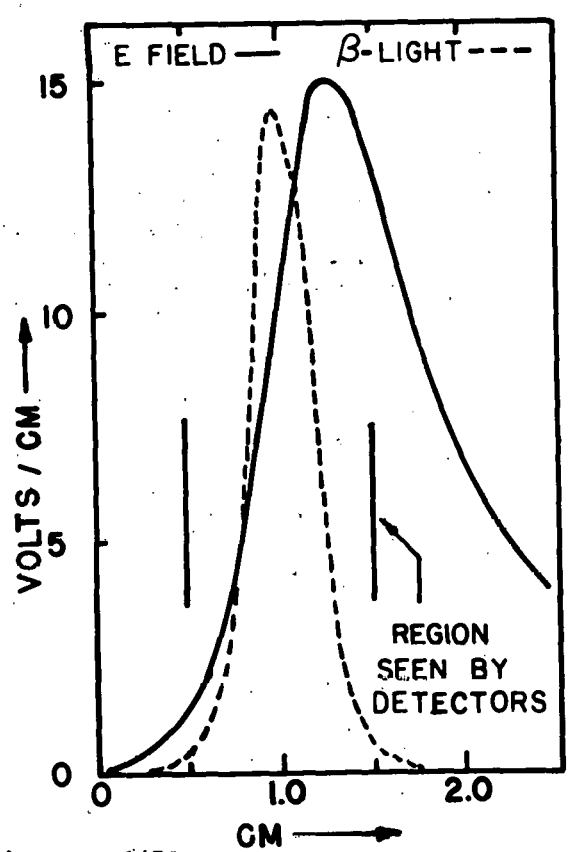

Fig. 2.4-12. A plot of the transverse static electric field and computed β-light distribution as a function of distance along the beam axis

vii. Purification of Nitric Oxide Detector Gas

E.G. Adelberger, W.B. Ingalls, H.E. Swanson and T.A. Trainor

A portable vacuum manifold for the purification of nitric oxide has been constructed for in situ replacement of the gas in the L_α detectors utilized in the hydrogen atom parity experiment. Dimers and other contaminants in the NO gas are condensed in a glass bulb cooled to approximately -120°C by an ethanol-LN_2 slurry. The NO gas is then condensed in a second bulb at LN_2 temperature and valved off. The first bulb is allowed to warm up and the contaminants pumped from the manifold. Three such separations are performed before the purified NO is transferred into the detector in the ultra high vacuum system via a transfer line passing through a vacuum feedtrough.

viii. H-Atom Control Computer

D. Peterson, D. Holmgren, and H.E. Swanson

As was discussed in last year's report,[12] a DEC PDP 11/03 computer was purchased to be used in the control and data acquisition system. Data communications to and from the 11/03 proceeds via IEEE-488 standard bus protocal (hereafter called Instrument Bus). Peripheral devices presently include a FLUKE 4800A digital volt meter, a KEPCO 12 bit power supply programmer, a CAL-COMP plotter, and a prototype experiment control interface. A set of Fortran callable subroutines and extensions to the BASIC interpreter allow high level language communication with bus devices. This software is restrictive as to data rates but presently meets our needs. It is clear however, that direct manipulation of the IBV-11 (instrument bus interface module) registers would allow considerably increased data rates should that become necessary.

The experiment control interface provides analog outputs which determine magnitudes and directions of electric and magnetic fields. In addition it has a series of single bit output and input channels for sense and control, and multiplexes the FLUKE DVM input allowing it to measure more than one analog signal. All analog components used in the interface are contained in a temperature stabilized oven to minimize thermal drifts. Analog outputs, in the case of electric fields, are amplified by a pair of high voltage op-amps in inverting configurations to obtain potentials symmetric about ground. Magnetic fields are generated using the analog signals to determine constant currents from KEPCO OPS power supplies where the sign bits are used to determine the sense of switching bridges. These bridges are described in a previous annual report,[13] with the significant difference being the use of newly available high power FETS which have much shorter switching times and a more linear behavior near zero current.

The data communications part of the experiment control interface is built around a MOTOROLA 6800 microprocessor and a 68-488 instrument bus integrated circuit. An MEK 6800 development kit was purchased and after the required instrument bus components were added, it provided both a convenient prototype and a means of programming using an attached key pad and display. To date, programs have been written to accept a block of data from the instrument bus and store it in memory. Thus field values calculated in the PDP 11/03 and

down loaded into microprocessor memory, can be sent to D/A converters which drive the E and B field supplies.

As an example it is desirable to reverse the sense of V without changing its magnitude. Since the field is generated with two orthogonal sets of capacitor plates, applying V $\sin(\phi)$ to one set and V $\cos(\phi)$ to the other allows first an initial positioning of the field at an arbitrary angle and then rotating ϕ through 180 degrees changes the sense without changing the magnitude, hence the desired effect. The switching waveform is still a square wave, but instead of having square edges, the transition proceeds sinusoidally. Having made the decision to build the system around the instrument bus, use of a microprocessor in the interface has an added benefit. The constraints of kHz switching speeds requires samples of the sine/cosine part of the waveform at about 10 microsecond intervals and instrument bus data transfer rates from the control computer are hopelessly slow even with efficient software. The microprocessor, however, is capable of the necessary sample rates as it just outputs the values previously sent from the 11/03 at its slower rates.

The interface software is presently taking form and makes use of the secondary addressing feature within the instrument bus protocal. The control interface itself is accessed using its primary address and a particular interface function (such as downloading the sine/cosine table) is obtained using a secondary address which is passed through and corresponds to a location in a jump table. The jump table contains the starting address of the desired routine. Additional functions can easily be added as required.

Software development was made much easier with the acquisition of a Fortran M6800 assembler which was modified to run on the control computer.[14] This allows writing 6800 code using instruction mnemonics and labels with the system editor. The assembler translates these mnemonics into hexadecimal representations of the instructions and calculates the address offsets from the label positions. The assembled machine language code can then be downloaded to the microprocessor memory via the instrument bus using a short hand keyed in loader and run.

As much of the initial exploratory data is being taken without the additional complexity of computer control, a scheme of flipping between any two field values initiated by a TTL logic pulse has been developed. The values are set by ten turn pots when the interface is operating in local mode.

ix. Microwave Generator

D. Peterson and H.E. Swanson

Microwave sources were designed and built for the 1608 and 2143 MHz cavities used in the experiment. These consist of commercially available microwave oscillators,[15] ferrite isolators,[16] and PIN modulators[17] as well as associated electronics for amplitude stabilization. The 1608 MHz main cavity oscillator was obtained with its frequency phase locked to a crystal standard, but this has been disabled allowing manual frequency adjustment until some means of remote mechanical tuning of the cavity is provided.

In operation, a pick-up loop intercepts a small fraction of the cavity's field (approximately 10%), which is rectified in a diode detector. The resulting DC level, when compared to a potentiometer setting, generates an error signal used to control output power by applying current to a PIN modulator. The sense of this current is such that power greater than desired increases the attenuation in the modulator. Cavity power is thus stabilized against such things as thermal shift of its resonant frequency. Drift beyond the range of the stabilization system causes an indicator LED to be lit and sets a corresponding error bit to be read by the control interface.

x. *Preliminary Studies of Atomic Transitions and Backgrounds*

E.G. Adelberger, T.E. Chupp and T.A. Trainor

With apparatus described elsewhere in this report we have carried out a number of preliminary observations prior to measurements of parity mixing in hydrogen. Our activities to date can be divided into two parts, the first using a short (5 cm) cylindrical rf cavity installed as early as possible to begin beam studies, and the second part dealing with our full scale, 50 cm long, square cross section rf cavity. Prior to a discussion of our results we describe some observed properties of our measurement system.

Details of our metastable beam source were given in last year's annual report and remain largely unchanged. The beam intensity is equivalent to about one pμA in each hyperfine state in a solid angle of .03 msr subtended by our detector geometry. The beam has a time structure dominated by AC ripple from the arc current supply and high frequency plasma oscillations.

The Lyman-α detector system for these studies was a single proportional counter with 1 cm diameter MgF_2 window and NO gas fill. This detector is 60-80% quantum efficient depending on length of time since last gas filling and intensity of incident radiation. This detector was mounted on a temporary aluminum frame which also supported two 6 mm diameter rods separated by 1.8 cm and used as metastable beam quench electrodes immediately in front of the detector. The geometrical efficiency was about 10^{-3}.

In order to eliminate microphonic noise originating in the bias battery detector bias was applied to the body of the detector and the center electrode was maintained at virtual ground by the preamp input. The applied bias was about 400 V and the resulting gas gain was about 120. With this gain and careful attention to ground loops in all parts of the apparatus the detector noise was dominated by fluctuations in the ion source output. This situation may change in the near future when we install two larger detectors and a spherical mirror assembly to increase the detector efficiency by a factor of 100 and also a monitor detector and an analog divider to reduce the effects of ion source fluctuations.

The detector current (in most cases proportional to β-state flux) was amplified by a PARC Model 181 current-to-voltage converter and then input to a PARC Model 186A lock-in amplifier. The lock-in reference (500 Hz) also triggered a square-wave voltage applied to quench plates in front of the solenoid. The

system thereby modulated the metastable beam intensity passing through the apparatus. This use of the lock-in amplifier removed the effect of a large "DC" offset to the β-state signal caused by spurious production of metastable atoms (perhaps by collisional excitation of ground state hydrogen on background gas in the solenoid).

The output of the lock-in was applied to the y-axis of a chart recorder whose x-axis was driven by a signal derived from the current supplies for the large solenoid. In this way automatic scans of β-state yield as a function of axial B-field strength in the interaction region of the experiment could be rapidly generated as system parameters were varied. In a typical scan the lock-in time constant was 1 sec, the preamp gain was 10^{-9} A/V, lock-in sensitivity was 1 mV and the recorder sweep corresponded to about 5 G/min. The noise level observed at the recorder referenced to the incident metastable beam flux was typically less than or about 10^{-6}.

Our first set of measurements was made with the 5 cm long cylindrical cavity resonating in the TM mode at about 1616 MHz. This cavity was intended for use as an α-state cleanup cavity following the main interaction region and had no isolated sections, so no DC fields could be applied. However, the beam itself provided a source of static electric field in the following way. The metastable beam has a finite emittance, representing a certain imperfect correlation between radial position of an atom and its divergence angle. For this reason essentially all trajectories in the beam make a non-zero angle with the axial magnetic field no matter how the beam is focussed or prepared. This means that there is an rms motional electric field corresponding to the finite beam emittance. We find that the typical rms field is between 0.1 and 0.6 V/cm depending on a number of parameters.

For proper alignment of the beam axis the average motional electric field is of course zero, and so this does not contribute to an interference effect. However, the rms field can contribute to formation of a $\alpha \rightarrow \beta$ resonances, since the transition probability goes as the square of the static field and has a non-zero average in this case.

With the rf field provided by the cylindrical cavity and the static field provided by nature we were able easily to observe the "allowed" $\alpha_+ \rightarrow \beta_o$ and $\alpha_o \rightarrow \beta_-$ transitions at 538G and 604G. The FWHM was 2-3 G for these resonances, as expected for a flight time in the rf of 0.16 μs. RF power levels corresponded to electric field values between 5 and 15 V/cm. Considerable power/broadening and resonance shifts were observed for the higher field strengths.

Observations of the "forbidden" $\alpha_o \rightarrow \beta_o$ and $\alpha_+ \rightarrow \beta_-$ resonances at 569G and 574G was complicated by several things. 1) The tails of the allowed resonances dominated the β-state yield at 570G and therefore degraded the S/N considerably. 2) At the higher rf power levels required in this shorter cavity and at the pressures ($\sim 1 \times 10^{-7}$ torr) encountered without our cryopanels the cyclotron resonance at about 574G is rather strongly excited. The result is one or more resonant dips in the β-state yield in the critical region of magnetic field strength due to absorption of rf power by orbiting free electrons in the cavity. 3) Shifting of the resonances at higher field intensity due to quadratic stark effect made their location and identification more difficult.

An important lesson from these studies was that a cavity of this type, coupling α levels and e levels to quench α-state atoms to the ground state is unsuitable for such α-state "cleanup" just because of the presence of motional electric fields which permit generation of unwanted β-state atoms outside the main interaction region. The appropriate method is to use instead a 2143 MHz cavity with transverse rf field (TE mode) which couples α levels to f levels to quench α-state atoms. In this case the motional static fields no longer contribute to β-state production because of a large level-energy mismatch.

In general, studies with this short cavity permitted semiquantitative comparison with our computer calculations, a convenient test of various refinements made to the detector-electronics system to enhance the S/N ratio, and analysis of various sources of background in the β-state flux entering the detector system.

Our most recent measurements have been made with the intended 50 cm long main cavity. This cavity has a square cross section and resonates in the TM_{110} mode at 1608 MHz. Each side panel has an isolated section about 30 cm long to generate a static transverse electric field. The resulting joints in the side panels are terminated in $\lambda/4$ slots to insure a high Q for the cavity and spoil unwanted modes of oscillation. The observed Q is about 5000. The cavity is fabricated of copper and gold-plated stainless steel.

Mounted directly on the external frame of the cavity are four Helmholz coils which provide a transverse magnetic field of up to 50G. The variation in strength of this transverse field has been carefully matched to that of the static electric field so that the resulting v X B motional field can be cancelled accurately. Four-fold symmetry of the structure about the beam axis enables arbitrary azimuthal orientation of B-field or E-field in the transverse direction.

Initial studies were made without the Helmholz coils. In this case (ignoring fringing fields) there is no component of the RF field perpendicular to the quantization axis, and so one expects only $\alpha_+ \rightarrow \beta_o$ and $\alpha_o \rightarrow \beta_-$ resonances. These were observed as expected, with FWHM $\sim$0.2G consistent with a flight time of about 1.5 μS in the interaction region.

A striking feature of these resonances is the very fast fall-off in the tail region. As an example the full width at 10^{-4} of the peaks was about 6 gauss. This is due to the relatively slow ($\sim$10 rf cycles) turn on and turn off of the field strength at entrance and exit of the cavity. Apertures in the end plates are about 1.5 cm diameter. The important consequence of these peak shapes is that in a broad magnetic field region ($\sim$30G) centered on the forbidden ($\alpha_o \rightarrow \beta_o$, $\alpha_+ \rightarrow \beta_-$) resonances of interest the tails of the allowed resonances do not contribute to the background.

An excellent example is shown in Fig. 2.4-13, again without Helmholz coils. In this figure a measure of the sensitivity achieved is the set of three small peaks in the center. These are allowed resonances for deuterium occurring in natural abundance in the atomic hydrogen beam (10^{-4}) and are therefore comparable in height to that expected for the forbidden hydrogen resonances ($\sim 10^{-6}$)

since the allowed peaks in this figure are about 10^{-2} of the incident metastable flux as expected for this set of EM field intensities.

Our principal efforts are now directed toward installation of the cryopumping system to reduce collisional excitation, refinement of our understanding of forbidden resonance formation in the real field geometries of our main cavity and commencement of automated asymmetry measurements with the apparatus at hand. In addition we are continuing studies of several markedly different EM field geometries which could be applied to this same measurement at 575G.

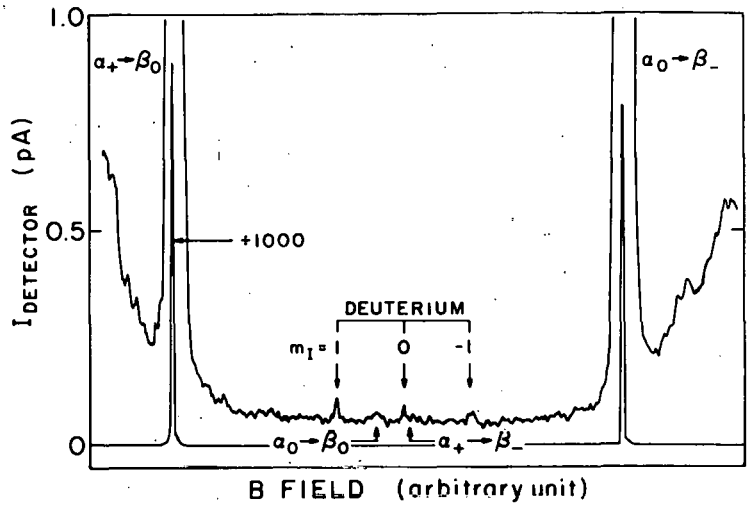

Fig. 2.4-13. B-field scan of spin-state region showing α-β resonances for hydrogen and deuterium.

1. R.R. Lewis and W.L. Williams, Phys. Lett. 59B, 70 (1975).
2. L.L. Lewis *et al.*, Phys. Rev. Lett. 39, 795 (1977).
3. P. Baird *et al.*, Phys. Rev. Lett. 39, 798 (1977).
4. R. Conti *et al.*, Phys. Rev. Lett. 42, 343 (1979).
5. C.Y. Prescott *et al.*, Phys. Lett. 77B (1978), 347.
6. E.G. Adelberger *et al.*, Bull. Am. Phys. Soc. 23, 546 (1978).
7. C.G. Ohlsen, J.L. McKibben, Los Alamos Scientific Lab Report LA3725.UC-34, Physics, TID-4500, 1967.
8. Nuclear Physics Laboratory Annual Report, University of Washington (1978), p. 10.
9. Robert Dicke, private communication.
10. K.J. Davis, E.N. Fortson and T.A. Trainor, University of Washington Nuclear Physics Laboratory Annual Report (1978) p. 20.
11. L.R. Canfield, G. Hass and J.E. Waylonis, Applied Optics 5, 45 (1966).
12. Nuclear Physics Laboratory Annual Report, University of Washington (1978), p. 31.
13. Nuclear Physics Laboratory Annual Report, University of Washington (1973), p. 11.
14. M6800 Fortran cross assembler program, TROLLOP, G.A.R. INTERFACE AGE, October 1977, p. 149; ERRATA INTERFACE AGE, December 1977, p. 134.
15. Frequency West Inc., Santa Clara, California.
16. Aertech, Inc., Sunnyvale, California.
17. Hewlett Packard, Model 8730.
18. Nuclear Physics Laboratory Annual Report, University of Washington (1978), p. 10.
19. Artech Corp., Falls Church, VA.

3.1 An Upper Limit for the Width of the Lowest T=2 State in ^{32}S

E.G. Adelberger, Y. Haque, P.G. Ikossi, K.A. Snover, and R. Von Lintig

The lowest T=2 state of ^{32}S ($J^\pi = 0^+$, E_x = 12.050 MeV) was identified in the isospin allowed (p,t) reaction.[1,2] In a comprehensive study of the γ-decay of this state using the $^{31}P(p,\gamma)^{32}S$ reaction Vernotte *et al.*[3] have shown that J=0 for the E_x = 12.050 MeV state (E_p = 3.289 MeV) and that it's γ-decay proceeds through $J^\pi = 1^+$, T = 1 levels in ^{32}S. The same authors have measured excitation functions for the $^{31}P(p,p_0)$ and (p,p_1) reactions using a 0.7 keV thick target and have set an upper limit of 170 eV for the width of the resonance $(\Gamma_p/\Gamma = 1)^2$ based on the fact that a detectable resonance effect was not observed. We estimated that an energy resolution of ∿1 keV a Γ = 170 eV $J^\pi = 0^+$ resonance should be seen at back angles as a ∿20% effect on the cross section. It was thus our judgment that an improvement on the upper limit for the width of this state was possible.

The T=2 state lies 6 keV above a strong $J^\pi = 4^-$ (p,p) resonance. Thus in our experiment we had no difficulty inferring the exact proton energy where the T=2 resonance is expected. We measured excitation functions at θ_L = 90°, 140° and 165° using pairs of detectors located symmetrically to the left and right of the beam. Several passes through the 'resonance' region were made with 0.5 keV and 0.1 keV thick targets. In most of these excitation functions we detected excess of counts of ≲ 8% at the expected resonance location but similar deviations were also observed below or above the 'resonance' energy (Fig. 3.1-1). The absolute normalization of the data was determined under the assumption that at 55° the cross section is Rutherford.

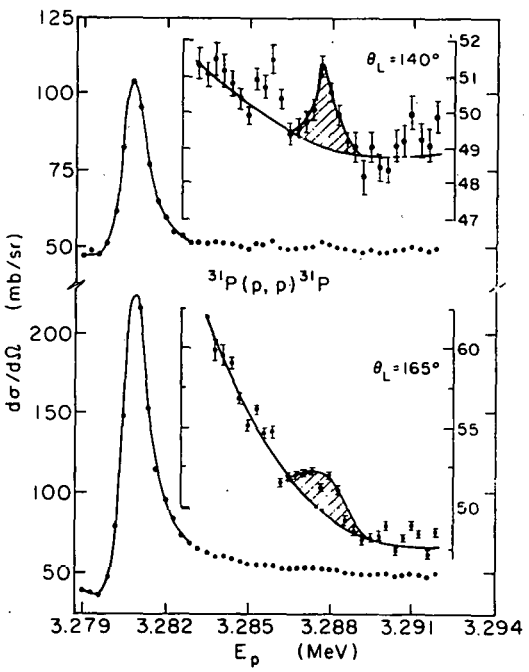

Fig. 3.1-1. Cross section excitation function in the region of the lowest T=2 states in ^{32}S. The lines are guides to the eye. The hatched areas represent what could be interpreted as the effect of the T=2 resonance. These excitation functions taken with a 0.1 keV thick target show the maximum deviation at the resonance energy.

Using our 0.5 keV thick target we investigated the energy resolution by measuring excitation functions over a narrow resonance at E_p = 3.223 MeV. The observed FWHM of the resonance effect was 0.86 keV. The natural width of this state once thought to be the T=2 analog is not known (Fig. 3.1-2). Using this measurement we can set an upper limit of 0.86 keV on

the overall energy resolution of this experiment.

At back angles an $\ell=0$ resonance is expected to appear mainly as a rise in the cross section which is consistent with the 'excess' of counts observed. Under the assumption that the relative phase of the resonance with respect to the background is 90° (this is close to what we expected for an $\ell=0$ resonance interfering with a Coulomb background) an upper limit on the width can be set. We estimated the area under the 'resonance' effect in six of our excitation functions where an excess of counts was observed at 140° or 165° (Fig. 3.1-2). The energy resolution was assumed to be Lorentzian. The widths consistent with these areas were less than 100 eV each and give an average of 69 ± 21 eV where the error includes a 10% uncertainty in the absolute cross section normalization and 15% uncertainty due to the phase of the resonance. Thus our data are consistent with $\Gamma < 90$ eV. This upper limit corresponds to an effect of ∿10% on the back angle cross sections. Another run is planned in order to improve these measurements.

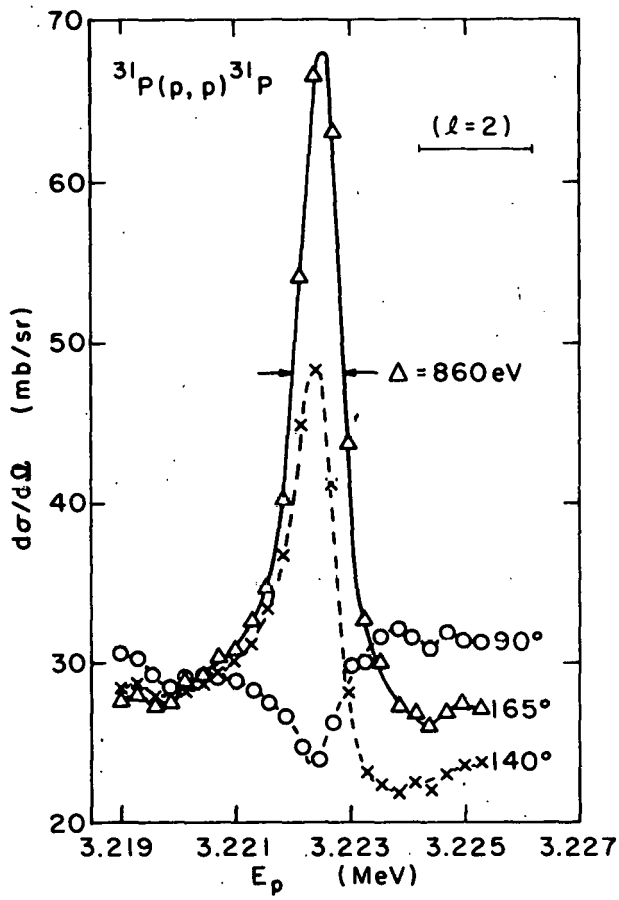

Fig. 3.1-2. Excitation functions taken with a 0.5 keV target indicating that the overall energy resolution is < 860 eV. The relative size of the resonance excursion at these angles is consistent with $\ell = 2$.

1. R.L. McGrath, J. Cerny, J.C. Hardy, G. Goth and A. Arima, Phys. Rev. C1, 184 (1970).
2. S.J. Freedman *et al.*, Phys. Rev., to be published.
3. J. Vernotte, S. Gales, M. Longevin and J.M. Maison, Phys. Rev. C8 (1973), 178.

3.2 J^π Assignments in ^{29}P and the Giant Gamow-Teller Resonance in the β^+ Decay of ^{29}S

E.G. Adelberger, Y. Haque, P.G. Ikossi, and K.A. Snover

As yet, relatively little is known about the spin flip giant resonances, the simplest of which is the giant Gamow-Teller (G-T) resonance. The most direct way of observing this resonance is in β decay. However in most cases the energy release in β decay is not sufficient to reach up into the giant resonance region. An exception occurs in the β^+ decay of the T = (N-Z)/2 = -3/2, T = 3/2 levels of the A = 4n + 1 nuclei. Here the combination of symmetry and Coulomb energies produce a very large energy release. In addition we expect a component of the giant G-T resonance to occur at relatively low excitation energies in the residual nucleus. The giant G-T resonance built on the T = 3/2 initial state has T = 1/2, T = 3/2, and T = 5/2 components and the T = 1/2 level is pushed down to low energies by the isospin splitting.

The β^+ decays of the T = 3/2 nuclei with A = 4n + 1 have been measured at Berkeley in a very nice series of experiments. We have reexamined the Berkeley results to see what we can learn about the G-T giant resonances. The first case we have looked at is ^{29}Si (ref 1). The results of ref 1 are displayed in Fig. 3.1-1. There is clear evidence for a concentration of β^+ strength at high excitation energies. Could this be the tail of the G-T giant resonance? The authors of ref 1 noted that the transitions to state at E_x = 8.106, 8.231, 8.532 are quite strong, with log ft = 4.8, 4.6, and 4.4 respectively. In addition a strong transition is seen to a level at E_x = 9.390 MeV with log ft = 4.4. They speculated that this strength might be due either to: 1) a Fermi component in the decays due to mixing with the $J^\pi = 5/2^+$, T = 3/2 level at E_x = 8.381 MeV; or 2) collective G-T strength. One can easily make a measurement capable of ruling out alternative 1)—namely determine the spins of the level at 8.106, 8.231, and 8.532 MeV. If the "enhanced" transitions are Fermi, then all 3 levels must have $J^\pi = 5/2^+$. All three levels had been observed as resonances in ^{28}Si + p and previous works had shown that all three resonances were ℓ = 2. In order to distinguish between $J^\pi = 5/2^+$ and $3/2^+$ we studied the $^{28}Si(\vec{p},p)$ reaction induced by polarized protons.

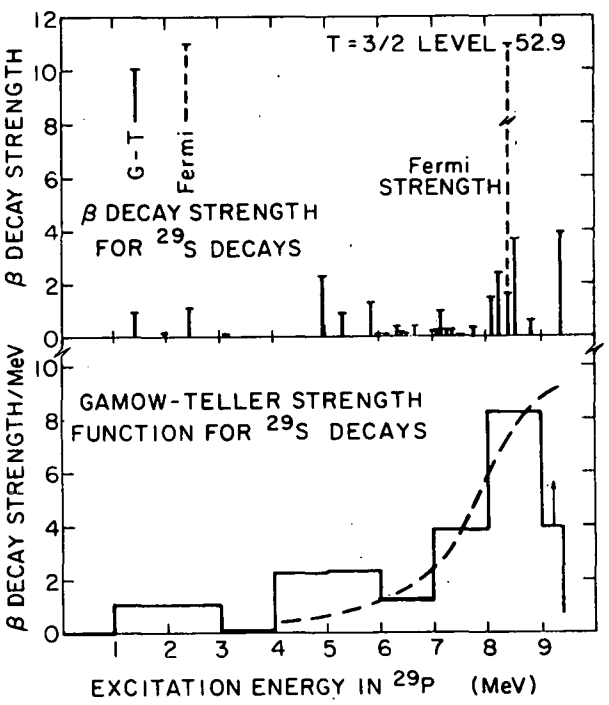

Fig. 3.2-1. β^+ decay strength ($|\langle f|H_\beta|i\rangle|^2$) for ^{29}S decays as a function of excitation energy in ^{29}P as measured in ref 1. Top: strength of individual transitions; bottom: strength in 1 MeV width bins.

Traditionally the choice of angles for the measurement of excitation functions in elastic scattering has been restricted to the back hemisphere in order to obtain reasonable resonance/background ratios. In analyzing power measurements the advantage of measuring at back angles is not so obvious since the analyzing power for proton scattering from a spin-0 target is an interference effect involving the spin-flip and non-spin-flip scattering amplitudes. For a region of overlapping resonances, it is generally very difficult to determine the properties of the background well-enough to permit unambiguous spin/parity assignments for resonances. We felt that this difficulty could be overcome if measurements were made at forward angles where the Coulomb cross section constitutes the main component of the non-spin-flip amplitude. Consideration of the kinematic separation between Si and C and O containments in the target and the anticipated energy resolution indicated that the elastic scattering peaks in the spectra could be resolved at angles of about 50° or greater.

Preliminary calculations of expected shapes of the analyzing powers for $\ell \leq 3$ with optical model backgrounds indicated that the shapes of the analyzing powers for $\theta < 70°$ remain stable under a wide range of the optical model parameters.

We measured the excitation functions for $^{28}Si(p,p_o)$ at θ_{LAB} = 55°, 70°, 90°, 115°, and 140°. At 55° and 90°, pairs of detectors were positioned symmetrically to the left and right of the beam. Single detectors were placed at 70°, 115°, and 140°. The solid angles subtended by the detectors ranged between 2 and 7 msr and the angular acceptance in the scattering plane was 1-3°. The target was self supporting ^{28}SiO containing ∿30 μg/cm^2 of ^{28}Si. It also contained ∿17 μg/cm^2 of Ta introduced when the Ta boat was overheated during the electron gun evaporation. This contaminant although otherwise undesirable provided a means of normalizing the relative solid angles of the several detectors to an accuracy better than 1% by comparison to Rutherford cross sections. The absolute cross section was obtained by normalizing the data at $\theta > 70°$ and E_p ∿5.86 MeV to the angular distribution data of ref. 3 (known to within ± 15%). The inelastic cross sections were measured at θ_{LAB} = 70°, 90°, and 115°. The polarized ion source was operated in the fast spin flip mode[4] with a beam current on target of ∿45 nA and polarization 0.67. The counting time for each data point was ∿3 min.

The off-line sums were performed using the automatic yield curve programs SMULTS written for the PDP 11/60 computer. This program uses kinematics to obtain the energy calibration of the spectra and shifts the windows appropriately for each energy as read from the "MULTSING" tape produced on-line. This procedure provides a consistent way of summing the peaks with minimum operator intervention. The background subtraction was performed by fitting a straight line to the peak-free region of each spectrum. Representative excitation curves are shown in Figs. 3.2-2a,b,c.

Although a resonance analysis of these data has not yet been performed, comparison of the 55° data to the predicted shapes of resonances for $\ell \leq$ (Fig. 3.2-3) allows a straight forward J^π assignment for the $\ell = 2$ states in this energy region. Thus the 8.106 and 9.390 MeV states have $J^\pi = 5/2^+$ and the 8.231 and 8.532 $J^\pi = 3/2^+$

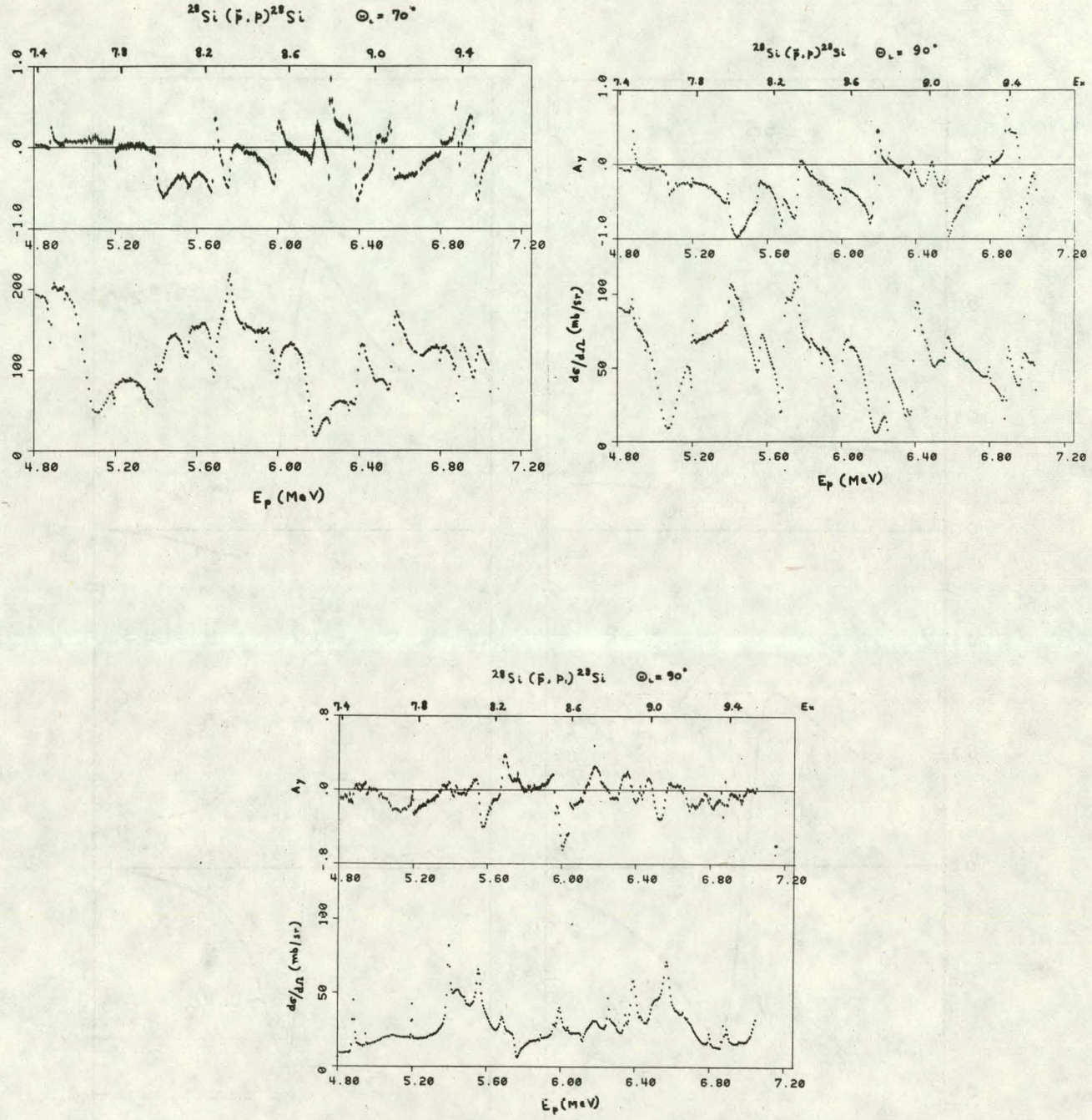

Fig. 3.2-2. Representative excitation curves for the $^{28}Si(p,p_o)$ and $^{28}Si(p,p_1)$ reactions.

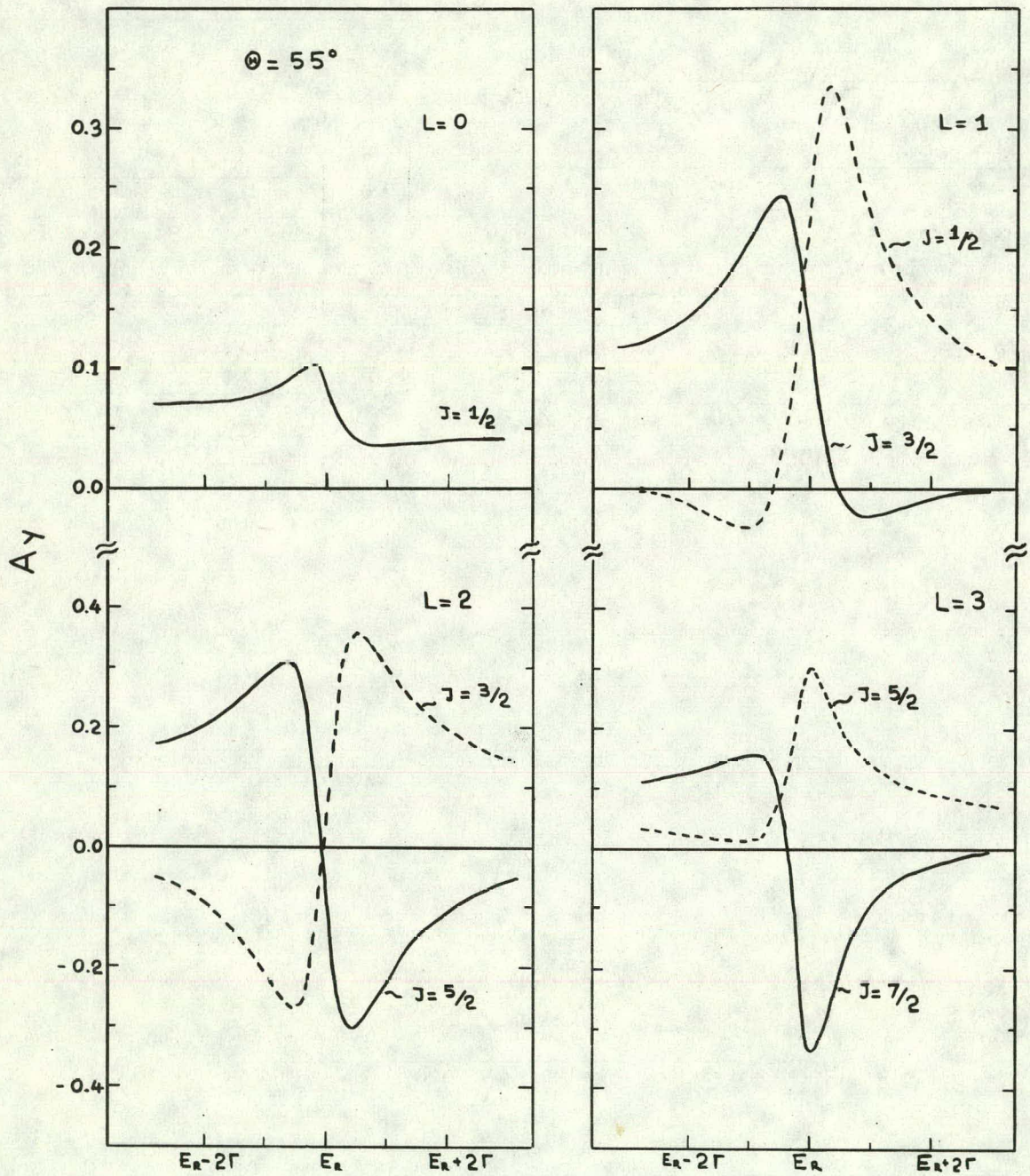

Fig. 3.2-3. Theoretical analyzing power resonance shapes calculated for $\Gamma_p/\Gamma = 0.5$ with an optical model background.

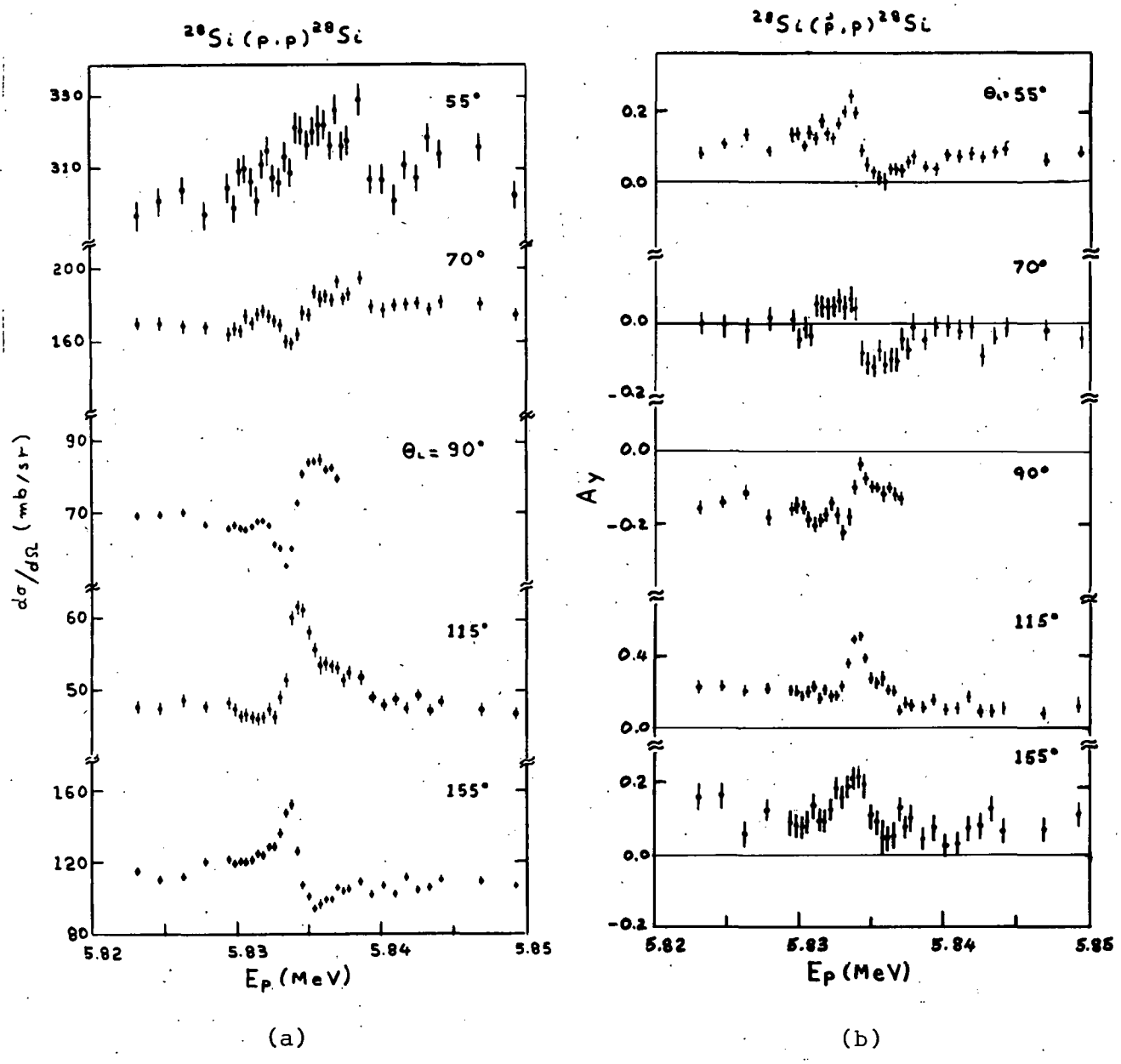

Fig. 3.2-4. Cross sections and analyzing powers excitation curves over the lowest T = 3/2 states in ^{28}P. The target for this measurement was ∿1 μgr/cm^2 thick in ^{28}Si. The shape of the analyzing power at 55° is consistent with $5/2^+$.

These assignments are substantiated by data taken over the lowest T = 3/2 state with a thinner target (Fig. 3.2-4). This state, the analog of the ground state of ^{29}Al and ^{29}S, must have $J^\pi = 5/2^+$. It has been seen as a resonance in proton scattering[3,5] and has been identified as the T = 3/2 analog from its excitation energy. Nevertheless all previous excitation function measurements could not unambiguously assign $J^\pi = 5/2^+$ to this resonance. Thus our excitation functions which display the expected J^π shape of the analyzing power data at 55°

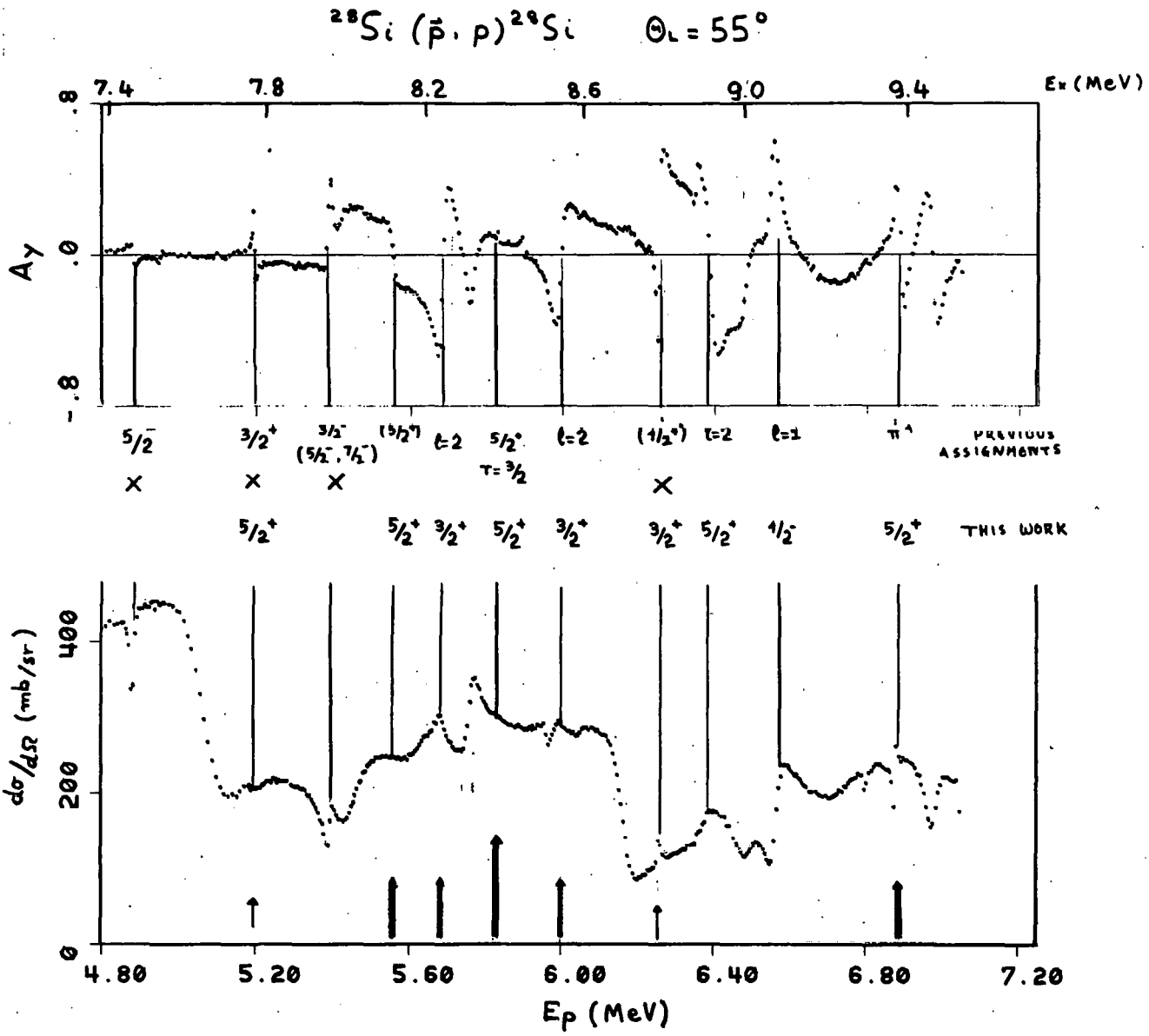

Fig. 3.2-5. The excitation functions for cross section and analyzing powers at $\theta_{LAB} = 55°$. The arrows at the bottom of the figure indicate states populated in the β-delayed proton experiment of ref. 1. Thick arrows denote the enhanced decays. Previous assignments are those of ref. 5. Crosses indicate disagreement with those assignments.

serve a twofold purpose: first, they confirm the assumption that $J^\pi = 5/2^+$ for the E_p = 5.834 MeV, T = 3/2 resonance, and second, they provide a consistency check for other spin assignments made in this energy region.

We have shown that two of the fast positron decays of ^{29}S to T = 1/2 states in this region populate $J^\pi = 3/2^+$ states and thus must be GT. Hence it is highly probable that the two strong β^+ transitions which populate $5/2^+$ states are also predominantly GT. We therefore conclude that the β^+ decays of ^{29}S reveal the tail of the giant GT resonance (see Fig. 3.2-1). The energy release is not sufficient to detect the complete GT strength and hence the peak seen in Fig. 3.2-1 is not the peak of the giant GT resonance but is due to a cut-off in the experimental sensitivity.

A comparison of the results of this work to the previous spin assignments[2] for some of the observed resonances is made in Fig. 3.2-5. It is disconcerning to see the serious disagreement with "definite" spin assignments of states with $E_x \sim 8$ MeV. Nevertheless a careful investigation of their origin[2] indicates that previous assignments were based on weak evidence.

In view of these disagreements we extended our data in a second run down to E_p = 3 MeV. We have also measured excitation functions from 7.0 to 7.3 MeV to investigate the region where a tentative identification[5] of the first excited T = 3/2 analog ($J^\pi = 1/2^+$) was made. Off-line analysis of these data is currently in progress. It is anticipated that a resonance analysis of all the data will provide information on resonance widths and strengthen the assignments of spin and parities. Similar measurements are planned for other N = Z even-even targets for $A \leq 40$.

1. D.J. Vieira, R.A. Gough and J. Cerny, Phys. Rev. C19, 177 (1979).
2. Endt and Van der Leun, Nucl. Phys. A310, 1 (1978) and references therein.
3. P.G. Ikossi, T.B. Clegg, W.W. Jacobs, E.J. Ludwig, and W.J. Thompson, Nucl. Phys. A274, 1 (1976).
4. E.G. Adelberger, W.B. Ingalls, H.E. Swanson and T.A. Trainor, Nuclear Physics Laboratory, University of Washington, 157 (1972).
5. B. Teitelmann and G.M. Temmer, Phys. Rev. 177, 1656 (1969)

3.3 Polarized Proton Scattering from Lead Isotopes

N.L. Back, H.C. Bhang, J.G. Cramer, T.A. Trainor, and R. Von Lintig

Since their discovery in 1964, isobaric analog resonances (IAR's) have proved to be a valuable spectroscopic tool for medium-weight and heavy nuclei. By measuring the partial width for proton elastic scattering from a target nucleus (Z,N) via an IAR in the compound nucleus (Z+1,N), one can obtain information on the single-neutron components of states in the parent nucleus (Z,N+1). Such an experiment is analogous to a (d,p) reaction with the same target, and provides spectroscopic information of comparable quality.

The IAR's are also observed in the inelastic scattering to many excited states of the target. By measuring the partial widths in these channels, one can determine the spectroscopic factors for various neutron particle-hole configurations in the final states. Generally, the excited states which resonate have odd parity (for even-even nuclei), since the particle and hole come from different major shells. One exception is the first 2^+ state, which is excited via a component in the IAR wave function consisting of a single particle weakly coupled to a 2^+ core. Thus, the partial widths for decay of an IAR to the first 2^+ state of the target provide information on this mixing in the parent state. Such an experiment would be analogous to a (d,p) reaction on an excited target.

Some recent experiments with IAR's have used polarized beams. This has several advantages. First, measurement of the analyzing power provides an additional independent piece of information. Second, the analyzing-power excitation function generally has a smaller and more slowly-varying background than does the cross-section excitation function. And finally, measurement of the analyzing power makes it possible to determine the spin of an IAR unambiguously. Thus, for elastic scattering and for inelastic scattering to collective states, polarized-beam measurements can be very valuable (for inelastic scattering to a non-collective state via an isolated resonance, the analyzing power has been shown by Harney to be identically zero[1]). A series of such experiments has been done by a group at Erlangen,[2] using N = 82 nuclei as targets. They measured the excitation functions for elastic scattering and for inelastic scattering to the first 2^+ state and were able to determine the spins, parities, single-particle components, and single-particle-plus-2^+-core components of a large number of states in the corresponding N = 83 nuclei.

We have begun a similar program, using ^{206}Pb and ^{208}Pb as targets. The states of interest are the ground state and first 3^- state of each nucleus and the first 2^+ state of ^{206}Pb. Our intention is to determine the partial widths for decay to these states from all the IAR's in the 15-18 MeV range; this includes the analogs of all of the single-neutron states in ^{209}Pb.

Self-supporting targets of ^{206}Pb and ^{208}Pb were used, with thicknesses of about 500 $\mu g/cm^2$. The proton beam was produced by the polarized ion source, operating in the spin-filter mode, with separate spin-up and spin-down runs. Typical beam currents were 50-70 nA on target, with an average polarization of about 68%. The scattered protons were detected by Si(Li) or surface-barrier detectors at angles of 120°, 135°, 150°, and 165°, all on the right side of the beam. In addition, there were monitor detectors at $\pm$ 35° and an in-line helium polarimeter to continuously monitor the beam polarization. To reduce the background in the detectors, a collimator telescope assembly was used so that each detector could see only the target and its immediate surroundings. Also, an aluminum shield was placed around the entire detector assembly, primarily to reduce back-scattering from the polarimeter and Faraday cup. Resolution was $\leq$ 45 keV FWHM.

The cross sections and analyzing powers for scattering from ^{206}Pb were measured for incident proton energies between 14.25 and 16.25 MeV. The data for θ = 150° are shown in Fig. 3.3-1. Only the statistical errors are shown. The relative normalization between the monitor and the four main detectors was deter-

mined by measuring the elastic scattering cross sections at 4.0 MeV, which is well below the Coulomb barrier. Unfortunately due to the large amount of multiple scattering in the target and polarimeter at this energy, it was not possible to normalize the monitor to the Faraday cup. Therefore, the absolute normalization was estimated using an optical model calculation at 14.25 MeV and 35°, and it could be in error by about 3%. Some data were also collected with a ^{208}Pb target, but they have not yet been analyzed.

The ^{206}Pb elastic-scattering data are being analyzed using a parameterized-background program. The background amplitudes are assumed to be smoothly-varying functions of energy, and are therefore expressed as Taylor-series expansions about the midpoint of the energy region of interest. They are then added to the resonance amplitudes. The program varies the background and resonance parameters simultaneously to obtain the best fit to the cross-section and analyzing-power data. This is done for each angle separately; the resulting resonance parameters are then compared for consistency and weighted averages are calculated.

The results to date are shown in Fig. 3.3-1 for 150°. To obtain this fit, five IAR's were used; the parameters are given in Table 3.3-1. Those parameters for which no errors are quoted were not permitted to vary in the search. In particular, the numbers for the $d_{5/2}$ doublet at 16.390 and 16.459 MeV were taken from Ref. 3, the energies of the $i_{11/2}$ and the first $d_{5/2}$ IAR's were calculated from the excitation energies of the corresponding states in ^{207}Pb, and the width of the $i_{11/2}$ IAR was fixed by assuming that the ratio of the $i_{11/2}$ and $g_{9/2}$ widths is the same for ^{206}Pb + p as for ^{208}Pb + p.[4]

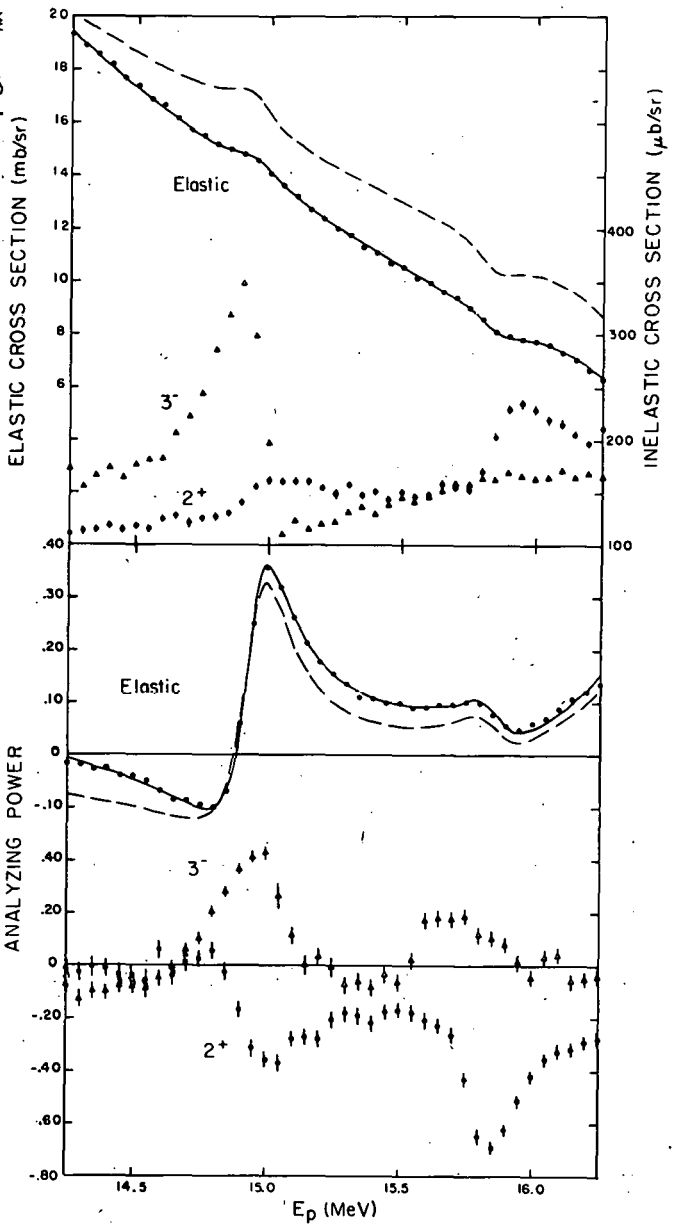

Fig. 3.3-1. Cross-section and analyzing-power data at θ_{lab} = 150° for ^{206}Pb($\vec{p}$,p_o) and ^{206}Pb($\vec{p}$,p') to the 2^+ (0.803 MeV) and 3^- (2.648 MeV) states. The solid curve is the best fit using parameterized background; the dashed curve is an optical-model calculation.

Also shown in Fig. 3.3-1 is an optical-model calculation, using the resonance parameters of Table 3.3-1 and the global optical-model parameters

Table 3.3-1. Resonance Parameters for IAR's in ^{207}Bi*

ℓ_j	Γ_p (keV)	Γ (keV)	E_R (MeV-c.m.)
$g_{9/2}$	19.87 ± 0.11	196.6 ± 1.1	14.8671 ± 0.0006
$i_{11/2}$	0.79 ± 0.07	173	15.640
$d_{5/2}$	6.14 ± 0.25	243 ± 8	15.773
$d_{5/2}$	10	308	16.390
$d_{5/2}$	35	308	16.459

of Becchetti and Greenlees.[5] The next step in the analysis involves finding a better set of optical-model parameters. The set which is obtained can then be used in the calculation of DWBA amplitudes for the inelastic scattering to the 2^+ and 3^- states.

1. H.L. Harney, Phys. Lett. 28B, 249 (1968).
2. H. Clement, G. Graw, R. Zenger, and G. Zöllner, Nucl. Phys. A285, 109 (1977).
3. S. Fiarman and N. Marquardt, Z. Phys. 221, 494 (1969).
4. M.P. Baker, J.S. Blair, J.G. Cramer, E. Preikschat and W. Weitkamp, in Proceedings of the Fourth International Symposium on Polarization Phenomena in Nuclear Reactions, edited by W. Grüebler and V. König (Birkhäuser, Basel, 1976), p. 781.
5. F.D. Becchetti and G.W. Greenlees, Phys. Rev. 182, 1190 (1969).

3.4 Analyzing Powers of Protons Inelastically Scattered From ^{76}Se

J.S. Blair, R. Risler, and T.A. Trainor

Because analyzing powers involve differences in nuclear amplitudes, they frequently provide more information concerning a reaction mechanism than do measurements of cross sections by themselves. In particular, measurements of analyzing powers of protons which inelastically excite low lying "collective" levels of nuclei offer the possibility of discriminating between the various collective models describing these states.

The nucleus ^{76}Se has been singled out for study since the isolated near-degenerate 0^+-2^+-4^+ triplet at roughly twice the energy of the first excited

(2^+) level at 0.559 MeV suggests that it might approach the model of an ideal harmonic vibrator. If this is the case, the members of the triplet will be populated through a double excitation mechanism, for which the analyzing powers are predicted to differ from those for single excitations.

Protons of 17.0 MeV have been scattered from a target of ^{76}Se, whose enriched abundance was 96%. Angular distributions of the analyzing power and cross section have been measured in the range 25° to 110° in the laboratory system. A preliminary analysis has been made of the analyzing powers for elastic scattering and inelastic scattering to the lowest strong 2^+ and 3^- levels as well as to the resolved 0^+-2^+-4^+ triplet with energies 1.122, 1.216, and 1.331 MeV, respectively.

The angular distributions of analyzing powers for elastic scattering and inelastic scattering to the first 2^+ level are in fair accord with optical model and DWBA calculations based on Becchetti-Greenlees parameters.[1] While the analyzing power to the second 2^+ level does differ considerably from that for the first 2^+ level, there are sufficient similarities to suggest that there is an appreciable single step contribution to the excitation of the second 2^+ level. Similarly, the analyzing powers for the 4^+ level have some qualitative resemblance to these calculated for a single step 4^+ excitation. The analyzing power for the 0^+ level has the largest uncertainty but indicates a moderately oscillatory pattern, though with a periodicity somewhat larger than that predicted for a single-step excitation. All these observations are quite tentative, however; more careful analyses of the data and additional calculations will be required before firm conclusions can be reached.

---

1. F.O. Becchetti, Jr. and G.W. Greenlees, Phys. Rev. 182, 1190 (1969).

3.5 Analyzing Power in the Continuum Portions of Particle Spectra

N. Back, H.C. Bhang, J.S. Blair, I. Halpern, W. Lynch, G.A. Miller, R. Risler, T.A. Trainor and W.G. Weitkamp

During the past year we have extended our analyzing power measurement to other nuclei to confirm the simple behavior we observe with $^{63}Cu(\vec{p},p')^{63}Cu$. To compare with our recent data the results for copper may be summarized briefly as follows:[1]

- Above E_x = 6 MeV, the analyzing power varies smoothly and slowly with angle and excitation energy.
- The analyzing power in the pre-equilibrium region is negative in the forward hemisphere and positive in the backward hemisphere.
- The analyzing power decreases from levels near 5% to very small values as the residual excitation energy increases.

With a polarized proton beam we bombarded ^{64}Zn, a nuclide very close to ^{63}Cu, and ^{103}Rh, which is substantially heavier but still of sufficiently low Z to provide a relatively high yield of outgoing scattered protons in the pre-equilibrium region.

The statistical error per channel in the evaporation region is ∿0.2% for ^{64}Zn and 0.3-1% for ^{103}Rh and in the pre-equilibrium region 0.2-0.5% for ^{64}Zn and 0.3-0.5% for ^{103}Rh with a 5-channel Gaussian smoothing. ^{64}Zn has a similar yield distribution in energy with more oxygen contamination than the ^{63}Cu target. This requires more careful attention to the residual oxygen impurity contribution in the evaporation region. In the pre-equilibrium region this contribution is far below the average value. The evaporation yield for ^{103}Rh is reduced due to the Coulomb barrier. We see only the high energy tail of the evaporation peak. Therefore, in the evaporation region the statistics are poor and other error contributions are dominant. However, we still obtain adequate yield in the pre-equilibrium region. The quality is comparable to that from the other targets, even though the slit scattering yield is larger than for the other targets.

Our major technical improvement during the past year has been concentrated on monitoring and eliminating slit scattering. Our old Δ-detectors were replaced by new 30 μ detectors which have a noise width about 28 keV. These permit better PID resolution and the ability to separate slit scattered protons from the detector aperture from the main proton group.

In order to determine the nature of the detector slit scattering we used the two parameter program RALPH which can event record particle ID as a function of total energy. For relatively high energy protons the PID value is independent of particle energy. However, the once-scattered protons from the detector slit lose energy between E and Δ detectors and are shifted in PID value. By putting a tight window on the proton PID peak we were able to cut most of the slit scattered particles, more than 95% from the evaporation region and a large portion (∿70%) from the pre-equilibrium region.

The other source of slit scattering is the beam defining aperture. With carefully aligned collimation an upper limit may be taken from data obtained at Livermore by A.D. Bacher *et al.*[2] Using their data we can estimate the contribution from collimator aperture less than 0.3% in the pre-equilibrium region. Compared to the average value of the analyzing power in this region (several %) the collimator scattering does not represent a significant contamination of the data.

For ^{64}Zn the behavior in the pre-equilibrium region is more or less the same as that in ^{63}Cu. The average analyzing powers in this region are negative (several %) in the forward hemisphere and positive (less than 1%) in the backward hemisphere. In the evaporation region, they are very small and of the order of magnitude of statistics (about 0.03%) (see Table 3.5-1).

For ^{103}Rh, the dip in the forward hemisphere is more pronounced than for ^{63}Cu and ^{64}Zn. In the backward hemisphere the behavior is mixed. The detailed behaviors are shown in Figure 3.5-1.

Negative analyzing powers in the forward hemisphere and monotonic variations with excitation energy in the pre-equilibrium region were common to all

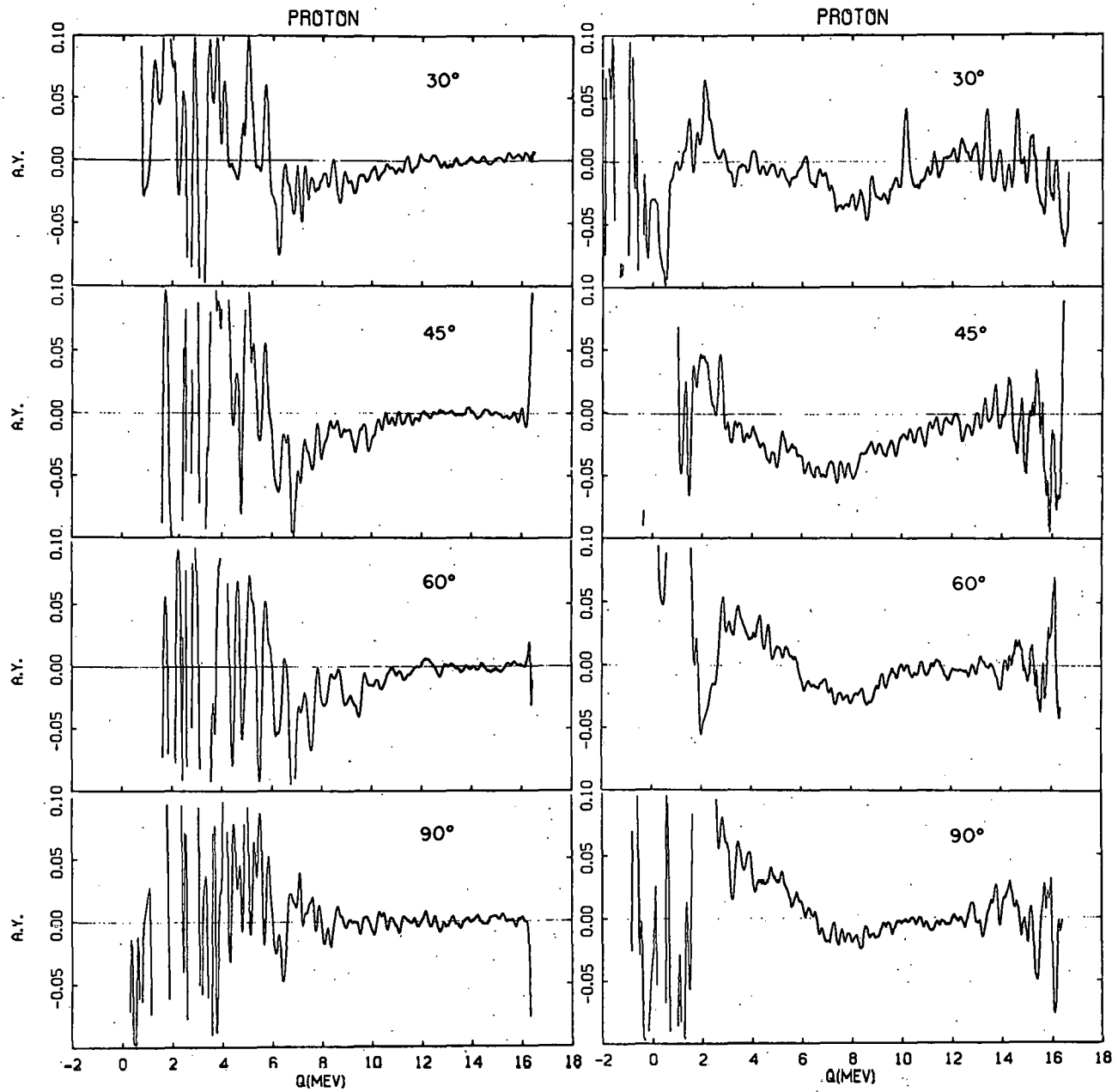

Fig. 3.5-1. Analyzing powers for $^{64}Zn(\vec{p},p')$ (left) and $^{103}Rh(\vec{p},p')$ (right) at E_p = 18 MeV are plotted against residual excitation energy, Q (MeV). ^{103}Rh (30°) and ^{64}Zn (60°) are not fully stripped of impurities.

Table 3.5-1. Average analyzing powers (%) for specified regions of excitation energy. The statistical errors are 0.03% to 0.06%. a) represents the ^{64}Zn data and b) represents ^{103}Rh.

	(a)				(b)	
θ E_x	6-10	10-13	13-16	θ E_x	6-10	10-13
30	-1.7	-0.34	-0.013	30	-2.4	-0.22
45	-2.1	-0.37	-0.068	45	-3.7	-1.2
60	-2.0	-0.36	-0.12	60	-1.8	-0.35
90	0.016	-0.11	0.05	90	0.08	0.35
120	0.66	0.16	0.055	120	0.25	0.36
150	0.34	0.03	-0.07	150	-1.0	0.26

three targets. The ^{103}Rh analyzing powers are somewhat more complicated than simple negative forward-positive backward behavior observed in the other cases. However, they still do not vary as much as the analyzing power for a typical discrete level.

The angular and energy behavior of the data at excitation energies above 6 MeV encourage us to look for a simple model for inelastic scattering to the continuum. The resemblance between the analyzing power patterns for $(\vec{p},p')$ and $(\vec{p},\alpha)$ in the pre-equilibrium region from ^{63}Cu and ^{103}Rh suggest that these analyzing powers are mainly entrance-channel effects. The pre-equilibrium behavior of the α-channel for the ^{64}Zn target is not clear since the discrete levels dominate. We have been exploring the properties of some classical models along these lines. We have also formulated a DWBA calculation in which the knockout of a bound nucleon leads to a final state with two particles in the continuum. The analyzing power is assumed to originate from the distorting effects of the entrance-channel spin-orbit interaction. (The spin-orbit interaction part of the direct nucleon-nucleon interaction causing the knockout may be neglected because of the small analyzing power observed in low-energy N-N scattering.) The corresponding computer code is under development.

1. Nuclear Physics Laboratory Annual Report, University of Washington (1977), p. 58.
2. Nuclear Instruments & Methods, 74, No. 2 (1969), p. 261

3.6 Experimental Search for the Spin-Isospin Flip Transitions $^{6}Li(^{14}N,^{14}C)^{6}Be$, $^{6}Li(^{14}N,^{14}N^{*})^{6}Li^{*}$

K. Aniol, N. Back, H. Bhang, and R. Puigh

The nucleon-nucleon interaction contains a Gamow-Teller (G-T) type term $V_{GT}(\underset{\sim}{\sigma}_i \cdot \underset{\sim}{\sigma}_j)(\underset{\sim}{t}_i \cdot \underset{\sim}{t}_j)$, in addition to spin flip and isospin flip terms. By studying the spin-isospin flip reactions with ^{6}Li as a target or projectile information about the G-T type of interaction can be obtained.

Previous measurements of spin-isospin flip reactions on T = 0 targets were performed with $^{6}Li + {}^{6}Li$[1,2] and $^{6}Li + {}^{40}Ca$, however, only an upper limit on the ^{40}Ca cross section was obtained.[3] The large Q value mismatch is unfavorable for the $(^{6}Li,^{6}He)$ reactions on even-even nuclei, therefore, we investigated the reactions on ^{14}N. Although the Q value for the spin-isospin reactions is favorable, the small M1 strength of the decay of the T = 1, 0^{+} state (2.3 MeV) in ^{14}N is not.

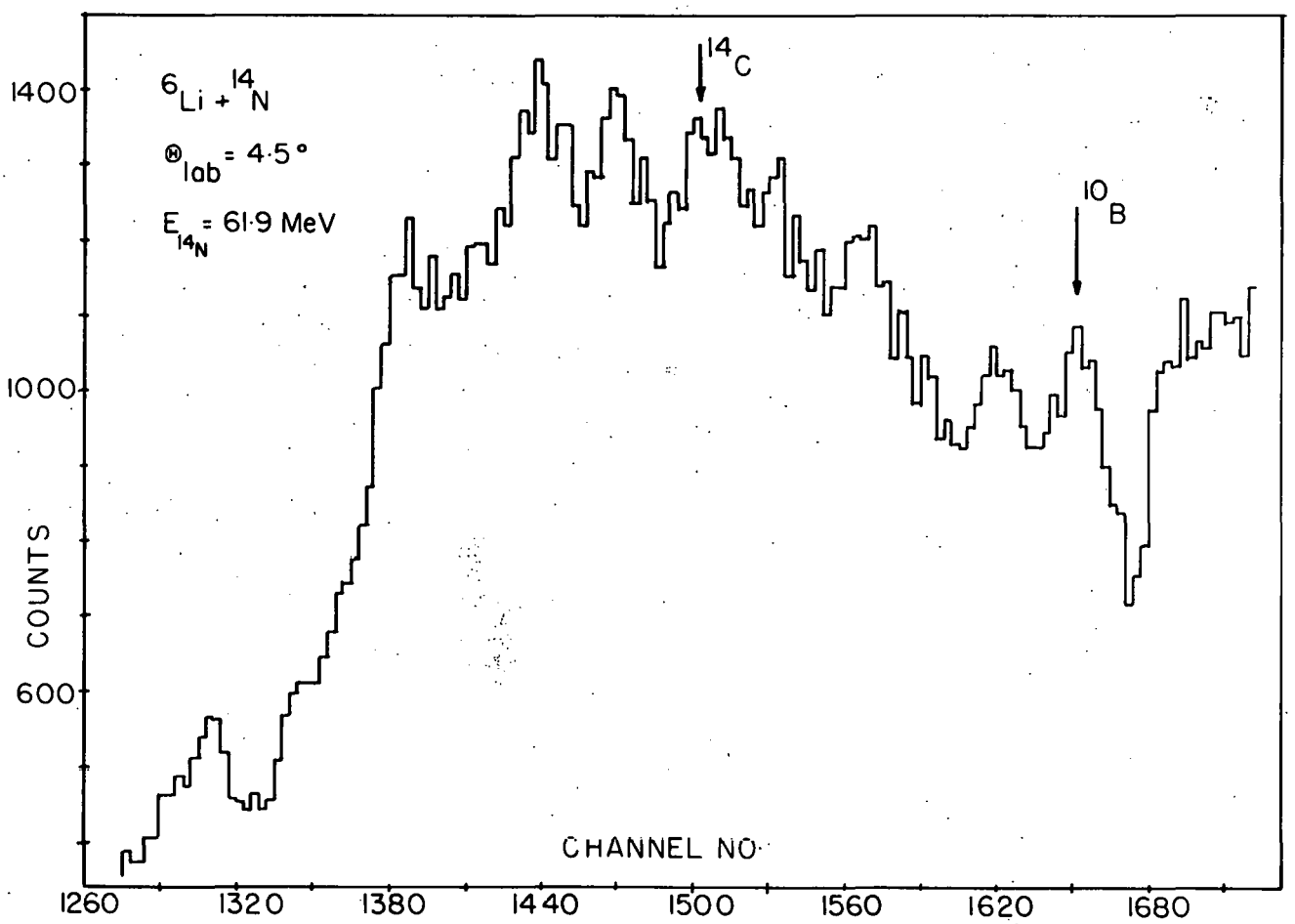

Fig. 3.6-1. Position spectrum of counts versus channel number. Increasing channel number correspond to increasing Bp for a given ion and charge state.

In the first measurement gamma decay of the 3.56 MeV level in ^{6}Li was sought. This was carried out with self-supporting ^{6}Li targets $\sim$2 mg/cm^2 and an ^{14}N beam. A NaI spectrum showed no evidence that the 3.56 MeV state in ^{6}Li was being populated.

In a second measurement a 300 μg/cm^2 ^{6}Li target was used and ^{14}C ions were sought at 4.5° in the lab. The magnetic spectrometer was used for this purpose. A position spectrum is shown in Fig. 3.6-1. A mask of Al and mylar was placed over a position sensitive gas counter in the focal plane. The goal was to eliminate the inelastically scattered ^{14}N ions. Some groups were observed superimposed upon what is probably breakup α particles from the excited states of ^{12}C. The arrow points to the expected location of the ^{14}C ground state. A peak is seen here, although all the impurities have not been identified yet. Analysis of these data is currently in progress, but it appears that extra criteria are needed to identify the ^{14}C group.

1. W.R. Wharton, J.C. Cramer, J.R. Calarco, K.C. Nair, Phys. Rev. 69 (1974), 156.
2. K. Nagatoni, D.P. Boyd, P.F. Donovan, E. Beardsworth, P.A. Assimekopoulos, Phys. Rev. Lett. 24 (1970), 675.
3. C. Goorde, T. Kammuri, Nucl. Phys. A221 (1974), 238.

4. RADIATIVE CAPTURE

4.1 Magnetic Dipole Strength in ^{16}O

P.G. Ikossi, K.A. Snover, and T.A. Trainor

Here we report on the discovery of magnetic dipole (M1) γ-ray transition strength built on the ground state of the doubly magic ^{16}O nucleus. The current work represents an extension of earlier studies described in last year's Annual Report.

This discovery is interesting in part because of the expectation that M1 strength should be weak, since the M1 operator has no radial dependence (in the long-wavelength approximation) and hence cannot excite the closed-shell component of the ground state wavefunction. Thus the magnitude of ground-state M1 strength in doubly magic N=Z nuclei such as ^{16}O provides a direct quantitative measure of core-breaking correlations in the ground-state wavefunction. Also, it would be very interesting to know if the M1 strength built on the ground-state of doubly-magic nuclei is concentrated in one or a few of the lowest 1^+, T=1 levels, as is the case in other light A=4n nuclei.

We studied the polarized proton capture reaction $^{15}N(p_{pol},\gamma_o)^{16}O$ in a region of semi-isolated resonances located between 16 and 20 MeV excitation energy and found that we can unambiguously identify concentrations of M1 strength. This differs from previous studies[1,2] of polarized proton capture at higher energies in ^{16}O and other light nuclei where structure is broad, E1 and E2 radiation is present everywhere, and it is very hard to say how much, if any, M1 radiation is present.

Our data were obtained with the 10" x 10" NaI spectrometer and ∿50 nA of ∿75% polarized protons from the University of Washington tandem accelerator, using a gas cell with a 0.9 mg/cm^2 Ni entrance window and enriched ^{15}N gas at a pressure of 125-250 Torr for an overall proton energy resolution of 40-60 keV.

We measured the cross section σ(θ) and analyzing power A(θ) at θ = 90° as a function of bombarding energy, in fine energy steps, to locate M1 and/or E2 resonances. Angular distributions were used to determine the multipole assignments of the resonances. The angular dependence is given in the usual fashion:

$$\sigma(\theta) = [\sigma\uparrow(\theta)+\sigma\downarrow(\theta)]/2 = A_o\left[1+\sum_{i=1}^{4} Q_i a_i P_i(\cos\theta)\right]$$

$$\sigma(\theta)A(\theta) = [\sigma\uparrow(\theta)-\sigma\downarrow(\theta)]/2P = A_o\sum_{i=1}^{4} Q_i b_i P_i^1(\cos\theta) \qquad (1)$$

where ↑ and ↓ refer to the direction of the beam polarization (with magnitude P) relative to $\vec{k}_{in} \times \vec{k}_{out}$ and the Q_i are angular attenuation coefficients.

Multipoles of order higher than 2 as well as magnetic quadrupole may be neglected here. Excitation curve measurements at $\theta = 90°$ are especially useful since at this angle the analyzing power arises only from interfering radiations of opposite parity. Hence the energy dependence of the 90° analyzing power can be used to determine the parity of resonances if the parity of the background is known.

The 90° cross section (Fig. 4.1-1) reveals a number of resonances which (excepting the E_x = 16.22 MeV resonances—see below) have all been previously identified as E1.[3] The E1 assignments were primarily based on the radiative strengths. For example, the strong resonance at E_x = 17.29 MeV ($\Gamma_p\Gamma_{\gamma_0}/\Gamma \sim 22$ eV) and the dominant multipole in the broad background between E_x = 16 and 18 MeV ($\Gamma_p\Gamma_{\gamma_0}/\Gamma \sim 30$ eV) would be difficult to explain with an assignment other than E1 (also an (e,e') experiment[4] assigned 1^- to the unresolved 17.14-17.29 MeV doublet). As required for E1-E1 resonance-background interference, we do not observe a resonance in A(90°) near E_x = 17.29 MeV (Fig. 4.1-1) while the asymmetric shape of σ(90°) has a natural explanation in terms of E1-E1 interference.

A strong resonance effect is apparent in A(90°) near 17.14 MeV. The shape is consistent with interference between the 17.14 MeV resonance and the broad background plus the tail of the 17.29 MeV resonance. If multipoles other than E1 contribute only weakly to the background, as suggested by the smallness of the off resonance A(90°) and a_1 (Fig. 4.1-1) and the a_3 and b_3 coefficients near this energy (not shown), then the 17.14 MeV resonance must be 1^+ or 2^+.

Angular distributions were measured at various energies and were all in good agreement with the Legendre

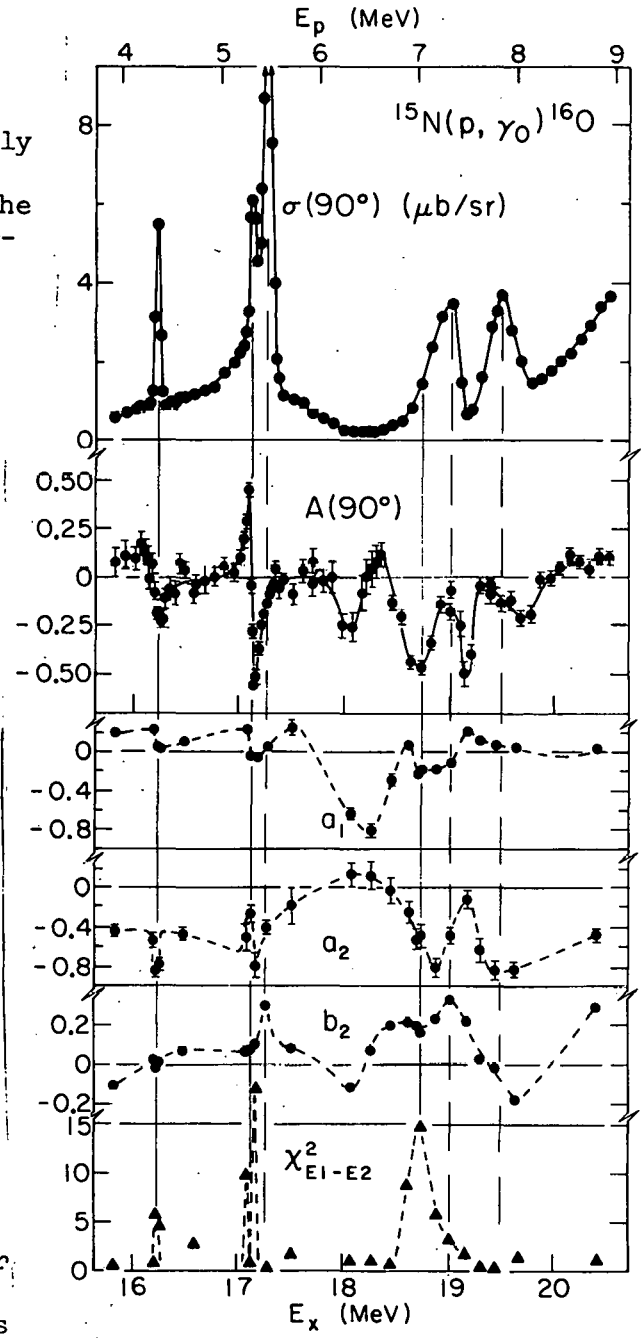

Fig. 4.1-1. Excitation curves for $^{15}N(p_{pol},\gamma_0)^{16}O$. Top part: σ(90°), A(90°) and the a_1, a_2, and b_2 coefficients (3rd and 4th order coefficients not shown). Bottom part: reduced χ^2 for the angular distribution fits assuming only E1 and E2 radiation.

expansion in equation (1). Further fits were performed to a T-matrix expansion in which the channel amplitudes and phases for each multipole were allowed to vary independently. When only E1 and E2 multipoles were included in this fit, there were energies where we could not obtain an acceptable fit, such as near 17.14 MeV (see the χ^2 plot in Fig. 4.1-1), indicating that M1 radiation is required. When M1 radiation was included in the analysis at these energies, a good fit was obtained, as illustrated in Fig. 4.1-2. We interpret this to imply that the 17.14 MeV resonance is M1.

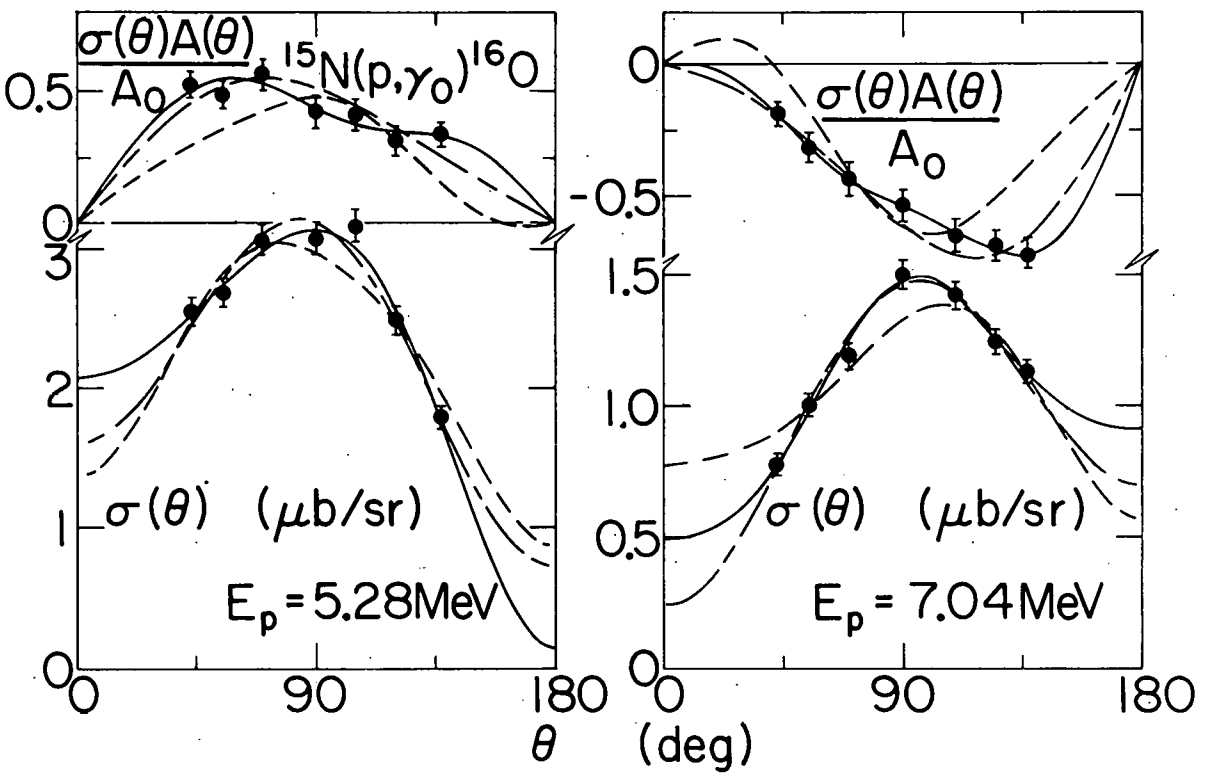

Fig. 4.1-2. Representative angular distributions which require M1 radiation. Solid curve: E1 + E2 + M1; dashed curve: E1 + E2; long-short dashed curve: E1 + M1 calculated fits.

In addition to the 17.14 MeV resonance, the strong resonance at E_x = 16.22 MeV also shows a pronounced effect in A(90°), indicating 1^+ or 2^+, and the χ^2 plot (Fig. 4.1-1) selects 1^+. The energy dependence of the Legendre coefficients further supports these assignments. For the 16.22 resonance, $a_2 = -0.98 \pm 0.10$ and $b_2 = +0.03 \pm 0.03$ and for the 17.14 MeV resonance $a_2 = +0.09 \pm 0.16$ and $b_2 = +0.05 \pm 0.05$. Neither of these resonances can be E2 since for this spin sequence, an E2 resonance must have $0.35 \leq a_2 \leq 0.71$. The smallness of the resonance b_2's gives additional support to the M1 assignments. For M1 transitions $b_2 \approx 0$ since $b_2 \propto \sin[\phi(p_{3/2}) - \phi(p_{1/2})]$ and spin-orbit distortions are small (for electric resonances, the interfering channels involve different ℓ's and hence b_2 need not be small).

The 16.22 MeV resonance has been previously assigned 1^+ from an electron scattering experiment,[4] in agreement with our observations and analysis. A resonance analysis of the data of Fig. 4.1-1 is consistent with our 1^+ assignments. Nevertheless, our M1 assignments cannot be made with absolute certainty. A broader M1 distribution (comparable in strength to the 17.14 MeV resonance) interfering with E1 resonances at 17.14 and 17.30 MeV might explain the data in this region. However, this would require a conspiracy of E1 channel phases to cause deviations of A(90°) from zero near 17.14 MeV but not elsewhere. Thus the evidence strongly supports the proposed 1^+ assignments.

The χ^2 plot in Fig. 4.1-1 indicates an additional region of concentrated M1 strength near E_x = 18.8 MeV. Since this resonance is not resolved from the 19 MeV E1 resonance in the cross section, we obtain only a lower limit on its strength based on the minimum M1 amplitudes needed to make an acceptable fit to our angular distributions in this region.

Our results are summarized in Table 4.1-1. Gamma-decay widths and reduced M1 strengths $B(M1)\downarrow = 86.4\ \Gamma_\gamma(M1)/E_\gamma^3$ in units of μ_0^2 (nuclear magnetons)^2 are based on the measured capture strengths along with rough experimental estimates for Γ_p/Γ for the 16.22 and 17.14 MeV states[5] and assuming $\Gamma_p/\Gamma \leq 0.5$ for the 18.8 MeV state. It is noteworthy that the total M1 strength in ^{16}O (Table 1)[6] of $\gtrsim 0.24\ \mu_0^2$ is a significant fraction of the known[6] M1 strength in the neighboring A=4n nuclei ^{12}C (0.93 μ_0^2 for 15.1→0.0) and ^{20}Ne (0.7 μ_0^2 for 11.2→0.0), and is fragmented in energy in contrast to the strength in these other nuclei.

Table 4.1-1. 1^+ States in ^{16}O. Results are from the present work, except where noted.

E_x(MeV)	Γ_{cm}(keV)	$\Gamma_p\Gamma_{\gamma_o}/\Gamma$(eV)	Γ_p/Γ	Γ_{γ_o}(eV)	$B(M1)\downarrow(\mu_0^2)$
16.22[a]	18 ± 3[a]	2.65 ± 0.22	0.73[a]	3.6 (5.1 ⊥ 0.0)[b]	0.073 (0.103 ± 0.016)[b]
17.14[a]	36 ± 5[a]	3.75 ± 0.50	0.58[a]	6.5	0.110
18.8	~250	≥ 1.8 ± 0.3	≤ 0.5	≥ 3.6	≥ 0.047
				TOTAL	≥ 0.24[c]

a Ref 5.

b Ref 4.

c Based on the average of the present work and ref 4 for the 16.22 MeV state

The two lowest 1^+ states that we see in ^{16}O are almost certainly the T=1 analogs of the 3.36 and 4.32 MeV states in ^{16}N, which are believed to be mainly

2 particle-2 hole (2p-2h) states.[5] Thus in ^{16}O we are seeing primarily the M1 strength built on the 2p-2h ground-state correlations.

Our observation of substantial M1 strength build on the ^{16}O ground state is consistent with a very recent shell-model calculation by Arima and Strottman,[8] in which Kuo-Brown and Gillet interactions were used, with active nucleons in the $1p_{1/2}$, $1p_{3/2}$, $1d_{5/2}$, $1d_{3/2}$ and $2s_{1/2}$ orbitals (the only restriction being that the $1d_{3/2}$ orbital could contain at most 1 nucleon). Only states below 29 MeV are calculated. Between 16 and 20 MeV, they predict several M1 states with a total strength of 0.27 μ_0^2 which is quite comparable to experiment. At higher energies an additional strength of 0.6 μ_0^2 is predicted to be fragmented over a number of levels. The ground-state wavefunction generated in this calculation has a 17% 2p-2h intensity.

On the other hand, the SU_3 shell-model calculations of Millener[9] predict only ~0.05 μ_0^2 of ground-state M1 strength between 16 and 20 MeV. The total M1 strength is predicted to be weak because the ground-state correlations are predicted to be mainly of maximum spatial symmetry [4^4] and hence cannot be excited by the dominant (spin) part of the M1 operator. The present experimental results appear to require the ^{16}O ground-state correlations to be mainly of lower spatial symmetry.

Here we give a qualitative explanation of how the total M1 strength in a doubly magic nucleus like ^{16}O could be as great as in a neighboring A=4n non-closed shell nucleus like ^{12}C. First, one must recall that the ground state of ^{12}C is ~80% $^{11}S[4^3]$, which contributes only very weakly to M1 excitations, for the reasons given above. As a consequence, the strength of the 15.11→0.0 transition is only ~1/4 of the prediction in the j-j coupling limit. On the other hand, very strong [B(M1) ~ 5 μ_0^2] transitions exist between $(1^+, 0)$ and $(0^+, 1)$ states in odd-odd nuclei. Thus if the 2p-2h correlations in the ground state of ^{16}O contribute to M1 excitations with an intrinsic strength comparable to these strong odd-odd transitions, then the total M1 strength in ^{16}O and ^{12}C can be comparable.

In the future it will be interesting to search experimentally for M1 strength at higher energies in ^{16}O, although this will probably be appreciably more difficult. This work has recently been published[10] (a preliminary account of this work appeared in ref. 2).

1. S.S. Hanna *et al.*, Phys. Rev. Lett. 32, 114 (1974).
2. K.A. Snover, Proceedings of the Third International Conference on Neutron Capture Gamma Ray Spectroscopy, Brookhaven National Laboratory, Sept. 1978 (Plenum Press, 1979, p. 319), and references therein.
3. E.D. Earle and N.W. Tanner, Nucl. Phys. A95, 241 (1967).
4. M. Stroetzel and A. Goldmann, Z. Physik 233, 245 (1970).
5. F. Ajzenberg-Selove, Nucl. Phys. A281, 1 (1977).
6. Here we omit the 1^+ state at 13.67 MeV with $\Gamma_{\gamma_0} \approx 8.5$ eV listed in ref. 5 since this disagrees with M. Stroetzel, Z. Phys. 214, 357 (1968) who found Γ_{γ_0} (M1) < 0.5 eV.
7. F. Ajzenberg-Selove, Nucl. Phys. A248, 1 (1975); A300, 1 (1978).
8. A. Arima and D. Strottman, Phys. Lett., to be published.
9. D.J. Millener, private communication.
10. K.A. Snover, P.G. Ikossi and T.A. Trainor, Phys. Rev. Let.. 43, 117 (1979).

4.2 Is the Strong 10.3 MeV → 0.0 MeV Gamma Decay in ^{40}Ca Magnetic Dipole?

P.G. Ikossi, K. Lesko, K.A. Snover, and T.A. Trainor

Our discovery of substantial magnetic dipole strength in the doubly magic ^{16}O nucleus prompts the question: What is known about magnetic dipole strength in other light N=Z doubly magic nuclei? The nucleus ^{40}Ca is the only other one that falls in this category. In his review article on "Electroexcitation of Nucleon Magnetic Dipole Transitions," Fagg reports a possible magnetic dipole excitation at 10.34 MeV in ^{40}Ca with $\Gamma\gamma_0 = 7.0\ ^{+2}_{-2}\ ^{9}_{2}$ eV. This corresponds to $B(M1)\uparrow = [0.53\ ^{+0}_{-0}\ ^{22}_{17}]\mu_0^2$ and thus constitutes a very strong M1 decay, more than twice as strong as the total M1 strength of $\geq 0.24\ \mu_0^2$ known in ^{16}O (see Section 4.1 of this report). Although the ground-state correlations are believed to be larger in ^{40}Ca than in ^{16}O, in light of experiment and theory on M1 transitions in ^{16}O it seems surprising that so much M1 strength should be concentrated in a single state in ^{40}Ca.

Preliminary results from a more recent electron scattering experiment[2] appear to confirm the magnetic character of this excitation. If it is indeed magnetic dipole, then it should stand out strongly in the ^{39}K(p,γ)^{40}Ca reaction, since only the p_0 and γ channel are open at this energy. There is only one strong γ_0 resonance in this reaction near this energy; namely, the E_p = 2043 keV resonance with $(2J + 1)\Gamma_p\Gamma\gamma_0/\Gamma = 31 \pm 5$ eV, which agrees with the electron scattering strength assuming $\Gamma_p >> \Gamma_\gamma$. We report here an attempt to determine the multipolarity of this resonance by looking for resonance-background interference. The technique is described in more detail in the ^{12}C($\vec{p}$,γ_0) and ^{15}N($\vec{p}$,γ_0) experiments in this section.

A thin potassium metal target was evaporated onto a silver backing mounted on solid copper and transferred in vacuum to the target chamber. The target was water-cooled and was bombarded with ∿400 nA of unpolarized protons and, in a separate measurement, ∿40 nA of 66% polarized protons. The results are shown in Fig. 4.2-1. Figure 4.2-1(a) shows a $\theta_\gamma = 90°$ resonance yield measurement (counts per 300 μC of collected change) for a window encompassing the full-energy γ_0 peak. The sharp rise indicates that the total resonance width $\Gamma < 2$ keV and the slow fall-off of the high-energy side of the resonance indicates a significantly non-uniform target.

If there is some real non-resonant γ_0 background present due to E1 direct capture or to the tail of the GDR, then M1 resonance-E1 background interference should show up in the 90° analyzing power (B_1 coefficient) and/or in the 55°-125° cross section difference (A_1 coefficient). Figure. 4.2-1(b) shows PσA(90°) and σ(90°) (relative units) measured with ∿66% polarized beam. There is clearly no evidence for a resonance effect in PσA(90°) and $[\sigma A]_{max} \leq 0.05$. Next, measurements were made at 55° and 125° over the resonance (here the detector was further from the target than it was for the 90° measurements). The counting efficiencies were different at the 2 angles due to γ-absorption at 55° in the Cu target backing. The relative efficiencies at these angles was determined to be 0.723 ± 0.024 from yield measurements at f = 8662 and 8670 kHz, where no interference is expected. Figure 4.2-1(c) shows plots of $(0.723)^{-1}\ Y_{55°} \pm Y_{125°}$

where the difference is shown in the top part and the sum in the bottom part. Although there is some evidence for a non-zero effect in the difference, its fractional magnitude is $\sim 75/2500 = 0.03$ which is within the uncertainty of ± 0.033 in the relative efficiency. Thus real resonance-background interference is fractionally less than 0.03.

How big would one expect real M1 resonance-E1 background interference effects to be in this case? Most of the non-resonant yield in Fig. 4.2-1(a) does not come from real γ_0 counts—an estimate of the real background/resonance yield ratio from these data is $\sim 0.001\ ^{+0.003}_{-0.001}$. If we simply scale the resonance effects observed in $^{12}C(\vec{p},\gamma_0)$, we would expect an effect of the order of 0.01 in $A_1(\max)/A_0(\max)$ and 0.02 in $[\sigma A(90°)]_{max}/[\sigma(90°)]_{max}$ for a background/resonance ratio of 0.01, assuming the ratio of energy resolution to natural width is comparable for the 2 experiments (this ratio is ~ 2.5 for the $^{12}C(p,\gamma)$ experiment). Thus it is clear that we need an order of magnitude improvement in the experiment in order to have a chance of observing an effect. Other effects such as smaller background/resonance ratio, larger energy resolution/natural width ratio, or destructive cancellations between the additional interfering amplitudes that may be present in the $^{39}K(p,\gamma_0)$ reaction may reduce the possible interference effects even further.

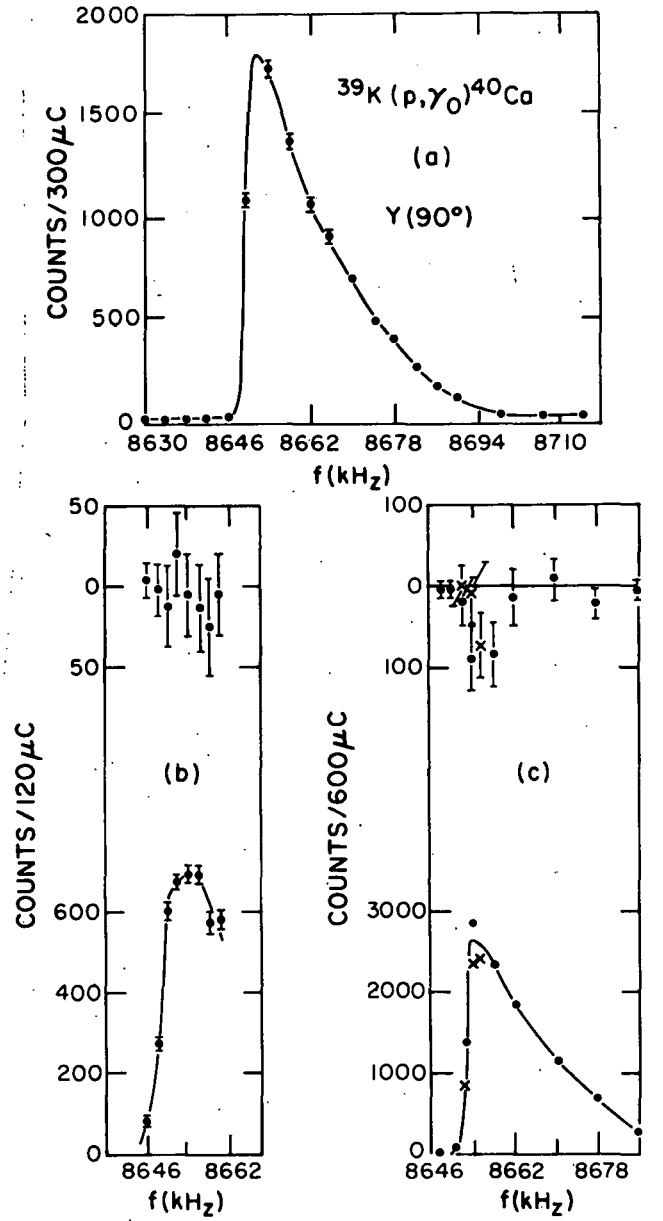

Fig. 4.2-1. Part (a) 90° excitation curve for the $^{39}K(p,\gamma_0)$ reaction near the $E_p = 2043$ keV resonance versus analyzing magnet NMR frequency. (b) 90° asymmetry (top part) and cross section (bottom part) measured with polarized beam. (c) 55°-125° yield difference (top part) and sum (bottom part).

1. L.W. Fagg, Rev. Mod. Phys. 47, 683 (1975).
2. L.W. Fagg, private communication.
3. P.M. Endt and C. VanderLeun, Nucl. Phys. A310, 557 (1978).

4.3 Unique Amplitude and Phase Determination for the $^{12}C(\vec{p},\gamma_0)^{13}N$ Reaction

E.G. Adelberger, P.G. Ikossi, K.A. Snover, and T.A. Trainor

Since the proton has intrinsic spin 1/2, angular momentum coupling rules in general allow at least 2 independent complex reaction amplitudes to contribute to proton radiative capture for each electromagnetic multipole involved. The actual number of possible reaction amplitudes depends on the spin sequence, and is simplest in the cases such as $^{12}C(\vec{p},\gamma_0)^{13}N$ where the intrinsic spin of the target and residual nuclei are 0 and 1/2 or vice-versa. In such cases only 2 complex reaction amplitudes may contribute for each multipole.

A determination of the capture amplitudes and phases would provide rather stringent restrictions on the details of the capture process, including the nuclear structure of resonances. Of particular interest would be a determination of this sort for the giant El resonance, which would serve as a test for the angular momentum composition of the GDR.

In the nuclear shell model, El photoexcitation of a p-shell nucleus primarily involves the excitation of nucleons from the p-shell to the sd-shell. Excitation from the p-orbital to the d-orbital is predicted to dominate, since $\langle p|El|d\rangle$ is significantly greater than $\langle p|El|s\rangle$. One way to get a handle on this very basic shell model prediction for the angular momentum composition of the GDR would be to measure the orbital angular momentum of nucleons ejected following photoexcitation, since these should be predominantly d-wave. For the ejection of protons (or neutrons) leaving the residual nucleus in its ground state (the time reversed radiative capture reaction), virtually all models of this reaction in the GDR region predict the dominance of d-wave nucleon emission as long as the target and residual ground states are related by the removal of a p-shell valence nucleon.

Currently the best information on this question comes from studies of polarized proton capture, where measurements of cross section and analyzing power severely restrict the possible solutions in a T-matrix decomposition of amplitudes and phases for capture through the GDR. Experiments on $(\vec{p},\gamma)$ in light nuclei with simple spin sequences typically restrict the possible GDR amplitudes and phases to 2 discrete sets of values or solutions, with one set requiring $d^2 >> s^2$ and the other $s^2 > d^2$. Two solutions occur because the cross sections and analyzing powers are bilinear in the amplitudes. Similar experimental results are found for all of the p-shell GDR $(\vec{p},\gamma)$ studies with simple spin sequences, including $^{12}C(\vec{p},\gamma_0)$, $^{14}C(\vec{p},\gamma_0)$ and $^{15}N(\vec{p},\gamma_0)$. This similarity suggests that one is observing the basic character of the GDR in these reactions and that more detailed effects having to do with the valence character of nucleons in

particular nuclei are unimportant at this level. Thus a measurement of the correct (physical) solution in one of these cases determines a general property of the GDR in the p-shell. We have, for the first time, succeeded in experimentally resolving the two-fold ambiguity in the amplitudes for the capture radiation.

We determined the physically correct solution for the GDR at E_p = 14.23 MeV in the $^{12}C(\vec{p},\gamma_0)^{13}N$ reaction, by studying the interference of the J^π = 3/2⁻, T = 3/2 M1(E2) resonance with the GDR background. The basic idea is to use resonance-background interference with a known resonance to determine unknown properties of the background. The lowest T = 3/2 resonance in ^{13}N is ideal for this purpose, since its important properties are all well-known.

Figure 4.3-1 shows data taken in the vicinity of the T = 3/2 resonance. The middle part of the figure displays the measured product of 90° cross section and analyzing power. The data show a clear interference effect which at 90° can be due only to interference of opposite parity radiations, i.e., the M1(E2) resonance interfering with the E1 part of the background. The curves are calculated for the 2 possible E1 solutions allowed by the analysis of $^{12}C(\vec{p},\gamma_0)$ angular distribution studies at E_p = 14 and 15 MeV.[1] The phase of the M1 resonance with respect to the E1 background was treated as a free parameter. The curves shown represent the best fit results using the known resonance parameters folded with a resolution function inferred from the measured σ(90°). The agreement between calculation and experiment for σA(90°) does not clearly distinguish between the 2 solutions.

Based on these fits one may calculate the expected effects in the A_1 Legendre coefficient in the cross section—the only other independent quantity which should show substantial interference effects. This is shown in the bottom part of Fig. 4.3-1 and the results indicate a substantial difference for the 2 possibilities. Initial

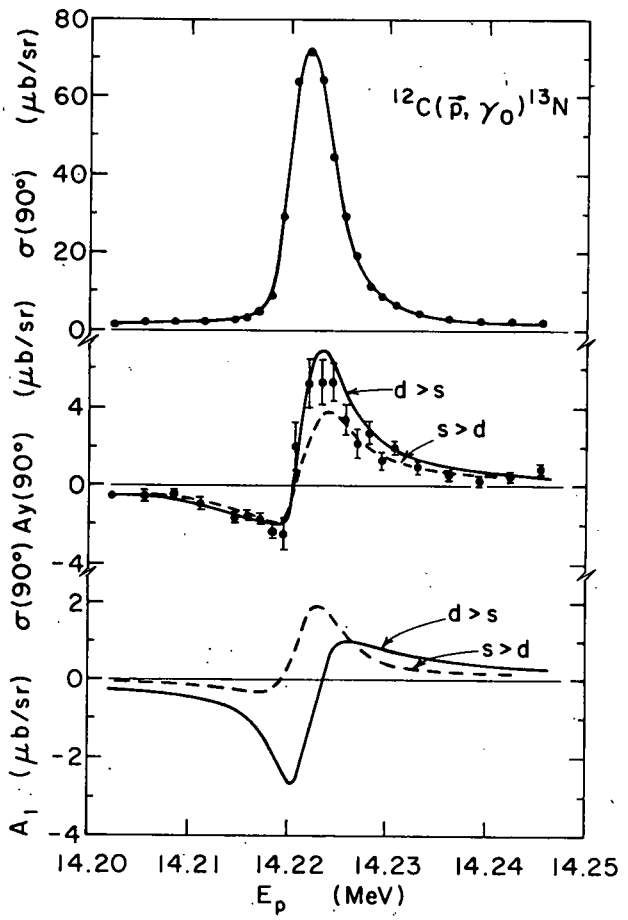

Fig. 4.3-1. Measured cross sections as a function of proton energy in the vicinity of the lowest T = 3/2 resonance. Top part: the 90° cross section, with the solid curve calculated using an asymmetric resolution function adjusted to fit the data. Middle part: the product of 90° cross section and analyzing power. Bottom part: calculated A_1 coefficients. The solid curves in the middle and bottom parts are for d > s and the dashed curves for s > d.

attempts to measure A_1 over the resonance based on sequential cross section measurements at 55° and 125° were fraught with difficulties due to small accelerator energy shifts (≲1 keV) that occurred during or between the measurements at each angle at a given energy. Most of these shifts were not big enough to significantly degrade the quality of the σ(90°) measurement, as shown in Fig. 4.3-1, but they caused serious problems in the cross section difference σ(55°) - σ(125°) used to derive A_1. [The maximum effect in A_1 is only ∿5% of A_0(max).] In a more recent run this problem was solved by simultaneously measuring excitation functions at 55° and 125° using the 10" x 10" spectrometer along with a 3" x 3" NaI. A preliminary analysis of these data indicates that the results strongly favor the d > s solution.

---

1. R.G. Helmer, M.D. Hasinoff, J.E. Bussoletti, K.A. Snover, and T.A. Trainor, to be published.

4.4 The Absolute Strength of the 13.03 MeV E2 Resonance in ^{16}O

P.G. Ikossi, K.A. Snover, and H.C. Bhang

We have studied the $^{12}C(\alpha,\gamma)$ reaction in the vicinity of the 13 MeV doublet in ^{16}O. Our investigation was prompted by the reported[1] discrepancy between the inelastic scattering results and the photonuclear E2 strength estimates.[2-5]

The data were taken in two different runs. In the first the target was a natural -C foil ∿95 μg/cm^2 and in the second an 84 μg/cm^2 isotopically enriched ^{12}C foil. We measured excitation functions at 90° at incident α-particle energies between 7.0 and 8.2 MeV. Also a total of 14 angular distributions were measured over the E_α = 7.9 MeV doublet and one at 7.1 MeV. The detector efficiency was determined by a comparison of the thick target yield of the E_x = 15.1 MeV T = 3/2 resonance in the $^{12}C(p,\gamma)$ reaction with the data of ref. 8. This measurement was done during the ^{12}C runs at exactly the same geometry used for the angular distribution measurements. The target thickness was measured from the energy loss of the 5.5 MeV α's from an ^{241}Am source passing through our ^{12}C target. The absolute data normalization factor deduced from these measurements was accurate to within ± 8%.

The absolute cross-sections were obtained by summing the same fraction of the photopeak summed in the $^{12}C(p,\gamma)$ efficiency measurement (92%-108%).

The angular distributions of the γ-rays were fitted under the assumption that only E1 and E2 radiations were present. Corrections due to finite detector geometry and transformation to the center of mass frame were taken into account. The resulting E1, E2 strengths and the interference term are shown in Fig. 4.4-1.

A resonance analysis was then performed to the 90° data together with the E1, E2 and interference cross sections obtained from the fits to the angular distributions. In this analysis the E1 resonances at E_α ∿7.1, 7.9 and the E2

resonance was included. Also the effect of the presence of an E1 or E2 background was investigated. During these investigations we found that the best fit resonance energies obtained by fitting the E_2 cross-sections alone were higher by about 50 keV than the one obtained from fits to all the data. Inclusion of a background linear in the E1 or E2 amplitudes reduced this discrepancy by ∿ 10-20 keV. It was thus concluded that this difference arose from insufficient determination of the phases involved. The results of the fits are shown in Table 4.4-1. The errors represent the maximum deviations observed in fitting different parts of the data separately and under the various assumptions for the backgrounds present. The actual values are taken for fits with no E2 background present and thus represent the total E2 strength underlying this energy region. An additional uncertainty of 8% was incorporated in the error for the resonance strengths to account for the uncertainty in the absolute cross section normalization. (Also a 5 keV uncertainty has been added to the error for the widths to account for an uncertainty of the straggling in the target.

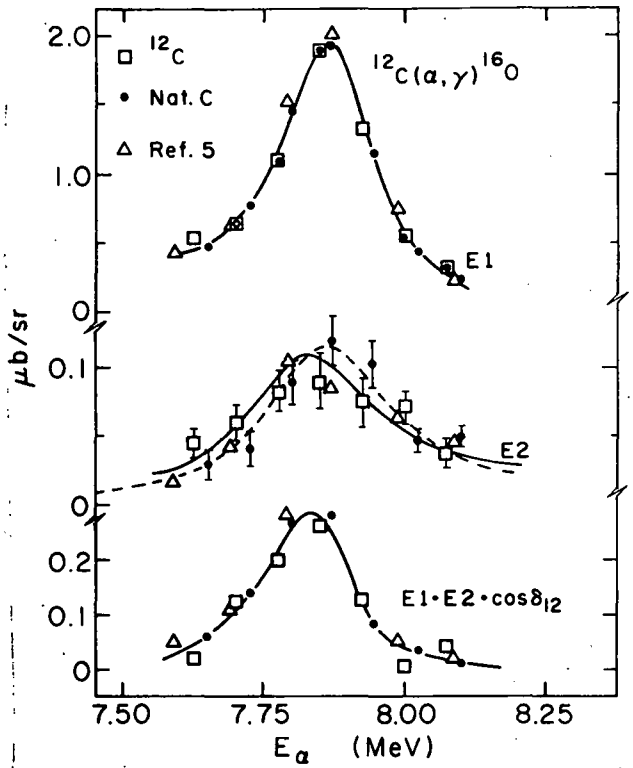

Fig. 4.4-1. Excitation functions of the E1, E2 and E1*E2*cos (ϕ_{12}) values deduced from the analysis of the angular distribution data. The solid lines represent best fit values obtained in fitting this data along with 90° excitation function data. The dotted line is the best fit obtained for the E2 cross-sections. The data of ref. 5 are included for comparison. The absolute energies were shifted by ∿ 10 keV and data normalization was adjusted so that the 90° data in both works are in agreement.

A comparison of our results to those of previous investigations is difficult. The reported values of the E1 cross-section on the peak of the 7.9 MeV resonance range between 1.13 (ref. 6) to 3.45 μb/sr (ref. 5). Our resonance E1 cross-section is 2.0 μb/sr which is lower than that of Larson and Spear (2.5 μb/sr) and also than that of ref. 2 (∿2.31 μb/sr). Therefore only a comparison of ratios of E2/E1 strengths is feasible. Mitchel and Ophel[4] give a ratio of E2 (E_α = 7.05 MeV) strength E1 (E_α = 7.90 MeV) of 0.03 ± 0.015 where the energies were presumably chosen at the peaks of the cross-section. In our analysis we find that the E2 resonance is located ∿50 keV below the E1 resonance. Since no information on the measured E1 and E2 cross-sections is given in ref. 4 we could not determine the cause of this discrepancy without a detailed analysis of their data. The ratio of the E2 cross-section at an energy 50 keV higher than the E1 resonance energy to the E1 resonance cross-section

Table 4.4-1. Summary of Present Results

E_R(MeV)	Γ(MeV)	$\Gamma_\alpha\Gamma_\gamma/\Gamma$(eV)	Γ_α/Γ(a)	Γ_γ(eV)
7.876 ± 0.006	0.139 ± 0.009	7.6 ± 0.7	0.35 ± 0.05	21.7 ± 3.7
7.822 ± 0.020	0.204 ± 0.015	0.43 ± 0.04	0.9 ± 0.1	0.48 ± 0.07

a) From ref. 7 (an average of the results of ref. 7 and earlier studies).

yields a ratio of strengths E2/E1 = 0.027 ± 0.006. This suggests that the scarcity of data in ref. 4 lead to a misjudgment of the exact location of the E_2 resonance

E_2/E_1 = 0.036 ± 0.012, corresponding to an E2 strength of 0.28 ± 0.09 eV when normalized to our data. This is lower than our estimate of 0.43 ± 0.04 eV. Nevertheless comparison of the values of the E2 cross-section calculated from the A_0, A_1 and A_2 coefficients in Table 2 of ref. 5 (see Fig. 4.4-1) indicates that this discrepancy is due to an underestimate of the area underneath the E2 resonance by the authors of ref. 5. It is apparent that when the same normalization is used the data of earlier works are in general agreement with our data. The differences arise from the procedures used in estimating the resonance strengths. The information given on these procedures is scarce. The detailed angular distributions in this work leave little room for error. The E2 strength deduced from our data is higher than the upper limit determined from the inelastic α' scattering. Due to the confusion in the literature on the absolute values of the (α,γ) cross-sections we are planning to repeat the normalization measurements. This will improve the accuracy of our preliminary results quoted above.

1. K.T. Knöpfle *et al.*, Phys. Rev. Lett. 35 (1975), 779.
2. K.A. Snover, E.G. Adelberger and D.R. Brown, Phys. Rev. Lett. 32 (1974), 1061.
3. J.D. Larson and R.H. Spear, Nucl. Phys. 56 (1964), 497.
4. I.V. Mitchel and T.R. Ophel, Nucl. Phys. 58 (1964), 529.
5. G. Kernel, W.M. Mason and V. Von Wimmersperg, Nucl. Phys. A167 (1971), 352.
6. T.R. Ophel *et al.*, Nucl. Phys. A273 (1976), 397.
7. T.P. Martin and P.P. Singh, Nucl. Phys. A180 (1972), 282.
8. R.E. Marrs, Ph.D. Dissertation (1975), University of Washington.

5.1 Importance of Two Step Mechanisms in the Production of ^{11}C from ^{13}C by π^- in the (3,3) Resonance Region

K. Aniol, D. Chiang, P. Drake, I. Halpern, and C. Haouat

Last year we reported some results from our cross section ratio measurement of $^{12}C(\pi^-,X)^{11}C/^{13}C(\pi^-,X)^{11}C$.[1]

In the course of interpreting these data we were led to the conclusion that a one step mechanism (knockout) followed by evaporation did not yield enough cross section to explain our $^{13}C(\pi^-,X)^{11}C$ cross sections. In particular, the yield of ^{11}C did not rise rapidly enough as a function of energy. The interpretation of this in terms of two step reactions is as follows. Below the resonance (< 180 MeV) a nucleon knockout results in a pion whose energy is even further away from the (3,3) πN resonance than the incident pion. Consequently, after scattering once the pion has a larger mean free path and a subsequent scattering has a smaller probability than the first. However, above the resonance (> 180 MeV) the first scattering results in a pion whose energy is nearer that of the resonance and the mean free path is shortened. This qualitatively accounts for the rapid rise of the $^{13}C(\pi^-,X)^{11}C$ cross section from 100 MeV to the resonance and its subsequent leveling off. To put these ideas into a quantitative form requires considerable computations. To make the calculations tractable we have done them in a semiclassical manner, approximating the pion and nucleon trajectories by straight lines. This allows us to use analytical forms for the pion and nucleon wave functions. A typical two step cross section is:

$$\sigma_j(b) = 2\pi b\,db \int_{-\infty}^{s} ds\; G\,\mu_o \frac{\rho_j(r)}{\rho_o} e^{-\mu_o L(s,b)} \int_{\theta_{min}} d\theta \frac{\frac{d\sigma_o}{d\Omega}}{\sigma_o} \sin\theta$$

$$X \int_0^2 d\phi\; G\,\mu(\theta) L(s,b,\theta,\phi)\; p_{np}(s,b,\theta,\phi) e^{-\mu(\theta)L(s,b,\theta,\phi)}$$

In this expression we calculate the cross section $\sigma_j(b)$ as a function of impact parameter b for knocking out a neutron in orbit j. The probability of scattering with this nucleon at a distance S is

$$\frac{G\mu_o}{\rho_o}\rho_j(r)\,ds$$

and the probability that the pion reaches point S is $e^{-\mu_o L(s,b)}$. Here μ_o is the central density mean free path, ρ_o is the central density, G is the fraction of interactions that are scattering and L(s,b) is the integrated path expressed in terms of the central density.

The outgoing pion has a reduced energy computed by free πN kinematics, but must lose a certain minimum (hence θ_{min} in the integral) energy to dislodge the bound nucleon. The probability for the pion to scatter into the angle Ω is determined by the free πN differential cross sections. Subsequent to the scattering the pion has a new energy which makes its outgoing mean free path $\mu(\theta)$ a function of θ. To approximate the second scattering the probability for one scattering in the integrated outgoing path $L(s,b,\theta,\phi)$ is assumed to be:

$$\mu(\theta)L(s,b,\theta,\phi)e^{-\mu(\theta)L(s,b,\theta,\phi)} .$$

The last term in the integral over φ, $P_{np}(s,b,\theta,\phi)$, is the probability for the outgoing neutron to emerge as a proton. The nucleon charge exchange is treated as a quasi elastic scattering and is discussed in a companion article. All three pion processes

$$\pi^+ + p \rightarrow \pi^+ + p$$

$$\pi^+ + n \rightarrow \pi^+ + n$$

$$\pi^+ + n \rightarrow \pi^0 + p$$

are treated and all processes which are one-step and two-step (i.e., the outgoing nucleon can also knockout a nucleon) are also treated.

The $\rho_j(r)$ are single particle wave functions (squared) and obtained from a potential that has central nuclear, Coulomb, and spin orbit parts. The shape of the well was chosen by comparison to electron scattering measurements. The well depth and radius parameters were chosen to match the r.m.s. radius[2] and binding energy of the $1p_{3/2}$ proton state. The total nuclear charge r.m.s. is 2.59 fm compared to the experimentally determined value of 2.45 fm from electron scattering.

For ^{12}C only $1p_{3/2}$ knockout is considered because for $1s_{1/2}$ knockout the resultant highly excited hole states in ^{11}C have an exceedingly small chance to gamma decay to bound states of ^{11}C. For ^{13}C, $1s_{1/2}$, $1p_{3/2}$, and $1p_{1/2}$ knockout are included. As a guide to how much 1p knockout strength there is in unbound states the spectroscopic factors from Cohen and Kurath[3] are used. The centroid for 1s knockout from ^{13}C lies above the neutron separation energy in ^{12}C.[4] The ratio R is finally written as

$$R = \frac{\sigma_{K.O.}(^{12}C, 1p_{3/2})}{f_s \sigma_{K.O.}(^{13}C, 1s_{1/2}) + f_p \sigma_{K.O.}(^{13}C, 1p) + \sum_{2\ step} \sigma_2(^{13}C, 1p)}$$

Here f_s and f_p represent the fraction of unbound states of $^{12}C^*$ that must decay by n emission. These are parameters which are related to the precompound and compound emission of neutrons from the 1s or 1p hole states produced in ^{12}C by 1p or 1s knockout from ^{13}C.

In Fig. 5.E-1 we compare the calculated cross sections using $f_s = 0.35$, $f_p = 0.15$ and $f_s = 0.15$, $f_p = 0.35$.

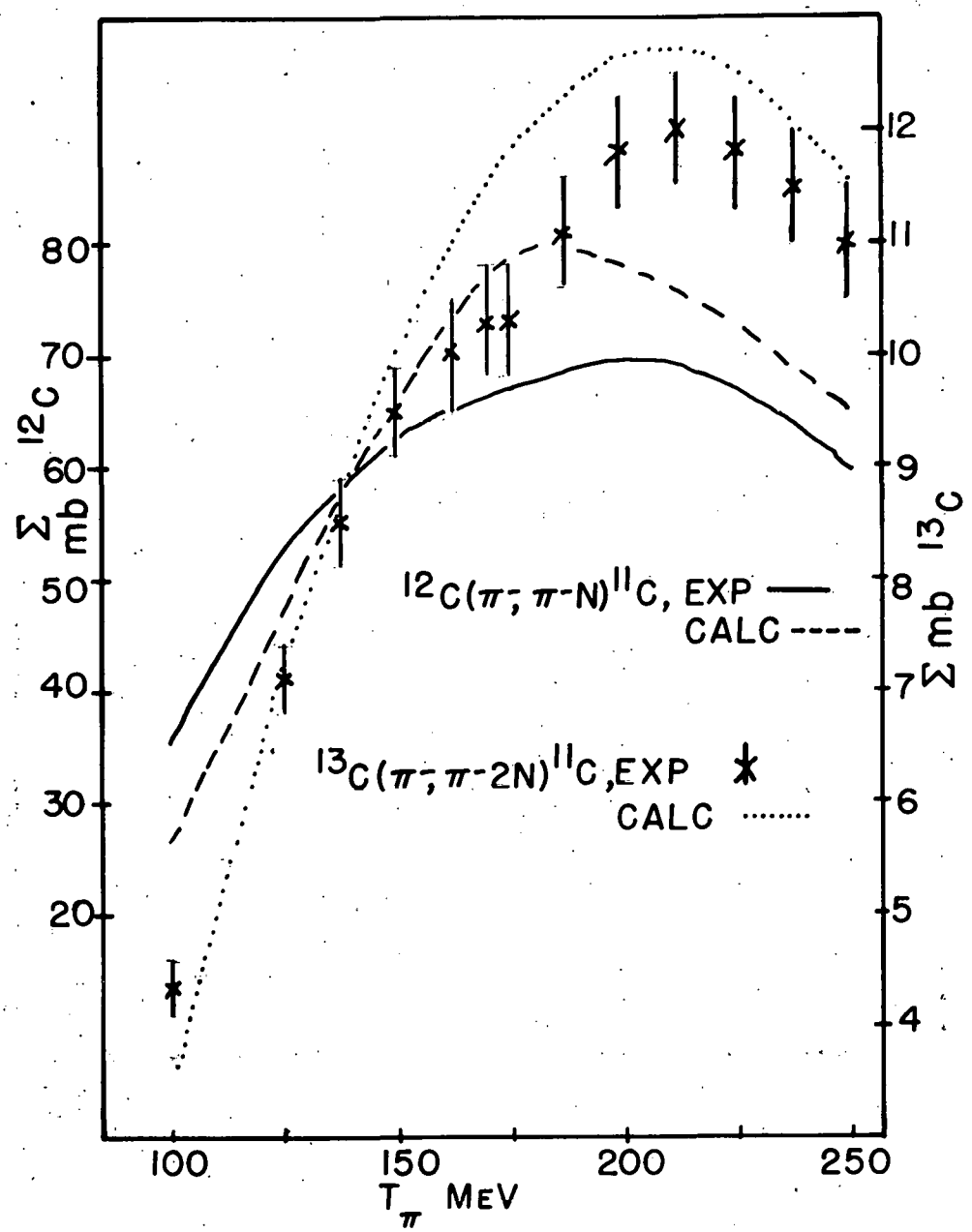

Fig. 5.1-1. Measured and calculated total cross sections of the $^{12}C(\pi^-,\pi^-N)^{11}C$ and $^{12}C(\pi^-,\pi^-2N)^{11}C$ reactions for $100 < T_\pi < 250$ MeV

Note that there are no adjustable parameters for ^{12}C. It is not the aim of this calculation to reproduce these cross sections in detail individually but rather their ratio. (The ^{12}C cross section comes from ref. 5.) In Fig. 5.1-2 the ratio is plotted. The data suggest there are two separate slopes above and below 175 MeV, with a flat connecting region of about 25 MeV. This two step calculation reproduces these features qualitative with essentially only two free parameters f_s and f_p. The calculated ratio for $T_\pi < 125$ MeV can be increased if the nucleon absorption is reduced for lower nucleon energies. The nucleon potential used here is $V = 50 - 0.14E_n + i(6 + 0.03\ E_n) + (58 + i4.65)\underline{t}\cdot\underline{T}$.

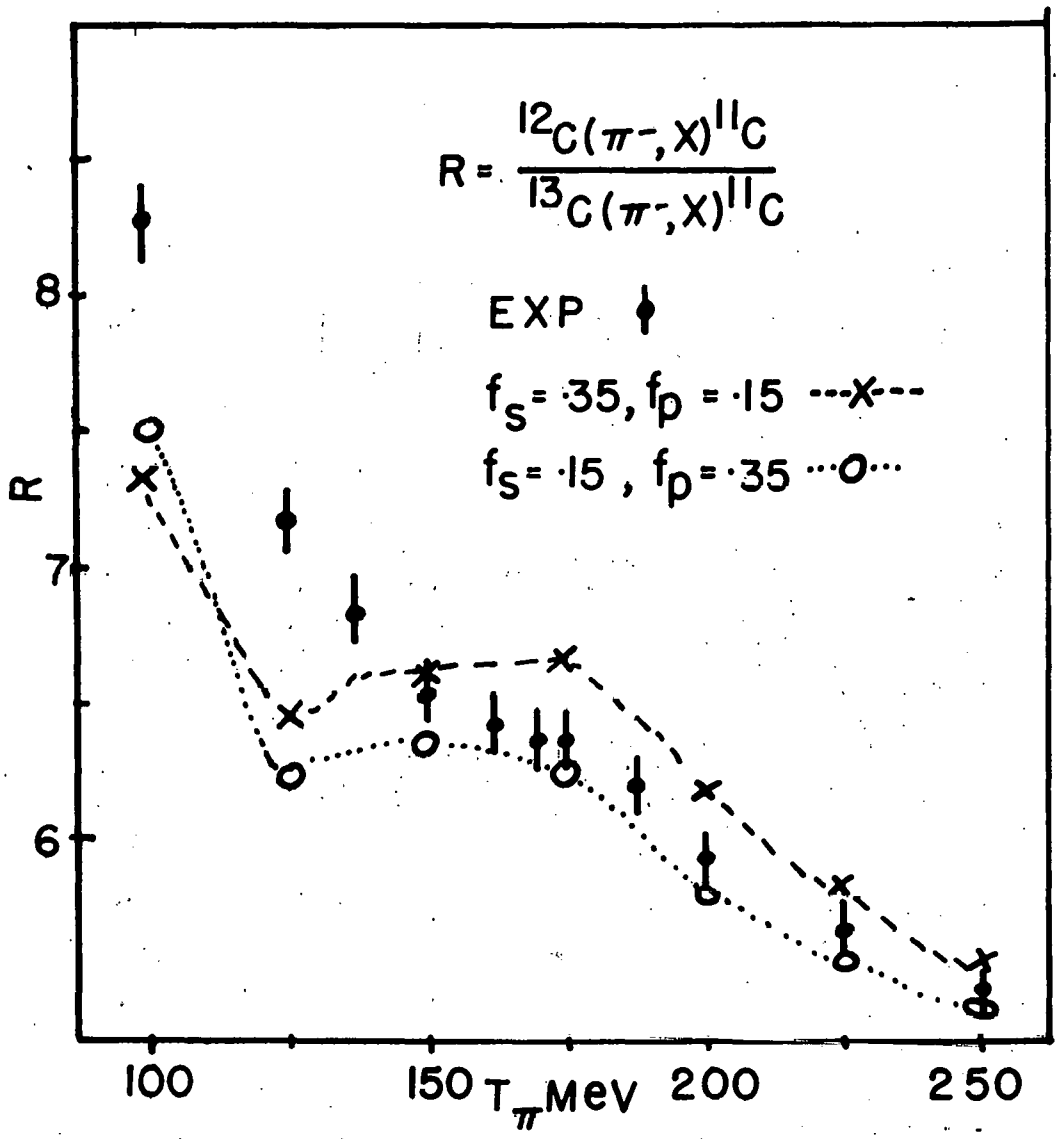

Fig. 5.1-2. Ratio of the ^{11}C production yield from ^{12}C compared to ^{13}C for $100 < T_\pi < 250$ MeV

1. Annual Report 1978, Nuclear Physics Laboratory, University of Washington, K. Aniol, D. Chiang, D. Drake, I. Halpern, and G. Haouat, p. 90.
2. I. McCarty *et al.*, Aust. J. Phys. 24 (1971) 661.
3. S. Cohen and D. Kurath, Nucl. Phys. A101 (1967) 1.
4. G. Jacob, Th.A.J. Moris, Rev. Mod. Phys. 38 (1966) 121.
5. B. Dropesky *et al.*, Phys. Rev. Lett. 34 (1975) 821.

5.2 Evaluation of the Nucleon Charge Exchange Cross Section for the $^{12}C(\pi^-/\pi^+)^{11}C$ Ratio

K. Aniol

In order to account for the activation data we obtained from the $^{13}C + \pi^{\pm} \rightarrow {}^{11}C + x$ and $^{12}C + \pi^{\pm} \rightarrow {}^{11}C + x$ measurements we reported last year[1] it has been necessary to calculate the nucleon charge exchange cross section for nucleons on $^{11,12}C$. Part of the model we are developing (see the companion article) requires evaporation subsequent to a nucleon knockout, and the charge exchange probability of the outgoing nucleon is particularly important.

The first calculation of this probability was performed by Hewson[2] using plane wave pions and distorted wave nucleons. This calculation was performed at only one energy. The goal was to reproduce the observed cross section ratio of $(^{12}C + \pi^- \rightarrow {}^{11}C + x)/(^{12}C + \pi^+ \rightarrow {}^{11}C + x)$ at T_π = 180 MeV.

A second calculation by Silbar and Sternheim[3] covered a large range of pion energies. This calculation is quite successful despite the great simplifications of their model.

Our calculation employs nucleon wavefunctions obtained by solving the Lane-Robson[4] coupled equations in a medium of constant density. This enables us to use analytical forms for the nucleon wavefunctions. A realistic form of the isospin potential $\underline{t}\cdot\underline{T}W(v)$ is surface peaked, but then the nucleon wavefunction no longer has a simple analytical form. The strength of our potential W_o in $\underline{t}\cdot\underline{T}W_o$ is determined so that its volume integral is equal to the volume integral of a surfaced peaked interaction used by Hewson. Using the value W_o so found our ratio at 180 MeV is 1.45 compared to Hewson's calculated value of 1.57. Thus, as far as the total cross section for nucleon charge exchange is concerned, our semiclassical calculation yields the same value as Hewson's distorted wave treatment.

For the calculation shown in Fig. 5.2-1 (solid line) the following optical potential was used:

$$V = (50-0.14E) + i10 + (58+i5.8)\underline{t}\cdot\underline{T}$$

For comparison the experimental data[5] and Silbar and Sternheim's[3] calculation (dashed line) are also known.

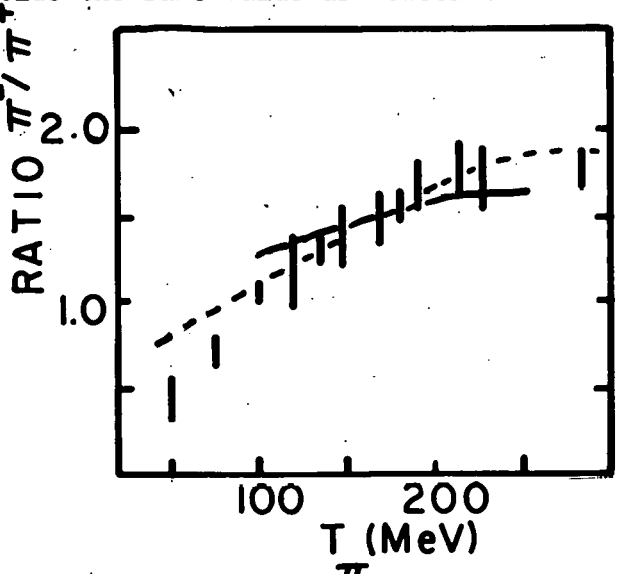

Fig. 5.2-1. Evaluation of the nucleon charge exchange cross section for the $^{12}C(\pi^-/\pi^+)^{11}C$ ratio

1. Annual Report 1978, Nuclear Physics Laboratory, University of Washington, K. Aniol, D. Chiang, D. Drake, I. Halpern, G. Haouat, p. 90.
2. P.W. Hewson, Nuclear Physics A133 (1969), 659.
3. M.M. Sternheim and R.R. Silbar, Phys. Rev. Lett. 34 (1975), 824.
4. B. Bayman in Proceedings of the International School of Physics Entico Fermi course XL, Academic Press, New York and London, 1969.
5. B.J. Dropesky, B.W. Butler, C.J. Orth, R.A. Williams, G. Friedlander, M.A. Yates, S.B. Kaufman, Phys. Rev. Lett 34 (1975), 821.

5.3 Backward Inclusive Scattering

G. Roy, G.A. Moss, D.A. Hutcheon, L. Greeniaus, R. Liljestrand, University of Alberta; N. Willis, A. Willis, Saclay; J. Arvieux, Grenoble; B. McCammis, University of Winnipeg; R. Woloshyn, TRIUMF; A. Stetz, University of Oregon; and K. Aniol, University of Washington

In a measurement at TRIUMF we have measured the backward inclusive scattering of 500 MeV protons from targets of C, Ta, and ^{4}He.

Interest in these types of reactions was sparked by the observation[1] of high energy nucleons and fragments emitted in the backward direction. Attempts to explain these energetic fragments have included collisions with clusters in the target,[2] exchange mechanisms[3] whereby the incoming proton interacts with the off-shell A-1 particles with the backward emission of a target nucleon, or collisions between the incident nucleon and an off-shell target nucleon.[4] In this last model[4] the scattering puts the target nucleon on shell and it is this nucleon which is detected in the backward direction. In this model[4] the observed spectrum is related to the momentum distribution of the target nucleon.

The proton spectra for $p + {}^4He \rightarrow p + x$ at $\theta = 90°$, 120°, and 160° are shown in Fig. 5.3-1. In each case we measured out to the elastic peak. Although all the models do well in explaining cross section and spectrum, only the model of ref. 4 predicts any appreciable analyzing power for the observed nucleons.

We also measured the analyzing power A across the proton spectrum for $^4He + \vec{p} \rightarrow p + x$ at three angles, 90°, 120°, and 160°. A preliminary analysis of the 90° analyzing power is presented in Fig. 5.3-2. The 120° and 160° analyzing powers are still being worked on, but at none of the angles does A seem to be very large. We are currently trying to interpret these results in terms of a modified form of the nucleon-nucleon scattering model of Amado and Woloshyn.[4]

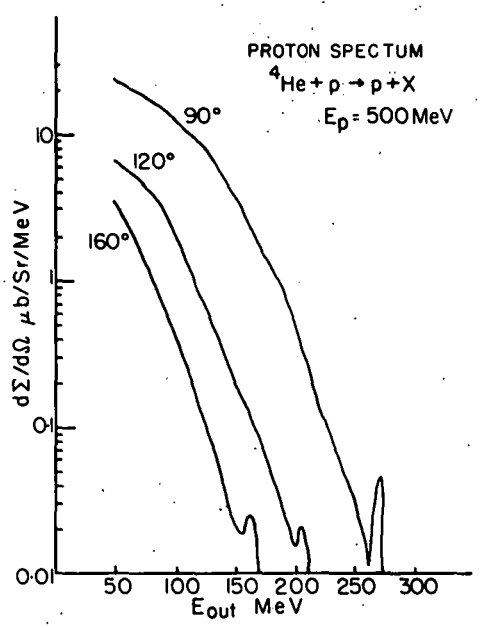

Fig. 5.3-1. Inclusive proton spectra for $^4He + P \rightarrow P + X$ at 90°, 120°, and 160° for 500 MeV proton.

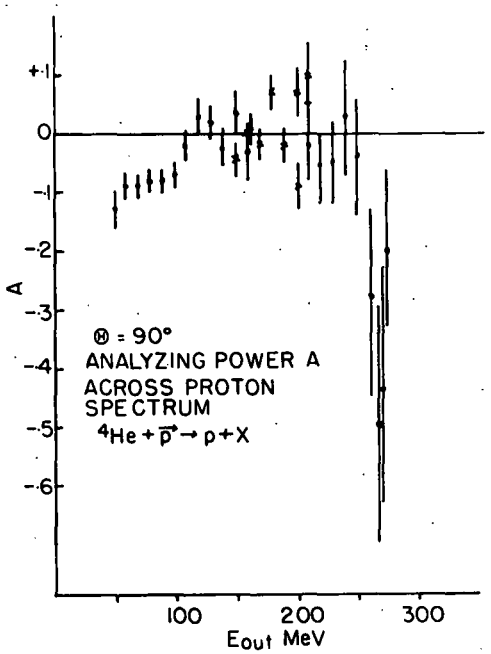

Fig. 5.3-2. Analyzing power of the inclusive proton scattering for the $^4He + \vec{P} \rightarrow P + X$ reaction at 90° for E_p = 500 MeV.

1. S. Frankel *et al.*, Phys. Rev. Lett. 36 (1976), 642; A.M. Poskanzer *et al.*, Phys. Rev. C3 (1971), 882; Yu, D. Bayukov *et al.*, Sov. J. Nucl. Phys. C3 19 (1974), 648.
2. T. Fugita, Phys. Rev. Lett. 39 (1977), 174.
3. H.J. Weber and L.D. Miller, Phys. Rev. C16 (1977), 726.
4. R.D. Amado and R.M. Woloshyn, Phys. Lett. 62B (1976), 253.

5.4 Inelastic Scattering of Pions to the Continuum

K. Aniol, D.T. Chiang, I. Halpern, G.A. Miller, and collaborators

Since the last Annual Report we have completed a two week run at LAMPF. During this run we measured the angular distribution of pion inelastic scattering on calcium and on magnesium at 67 MeV. In addition we obtained spectra on other targets at a few angles and of calcium and magnesium at a few nearby energies.

Most of the data of this run have been analyzed. We show in Fig. 5.4-1 sample spectra at 80° from various targets. Clearly at 67 MeV incident pion energy the Ca spectrum shows a pronounced structure around 18 MeV excitation energy. A slightly weaker bump can also be seen in the Mg spectrum at about the

same energy. Such structures were not observed in the heavier targets such as Zr, Sn and Pb at the few angles where measurements were made. This is probably to be explained by the larger continuous background yield in the heavier targets and the limited statistics. The spectra from all targets showed sharp bumps at back angles with excitation energies less than 10 MeV. In some cases these sharp lines could be identified with well-known inelastic excitations measured with other projectiles.

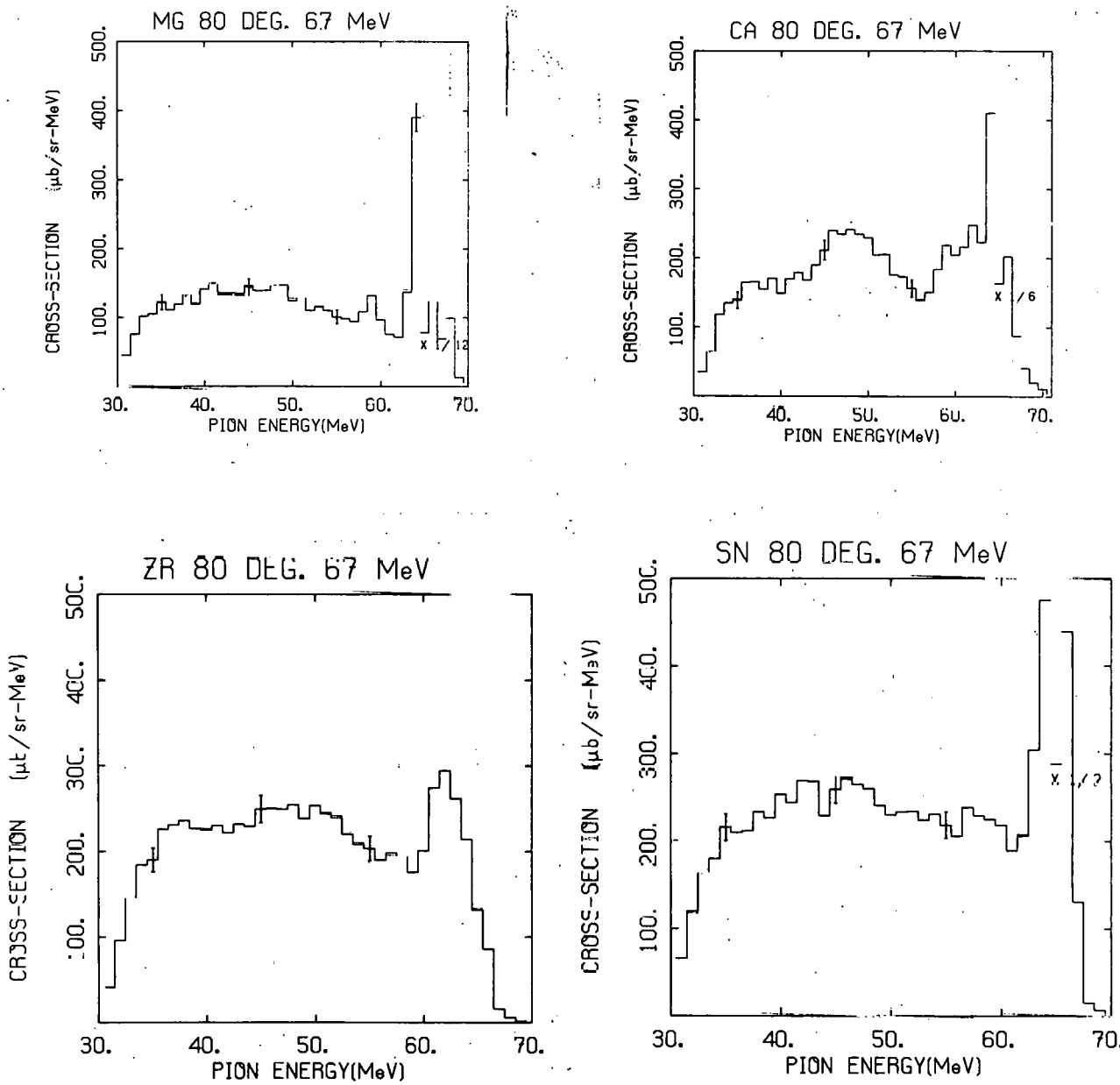

Fig. 5.4-1. Inelastic pion spectra at 80° for several targets and energy. Error bars shown are statistical.

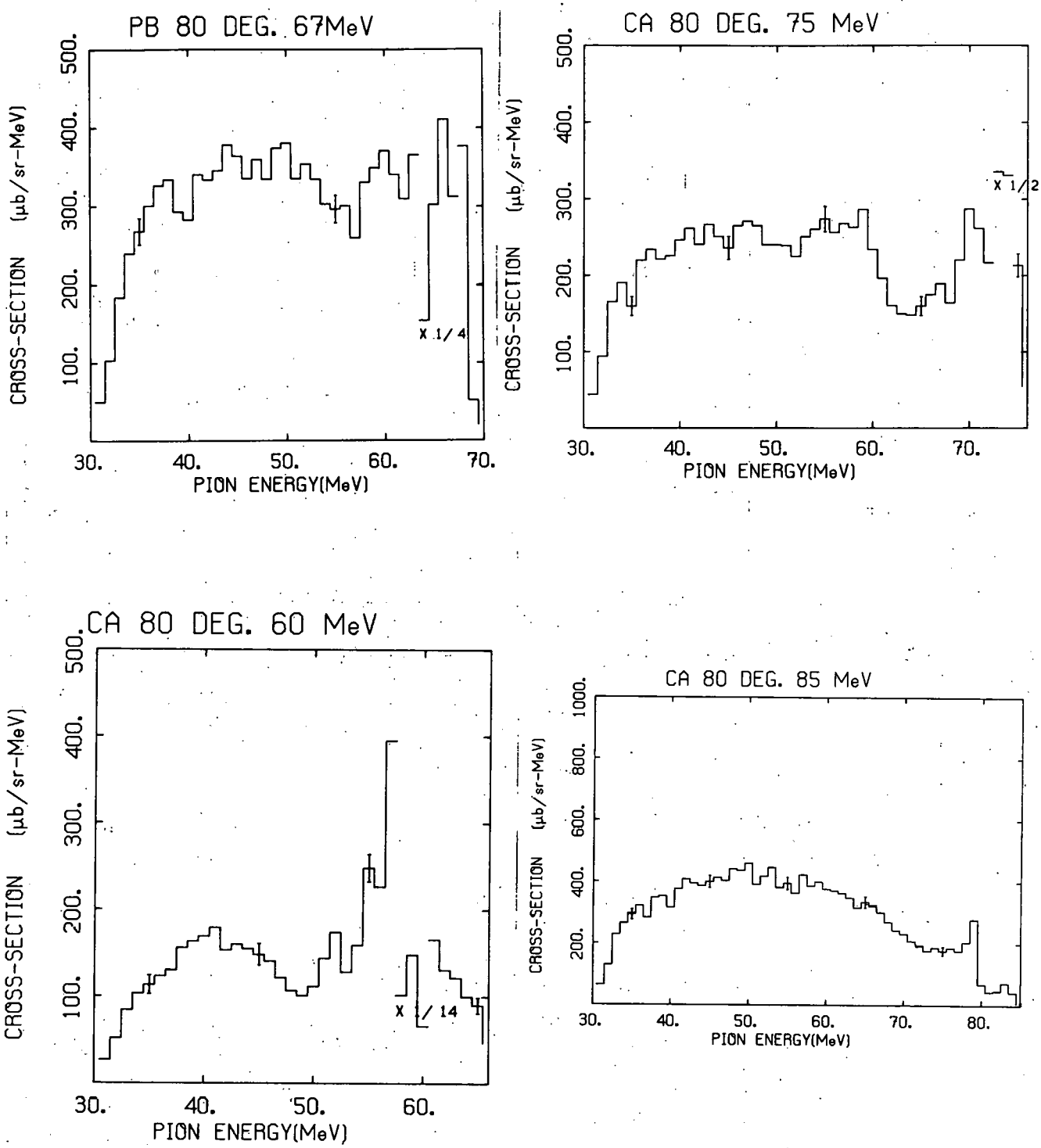

Fig. 5.4-1. (Continued)

Guided by the work of Yamagata, et al.,[1] we have decomposed the Ca structure between 10 and 20 MeV into two separate bumps, one located at 18 ± 1 MeV and the other at 13 ± 1 MeV. Figure 5.4-2 shows the extracted cross sections. Also shown are distorted wave calculations of isoscalar monopole (GMR), isovector dipole (GDR), isoscalar quadrupole (GQR), and octupole (GOR) angular distributions using a Kisslinger model optical potential. The angular distribution of the 18 MeV bump can be fitted by a linear combination of either GDR and GQR or GDR and GOR. In contract to the work of Yamagata, et al., where only GQR and GOR modes were excited in this region, we find it necessary to include GDR. This is probably to be expected because of the pion's large isovector interaction strength.

The strength of the 13 MeV state is weak. For those angles near 80° the state was not well resolved from the 18 MeV state and the cross sections had to be estimated. The resulting angular distribution somewhat resembles the calculated monopole angular distribution.

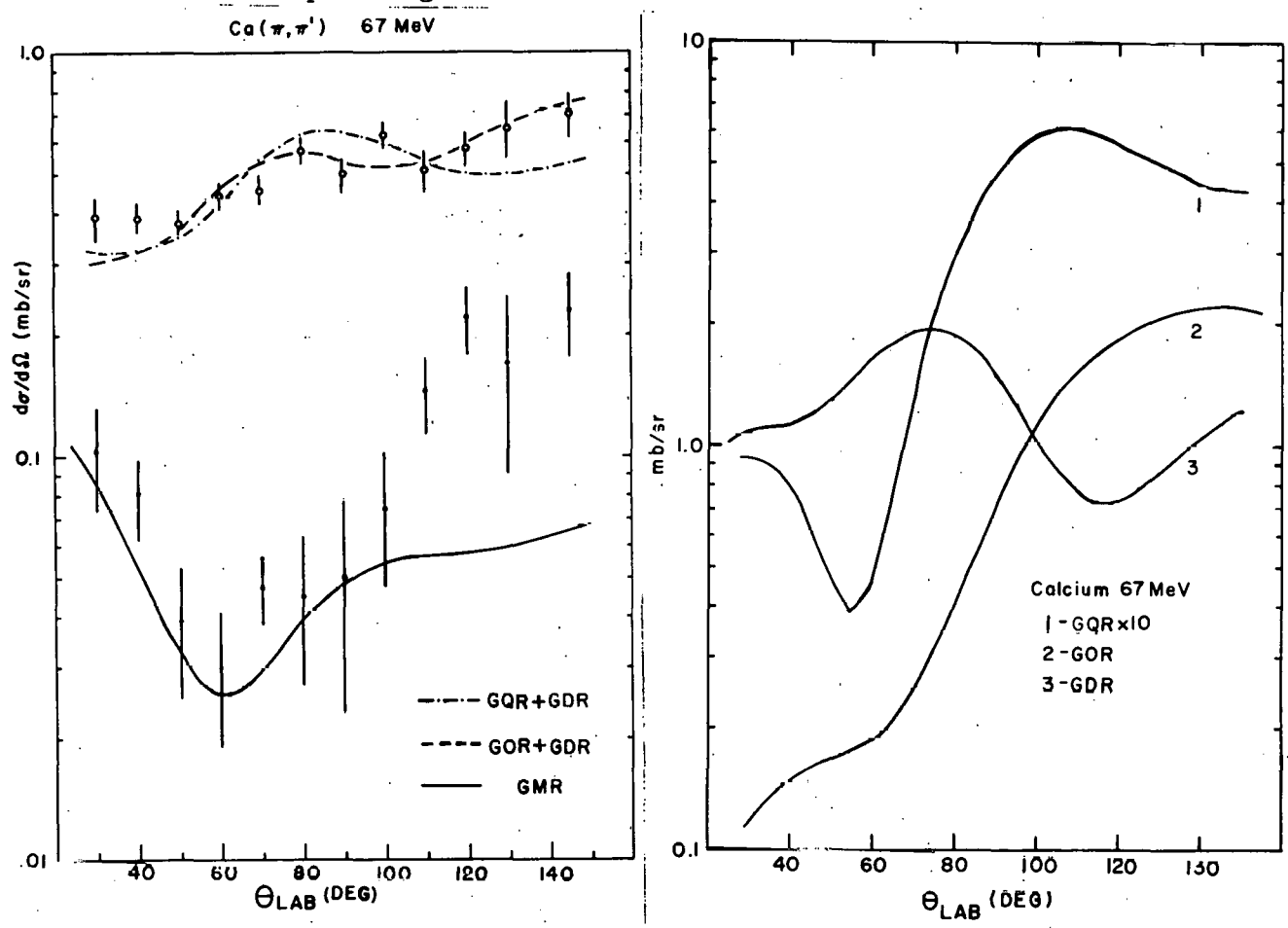

Fig. 5.4-2. Extracted peak cross sections for calcium are shown along with DWIA calculations for the various modes (solid curves). Linear best fits are also shown by dash curved and dash and dot curve.

It should be pointed out that because of an improvement in the GDR calculation we are now able to fit the angular distribution of the 19 MeV bump in the Li data which was reported in the last Annual Report. This bump was found to be fitted by sum of GDR and GQR excitations. Figure 5.4-3 shows the data and the best fit of the calculated angular distribution in Ni.

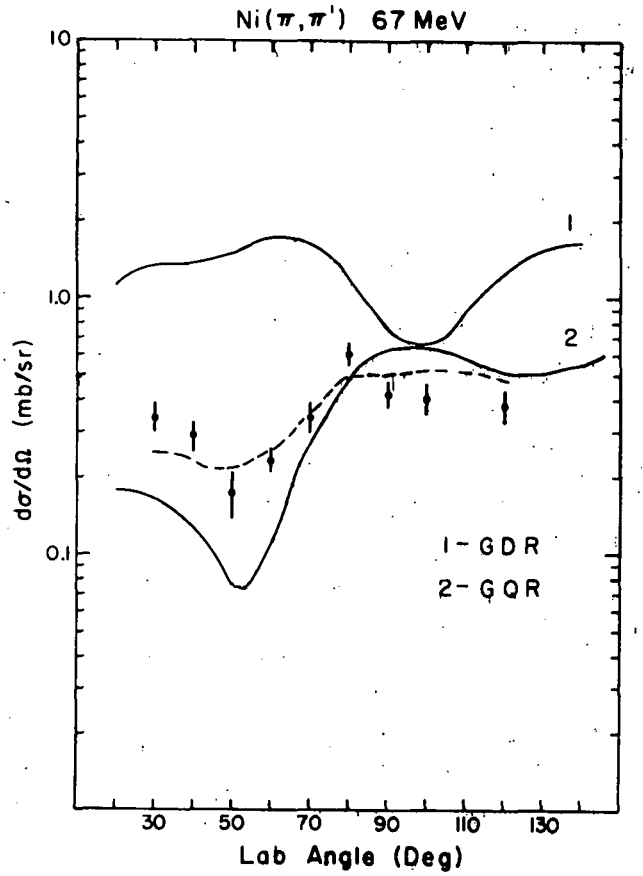

Fig. 5.4-3. Ni data obtained last year are shown with 1) GDR calculation and 2) GQR calculation and linear best fit (dash line).

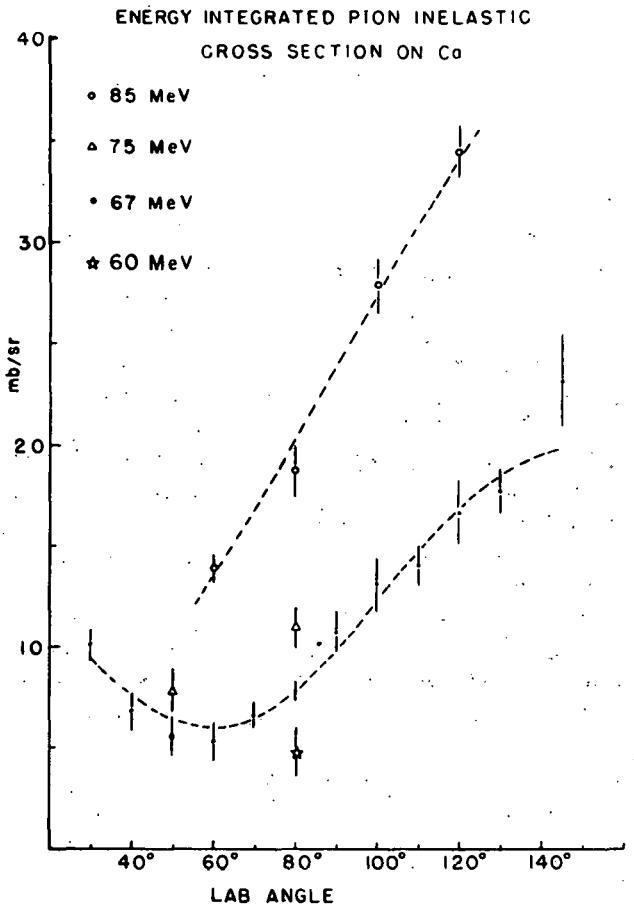

Fig. 5.4-4. Energy integrated cross sections on Ca are plotted as a function of the lab angle. Dash lines are Legendre polynomial fits. Error bars represent estimated errors due to low energy extrapolation.

As we have pointed out before, besides identifying structures, we are also interested in the general behavior of the total inelastic scattering cross section. In Fig. 5.4-4 we show the energy integrated inelastic scattering cross section as a function of lab angle for calcium. Data at four different incident pion energies are shown. It is clear from this figure that the inelastic pion

scattering cross section is strongly energy dependent in this energy range. For those targets (Mg, Ca, Ni) for which we have sufficient data we have made Legendre polynomial fits to the data and integrated the fits to obtain the total inelastic scattering cross section. For those targets where we did not measure a complete angular distribution we have estimated the total inelastic cross section on the assumption that their energy integrated cross sections displayed the same backward peaked angular distribution as Ca. As shown in Fig. 5.4-5 we find the total inelastic pion cross section depends on target mass number A according to $A^{1/2}$ for the heavier targets. The A dependence is somewhat steeper for lighter targets.

In the future we plan to improve the statistical accuracy of some of these measurements, and to extend the measurements to other targets and incident energies. We continue to be interested in the total inelastic spectra as well as in the conspicuous resonant structures that appear in these spectra. The fact that the GDR is strongly excited by pions leads one to believe that the isovector quadrupole should also be strongly excited by pions. We would very much like to search for evidence of the isovector quadrupole if we can obtain data with sufficient statistics to see it. We would like to compare our results on the total inelastic scattering to direct or indirect results on true meson absorption. The comparison is a measure of the competition between these processes which in turn depends on the basic interaction mechanisms of mesons propagating in nuclear matter.

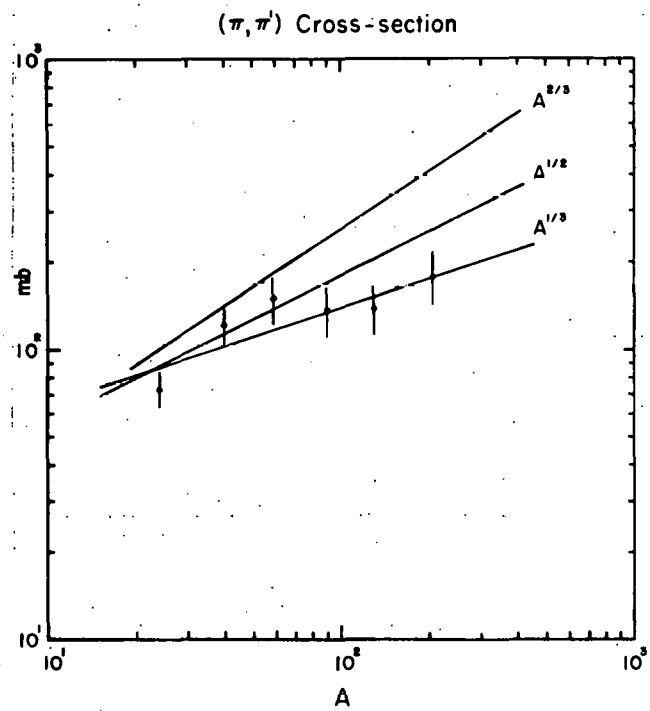

Fig. 5.4-5. Total inelastic scattering cross section plotted as a function of mass number

1. T. Yamagata *et al.*, Phys. Rev. Lett. 40, 1638 (1978).

6. HEAVY ION INDUCED REACTIONS

6.1 Comparison of the 180° Elastic Excitation Functions at Low Bombarding Energies for $^{12}C + ^{28}Si$, $^{13}C + ^{28}Si$, $^{12}C + ^{32}S$, and $^{13}C + ^{32}S$

N. Back, Y.-d. Chan, J.G. Cramer, H. Doubre, A. Lazarrini, S.Y. Lee,[a] W. Lynch, R.J. Puigh, and M.Y. Tsang

We have measured the 180° elastic excitation functions for $^{12}C + ^{28}Si$, $^{13}C + ^{28}Si$, $^{12}C + ^{32}S$, and $^{13}C + ^{32}S$ at low bombarding energies (6 to 10 MeV [c.m.] above the Coulomb barrier depending on the reaction). One purpose of these measurements is to look for any persistence of structures similar to those reported at higher energies[1,2,3] and also to obtain complimentary information on the possible systematic dependences of these structures.

The experimental method of using kinematically reversed techniques introduced in Ref. 1 was used. A Browne-Buechner magnetic spectrometer equipped with a gas proportional detector of large vertical acceptance in the focal plane was positioned at 0° (lab) with respect to the beam direction to detect the recoiling target particles (^{12}C,^{13}C). The acceptance angle in the scattering plane is 0° ± 2° (180° ± 4° in c.m.). Targets were self-supporting foils of isotopic ^{12}C and ^{13}C foils of ∿50 and 100 μg/cm^2 thick. To obtain the relative normalization, a thin gold layer was evaporated on the carbon targets and a Si monitor detector was mounted at θ_{lab} = 155° to detect the Coulomb scattered beam particles from the Au layer. Energy degrading nickel and molybdenum foils of various thickness (1.6-4.0 mg/cm^2) were mounted behind the target foils to remove the degeneracy in magnetic rigidity[1] between the recoiling target and beam particles. Gold and chemically treated silver masks of different thickness were also mounted in front of the focal plane detector to stop the residual beam. The absolute cross sections were normalized to the Rutherford cross section at the lowest measurement energies, which in all cases were well below the Coulomb barrier. A sample position spectrum for the $^{12}C + ^{32}S$ reaction is shown in the inserts of Fig. 6.1-1(a). The resolution of the position spectrum was sufficient to separate the elastic and the first inelastic peaks at this kinematic region.

The results of the 180° excitation function measurements are summarized in Figs. 6.1-1(a) and 6.1-1(b). Within the energy range we have investigated, the excitation function data exhibit a very strong systematic dependence as can be observed by comparing results from the ^{12}C and ^{13}C targets for both ^{28}Si and ^{32}S beams. The ^{12}C results show strongly oscillatory pattern superimposed on an exponentially falling tail. Results for the ^{13}C target are much smoother. This systematic dependence can be understood in terms of the differences in the availability[4] of open direct channels in carrying away the entrance channel angular momenta.

Additional forward angular distributions for the $^{12}C + ^{32}S$ system had been measured at $E_{lab}(^{32}S)$ = 60, 65, 70, 80, 90, and 99 MeV with conventional particle detection methods. Thin carbon targets (∿8 μg/cm^2) were used. Results for the angular distribution measurements are summarized in Fig. 6.1-2. The

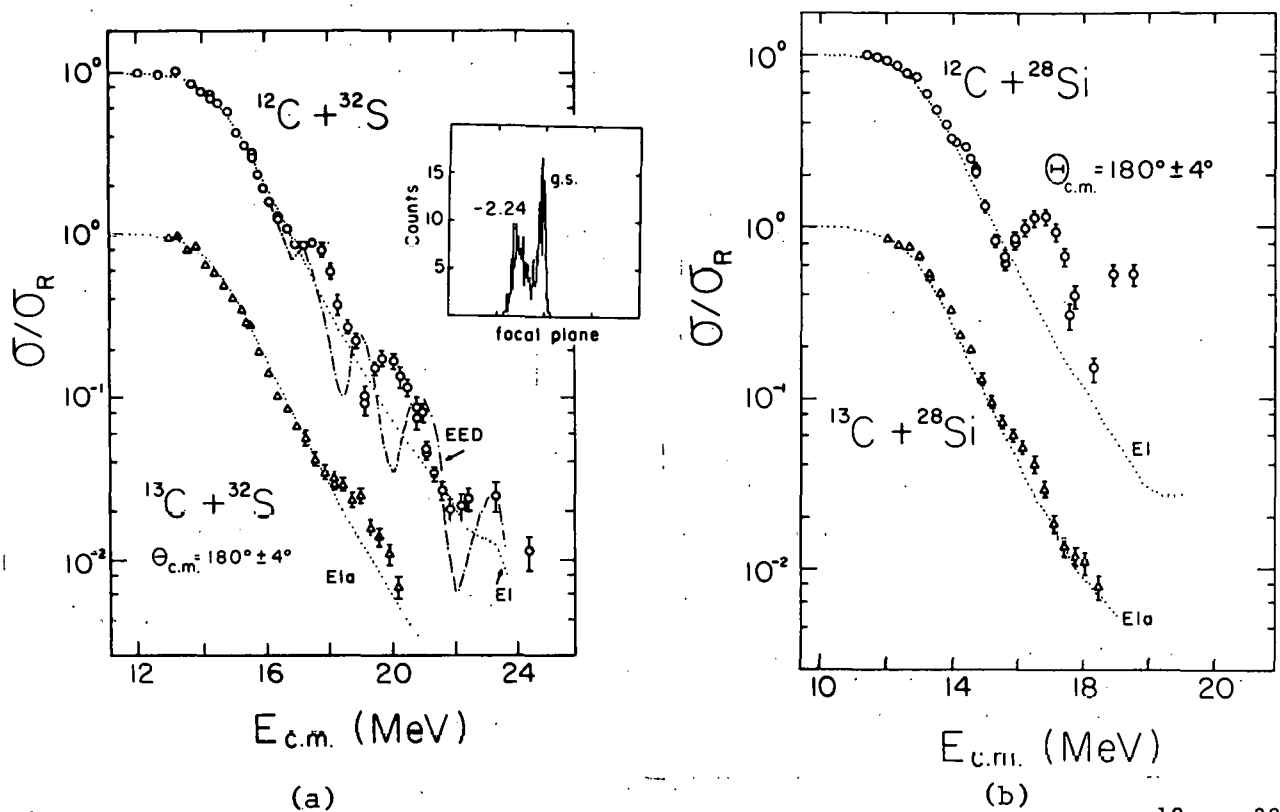

Fig. 6.1-1. 180° ± 4° (c.m.) elastic excitation function data for (a) $^{12}C + ^{32}S$, $^{13}C + ^{32}S$ and (b) $^{12}C + ^{28}Si$, $^{13}C + ^{28}Si$. Optical model calculations are indicated by dotted and dash-dotted curves. The insert in (a) is a focal plane spectrum for $^{12}C + ^{32}S$ at $E_{c.m.}$ = 21 MeV.

backward angle portion of the 80 MeV data had been obtained by detecting the recoiling ^{12}C in the forward angles by a solid state telescope.

In order to understand what these observed low energy structures (Fig. 6.1-1(a) and (b)) may imply, optical model studies have been carried out. Global parameter searches on the forward elastic angular distribution (Fig. 6.1-2) have been performed and the resulting best fit 6-parameter Woods-Saxon potential (set EI) is listed in Table 6.1-1 with calculated results shown by solid curves in Fig. 6.1-2. Also shown (dashed curves) are predictions from the global potential set EI8[5] originally deduced from the $^{28}Si + ^{16}O$ system.

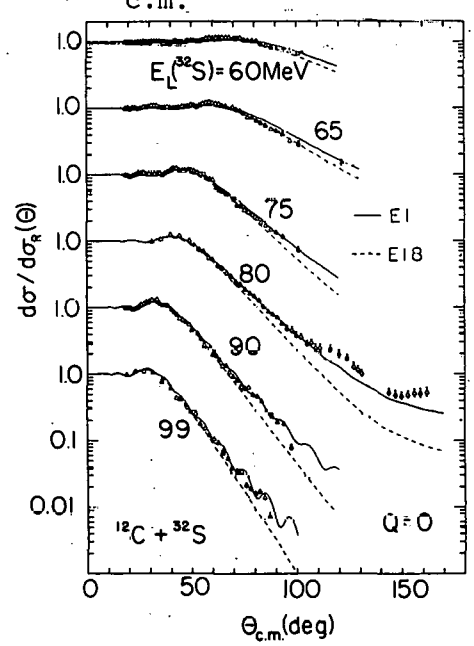

Fig. 6.1-2. Elastic angular distribution data for $^{12}C + ^{32}S$. The solid and dashed curves are optical model calculations.

Table 6.1-1. Optical model potential parameters used in the calculations. All form factors are Woods-Saxon r_c = 1.00 fm, and $R = r(A_p^{1/3} + A_T^{1/3})$

Set	V_o(MeV)	v_v(fm)	a_v(fm)	W_o(MeV)	r_w(fm)	a_w(fm)
EI	30.0	1.304	0.464	5.0	1.331	0.399
EIa	30.0	1.331	0.464	5.0	1.331	0.399
EED	30.0	1.304	0.464	$0.05\exp(0.185E_{cm})$	1.331	0.399

The elastic 180° excitation functions as calculated by potentials EI and EIa are indicated by dotted curves in Figs. 6.1-1(a) and (b). Potential EIa is identical to EI except for a slightly adjusted radius parameter to reproduce the excitation functions involving the ^{13}C target. As can be seen from the figure, structures in the data can not be reproduced by these potentials.

One factor that has not been included is the energy dependence of the absorption, which is expected to be important for the low energy region due to reaction phase space considerations. To investigate this, a sample calculation for the ^{12}C + ^{32}S system with potential EED, which is identical to EI except for an exponentially energy dependent absorption part, is shown by the dash-dotted curve in Fig. 6.1-1(a). The qualitative feature of the data can be reproduced, but with the calculation predicting more peaks than the data indicated. Even though potentials EI and EED predict very different behavior for the cross section at the backward angles, both predictions are comparable in the forward angular region.

Semi-classical analysis methods[6] have been applied to the above potential. Results so far have indicated that the multiple reflection of the internal wave causing strong interference with the barrier wave is responsible for the structures in the backward cross sections. However, these multiple reflections are comprised of many partial waves and are therefore different from the pure partial wave molecular resonance picture.

Further analysis of the data including parity-dependent potentials and generalized form factors[7] is in progress.

---

a Present address: Physics Dept., SUNY, Stony Brook, New York.

1 J. Barrette, M.J. LeVine, P. Braun-Munzinger, G.M. Berkowitz, M. Gai, J.W. Harris, and C.M. Jachcinski, Phys. Rev. Lett. 40, 445 (1978).

2 M.R. Clover, R.M. DeVries, R. Ost, M.J.A. Rust, R.N. Cherry Jr., and H.E. Gove, Phys. Rev. Lett. 40, 1008 (1978).

3 S.M. Lee, J.C. Adloff, P. Chevallier, D. Disdier, V. Rauch, and F. Scheibling, Phys. Rev. Lett. 42, 429 (1979).

4 R.W. Shaw Jr. R. Vandenbosch, and M.K. Mehta, Phys. Rev. Lett. 25, 457 (1970).

5 J.G. Cramer, R.M. DeVries, D.A. Goldberg, M.S. Zisman, and C.G. Maguire, Phys. Rev. C14, 2158 (1976).
6 D.M. Brink and N. Takigawa, Nucl. Phys. A279 159 (1977). N. Takigawa and S.Y. Lee, Nucl. Phys. A292 173 (1977). S.Y. Lee, N. Takigawa and C. Marty, Nucl. Phys. A308 161 (1978).
7 Y.-d. Chan and S.Y. Lee, University of Washington Nuclear Physics Laboratory Annual Report, p. 130, 1978.

6.2 Coincidence Study of the $^{27}Al(^{16}O,^{12}C\alpha)^{27}Al$ Reaction at 65 MeV

W.G. Lynch, R.J. Puigh, A.G. Seamster, M.B. Tsang, and R. Vandenbosch

Last year we reported[1] on the measurement of the C-α angular correlation for the reaction $^{27}Al + ^{16}O$ at 65 MeV. Two DE-E telescope counters were used to detect C and α particles in coincidence. This system suffered from the following disadvantages:

1. Cutoff of low energy α-particles at backward angles due to the finite thickness of the DE counter.

2. Our present multiparameter on-line data acquisition program (RALPH)[2] only accommodates four parameters in coincidence. However, coincidence experiments with two telescope counters require five parameters, namely DE_C, E_C, DE_α, E_α, and the time difference (TAC) between events in the two telescope counters. In order to meet the limitations of RALPH, the TAC spectrum was recorded off line on the ND2400 and two gate signals which correspond to the real and random part of the TAC spectrum were set electronically to route each of the DE and E spectra into two parts, real and random. It would have been much better if we could have event-recorded the TAC parameter during the experiment.

In order to solve the above difficulties, we have also taken data using a single counter instead of a telescope to detect α particles. The α particles were identified by measuring the time difference between arrival of an event in the C-telescope counter and the arrival of a coincident event in the single counter. The results of this new data taking system have been so successful that we can use four single counters routed to one ADC. Thus we were able to take data for four different α-angles at once.

The oxygen and carbon contaminants in the target were determined by backward angle scattering of low energy protons. Their presence is less than 1% atomic abundance. We further reduced carbon buildup during the experiment by installing a liquid nitrogen cold trap with an attachment of copper tubing around the targets.

Figure 6.2-1 shows the schematic view of the experimental setup. Coincidence events were detected with the C-telescope fixed at θ_C (θ_C = 30° and 40°). The detectors were moved in and out of the reaction plane which is defined by the beam and the C-telescope. The out-of-plane angles investigated are in the plane containing the recoil direction of $^{31}P^*$.

We assume in our data analysis a 3-body final state as given by $^{27}Al + {}^{16}O \rightarrow {}^{12}C + \alpha + {}^{27}Al + Q3$. All the data to be shown correspond to C-α coincident events with Q3 = -7.16 ± 1.13 MeV unless otherwise stated. As one of the objectives of this experiment is to understand the evaporation contribution to this exit channel, we can also represent the reaction as sequential breakup: $^{27}Al + {}^{16}O \rightarrow {}^{12}C + {}^{31}P^*$; $^{31}P^* \rightarrow \alpha + {}^{27}Al$. All the angular correlation data shown in this report are plotted in the center of mass frame of $^{31}P^*$ which has an excitation energy of about 14.5 MeV. Thus 0° represents the recoil direction.

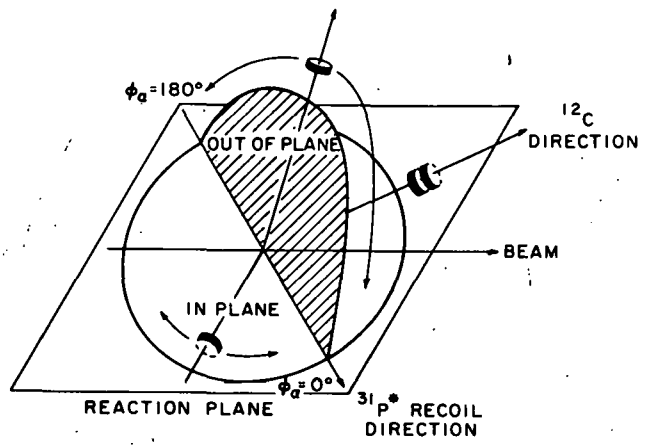

Fig. 6.2-1. Schematic view of the experimental arrangement (adapted from ref. 4)

Figure 6.2-2 shows the C-α angular correlation with the C-telescope fixed at 30°. We observe forward peaking towards the beam axis as reported last year rather than peaking at the recoil direction as reported previously.[3] Data taken with the new TOF method, indicated by open triangles; were normalized to the old data taken with two telescopes. At θ_α^{lab} = 17° and 43° around the C-telescope, we observed another separate group of events with low C-energy and high α-energy. These events can be clearly seen on Fig. 6.2-3. Figure 6.2-3 shows a 2-D plot of C energy vs. α energy for the C-α coincidence events at these angles. These events are attributed to fragmentation of the ^{16}O nucleus and can be cleanly separated at these angles. Cross sections that include this group (crosses) and data that exclude this group of events (solid circles) are both plotted at θ_α^{cm} = -87° and -118° in Fig. 6.2-2(a). Figure 6.2-2(b) shows the less complete C-α angular correlation for θ_C = 40°. Contrary to the 30° data, this correlation does not peak strongly in the forward direction but instead exhibits a broad distribution consistent with a maximum in the recoil direction of $^{31}P^*$.

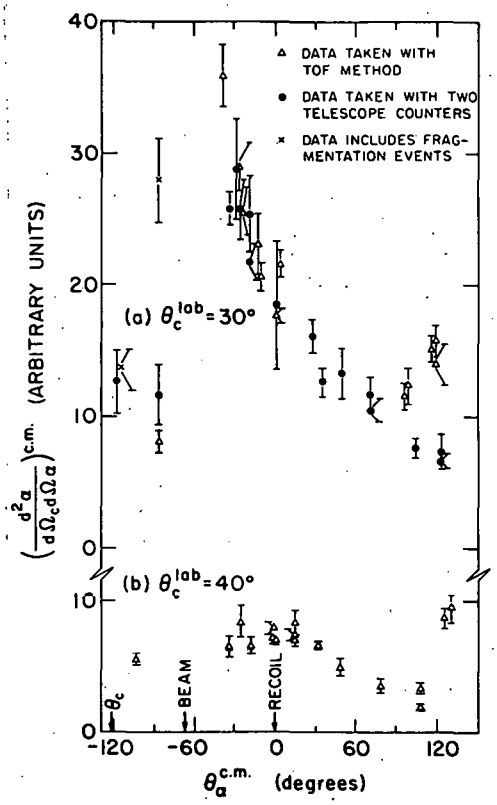

Fig. 6.2-2. In-plane angular correlation of C-α coincident events as a function of α-particle angle in $^{31}P^*$ recoil center of mass system. The recoil direction of $^{31}P^*$ is defined as 0°. a) θ_C = 30°; b) θ_C = 40°.

Even with a single counter, there is still a cutoff of low energy α particles which stop in the finite thickness

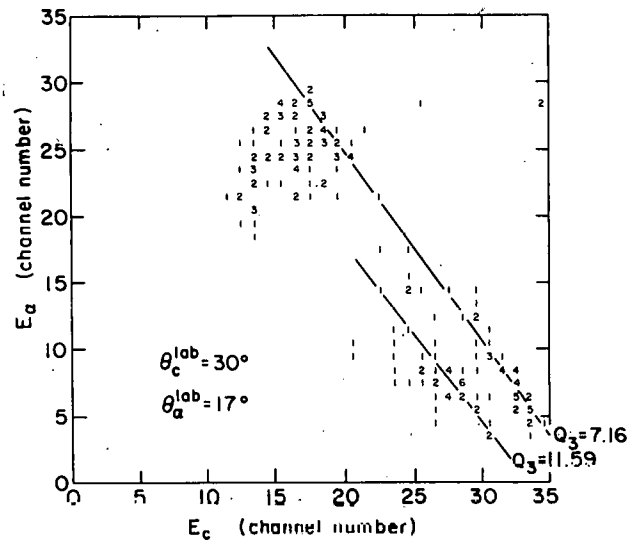

Fig. 6.2-3. 2D plot of E_c vs E_α for C-α coincidence events at $\theta_c^{lab} = 30°$ and $\theta_\alpha^{lab} = 17°$

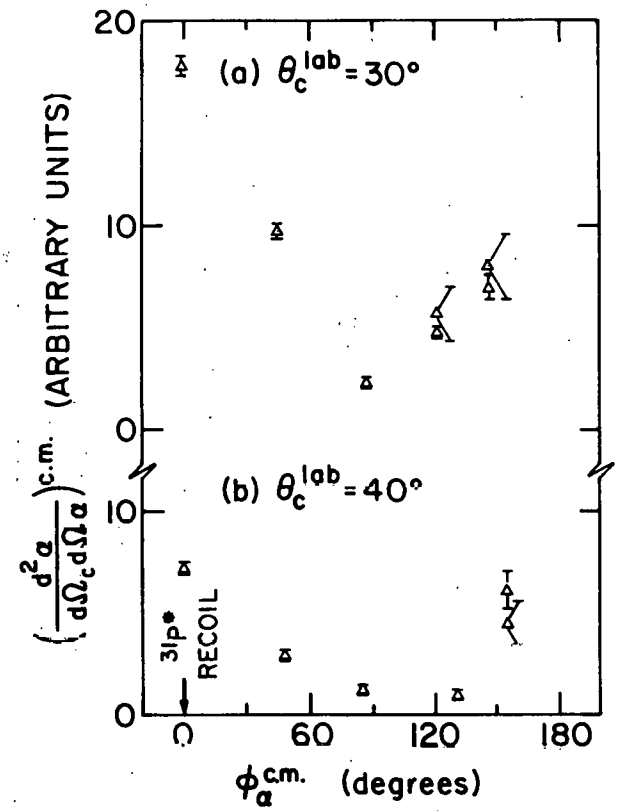

Fig. 6.2-4. Out-of-plane C-α angular correlation of C-α coincident events as a function of α-particle angle in $^{31}P^*$ recoil center of mass system. The recoil direction of $^{31}P^*$ is defined as 0°. a) $\theta_c = 30°$; b) $\theta_c = 40°$

of the ^{27}Al target (∿1 mg/cm^2) at very backward angles. Thus we cannot unambiguously extract the contribution due to evaporation from the in-plane data for $\theta_c = 30°$. In order to further understand this reaction, we have taken out-of-plane data as described above. Figure 6.2-4(a) shows the out-of-plane angular correlation with $\theta_c = 30°$. The data is asymmetric about 90° in the center of mass frame. If we assume the angular correlation of the evaporative products is symmetric about 90° in the center of mass frame of $^{31}P^*$, the evaporation component is much larger than was expected earlier.[3] For $\theta_c = 40°$, Fig. 6.2-4(b) shows that the out-of-plane angular correlation is fairly symmetric indicating that most of the events are evaporation products when C is detected beyond the grazing angle of the $^{27}Al + {}^{16}O$ reaction.

1. Nuclear Physics Laboratory Annual Report, University of Washington (1978), p. 66.
2. Nuclear Physics Laboratory Annual Report, University of Washington (1977), p. 177.
3. J. Harris *et al.*, Phys. Rev. Lett. 38, 1460 (1977).
4. J.P. Wurm, Proceedings of IPCR Symposium on Macroscopic Features in Heavy Ion Collision, Hakone, Japan, p. 108 (1977).

6.3 Relativistic Coulomb Effects in Sub-Coulomb Heavy Ion Elastic Scattering

H. Bhang, J.G. Cramer, W.G. Lynch, R.J. Puigh, and M.B. Tsang

We have been investigating the elastic scattering of heavy ions at energies far below the Coulomb barrier to look for deviations from Rutherford scattering. In this report we will discuss first some of the theoretical effects that may be present at these energies. This will be followed by a discussion of the experimental method and a treatment of the systematic errors which can occur with this method. We will conclude with a discussion of the data we have taken to date.

A. Theoretical Discussion

1) Relativistic Wave Equation

We confine ourselves to the study of spin zero-spin zero elastic scattering. In our search for a wave equation for elastic scattering we have tried as candidates the Klein-Gordon equation, the Relativistic Schroedinger equation[1], and the Bethe-Saltpeter equation using the Feynman rules for one photon exchange. All these approaches yield to lowest order a radial equation of the following form:[2]

$$\left(\frac{1}{\rho^2}\ \frac{d}{d\rho}\left(\rho^2\ \frac{d}{d\rho}\right) - \frac{\ell(\ell+1) - \gamma^2}{\rho^2} - 2\eta/\rho + 1\right) R_\rho(\rho)$$

with
$\rho = kr$
η = Sommerfeld parameter
$\gamma^2 = [z_1 z_2 \alpha]^2$ for Klein-Gordon equation
$\gamma^2 = \mu^2\left(\frac{1}{m_1^2} + \frac{1}{m_2^2}\right)[z_1 z_2 \alpha]^2$ for Bethe-Saltpeter equation
$\gamma^2 = c^6\mu^3\left(\frac{1}{E_1^3} + \frac{1}{E_2^3}\right)[z_1 z_2 \alpha]^2$ for Relativistic Shroedinger equation
$\mu = E_1 E_2/[(E_1 + E_2)c^2]$
E_1 = total energy (including rest mass) of particle one in C.M.
E_2 = total energy of particle two in C.M.
α = fine structure constant
c = speed of light

We have calculated the effect of the γ^2 term using the optical model code HOPREL.[3] In Fig. 6.3-1 we show calculations of the differential cross section for ^{12}C + ^{208}Pb at 40 MeV and in Fig. 6.3-2 we show the excitation function $\sigma(150°)$ from 0 to 60 MeV. Both curves are plotted as the ratio to the Rutherford cross section. The total deviation is of the order of 0.5%.

2) Q.E.D. Corrections

There is considerable evidence that vacuum polarization must also be considered at these energies. Rafelski[4] has calculated the deviation from elastic scattering caused by vacuum polarization to be the order of 0.5% in a classical calculation. We have not as yet included vacuum polarization in HOPREL. Other

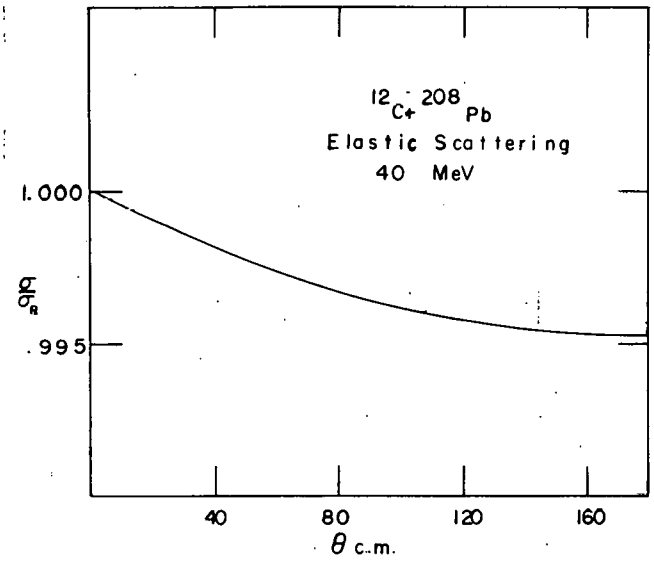

Fig. 6.3-1. Calculation of the differential section for 40 MeV ^{12}C + ^{208}Pb elastic scattering using the Klein-Gordon equation. The differential cross section is plotted as the ratio to the Rutherford cross section.

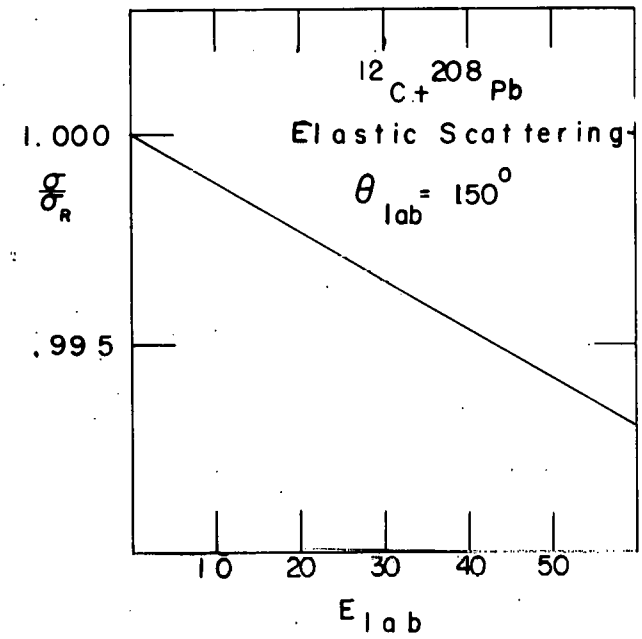

Fig. 6.3-2. Calculation of the excitation function at 150° in the center of mass for ^{12}C + ^{208}Pb elastic scattering using the Klein-Gordon equation. The differential cross section is plotted as the ratio to the Rutherford cross section.

Q.E.D. corrections which may be of importance are those that involve the "seagulls" or double photon vertex peculiar to spin-zero Q.E.D. Once effective potentials for these diagrams are obtained, they can be included in the equation for elastic scattering by using the framework of the Bethe-Saltpeter equation.

3) Coulomb Excitation

We have estimated the deviation from Rutherford scattering due to Coulomb excitation. For low lying discrete states the effect of long range absorption was estimated using the semi-classical formula of Baltz *et al.*[6] This formula has been tested by Doll *et al.*[7] and predicted well the observed deviation in the Sm isotopes. For ^{12}C + ^{208}Pb and ^{16}O + ^{208}Pb elastic scattering this effect was negligible. Nuclear polarization, i.e., the effect of virtually exciting the giant dipole state, was estimated using the semi-classical formula of Baur *et al.*[8] This formula is untested at present and predicts the deviation from Rutherford scattering to increase with energy as E^3 as indicated in Table 6.3-1.

4) Nuclear Potential Scattering

The deviation from Rutherford scattering due to nuclear potential scattering decreases exponentially with decreasing energy. The deviation decreases so

Table 6.3-1. Percent Deviation From Rutherford Scattering at 180° From Nuclear Polarization

E_{lab}	$^{12}C + ^{208}Pb$	$^{16}O + ^{208}Pb$
50	0.26%	0.13%
40	0.13%	0.07%
30	0.06%	0.03%
20	0.02%	0.01%

rapidly that it is easy to place upper limits on the deviation despite the ambiguities in the optical potential. For both $^{12}C + ^{208}Pb$ and $^{16}O + ^{208}Pb$ the deviation is less than 0.02% at 42 MeV and 50 MeV lab bombarding energy, respectively.

B. Experimental Discussion

In a measurement of elastic scattering one can vary scattering angle or the incident energy. It is easier to eliminate sources of systematic error having to do with detector geometry and count rate if the detector angles are not varied.

We have measured excitation functions for $^{12}C + ^{208}Pb$ and $^{16}O + ^{208}Pb$ elastic scattering. We placed 10 detectors symmetrically on left and right sides of the beam at angles of ±30°, ±140°, ±150°, ±160°, and ±170°. The detectors were not moved during the experiment. The targets were 13 $\mu g/cm^2$ and 25 $\mu g/cm^2$ ^{208}Pb strip targets evaporated on 10 $\mu g/cm^2$ C foils. The ^{208}Pb strip was 1 mm wide and aligned within 0.3 mm with respect to the target changer. A beam tube aperture 6 mm horizontal and 18 mm vertical 10 meters upstream combined with target strip to confine the phase space of the beam.

In the following sections we will estimate the system errors for this experimental configuration. We consider as sources of systematic error: beam angle and position, multiple scattering, detector finite size effects, and peak extraction ambiguities. We consider only first and second order effects.

5) Beam Angle and Position

During the experiments the ratio of the number of counts in the left 30° detector over the right 30° detector can be used to monitor shifts in the horizontal position and angle of the beam. Each 30° detector had normally 5×10^5 counts so that this ratio had a statistical uncertainty of 0.2%. This number remained constant within statistics independent of beam energy but was dependent on the choice of target where the ratio changed by less than 1%. This translates into an angle shift of $\Delta\theta < 0.04°$. At all angles the count ratio in the left detector and right detector were equal to within 3%. As a consequence we can roughly estimate the systematic error due to horizontal beam motion at

about 0.03%. At the present time we are more sensitive to vertical motion. We did not place detectors out-of-plane to monitor the vertical beam motion. Based on the length of the vertical strip we can estimate the systematic error less than 0.1%. This we plan to improve.

6) Multiple Scattering

The target thicknesses were chosen to keep the correction due to multiple scattering less than 0.02%. We did not observe any statistically significant difference between data taken with a 13 $\mu g/cm^2$ target and data taken with the 25 $\mu g/cm^2$ target.

7) Detector Finite Size Effects

Since we did not move the detectors during the experiment, to several orders the measurement is independent of the details of the detector geometry. We have not done more detailed analysis as yet.

8) Peak Extraction Ambiguities

At beam energies $E_{lab} > 20$ MeV the integrated peak to integrated background ratio is reasonably stable and greater than 1×10^3. As the energy decreases below 20 MeV, this ratio deteriorates to 5×10^2 at 10 MeV. We have extracted the peak areas by hand and would estimate the errors in peak extraction to be 0.1% for energies greater than 20 MeV and less than 0.2% for energies less than 20 MeV. We are writing a peak fitting routine for use on the new computer in order to obtain more accurate numbers.

C. Discussion of Data

In Table 6.3-2 we present preliminary data for $^{12}C + ^{208}Pb$ elastic scattering. In Table 6.3-3 we present data for $^{16}O + ^{208}Pb$ elastic scattering. These numbers are the ratio of the sum of the eight backward angle peak areas for $\theta_{lab} = \pm 140°, \pm 150°, \pm 160°$, and $\pm 170°$ divided by the sum of the $\pm 30°$ peak areas. The errors are statistical errors. The absolute magnitude of these ratios has no significance since it is a function of the detector solid angles.

Table 6.3-2. Backward to Forward Angle Ratio $^{12}C + ^{208}Pb$

E_{lab}	Ratio
15	1.008 ± 0.006
20	1.0062 ± 0.0007
25	1.0035 ± 0.0007
30	1.003 ± 0.001
35	1.0027 ± 0.0007
40	1.0014 ± 0.0009

Table 6.3-3. Backward to Forward Angle Ratio for $^{16}O + {}^{208}Pb$

E_{lab}	Ratio
16	0.8575 ± 0.0007
22	0.8556 ± 0.0007
28	0.8543 ± 0.0007
34	0.8522 ± 0.0007
50	0.8508 ± 0.0013

What is significant is the energy dependence of these ratios. For Rutherford scattering the ratios should be energy independent. Instead the ratios decrease with increasing energy. This is consistent with the existence of a net long range attractive potential.

D. Conclusion

We have made progress in both the theoretical and experimental aspects of the problem although we cannot make a definitive statement in either area. In the theoretical domain there is considerable evidence for effects coming from the use of a relativistic wave equation and for the vacuum polarization potential and nuclear polarization potentials. Many questions remain. In the experimental domain preliminary data is consistent with the existence of a long range attractive potential like those expected from a relativistic wave equation or nuclear polarization. It should be mentioned that due to the angles chosen for measurement, this experiment is not expected to be sensitive to the repulsive potential coming from vacuum polarization.[4]

---

1. The name Relativistic Shroedinger equation refers to the equation: $[\sqrt{p_1^2 + m_1^2} + \sqrt{p_2^2 + m_2^2} + V_{coul} - E]\psi = 0$. It was labeled as this in a LAMPF report by Leon Keller. It is described in detail in ref. 9.
2. The reduction of the Relativistic Shroedinger equation and Bethe-Saltpeter equation to this particular local form will be published at a later date.
3. See Section 10.4 of this report.
4. Johann Rafelski, Phys. Rev. C 13, 2086 (1976).
5. Bjorken and Drell, Relativistic Quantum Fields, McGraw-Hill (1965).
6. A.J. Baltz, S.K. Kauffmann, N.K. Glendennig, and K. Pruess, Phys. Rev. Lett., Vol. 40, No. 1, p. 20.
7. P. Doll *et al.*, LBL-7195 (1978).
8. G. Baur, F. Rosel and D. Trautmann, Nuc. Phys. A288, pp. 113-131 (1977).
9. M.K. Liou and M.I. Sobel, Phys. Rev. C 7, 2044 (1973).

6.4 A Search for Non-fusion in the Reaction $^{16}O + {}^{16}O$ at E_{cm} = 34 MeV

H. Doubre, A.J. Lazzarini, A. Seamster, and R. Vandenbosch

Time-dependent Hartree-Fock calculations[1] indicate that the 160 + 160 reaction at high energy does not lead to compound nucleus formation for the lowest impact parameters. At E = 40.5 MeV (c.m.) the three-dimensional calculation[2] predicts that this is the case for orbital angular momenta L < 12 $\hbar$ and that the two 160 nuclei scission back into the entrance channel with kinetic energies close to their Coulomb-plus-centrifugal barriers. The same calculation indicates that the partial waves L $\geq$ 35 $\hbar$ contribute to inelastic and quasi-elastic processes.

The internal excitation imparted to each nucleus from L < 10 h collisions is roughly E_x (160) = 12-13 MeV. This is significantly above the alpha-emission threshold in 160, and one does not expect to see much yield in the 160 + 160 final state even if the TDHF predictions were taking place. Accordingly, we have studied the 160 + 160 reaction at E = 34 MeV (c.m.). At this energy the TDHF calculations still predict non-fusion for low impact parameters and one can estimate that the excitation energy in the exit channel will not be sufficient to lead to decay of the 160 nuclei before detection.

The targets were obtained from the oxidation in dry air of ^{6}Li foils of 100-300 $\mu g/cm^2$ initial areal density. The measurement was performed using a kinematic coincidence between a time-of-flight spectrometer on one side of the beam axis and a large area silicon surface barrier position sensitive detector on the other. The time-of-flight spectrometer consisted of a time zero carbon foil channel plate pick-off[3] and a cooled 450 mm^2 200 μm thick surface barrier detector. The time resolution was typically 450 psec, adequate to provide unit mass resolution up to msss 20 with the flight path used (90 cm). Figure 6.4-1 shows a typical mass spectrum measured with the instrument. The angular acceptance of the spectrometer was 0.8 msr ($\pm$ 0.8°) On the other side of the beam, the PSD spanned an angular range $\Delta\phi$ = 5° and 20 < θ4 < 45°. Measurements of events in kinematic coincidence were performed at θ3 = 18, 25, 28, and 35°. For these events the quantities E3, TOF3, E4, and xE4 were measured and recorded event by event onto magnetic tape.

To determine real 2-body events proceeding from the 160 + 160 reaction, the longitudinal and transverse components of momentum for particle 3 ($P3_{||}$ and $P3_{\perp}$) relative to the beam direction were calculated for each event. Assuming $M4_{\perp}$ = (M1 + M2) - M3, one can calculate similar quantities $P4_{||}$ and $P4_{\perp}$. A 2-body event proceeding from 160 + 160 should yield missing momenta, $\Delta P_{||}$ = $\vec{P}$ (beam) - ($P3_{||}$ + $P4_{||}$) and $\Delta P_{\perp}$ = $P3_{\perp}$ - $P4_{\perp}$, equaling zero. A two-dimensional plot of these quantities is shown in Fig. 6.4-2. From the spectrum it is possible to separate events coming from the 160 + 160 → 160 + 160 reaction (area A) from those proceeding from either the 160 + ^{12}C → 160 + ^{12}C reaction from ^{12}C on the target, or from 3-body events arising from the decay of the 160 scattered towards the PSD (a mass measurement of particle 3 constrains it to be mass 16).

Energy spectra for 160 nuclei detected in the time-of-flight spectrometer subject to the above conditions are shown in Fig. 6.4-3. The high energy cutoff in the spectra occurs because of the requirement for a coincidence between

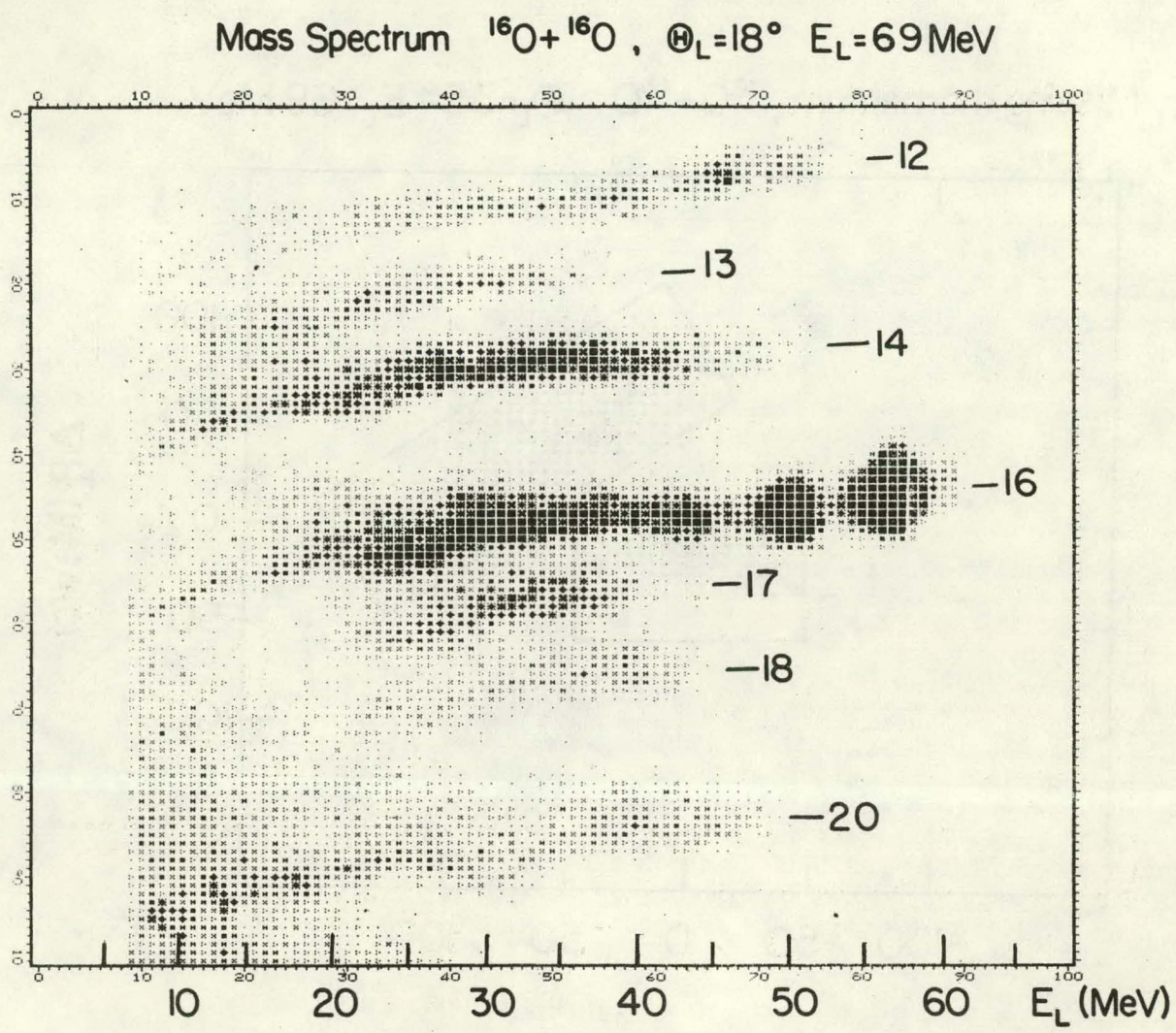

Fig. 6.4-1. Mass spectrum from time-of-flight spectrometer

the two detectors. There is no obvious enhancement of events at the lower kinetic energies which would be characteristic of the inelastic "splash back" from low partial waves. If we ascribe the yields delimited by solid lines in the figures to this process, we obtain a rough upper limit of the differential cross section at 35 to 28° of 1.2 ± 0.6 mb/sr, which is essentially consistent with $L_{min} < 1\ \hbar$.

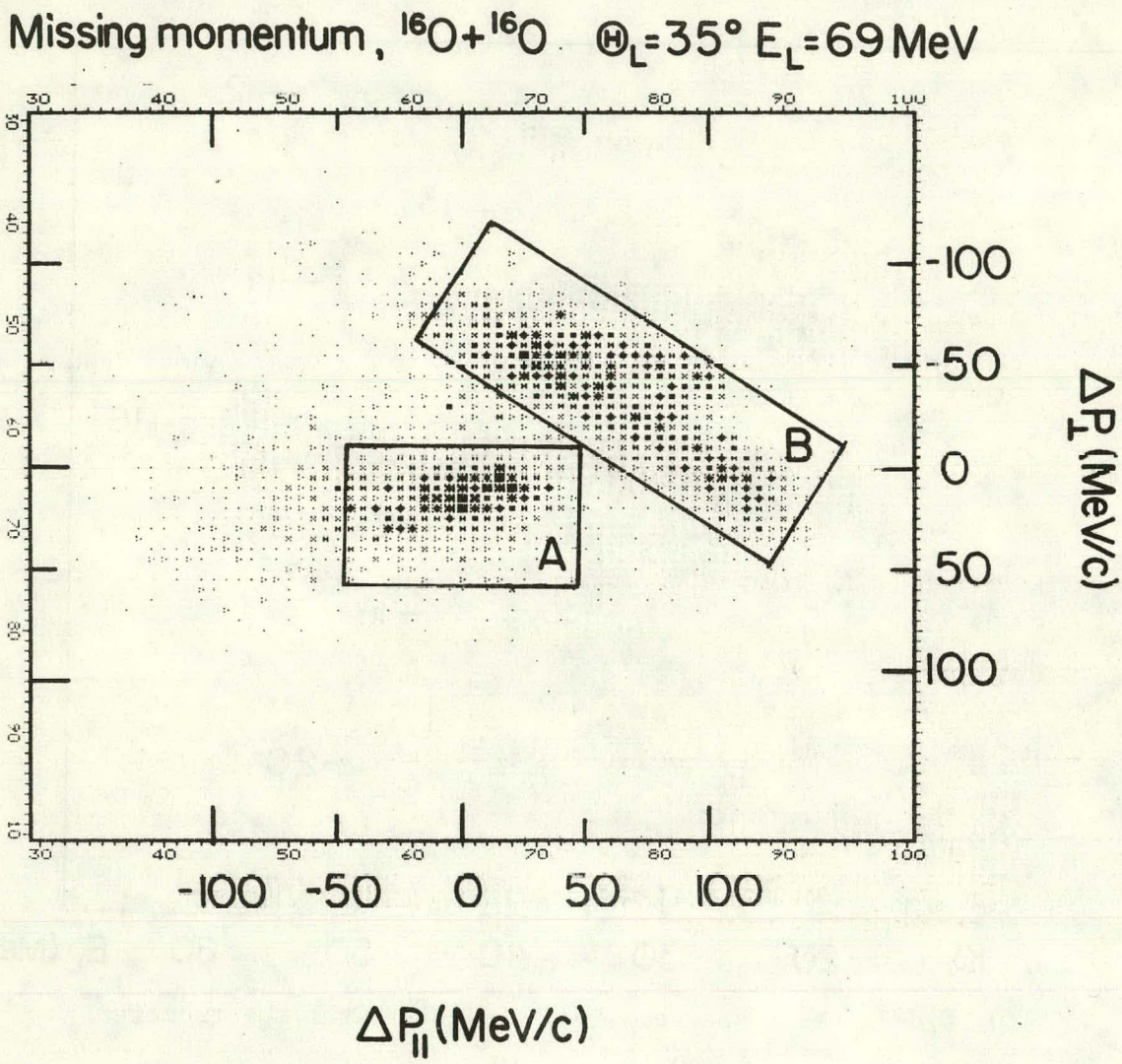

Fig. 6.4-2. Missing momentum obtained with 2-body kinematics

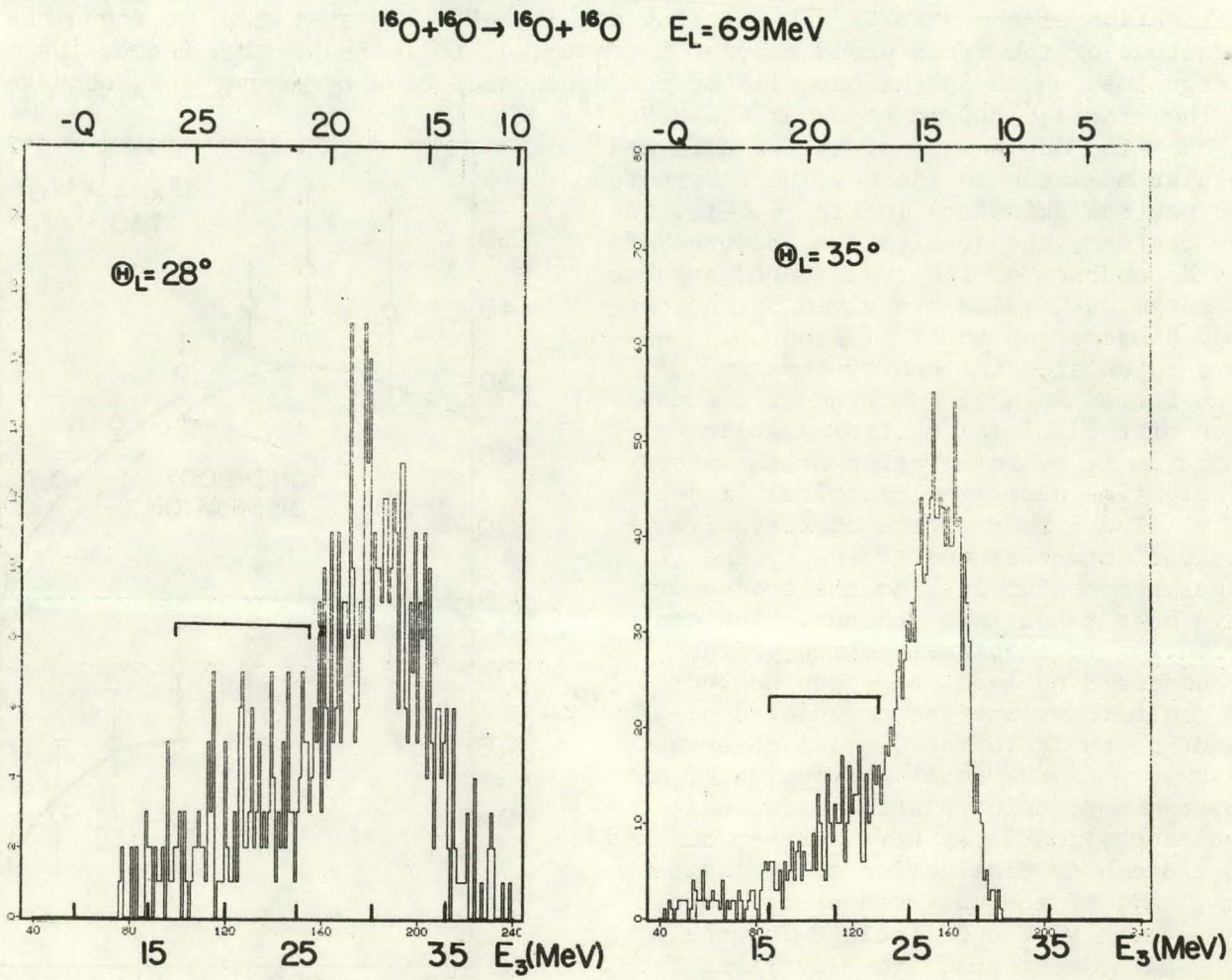

Fig. 6.4-3. ^{16}O energy spectra obtained for inelastic $^{16}O + ^{16}O \rightarrow ^{16}O + ^{16}O$ events

1. H. Flocard, S.E. Koonin, M. Weiss, Phys. Rev. C17 (1978), p. 1682.
2. S.E. Koonin, private conversation.
3. A.M. Zebelman *et al.*, Nucl. Instr. & Methods 141, 439 (1977).

6.5 Magnitude and Alignment of Angular Momentum Transfer in Deeply Inelastic Scattering

P. Dyer,[†] L. Nunnelley,[††] R.J. Puigh, T.D. Thomas,[†††] R. Vandenbosch, and M.S. Zisman[††††]

In last year's annual report we presented the initial results of our investigation of the $^{86}Kr + ^{238}U$ reaction at 710 MeV.[1] At that time we found the magnitude of the transferred angular momentum, J, to increase with increasing energy loss which is the opposite of the dependence of J on energy loss observed in the $^{86}Kr + ^{209}Bi$ reaction at 610 MeV.[2,3] We show the dependence of the transferred angular momentum on the Q-value (corrected for neutron emission) in Fig. 6.5 1a. As one can see, the qualitative features of the dependence of the transferred angular momentum on Q-value are given by the one-body dissipation model of Randrup.[4] We have calculated the energy loss and transferred angular momentum as a function of the initial orbital angular momentum ℓ_i by integration of the energy dissipation along the classical trajectory. The effect of the conservative nuclear potential and of energy and angular momentum loss on the trajectory have been taken into account. The contribution to the Fermi motion of the transferred nucleons has been neglected. In order to relate the calculated dependence on ℓ_i to the Q-value observable we have made the usual assumption of an inverse monotonic relation between ℓ_i and energy loss. We have further assumed that one-body dissipation accounts for only half of the observed energy loss, in keeping with our findings for the Kr + La system[5] and with deductions from the widths of charge distributions in other systems.[6,7] The resulting expectation for the transferred angular momentum due to one-body dissipation is given by the dashed line in Fig. 6.5-1a. The qualitative dependence on Q-value is reproduced very well, while the absolute magnitude is considerably underestimated. In addition to the successful account of the decrease in the angular momentum as one approaches small energy losses, the calculation also predicts less of a decrease in angular momentum for the largest energy losses than was predicted or observed

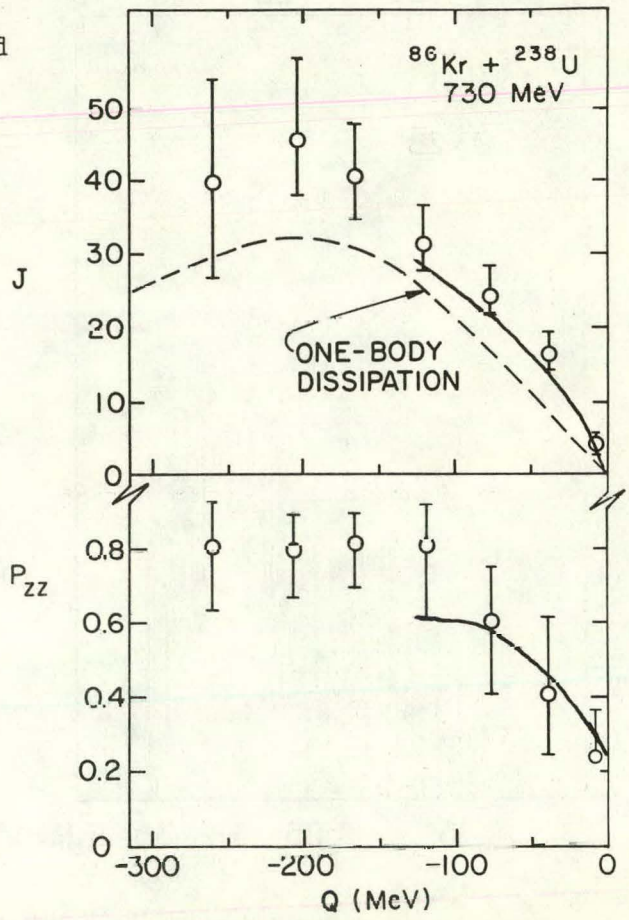

Fig. 6.5-1. Dependence of the a) angular momentum J transferred to the heavy fragment and b) alignment P_{zz} of the transferred angular momentum on Q-value. The dashed curve in a) is a calculation of the contribution of one-body dissipation to the transferred angular momentum using the Randrup model. The full curves are results of a microscopic calculation described in the text.

in the Kr + Bi system,[3] although in the latter system the predicted beginning of the decrease in angular momentum as one approaches the quasi-elastic region was not observed. Because of the high fission barrier of ^{209}Bi most of the quasi-elastic region was inaccessible for study in that system. The calculated differences between the two systems in the deeply inelastic region appear to be related to the differences in the bombarding energy. In the case of 730 MeV bombardment of U there is more energy to dissipate and one does not reach the rolling limit of the model except for the largest inelasticities. For the 610 MeV bombardment of Bi the necessary energy dissipation to reach the rolling limit is less and an angular momentum transfer decreasing with increasing energy loss is observed.

We have also determined the dependence of the alignment of the angular momentum transfer on Q-value. To facilitate the deduction of the alignment we have assumed the distribution of M_x values can be described by the coupling on a vector of length J_1 directed along the z axis with a vector of length J_2 uniformly distributed in the x-z plane resulting in a vector of average total length J. Moreover, we have assumed $\langle M_y \rangle = 0$ on the basis of likely mechanisms for creating the de-alignment in the collision process. The degree of alignment of the angular momentum along the z axis can then be expressed in terms of the alignment parameter $P_{zz} = 3/2\ [\langle M_z^2 \rangle / \langle J^2 \rangle] - 1/2$, where $\langle M_z \rangle = \langle J^2 \rangle - 1/2\ \langle J_2^2 \rangle$. The parameter J and J_2 are determined from simultaneous fitting of the in-plane and out-of-plane data using a formalism described elsewhere.[1-3] $P_{zz} = 1$ denotes complete alignment and $P_{zz} = 1/4$ denotes a random orientation in the x-z plane. The P_{zz} values obtained from the fitting are shown in Fig. 6-5-1b. The alignment is seen to decrease as the energy loss becomes small, a result first predicted by a transport model.[8]

We have developed a simple microscopic statistical model to elucidate the origin of the variation of alignment with energy loss. The mechanism for transferring angular momentum and dissipating energy is nucleon exchange, as assumed in the one-body proximity friction model. We take into account the contributions of both the internal motion of the nucleons and the relative motion of the two fragments.

In its simplest form, it is applicable to peripheral reactions where the assumption that exchange takes place through a small window along the internuclear axis is most valid. It also requires a knowledge of the number of transferred nucleons. The first point to be made is that the average velocity of the nucleons due to their kinetic energy of internal motion (Fermi motion) is larger than the velocity of relative motion. This is because the Fermi energy is much larger than the bombarding energy expressed in energy per nucleon. However, as more nucleons are exchanged, the aligned components of the angular momentum, which are all colinear, grow more rapidly than the resultant of the randomly oriented components due to the Fermi motion. Finally, one must couple the two final contributions to obtain the total angular momentum transfer. The alignment is determined by the relative magnitude of the two contributions. The results from the model are compared with the data in Fig. 6.5-1. It can be seen that the simple model gives a surprisingly good account of both the dependence of the alignment and the magnitude of the transferred angular momentum. The alignment is small for small energy losses because the randomly oriented component of the angular momentum arising from the Fermi motion is larger than the aligned component. The alignment increases for increasing energy loss because

the randomly oriented component of J increases as the square root of the number of nucleon exchanges whereas the aligned component increases linearly with the number of exchanged nucleons.

During the past year we have extracted the dependence of the transferred angular momentum upon charge transfer as determined from the counter telescope determination of the Z of the projectile-like reaction product. In order to be consistent in our extraction of J for different charge transfers the following procedure was employed in determining K_0^2 which is used in characterizing the distribution of K states of the fissioning nucleus. The parameter K_0^2 is taken from the analysis of light ion compound nuclear reactions of known angular momentum input. If in the analysis of these light ion data the ℓ-wave distribution is modified to account for incomplete fusion, then Clark et al.[9] has found for uranium-like nuclei a linear relationship between K_0^2 and $E_f^{1/2}$ where E_f is the excitation energy of the fissioning nucleus minus its saddle point energy. Also, in our study of the Kr + Bi fission fragment data[2,3] we found a linear relationship between K_0^2 and $E_f^{1/2}$ for the less fissile Ac-like nuclei. Therefore, we have assumed such a linear relationship to hold for all fissioning nuclei from the Kr + U reaction. To be consistent in our extraction of K_0^2 the constant of proportionality between K_0^2 and $E_f^{1/2}$ for our Q and Z divided data was determined by comparing the calculations of Huizenga, et al.[10] to the low energy data of Reising, et al.[11] These data span a range of nuclei between Bi and Cf and have been corrected for first chance fission.

Since the Z distribution detected in the counter telescope is sharply peaked around Z = 36 (corresponding to Kr), we have used K_0^2 values for uranium to fit the Q-divided data. The values of K_0^2 for the Q and Z divided data are then corrected for the neutron emission competition with fission (Γ_n/Γ_f). This correction is largest for the less fissile nuclei and leads to lower average value of the excitation energy associated with the fissioning nucleus for a given Q-value and hence to a smaller value of K_0^2.

Table 6-5-1 displays the magnitude of the angular momentum transfer as a function of $\overline{Q}$, the weighted average Q-value corrected for neutron emission, and Z_L, the charge of the nuclei detected in the counter telescope. The uncertainty in Z_L is $\pm$ 1-1/2 units. Due to the extra sorting conditions placed upon these events, the statistical uncertainty associated with these extracted values of the angular momentum transfer are large. We find that for the more fissile nuclei ($Z_L \leq 36$) the extracted angular momentum transfer for a given $\overline{Q}$ is independent of the charge (mass) transfer at the "end" of the deep inelastic scattering process. We have also observed this behavior for the large energy losses in the Kr + Bi reaction.[3] However, for the less fissile nuclei ($Z_L < 36$) we find the extracted values of $\overline{J}$ to be qualitatively lower for each $\overline{Q}$ than the values of $\overline{J}$ for the more fissile nuclei. If one expected angular momentum fractionation to be important, then one would expect to extract larger values of $\overline{J}$ for the less fissile nuclei. Therefore no evidence was found for angular momentum fractionation. At this time we feel the trend of decreasing J values with increasing Z of the fissioning nucleus may be due to overestimating the correction to E_f due to Γ_n/Γ_f thus leading to too small of values for K_0^2. We are currently planning to obtain better estimates of Γ_n/Γ_f which will hopefully lead to better agreement between the $\overline{J}$ extracted for more fissile and less fissile nuclei.

Table 6.5-1. Table of Extracted $\overline{J}$ for Q, Z Divided Data.

$\overline{Q}$ (MeV)	$Z_L = 30$	$Z_L = 33$	$Z_L = 36$	$Z_L = 39$	$Z_L = 42$
238	44^{+20}_{-16}	45^{+15}_{-12}	41^{+15}_{-7}	28^{+32}_{-8}	30^{+20}_{-10}
238	44^{+20}_{-16}	45^{+15}_{-12}	41^{+15}_{-7}	28^{+32}_{-8}	30^{+20}_{-10}
190	45^{+15}_{-10}	50^{+10}_{-6}	37^{+13}_{-9}	27^{+15}_{-7}	28^{+22}_{-9}
142	49 ± 11	43^{+8}_{-6}	41^{+9}_{-7}	25^{+12}_{-6}	20^{+30}_{-17}
92		36 ± 6	26^{+7}_{-4}	34^{+16}_{-10}	
47		23^{+5}_{-4}	25 ± 3	5^{+20}_{-3}	
10			7^{+3}_{-2}		

† Cyclotron Lab, Michigan State University, East Lansing, Michigan 48824.
†† Radiation Center, Oregon State University, Corvallis, Oregon 97331.
††† Lawrence Berkeley Laboratory, Berkeley, California 94720.
†††† Chemeketa Community College, Salem, Oregon 97309.

1. R.J. Puigh, P. Dyer, T.D. Thomas, R. Vandenbosch, and M.S. Zisman, Nuclear Physics Laboratory Annual Report, University of Washington (1978), p. 67.
2. P. Dyer, R.J. Puigh, T.D. Thomas, R. Vandenbosch, and M.S. Zisman, Nuclear Physics Laboratory Annual Report, University of Washington (1978), p. 75.
3. P. Dyer, R.J. Puigh, R. Vandenbosch, T.D. Thomas, M.S. Zisman, and L. Nunnelley, Nucl. Phys. (in press).
4. J. Randrup, Ann. Phys. 112 (1978), 356.
5. R. Vandenbosch, M.P. Webb, P. Dyer, R.J. Puigh, R. Weisfield, T.D. Thomas, and M.S. Zisman, Phys. Rev. C17 (1978), 1672.
6. W. Schröder and J.R. Huizenga, Ann. Rev. of Nucl. Sci. 27 (1977), 465.
7. In a recent letter F. Beck *et al.*, [Phys. Lett. 76B (1978), 35] report calculations which purport to account for the energy loss implied from the z distribution data with a one-body dissipation model. It turns out, however, that they used too large a value for the radius constant r_o (1.226), resulting in serious disagreement in the grazing ℓ and the angular distribution near the quarterpoint angle.
8. S. Ayik, G. Wolschin, and W. Nörenberg, Z. Physik (1978), 271.
9. R.G. Clark, W.G. Meyer, M.M. Minor, C.T. Roche, and V.E. Viola, Z. für Physik 274 (1975), 131.

10. J.R. Huizenga, A.N. Behkami, and L.G. Moretto, Phys. Rev. 177 (1969), 1826.
11. R.F. Reising, G.L. Bate, and J.R. Huizenga, Phys. Rev. 141 (1966), 1161.

6.6 Discrete γ Anistropies for the 600 MeV ^{86}Kr + ^{166}Kr Reaction

H. Doubre, A. Lazzarini, R. Puigh, A. Seamster, T.D. Thomas,† R. Vandenbosch, and M. Zisman††

In recent years several methods have been used to investigate the transferred angular momentum in deeply inelastic collisions. Measurements involving both γ multiplicity[1,2] and fission fragment angular correlation[3,4] techniques have shown that the magnitude of the angular momentum transfer is large. From fission fragment angular correlation studies the meaured alignment of the transferred angular momentum is also found to be large. However, the angular distribution of continuum γ's have been found to be isotropic.[2] This could imply either that the initial alignment which one intuitively expects and which is indicated by the fission fragment data has been washed out by particle emission at the last stages of de-excitation or that the relative importance of dipole transitions in the continuum is larger than has sometimes been assumed.

In the hope of resolving this issue we undertook the investigation of the ^{86}Kr + ^{166}Er reaction at 600 MeV. We chose ^{166}Er as a target since it is a deformed nucleus in a mass region where there are many deformed nuclei. The purpose of the experiment was to measure the anisotropy for discrete γ transitions which are known to correspond to stretched E2 γ emission. If these anisotropies are larger than one (which corresponds to an isotropic distribution) then one must conclude that some of the alignment is preserved throughout the de-excitation process.

The experimental set-up is shown in Fig. 6.6-1. This experiment was performed at the Super-HILAC with a 600 MeV ^{86}Kr beam and an enriched ^{166}Er target. The thin walled cylindrical Al chamber was oriented with its axis parallel to the floor so that two GeLi's could be used simultaneously to measure γ's both in and out of the reaction plane. The solid state counter telescope was mounted at 28° which is slightly forward of the quarter-point angle and it was used to

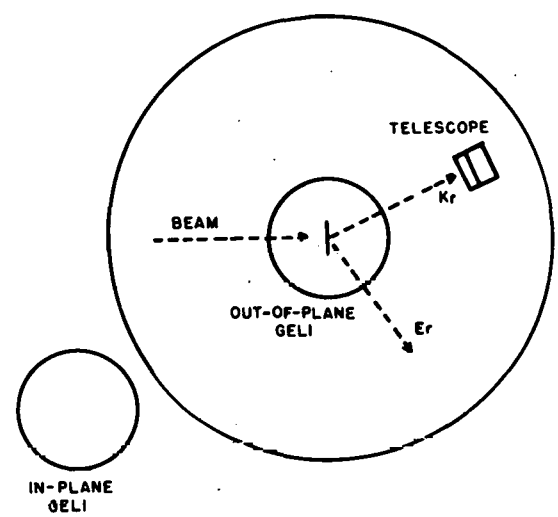

Fig. 6.6-1. Schematic of experimental set-up. The arrows correspond to the beam direction, the direction of the Kr-like particles (as determined by the counter telescope angle), and the direction of the Er-like recoils (corresponding to deep inelastic scattering). Also shown are the orientation and position of the in-plane and out-of-plane (small circles) GeLi's cryostats.

give both charge transfer and energy loss information for each event. Two 40 cc cylindrical GeLi's were used. One was mounted at 138° which is normal to the recoil direction for deep inelastic events and was used to measure the in-plane γ's, the other detector was normal to the reaction plane defined by the beam and counter telescope. Since both GeLi's were normal to the recoil direction the doppler shifts are minimized. Thin copper absorbers were placed between the target and each of the GeLi counters to reduce the number of x-rays seen in the counters. The relative efficiency between these two GeLi's was determined by measuring the yields from calibrated sources mounted at the target position. Coincidence data were taken between the counter telescope and each of the GeLi's and then event recorded on tape for subsequent off-line analysis.

Typical γ spectra from these data may be seen in Fig. 6.6-2. Shown here are two γ spectra for different Q-bins and for events with Z = 36 ± 1 being detected in the counter telescope. The bottom spectrum corresponds to a Q of -32.5

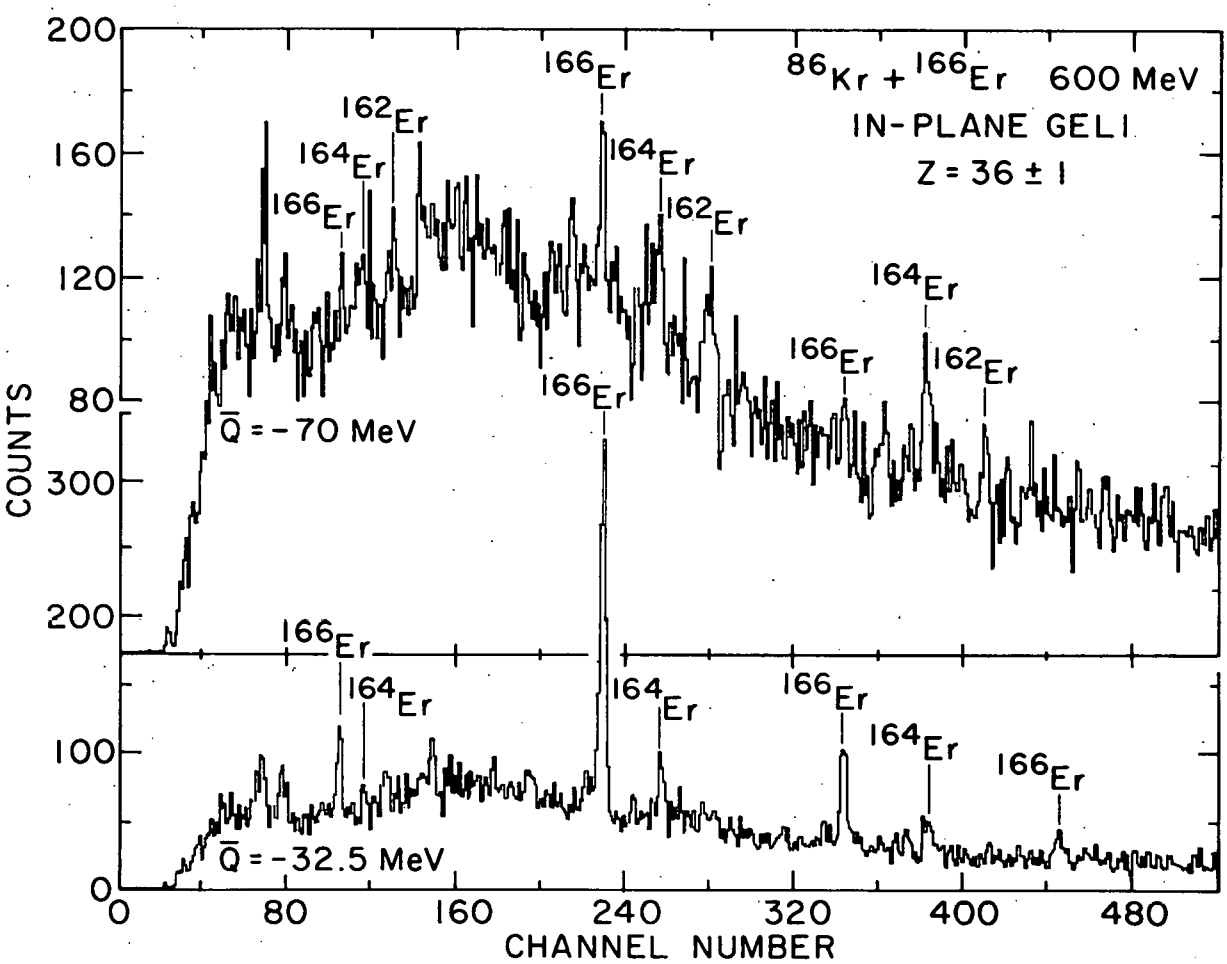

Fig. 6.6-2. Typical γ spectra corresponding to Kr events being detected in the counter telescope. The bottom spectrum corresponds to a Q-bin centered at -32.5 MeV and the top spectrum corresponds to a Q-bin centered at -70 MeV.

MeV and is dominated by the Coulomb excited ground state rotational band in ^{166}Er. Also seen are the ground state rotational band transitions in ^{164}Er. The top spectrum corresponds to a more negative Q of -70 MeV. Now one sees the relative yields for the ^{166}Er rotational band are reduced and several members of the Er rotational band are seen. However, the top spectrum also points out the problem encountered in the analysis of these data. These spectra represent four days of running time with typical beam currents of 20 to 40 enA which was the largest beam currents we could handle due to counting rate limitations. Since the relatively small γ peak yields were on a large background the statistical uncertainties were large. To optimize our yield to background ratio and thus reduce our statistical uncertainty we have sought suitable gates on the counter telescope parameters.

The technique to obtain this optimization of yield to background is indicated in Fig. 6.6-3 which shows the sum of the yields for discrete γ peaks for a particular nucleus divided by the total number of γ's and plotted as a function of excitation energy in the system. The Z shown at the top of each pair of graphs indicates the gating region in the counter telescope. For the Yb nuclei we find the nucleus with fewer neutrons, ^{166}Yb, is seen for larger excitation energies than the more neutron rich ^{168}Yb. Moreover, the normalized γ yield for ^{168}Yb appears to peak at a larger excitation energy than ^{168}Yb. These observations are qualitatively seen for the Er and Dy isotopes as well. To maximize the statistics for a given γ transition we therefore widened our gate in Q to include the region where the normalized γ yield was greater than 2.5.

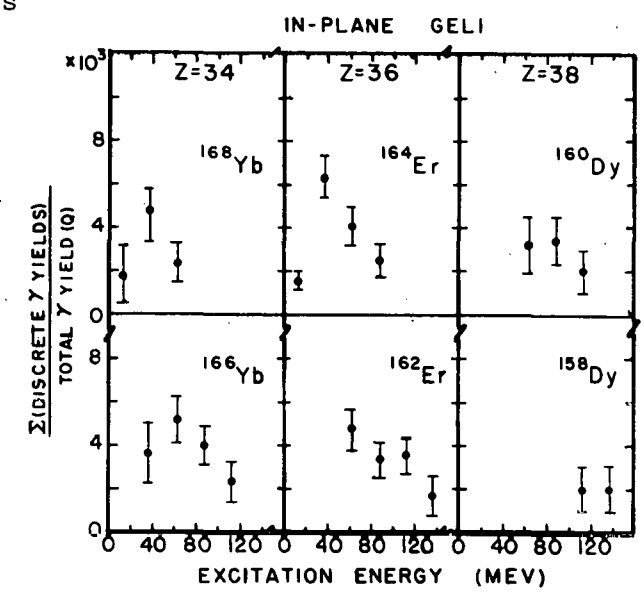

Fig. 6.6-3. Sum of the yields for the $6^+ - 4^+$, $4^+ - 2^+$, and $2^+ - 0^+$ transitions for a given nucleus divided by the total γ yield and shown as a function of the excitation energy on the composite system.

Shown in Fig. 6.6-4 are the γ anisotropies for several nuclei plotted as a function of excitation energy in the system. This γ anisotropy is just the ratio of the yield for a particular transition in the in-plane GeLi to the yield for the same transition seen in the out-of-plane GeLi and corrected for their relative efficiency. Shown here are the γ anisotropies for the three lowest transitions in the ground state rotational band for ^{164}Er and ^{162}Er, ^{166}Yb, and ^{160}Dy. We find the anisotropy for the $2^+ - 0^+$ transition for each nucleus is consistent with a value of one which indicates an isotropic distribution. This isotropic distribution is due to reorientation effects which are allowed by the relatively long half-life (∿ 2 ns) associated with many 2^+ levels of nuclei in this mass region. That we also measure an anisotropy of 1 for the $2^+ - 0^+$ transition tends to give us confidence

in our data reduction. Note that the $6^+ - 4^+$ and $4^+ - 2^+$ transitions in each nucleus have anisotropies which are larger than one and thus indicating a degree of alignment for the system. Moreover, there appears to be a trend of increasing anisotropy as one increases the excitation energy in the system. This can better be seen in Fig. 6.6-5. Shown here are the γ anisotropies which we have extracted to date. To reduce the statistical uncertainty we have summed the yields for the $6^+ - 4^+$ and $4^+ - 2^+$ transitions to obtain the anisotropies. The error bars reflect the statistical uncertainty associated with each anisotropy. We find that at small excitation energies the anistropies are only slightly larger than one. As the excitation energy in the system increases the anisotropy tends to increase reaching a maximum value of $\sim$2.0 for an excitation energy of $\sim$66 MeV. Because of the relatively poor statistics associated with the experiment we did not observe any strong γ lines for excitation energies of 90-100 MeV which correspond to the peak in the deeply inelastic cross section for this system, hence no anisotropies were extracted for the larger excitation energies. The curve corresponds to a calculation based upon a microscopic model.[4] This calculation assumes the angular momentum transfer and its corresponding M state distribution to be due to particle exchange and has as its limiting value the "rolling limit." This calculation has been used successfully to fit the $^{86}Kr + ^{238}U$ alignment data obtained from our fission fragment studies.[3] The calculation shown here has been corrected for neutron and statistical γ emission and predicts a slightly increasing value for the anisotropy with increasing excitation energy. This calculation is consistent with the measured anisotropy in the quasi-elastic region but tends to underestimate the measured alignment at the higher excitation energies.

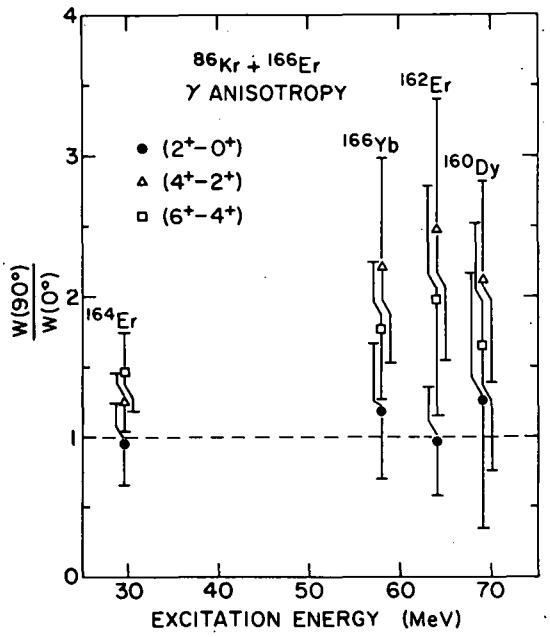

Fig. 6.6-4. γ Anistropies for the $6^+ - 4^+$, $4^+ - 2^+$ and $2^+ - 0^+$ transitions in ^{164}Er, ^{162}Er, ^{160}Dy, and ^{166}Yb. The dashed curve in the figure corresponds to an isotropic distribution.

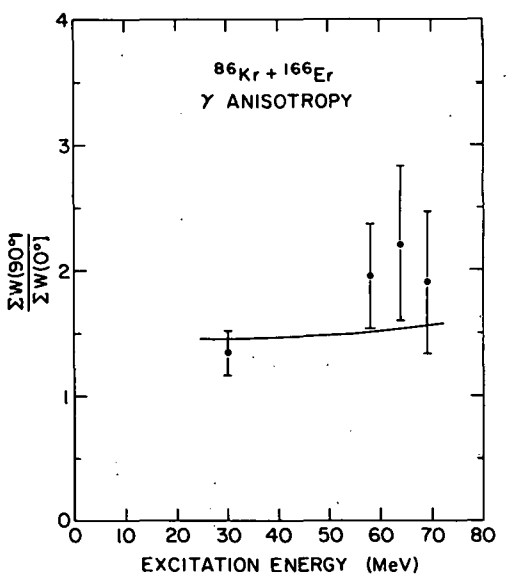

Fig. 6.6-5. γ Anisotropies from summed yields of the $6^+ - 4^+$ and $4^+ - 2^+$ transitions. The solid curve is from a microscopic calculation explained in the text.

In conclusion since our measured anisotopies for discrete E2 transitions were greater than one, one must conclude that these nuclei maintain some degree of alignment throughout the deexcitation process. In the light of the continuum γ studies one must conclude that dipole transitions play a non-negligible role. And finally, the comparison of the γ anisotropies with the microscopic calculation, which is based on parameters successful in describing the alignment in the sequential fission angular correlation, indicates that the alignment implied by gamma ray and fission fragment techniques are consistent if one takes care to define the multipolarity of the gammas detected.

---

† Radiation Center, Oregon State University, Corvallis, Oregon 97331.
†† Lawrence Berkeley Laboratory, Berkeley, California 94720.

1. A. Olmi, H. Sann, D. Pelte, Y. Eyal, A. Gobbi, W. Kohl, U. Lynen, G. Rudolf, H. Setlzer, and R. Bock, Phys. Rev. Lett. 41, 688 (1978); P.R. Christensen, F. Folkmann, Ole Hansen, O. Nathan, N. Trautner, F. Videback, S.Y. vander Werf, H.C. Britt, R.P. Chestnut, H. Freisleben, and F. Puhlhofer, Phys. Rev. Lett. 40, 1245 (1978).
2. R.A. Dayras, R.G. Stokstad, C.B. Fulmer, D.C. Hensley, M.L. Halbert, R.L. Robinson, A.H. Snell, D.G. Sarantites, L. Westerberg, and J.H. Barker, Phys. Rev. Lett. 42, 697 (1979).
3. P. Dyer, R.J. Puigh, R. Vandenbosch, T.D. Thomas, L. Nunnelley, and M.S. Zisman, Nucl. Phys. (in press); P. Dyer, R.J. Puigh, T.D. Thomas, R. Vandenbosch, and M.S. Zisman, Nuclear Physics Laboratory Annual Report, University of Washington (1978), p. 75.
4. R.J. Puigh, P. Dyer, R. Vandenbosch, T.D. Thomas, L. Nunnelley, and M.S. Zisman (submitted to Physics Letters); R.J. Puigh, P. Dyer, R. Vandenbosch, T.D. Thomas, and M.S. Zisman, Nuclear Physics Laboratory Annual Report, University of Washington (1978), p. 67.

6.7 Implications about Nuclear Dynamics from Comparison of TDHF and Frozen Spheres Proximity Friction Model Calculations

R. Vandenbosch

The recent availability of time-dependent Hartree-Fock (TDHF) calculations for reactions with very heavy ions has provided an important testing ground for the time-dependent mean-field approximation. A recent calculation[1] for the $^{84}Kr + ^{209}Bi$ reaction at 600 MeV has reproduced quite well the angular and energy loss characteristics of the experimental data. To the extent that the model has been verified by comparison with experiment one can then examine the results of the model to learn about the dynamics of the collision. K.T.R. Davies has kindly made available some of the computer outputs for the aforementioned reaction. We have compared these results with those from a frozen spheres one-body dissipation model[2] to elucidate some aspects of the collision.

An example of a collision is shown in Fig. 6.7-1, where we see snapshots of the half-density profiles at various times. This is a fairly peripheral collision—the grazing angular momentum for this system is about 275. The

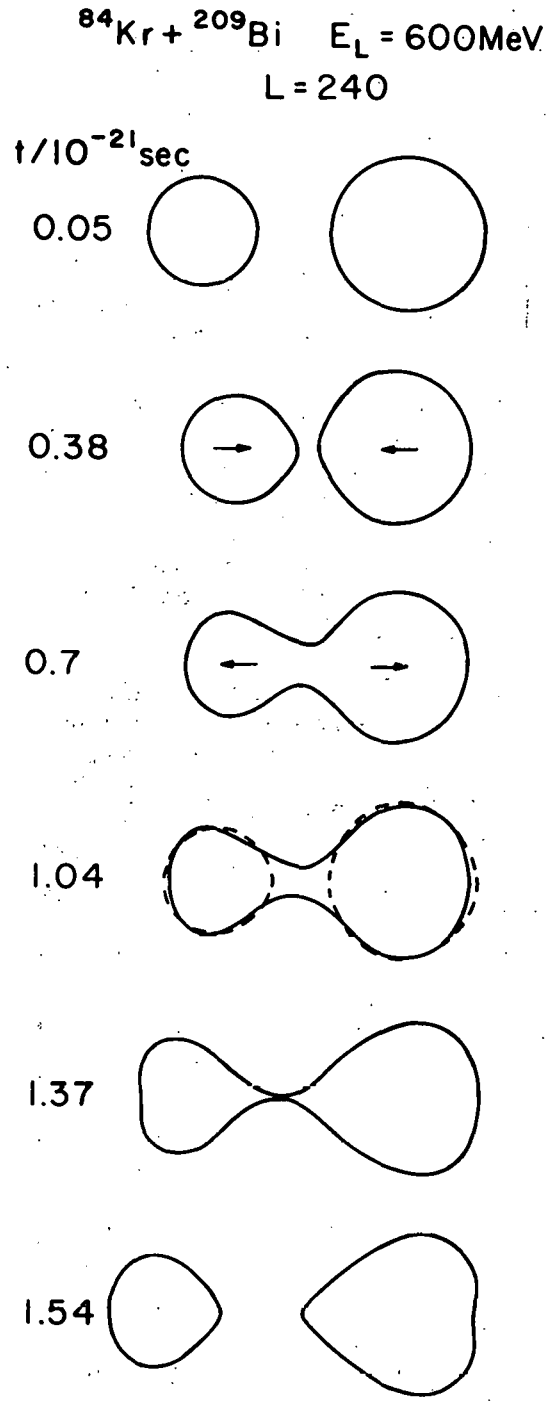

Fig. 6.7-1. Half-density contour profiles from the TDHF calculation of Davies *et al.*[1]

apparent very thin neck in one of the snapshots is of course an artifact of only showing the half-density contours. The time dependence of the distance between the centers of gravity, the neck diameter (specified by the half-density contours), the energy dissipated into internal degrees of freedom, and the angular momentum transferred into intrinsic rotation are shown in Fig. 6.7-2. The most interesting feature revealed here is the rapid formation of a neck which

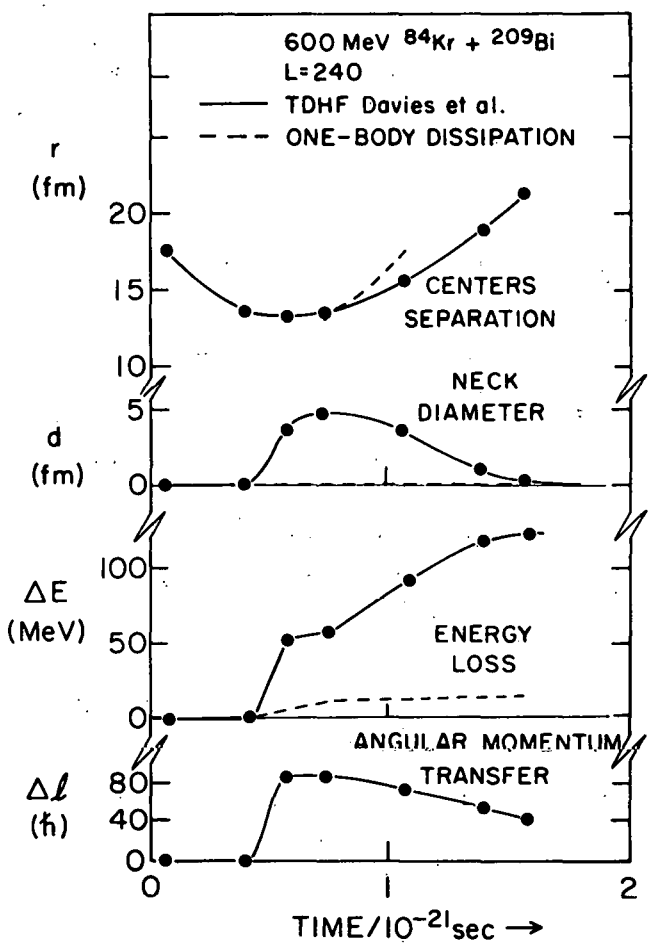

Fig. 6.7-2. The full curves give the results of the TDHF calculations of the centers of mass separation, neck diameter, energy loss, and angular momentum transfer as a function of time. The dashed curves give results for one-body dissipation in the frozen spheres approximation.

occurs very near the classical turning point. Very little energy is dissipated until after the neck is formed, at which point the energy dissipation increases very rapidly. The importance of neck formation can be seen very clearly by comparison with calculations of one-body energy dissipation in the frozen spheres approximation. We use the "window" formalism of Randrup[2] which takes into account the effects of the diffuse nuclear surface. The trajectories for the two models are fairly similar, with nearly identical separation distances at the turning point. In the absence of nuclear deformations the nuclear density does not saturate in the region between the nuclei, and the energy loss is small (about 10 MeV) and symmetric about the turning point as illustrated by the dashed curve in Fig. 6.7-2.

It is interesting to inquire as to whether the greatly increased energy dissipation in the TDHF calculation is a result of collective excitations or whether the neck formation has enabled one-body dissipation to proceed at a much greater rate. The latter possibility can be tested in an appropriate manner by calculating the one-body dissipation along a trajectory which results in a "neck thickness" equal to that given by the TDHF calculation. Such a trajectory (with a turning point at 11.1 fm) results in a one-body dissipation of more than 60 MeV. From this we conclude that one-body dissipation is the major contributor to the rapid energy dissipation near the turning point. On the other hand the energy dissipation which persists at a slower rate as the neck stretches in the exit channel is apparently primarily a collective (shape) excitation.

The differences between the frozen spheres and TDHF calculations are most pronounced for the peripheral partial waves such as the one just examined. For smaller partial waves where considerable overlap occurs even in the absence of deformation degrees of freedom the differences in the energy loss are not as dramatic but still very significant. This is illustrated in Fig. 6.7-3. The approximate factor of two discrepancies between the frozen spheres one-body dissipation and the TDHF is very similar to the factor observed in a comparison of one-body dissipation with experiment in the Kr + La system.[3]

Finally we compare the calculated angular momentum transfer with our recent experimental results.[4] This is the least meaningful comparison because of the approximations employed in these particular calculations. Axial symmetry was imposed and the system was assumed to clutch upon contact. The calculated angular momentum transferred is therefore primarily determined by the rigid body moment of inertia just after the neck breaks. Experiment and calculation are compared in Fig. 6.7-4. The two curves for the TDHF calculations are the upper and lower limits correspond-

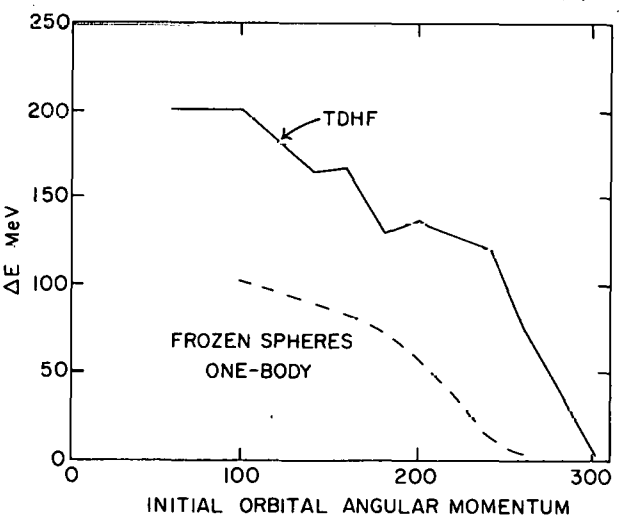

Fig. 6.7-3. Comparison of TDHF and one-body dissipation calculations of energy loss as a function of initial orbital angular momentum l.

ing to the values given by the computer output "snapshots" before and after neck scission.

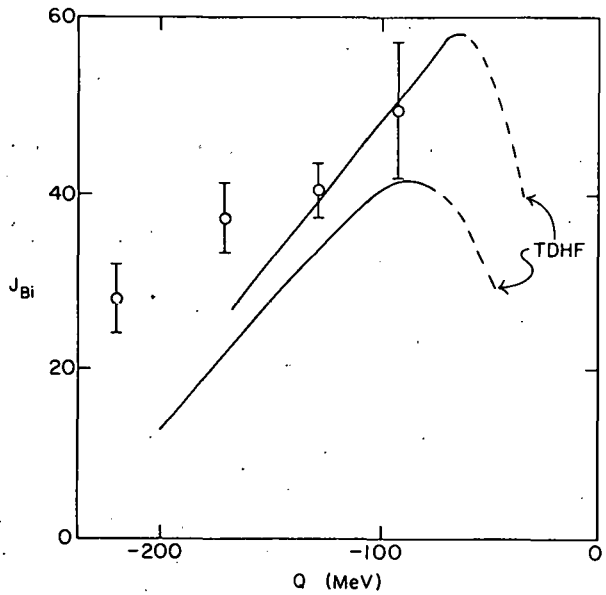

Fig. 6.7-4. The two curves define the possible range of values from the TDHF calculation and the points are from the experiment of Dyer *et al.*[4]

1. K.T.R. Davis, V. Maruhn-Rezwani, S.E. Koonin and J.W. Negele, Phys. Rev. Lett. 41, 632 (1978).
2. J. Randrup, Ann. Phys. 112, 356 (1978).
3. R. Vandenbosch, M.P. Webb, P. Dyer, R.J. Puigh, R. Weisfield, T.D. Thomas, and M.S. Zisman, Phys. Rev. C17, 1672 (1978).
4. P. Dyer, R.J. Puigh, R. Vandenbosch, T.D. Thomas, M.S. Zisman, and L. Nunnelly, Nucl. Phys. A322, 205 (1979).

6.8 Fusion Cross Sections for Very Heavy Systems From a Simple Potential Trapping Model

R. Vandenbosch

Reactions between very heavy nuclei become dominated by deeply inelastic rather than fusion processes as the product of the projectile and target number increases. It is desirable to try to systematize and understand the dependence of the fusion cross section on bombarding energy and projectile target system. The simplest models for fusion cross sections relate the fusion cross section to the surmounting of a fusion barrier or the reaching of a critical distance. Another suggestion for the criterion for fusion is the existence of a pocket in the total ion-ion potential, defined by the sum of the Coulomb, nuclear, and

centrifugal potentials. For any particular nuclear potential there is a maximum ℓ value for which such a pocket can exist, leading to a critical angular momentum above which fusion cannot occur. A number of workers have emphasized the importance of taking into account energy dissipation in the entrance channel; it is presumed that for fusion to occur sufficient energy loss must occur for the ions to be trapped in the pocket in the interaction potential. It is possible in such a model for fusion to fail to occur even when a pocket exists in the internuclear potential if insufficient energy dissipation occurs.

Bondorf et al.[1] and Gross et al.[2] were among the first to use phenomenological potentials, including a dissipative part, to fit fusion cross sections. More recently Birkelund et al.[3] have used a proximity potential including dissipation to calculate fusion cross sections. Assuming a trapping criterion they were able to account fairly well for the energy dependence of fusion cross sections for light and medium mass projectile-target systems. We consider here how well the proximity potential does in accounting for the disappearance of fusion in heavy systems. We have used the trajectory program described previously,[4] modified to include one-body dissipation,[5] to calculate the fusion cross section for a number of heavy systems. These calculations take into account both energy dissipation and transfer of angular momentum from orbital motion into internal fragment rotation. The results for a number of systems spanning a wide range of projectile and target combinations are shown in Fig. 6.8-1. The qualitative trend of the disappearance of fusion with increasing $Z_1 Z_2$ product is reproduced. The energy dependence of fusion cross sections for heavy systems is not well known, but comparisons with scanty data for the $^{40}Ar + ^{238}U$ and $^{84}Kr + ^{65}Cu$ systems indicate that the model predicts a larger drop in the fusion cross section with increasing energy than is observed experimentally.

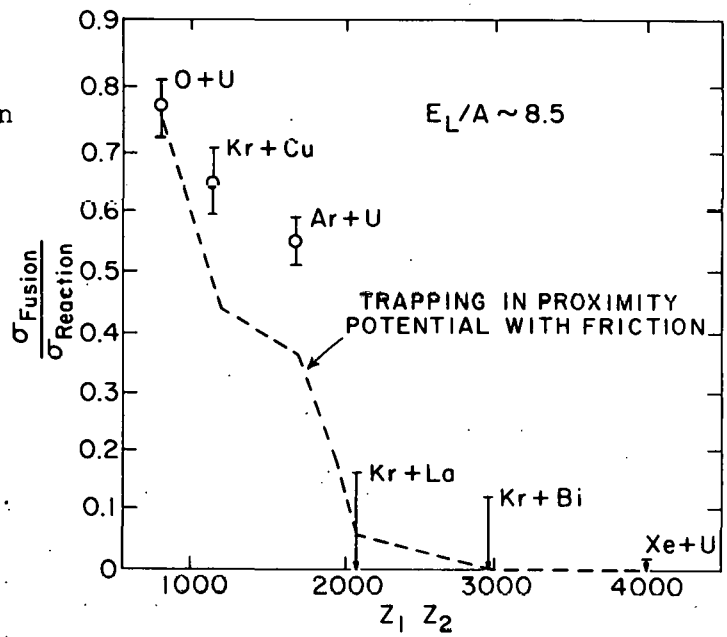

Fig. 6.8-1. Ratio of fusion cross section to total reaction cross section as a function of the product of the projectile and target atomic numbers. The experimental data is represented by circles or upper limit bars, and the dashed line connects the calculated values.

It should be emphasized that any successes of this model must be considered somewhat fortuitous. The model assumes frozen spherical shapes throughout the scattering process, whereas more complete dynamical models[6] show the importance of the neck degree of freedom. In spite of this limitation however it has been shown to be useful in accounting for many features of fusion cross sections.

1. J.P. Bondorf, M.I. Sobel, and D. Sperber, Phys. Rept. C15, 83 (1974).
2. D.H.E. Gross and H. Kalinowski, Phys. Lett. 48B, 302 (1974).
3. J.R. Birkelund, J.R. Huizenga, J.N. De, and D. Sperber, Phys. Rev. Lett. 40, 1123.
4. R. Vandenbosch and R. Weisfield, University of Washington Nuclear Physics Laboratory Annual Report, 1977, p. 179.
5. R. Vandenbosch, M.P. Webb, P. Dyer, R.J. Puigh, R. Weisfield, T.D. Thomas, and M.S. Zisman, Phys. Rev. C17, 1672 (1978).
6. See discussion of TDHF calculations in Section 6.7 of this report.

6.9 Does the $^{4}He + ^{24}Mg$ Fusion Cross Section Exhibit Oscillations Like That of $^{12}C + ^{16}O$?

K.G. Bernhardt, A. Bice, H. Bohn, Y-D. Chan, K.C. Green, R. Sielemann, R. Weisfield and R. Vandenbosch

In the previous annual report[1] we presented some preliminary results on the excitation functions for several alpha-out compound nuclear exit channels. The yield of gammas for the 4^+ to 2^+ transition in ^{24}Mg from the $^{4}He + ^{24}Mg$ reaction was only successfully measured over a rather short range of bombarding energy but did not reveal any structure similar to that seen for this transition in the $^{12}C + ^{16}O$ reaction. A more extended excitation function for many of the alpha-out channels was obtained by summing the particle yield to the lowest six states in ^{24}Mg. An integration over 18 excitation functions taken at angles between 80° and 175° was performed to damp out Ericson fluctuations. This excitation function revealed some structure but the structure was not correlated with that seen in the $^{12}C + ^{16}O$ system when the energy scale was adjusted to match excitation energies in the compound nucleus ^{28}Si.

The motivation for this experiment can be explained with the aid of Fig. 6.9-1. Here we have plotted the grazing angular momentum for the two entrance channels as a function of the channel energy for the $^{12}C + ^{16}O$ reaction. The grazing angular momentum is taken as that value of ℓ for which the optical model transition coefficient is equal to one-half. The optical model potentials are from refs. 2 and 3. The channel energy scale for this $^{4}He + ^{24}Mg$ channel has been shifted by 6.8 MeV to match excitation energies in the ^{28}Si compound nucleus. The curves of the grazing angular momenta for the two systems cross at about 14 MeV. If the yrast band of the compound nucleus was limiting the fusion cross section in this energy region then correlated structure might be expected. Since this experiment was performed, results of Glas and Mosel's calculation of the yrast band for ^{28}Si have become available.[4] These calculations are based on a Nilsson model using the Strutinsky method for rotating nuclei. Pairing effects have not been included. Their results for ^{28}Si are shown as a dotted line in Fig. 6.9-1. It is seen that the yrast band does not provide a limitation to the fusion cross section. This is primarily a consequence of deformation effects and is generally the case in this mass region, as has been discussed by

Mosel.[5] Another possible origin of the oscillations in the fusion cross section is an odd-even effect on the compound or pre-compound level densities which could influence the competition between fusion and direct channels. If an odd-even effect were operative the periodicity would be different for the two systems and there would not necessarily be phase matching at the energy where the grazing angular momenta cross, as these curves give the angular momenta associated with absorption from the elastic channel and not the critical angular momenta associated with fusion. It would therefore be interesting to extend the $^{4}He + ^{24}Mg$ measurements over a broader range of energy to see if there is structure with a larger periodicity than in the $^{12}C + ^{16}O$ system.

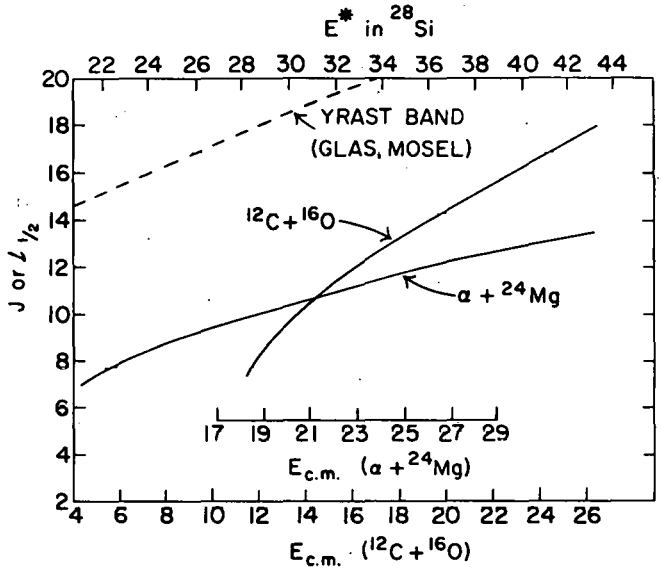

Fig. 6.9-1. Grazing angular momenta for the $^{12}C + ^{16}O$ and $^{4}He + ^{24}Mg$ entrance channels as a function of ^{28}Si excitation energy. The dashed line is a theoretical calculation of the yrast band.

We conclude this report with the presentation of some additional results supporting the compound nuclear origin of the inelastic alpha particles at angles in the background hemisphere. Angular distributions for the ground state, first excited 2^+ state, and the unresolved 4^+ and 0^+ states at 6.0 and 6.4 MeV are shown in Fig. 6.9-2. These distributions are obtained by averaging over five energies between 22.9 and 24.1 MeV to damp the Ericson fluctuations. We have also performed Hauser-Feshbach calculations, and the results, normalized to the back-angle data, are also shown. Except for the ground state (elastic) transition, where evidence of a direct contribution at forward angles is evident, the calculations account for the average shape quite well. The normalization factors between the statistical model and experimental values are given in Table 6.9-1, and are typical of the errors in such calculations due to uncertainties in level density and optical model parameters.

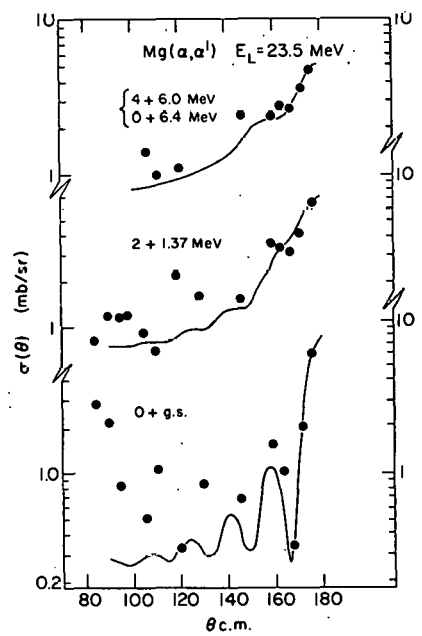

Fig. 6.9-2. Experimental angular distributions compared to Hauser-Feshbach calculations normalized to the back-angle data.

Table 6.9-1. Back-Angle Ratios of Experimental to Calculated Cross Sections

State(s)	$\sigma_{(exp)}/\sigma_{(calc)}$
0^+ g.s.	1.8
2^+ 1.37 MeV	2
2^+, 4^+ } 4 MeV	1.3
3^+ 5.2 MeV	1.1
4^+ 6.0 MeV, 0^+ 6.4 MeV }	1.8

1. Nuclear Physics Laboratory Annual Report, University of Washington (1977), p. 98.
2. R.E. Malmin, J.W. Harris and P. Paul, Phys. Rev. C18, 163 (1978).
3. P.P. Singh, R.E. Malmin, M. High and D.W. Devins, Phys. Rev. Lett. 23, 1124 (1969).
4. D. Glas and U. Mosel, to be published.
5. U. Mosel, International Conference on Nuclear Interactions, Canberra, Australia, August 1978.

6.10 Total Cross Sections for Inelastic Scattering of Very Energetic Heavy Ions

J.S. Blair

In last year's annual report we analyzed[1] some recent measurements[2,3] of the cross sections for producing discrete gamma rays, corresponding to transitions between levels in the target nucleus, when the incident projectiles were relativistic heavy ions. In this analysis we assumed that: a) the excited particle-stable states were reached in a single-step direct interaction; b) the inelastic diffraction model sufficed as an approximation to full DWBA calculations of the inelastic cross sections; and c) the magnitudes of the inelastic cross sections were characterized by the same values of the collective parameter $(\beta_L R)^2$ as are obtained in analyses of inelastic scattering of low-energy projectiles.

To the extent that values of ($\beta_L R$) are available for all important excitations of particle-stable levels and the gamma ray branching of such levels is also known from studies in low energy nuclear physics, one can then predict the gamma ray production cross sections. The only unknown parameter entering these is the diffuseness of the so-called shadow or profile function. Thus, by comparing observation to calculations, we can determine how wide is the penumbra of the shadow produced by relativistic heavy ions incident on the nucleus, a quantity otherwise inaccessible to measurement at the present time.

In the previous analysis, preliminary values for gamma ray production cross sections for ^{207}Pb and ^{88}Sr targets bombarded by ^{12}C ions were consistent with a fairly sharp-edged shadow for which the Fermi-shape diffuseness had the value 0.35 fm. On the other hand, with this value the cross section for producing the 3.73 MeV E3 gamma ray of ^{40}Ca was greatly overpredicted when we used the same diffuseness and so our report ended on an uncertain note.

Subsequently there have been further developments and extensions which have led us to conclude now that the penumbra for relativistic ^{12}C ions is fairly broad, in contrast to our initial inclinations. These developments are:

1) It has been found[2] that experimental difficulties, specifically the contribution of gamma rays from secondary reactions, caused the original Pb cross sections to be overestimated. Similar worries exist for the ^{88}Sr cross sections and, further, it is likely that our calculations have not taken into account all the important excitations of particle-stable levels for this nucleus. Therefore, we must withdraw the conclusions based on analysis of the Pb and Sr data.

2) A more careful analysis of the ^{40}Ca experiment has been carried out which corroborates our earlier result for that nucleus. The ratio of diffuseness to half-amplitude radius, d/R, is found to equal or exceed 0.10 so that d is nearly double the value previously advocated.

3) Most important, the recent paper by Shibata et al.[2] also contains the cross sections for producing gamma rays with 1.6 GeV α-particles. The importance of this is that there also exist[4] measurements of the differential elastic cross section and inelastic cross sections to the first 3^- and 5^- levels of ^{40}Ca for α-particles of nearly the same energy, 1.37 GeV. Thus, we can analyze directly these differential cross sections in terms of the diffraction model, determine in this way the ratio d/R, and then check whether our calculated gamma-ray production cross sections agree with experiment when we use this same value for (d/R). More succinctly, these data and their analysis provide a means for checking the accuracy of our procedures.

The diffraction model yields a tolerable fit to elastic scattering of 1.37 GeV α-particles with the parameters R = 4.72 and d = 0.64 fm. Reasonable fits to the inelastic cross sections are also found when the same parameters are used; the extracted values of βR agree with values determined in low energy scattering experiments. For these values of R and d, the predicted value of the

cross section for producing the 3.73 MeV γ-ray is 9.4 mb, which is within the uncertainties of the cross section meaured for 1.6 GeV α-particles, 7.2 ± 2.4 mb. This correspondence for the case of α-particle excitation gives us confidence that our procedures are reliable when the projectiles are very energetic heavy ions.

1. Nuclear Physics Laboratory Annual Report, University of Washington (1978), p. 71.
2. T. Shibata *et al.*, Nucl. Phys. A308, 513 (1978).
3. T. Shibata and H. Ejiri, private communication.
4. G.D. Alkhazov *et al.*, Nucl. Phys. A280, 365 (1977).

6.11 Measurement of Total Reaction Cross Sections in Heavy Ion Collisions at Energies Between 35 MeV/A and 200 MeV/A

J.G. Cramer, R.M. DeVries, C.R. Gruhn, J.C. Peng, and H.E. Weiman

We are continuing our preparations for measurement of total reaction cross sections in the collision of near-relativistic heavy ions, to be performed at the LBL Bevalac, using beams of ^{4}He, ^{12}C, and ^{20}Ne on targets of ^{12}C, ^{40}Ca, and ^{208}Pb. The scientific motivations of this experiment are two-fold: first, there is evidence both from the analysis of gamma ray data at Bevalac energies[1] and from the systematics of total reaction cross section data with lighter projectiles in the same E/A region[2] that a surprising "transparency" exists in all systems studied at about E/A = 100 MeV/nucleon. This region is characterized by a dramatic drop in the total reaction cross section. It occurs in roughly the region where the S-wave nucleon-nucleon phase shift becomes negative (i.e., the nuclear force becomes repulsive) due to the repulsive core of the interaction. It is thus of great interest to study the total reaction cross section as a function of energy for heavier projectiles to determine whether this transparency persists. It is worth noting that up to now the prevailing view has been that heavy ion collisions in this energy region are "black," i.e., that absorption is complete and the cross sections are geometric. Evidence to the contrary would require the revision of many ideas about heavy ion collisions.

A second motivation for this work is that if the transparency exists, it can be exploited to gain a clearer picture of the detailed processes which occur in the collision of heavy ions, since such processes in this energy region would no longer be masked by strong absorption. As an example, there have been a number of suggestions that compressional thresholds may occur in the collisions of near-relativistic heavy ions when, for instance, the velocity of the projectile reaches the speed of sound in the target nucleus. Experiments specifically designed to search for such effects have thus far provided no convincing indication of their existence. If these or any other threshold effects exist in the domain of interest, however, they would be likely to be reflected in the total reaction cross section, *provided the latter is not completely dominated by strong absorption.* Thus, a verification that transparency is indeed present at the collision velocities of interest opens the possibility of observing completely new phenomena in the collisions of near-relativistic heavy ions.

We plan to carry out this experiment using two main techniques: (1) the traditional beam attenuation method, employing a set of detector telescopes placed directly in the beam, and (2) measurement of the forward angle elastic differential cross section in the vicinity of the quarter point as a consistency check on method (1) above. We have constructed the scintillation counter telescope system required to implement method (1) and have carried out two calibration runs on the system using the 120 MeV ^{3}He beam of the LBL 88" cyclotron. The experiment will be performed on the new Low Energy Beam Line of the Bevalac, and a beam development run on this line is tentatively planned for this summer. Due to scheduling difficulties and the planned shutdown of the Bevalac, subsequent runs will probably not be possible until October 1979 or later.

6.12 On the Variations in Fusion Cross Sections for Different Light Heavy Ion Systems

R. Vandenbosch

In the last few years precision measurements[1-10] of fusion cross sections for ^{12}C and ^{16}O projectiles on p and s-d shell nuclei have revealed some significant variations from system to system. Although there was at first some indication of an approximate 200 mb discontinuity between p and s-d shell nuclei, counter examples to this trend have also been reported.[3,4] It seems important to understand to what extent these variations can be understood in terms of known properties of the nuclei, such as their geometrical properties, so that the possible dependence on other properties, such as the availability of high spin states to carry the angular momentum, can be isolated. To this end we have attempted to incorporate the known geometrical properties in a particular dynamical model for the fusion process. We consider two heavy ions interacting by both conservative and dissipative forces. The conservative forces are derived from the proximity potential,[11] and the dissipative forces from proximity friction.[12] The microscopic origin of the latter is nucleon exchange between the moving nuclei. We integrate the equations of motion to determine the trajectory of the ions. If the reactants get trapped in the internuclear potential by energy dissipation we assume that the nuclei will eventually fuse to form an amalgamated system.

The proximity potential depends on the radii and diffuseness of the nuclei involved. For not too light nuclei it has been suggested that one might calculate the half-density radius C from $C = R(1 - b^2/R)$ with $R = 1.28\ A^{1/3} - 0.76 + 0.8/A^{1/2}$ and $b = 1$. For lighter nuclei the diffuseness is smaller and the half-central-density radius is larger than given by these "standard" parameters. We have therefore gone back to the electron scattering results[13-15] for charge density distributions and extracted half-central-density radii and diffusenesses for self-conjugate nuclei. Since most matter density radial dependences are not well known, we have assumed the neutron and proton densities are the same for light self-conjugate nuclei, and have interpolated according to an $A^{1/3}$ dependence for non-selfconjugate nuclei. The values used, an average over several determinations in many cases, are listed in Table 6.12-1. We have used these parameters to calculate fusion cross sections for a variety of light heavy ion systems. Most of these systems exhibit experimental maximum fusion

cross sections at energies between 20 and 26 MeV (c.m.), and we compare the calculated and experimental values at the energy corresponding to the maximum of the fusion cross section in Fig. 6.12-1. There are no adjustable parameters in these calculations. The calculations reproduce the general trend of the data, but fail to fully reproduce some of the "structure" in the data, such as the difference in the moderate energy fusion cross sections for the $^{12}C + ^{14}N$ and $^{10}B + ^{16}O$ systems, and the somewhat larger than average fusion cross sections for nuclei with a few sd-shell nucleons. The largest discrepancies occur for systems where one of the reactants has more neutrons than protons, and may reflect a failure of our assumption that neutrons and protons have similar radial density distributions. (It should be remarked that the uncertainties in the charge density radii, as evidenced by variations between the results of different measurements, leads to an uncertainty in the calculated cross sections of 5-10%.)

Table 6.12-1. Half-central-density radius C and diffuseness b values deduced from electron scattering results. The values in parentheses were obtained by interpolation

Nucleus	C	b
^{10}B	2.15	0.88
^{12}C	2.26	0.83
^{14}N	2.44	0.78
^{15}N	(2.48)	(0.84)
^{16}O	2.65	0.82
^{17}O	(2.69)	(0.88)
^{18}O	(2.72)	(0.93)
^{19}F	(2.75)	(0.99)
^{20}Ne	2.79	1.04
^{24}Mg	2.92	1.05

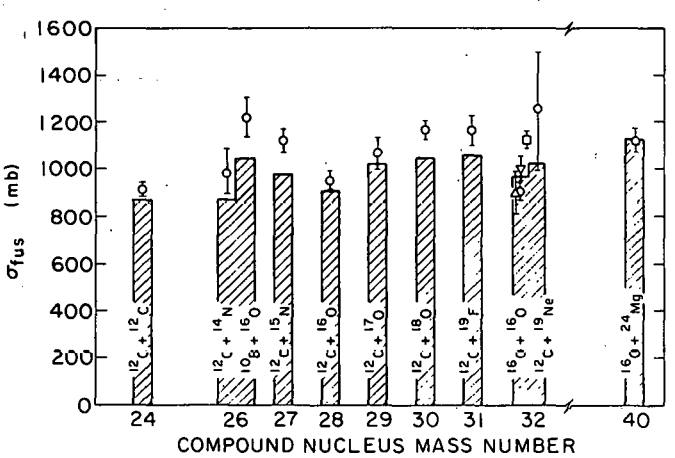

Fig. 6.12-1. Comparison of calculated (histogram) and experimental (points) fusion cross sections

The fusion cross section for the $^{10}B + ^{16}O$ system has recently been shown[4] to exhibit an anomalous behavior relative to nearby systems. The fusion cross section continues to rise to nearly the highest energy investigated, with a maximum cross section approximately 35% larger than that for the $^{12}C + ^{14}N$ system leading to the same compound nucleus. These results, together with our calculations for these systems, are shown in Fig. 6.12-2. The calculations fail to account for the dramatic difference between the two systems. What differences there are in the calculation arise primarily from the larger average diffuseness for the $^{10}B + ^{16}O$ system, with a smaller difference in the same direction arising from a few percent difference in the sum of the radii.

We have examined the sensitivity of the calculation to the strength of the dissipative forces. (Comparison of the model with energy losses associated with deeply inelastic collisions between much heavier nuclei indicate this

"frozen spheres" model underestimates the energy dissipation (see Section 6.7 of this report). For energies below about 40 MeV (c.m.) the calculated fusion cross sections are quite insensitive to the strength of the dissipative force, varying by only a few percent for changes of a factor of two in the strength of the friction term from that given by the model. At high energies, above the break in the calculated fusion cross sections, the results become more sensitive to the rate of energy dissipation. The break appears to arise from the fact that one has reached incoming ℓ values large enough that it is difficult to both dissipate sufficient angular momentum to reach an ℓ value for which the total internuclear potential still exhibits a pocket and to dissipate sufficient energy to be trapped in that potential pocket. The potential pocket disappears at $\ell \sim 17$ for the $^{12}C + ^{14}N$ system. It is important to recognize that an essential ingredient of this model is the dissipation of angular momentum as well as energy. This is illustrated in Fig. 6.12-3a, where we see that the potential for $\ell = 19$ does not exhibit a pocket but that sufficient angular momentum is transferred from relative orbital motion to intrinsic degrees of freedom during the collision to reach an ℓ value exhibiting a pocket. In the example in Fig. 6.12-3a sufficient energy is lost for the system to become trapped, whereas the next higher partial wave does not follow a trajectory with sufficient damping to be trapped (Fig. 6.12-3b).

The reason for the failure of the calculations to reproduce the energy at which the cross section starts to decrease rapidly is not clear. It may simply reflect the inadequacies of the model, particularly the frozen shapes assumed. It may also reflect

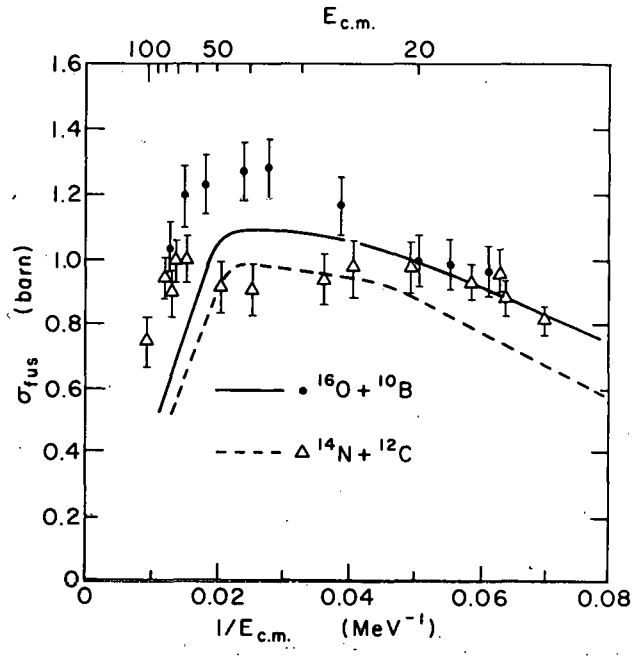

Fig. 6.12-2. Energy dependence of the fusion cross sections for the two entrance channels leading to the ^{26}Al compound nucleus. Data from refs. 2-4.

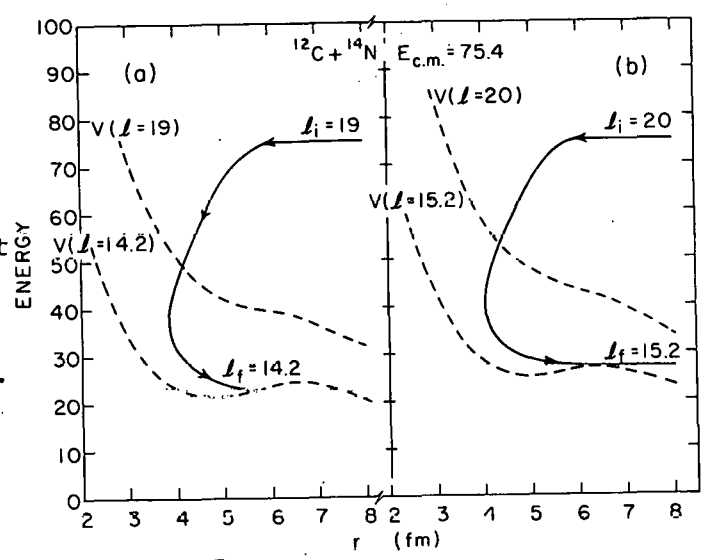

Fig. 6.12-3. The dashed curves are the total internuclear potentials for selected ℓ values. The full curves give the trajectories in E-r space. The trajectory in a) is for $\ell_i = 19$, which leads to fusion. The trajectory in b) is for $\ell_i = 20$ at the same initial energy.

the fact that the dissipative term includes only "sliding" friction and not "rolling" friction. This latter effect may account for the underestimation of the differences between the two systems, since rolling friction would be relatively more important in a more asymmetric system. Other factors which may play a role in determining the differences between the two systems is the fact that the excitation energy of the compound system for a given $E_{c.m.}$ is larger for $^{10}B + ^{16}O$ than for $^{12}C + ^{14}N$. The channel spins are also larger for the former system.

1. P. Sperr *et al.*, Phys. Rev. Lett. 36, 405 (1976); Phys. Rev. Lett. 37, 321 (1976).
2. R.G. Stokstad *et al.*, Phys. Rev. Lett. 36, 1529 (1976).
3. M. Conjeaud *et al.*, Nucl. Phys. A309, 515 (1978).
4. J. Gomez del Campo, R.A. Dayras, J.A. Biggerstaff, D. Shapira, A.H. Snell, P.H. Stelson and R.G. Stokstad, Phys. Rev. Lett. 43, 26 (1979).
5. B. Fernandez *et al.*, Nucl. Phys. A306, 259 (1978).
6. J.J. Kolata *et al.*, Phys. Rev. C16, 891 (1977).
7. A. Hertz *et al.*, Phys. Rev. C 18, 2780 (1978).
8. S.L. Tabor *et al.*, Bull. Am. Phys. Soc. 22, 630 (1977).
9. I. Tserruya, Phys. Rev. C 18, 1688 (1978).
10. J.L.C. Ford, Jr. *et al.*, Bull. Am. Phys. Soc. 24, 570 (1979).
11. J. Blocki *et al.*, Ann. Phys. 105, 427 (1977).
12. J. Randrup, Ann. Phys. 112, 356 (1978).
13. H.R. Collard, L.R.B. Elton, and R. Hofstadter, in Nuclear Radii, Landolt-Bornstein, NS Group 1, Vol. 2 (1967).
14. C.W. deJager, At. Data & Nucl. Data Tables 14, 485 (1974).
15. W.J. Gerace and G.C. Hamilton, Phys. Lett. 39B, 481 (1972).

6.13 Elastic Scattering of ^{4}He, ^{7}Li and ^{9}Be from ^{28}Si in the Nuclear Rainbow Region

J.G. Cramer, R.M. DeVries, D.A. Goldberg, A.G. Seamster and M.S. Zisman

This work is a continuation of our investigations of the systematics of heavy ion elastic scattering at energies up to the region where nuclear rainbow scattering occurs.[1] In last year's Annual Report we reported the measurement of ^{9}Be elastic scattering at 120 MeV and 20.6 Mev.[2] These data have now been analyzed with the optical model and a set of potentials obtained. In addition, we have measured new data on ^{7}Li scattering on ^{28}Si at 140 MeV using the LBL 88" Cyclotron and also new data on the scattering of ^{4}He from ^{28}Si and ^{27}Al at 142 MeV using the University of Maryland Cyclotron. The latter data are presently being analyzed.

Analysis of the ^{9}Be data shows that the elastic scattering of this projectile from ^{28}Si is dominated at all energies by strong absorption, removing much of the sensitivity to the real potential and preventing a unique determination of potential parameters. A number of optical potentials have been used to fit a ^{9}Be data set spanning bombarding energies between 13 MeV and 201.6 MeV. Six representative potentials are given in Table 6.13-1 below. We note that

Table 6.13-1. $^{9}Be + ^{28}Si$ Optical Potentials

Set	V (MeV)	r_R (fm)	a_R (fm)	W (MeV)	r_I (fm)	a_I (fm)	θ_{NR} (deg)
G90	300.0	0.567	0.942	41.1	1.054	0.782	-81
G92	150.0	0.703	0.944	27.6	1.150	0.753	-46
G89	100.0	0.767	0.960	23.1	1.191	0.736	-31
G84	75.0	0.776	1.012	29.8	1.143	0.744	-22
G95	15.0	1.149	0.914	24.4	1.185	0.701	- 2
G38	13.8	1.244	0.652	503.2	0.617	0.825	- 3

there is little sensitivity to the central depth of the real well, since V varies from 13.8 MeV to 300 MeV, and that the imaginary potential varies over an even larger range. Moreover, the estimated nuclear rainbow angle, θ_{NR}, as given in the right hand column of the Table varies from -81° to -2°. We take this as an indication that the very strong absorption in this system has eliminated most of the sensitivity to nuclear rainbow scattering for this system.

An analysis of the region of sensitivity of the ^{9}Be scattering data, using the Notch Perturbation Method,[3] reveals that the ratio of real to imaginary potential over the region of maximum sensitivity is relatively independent of bombarding energy and maintains a fairly constant value of about $V(R_S)/W(R_S) = 0.8$. This may be related to the inability of the analysis of the data set to determine a unique potential. Moreover, it suggests that a 4-parameter Woods-Saxon optical potential with V/W = 0.8 would probably be adequate to describe the data set.

An account of the ^{9}Be analysis will be published in the proceedings of the BNL *Symposium on Heavy Ion Physics from 10 to 2000 MeV/AMV*.

1. R.M. DeVries, D.A. Goldberg, D.W. Watson, M.S. Zisman and J.G. Cramer, Phys. Rev. Lett. 39 450 (1977) and references contained therein.
2. University of Washington Nuclear Physics Laboratory Annual Report (1978), Section 6.9, p. 86.
3. University of Washington Nuclear Physics Laboratory Annual Report (1976), Section 12.3, p. 115 and J.G. Cramer and R.M. DeVries (to be published).

7. RESEARCH BY USERS AND VISITORS

7.1 Simulation of In-Reactor Creep

C.H. Henager† and P.L. Hendrick*

Materials placed under stress and subjected to the elevated neutron fluxes of both breeder and fusion reactors will exhibit a form of accelerated deformation termed irradiation-induced creep. Due to the difficulty, cost and time required in making precise in-reactor creep measurements, there is a world-wide interest in simulating in-reactor creep by bombarding materials of interest with energetic light ions under well-controlled conditions. Such experiments could enhance our understanding of the operating creep mechanism and permit screening of potential reactor alloys. Several early experiments have demonstrated the ability to simulate irradiation-induced creep and have generated a limited amount of creep data.[1-4]

The Radiation Effects on Metals program supported by the Division of Basic Energy Sciences, U.S. Department of Energy at Battelle Northwest is conducting a creep simulation program using the tandem Van de Graaff accelerator at the Nuclear Physics Laboratory. Development of an irradiation creep apparatus located on the straight-ahead line in Cave III, has been completed.[5]

Early experiments compared the creep response of high purity Ni under conditions of continuous and cyclic irradiation with 17 MeV deuterons.[6,7] The cyclic irradiation approximated the expected duty cycle of a tokamak, a fusion power plant. The significant result of this series of experiments was that cyclic irradiation creep expected for tokamak plants may be greater than that expected for continuous irradiation.

At the present time a series of experiments is underway to determine the stress dependency of irradiation creep in Ni. Continuous irradiations with 17 MeV deuterons are performed at 200°C with stresses ranging from 0.8 to 0.25 of the yield stress. To date, four irradiations at 3 different stress levels have been completed.[8] These preliminary results are in agreement with irradiation creep data for Ni observed at the Naval Research Laboratory.[4]

---

† Graduate student, Department of Metallurgy, Mining, and Ceramic Engineering, University of Washington and Battelle Northwest, Richland, Washington.

* Battelle Northwest, Richland, Washington.

1. S.D. Harkness, F.L. Yagee, and F.V. Nolfi, Jr., ANL-7883, Argonne National Laboratory, 1972.

2. P.L. Hendrick, A.L. Bement, Jr., and O.K. Harling, Nucl. Instr. and Methods 124, 389 (1975).

3. R.J. McElroy, J.A. Hudson, and R.S. Nelson, Proceedings of the International Conference on Radiation Effects and Tritium Technology for Fusion Reactors (CONF-750989, Vol. II), 1975.

4. P.L. Hendrick, D.J. Michel, A.G. Pieper, and R.E. Surratt, J. of Nuclear Materials 59, 229 (1976).

5. P.L. Hendrick, Light Ion Irradiation Creep Apparatus, Nuclear Instruments and Methods 161, 345 (1979).
6. E.P. Simonen and P.L. Hendrick, Light Ion Irradiation-Induced Creep Mechanisms in Nickel, Proc. of First Topical Meeting on Fusion Reactor Materials, Miami Beach, 1979.
7. E.P. Simonen, P.L. Hendrick, *ibid.*, accepted for publication in J. Nuclear Mat., 1979.
8. C.H. Henager, J.L. Brimhall, Creep in Ni Bombarded with 17 MeV Deuterons, abstract accepted for presentation at International Conf. on Fundamental Mechanisms of Irradiation-Induced Creep and Growth, Chalk River, Canada, May 8-10, 1979.

7.2 Energetic Particle Damage Studies of Metals

E.R. Bradley*, R.H. Jones* and D.L. Styris*

Radiation damage studies of proposed fusion reactor materials are presently being performed with a variety of high energy particles including neutrons produced by T(d,n) and Be(d,n) reactions, light and heavy ions, electrons, and fast and thermal neutrons. Each particle and particle source has unique capabilities which help compensate for the inadequate neutron fluxes and irradiation volume of presently available fusion neutron sources.

Energetic light ions are attractive for simulating the radiation damage effects of 14 MeV neutrons on microstructure and mechanical properties because of their range, high available fluxes ($>10^{14}$ p/cm^2-s), and primary knock-on spectra which closely simulate those produced by 14 MeV neutrons in some materials. Calculations by Logan et al.[1] and Omar et al.[2] indicate that the recoil energy spectrum of 16 MeV protons closely simulates that of 14 MeV neutrons in niobium, nickel and several other metals. Damage energies and displacement cross-sections reported by Omar et al.[2] indicate that the high energy recoil damage produced by 16 MeV protons and 14 MeV neutrons are very similar while the low energy (<10 KeV) recoil damage differs. Transmission electron microscopy observations by Mitchell et al.[3] showed a similarity between the size and density of defect clusters in copper irradiated with 16 MeV protons and 14 MeV neutrons.

The damage induced in metals by 16 MeV protons from the University of Washington tandem is being compared to that induced by neutrons from the T(d,n) source at Lawrence Livermore Laboratory and the Be(d,n) source at U.C. Davis. This comparison is being made on the basis of irradiation induced point defect cluster size and spatial density and flow stress increase.

Wire and foil specimens are irradiated with a 3 μa beam of 16 MeV protons while cooled by a flowing helium stream. The temperature is monitored by thermocouples in the same plane as the specimens and the total fluence is determined by a vacuum faraday cup and vanadium dosimeters.

The damage induced in nickel and niboium at 20°C by 16 MeV protons has been found to exhibit many similarities to that induced by 14 MeV neutrons. In nickel, the similarities include: 1) equal defect cluster diameters; 2) equal defect cluster densities at 10^{17} particles/cm^2; 3) a saturation in the cluster density of proton and neutron irradiated nickel on a damage energy basis; and 4) a close, but not exact, correlation in the yield stress increase on a particle fluence basis. In niobium, the similarities include: 1) the magnitude of the lower yield stress increase; and 2) the fluence dependence of the yield stress increase.

---

* Battelle Northwest, Richland, Washington.

1. C.M. Logan, J.D. Anderson. and A.K. Mukherjee, Journal of Nuclear Materials, 48, 223 (1973).
2. A.M. Omar, J.E. Robinson, and D.A. Thompson, Journal of Nuclear Materials, 64, 121 (1977).
3. J.B. Mitchell, C.M. Logan, and C.J. Echer, Journal of Nuclear Materials, 48, 139 (1973).

7.3 Pulsed Radialuminesceni Studies*

M.L. West† and J.H. Miller†

Pulsed radialuminesceni techniques were used to investigate the fluorescence response of dilute salutions of benzene in cyclohexane for proton and α particle excitation. Intra-track quenching from radicals created along individual particle tracks was observed. This intra-track quenching is proportional to the mean stopping power of the incident particles. However, for protons and α particles of the same mean stopping power, the quenching is different. These results are consistent with our model prediction. Protons and α particles of the same mean stopping power have different track radii and hence different initial distribution of radiolysis species along the track region.

---

† Battelle Pacific Northwest Laboratories.

7.4 Total Body Calcium by Neutron Activation

C.H. Chesnut, G.M. Hinn, T.K. Lewellen, R. Murano, and W.B. Nelp

The Division of Nuclear Medicine is continuing its measurements of total body calcium by means of whole-body neutron activation and whole-body counting. The cyclotron is used as the neutron source, and the 3.1 MeV gamma ray of 8.7 minute ^{49}Ca is counted.[1]

The two year program to test the efficacy of the drugs Winstral (Winthrop Laboratories) and Calcitonin (Armour) in the control of postmenopausal osteoporosis is nearly completed.

A cooperative program was started with Dr. Recker of Creighton University in Omaha to measure calcium on 15 patients under study at that institution. Thirteen patients from the University of Washington and the Veteran's Administration Hospitals Kidney Centers were given calcium measurements. A total of 145 calcium measurements were made in 1978.

---

1. Nuclear Physics Laboratory Annual Reports, University of Washington, 1968-1976.

7.5 [N-$^{11}CH_3$]-Morphine

D.R. Allen, P.L. Beaumier, and D. Hartnett

$^{11}CO_2$ was produced by the $^{14}N(p,\alpha)^{11}C$ reaction and converted to $H_2^{11}CO_3$ which was then used to tag morphine.[1] By imaging the annihilation radiation from ^{11}C it may be possible to answer some questions about the behavior of morphine in the body.

---

1. D.R. Allen and P.L. Beaumier, Second International Symposium on Radiopharmaceutical Chemistry, Oxford, 1978.
2. P.L. Beaumier, thesis, University of Washington School of Pharmacy, 1978.

7.6 Radioisotope Production for Lung Imaging in Nuclear Medicine

D.R. Allen, C.H. Chesnut, D. Hartnett, T.K. Lewellen, H.I. Modell, R. Murano, W.B. Nelp, and T. Rudd

$^{81m}Kr(t_{1/2}$ = 13 sec) was produced on two occasions to test its usefulness in making images of the ventilated lung with the gamma ray cameras at the University of Washington Hospital. These images are potentially useful both as a diagnostic tool for patient care in the Nuclear Medicine Clinic and for respiratory research in the Department of Physiology and Biophysics.

4.7 hour ^{81}Rb is produced as previously described,[1] and adsorbed on an exchange column. The ^{81m}Kr is flushed out by air into a breathing system. The short life permits repeated studies, allowing one to observe, for instance, the effect of exercise.

Two anesthetized dogs were studied. Manipulations were performed to force changes in the ventilation pattern, and the results were clearly visualized.

Several human subjects were also studied and showed normal ventilation patterns.

---

1. Nuclear Physics Laboratory Annual Report (1978).

7.7 Fast Neutron Beam Radiotherapy—Medical Radiation Physics*

J. Eenmaa† and P. Wootton†

The Medical Radiation Physics Division continued its routine support of neutron beam radiobiology, and renovated the neutron therapy beam systems in preparation for resumption of treatment of cancer patients. These treatments were resumed March 1, 1979. The division acquired and will cooperate with the NPL staff in installing a solid-state process-controller for improved cyclotron operation. An improved power supply for the main magnet will follow. Work on the U.S. Fast Neutron Beam Dosimetry protocol nears completion.

---

* Supported by NCI Grant No. CA-12441
† Division of Medical Radiation Physics, Department of Radiology, University of Washington.

7.8 Combined 1,3-Bis(2-chloroethyl)-1-nitrosourea (BCNU) and Neutron Therapy of a Rat Brain Tumor*

J.P. Geraci† and A.M. Spence††

During the past year the effects of cyclotron neutrons, ^{137}Cs gamma rays and BCNU (a chemotherapeutic agent), or combinations thereof on a ethylnitrosourea-induced astrocytoma transplanted to the intracerebral site in rats have been examined. Untreated control animals usually succumb from the mass effect of relentless tumor growths 21 days after implantation. Death in these animals is proceeded by several days of neurological signs, i.e., lethargy, convulsions, and impaired righting responses and hind limb paresis. Necropsy revealed massive superficial cerebral hemisphere tumors which were frequently associated with caudal displacement of the cerebellum and brain stem. A similar observation is often seen in brain tumor patients at autopsy. Single dose whole-head neutron or photon irradiation one week after tumor implantation delayed the onset of neurological signs and prolonged survival. The increase in mean survival of the animal was dose-dependent for both types of irradiation (Figs. 7.8-1 and 7.8-2). The effects of BCNU and radiation on mean survival time appears to be additive and independent of dose and type of irradiation.*

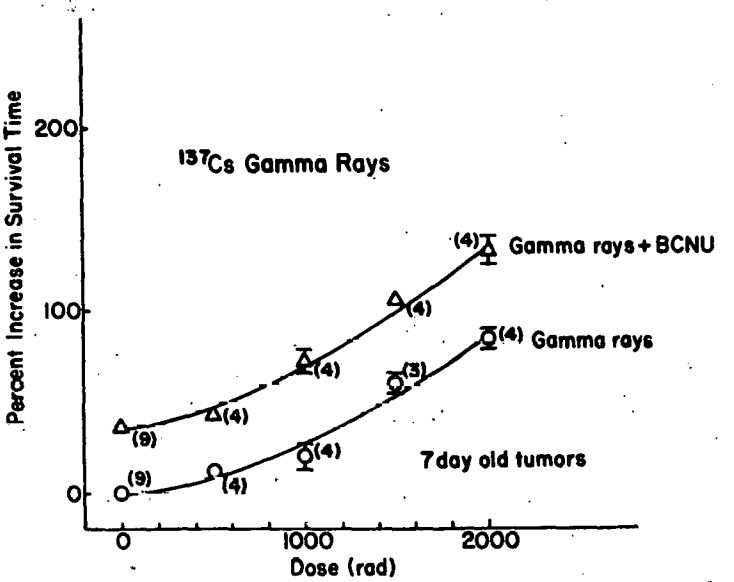

Fig. 7.8-1. Increase in survival time for ^{137}Cs gamma rays

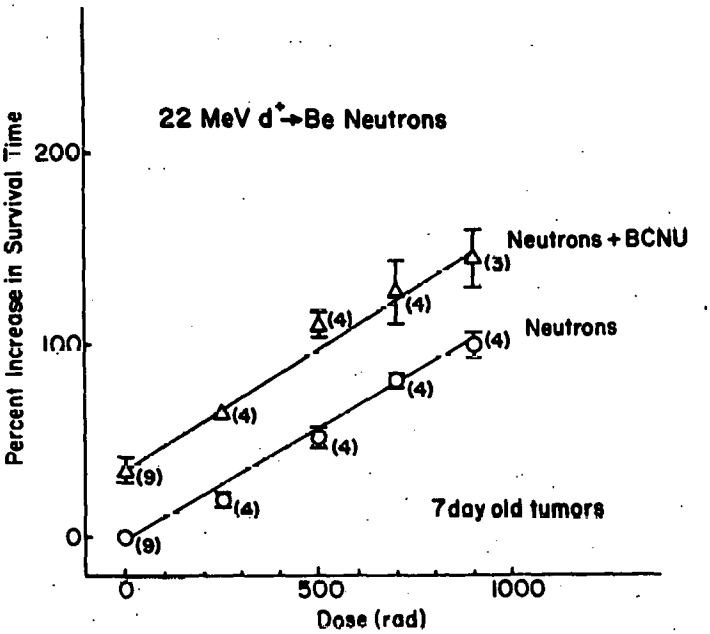

Fig. 7.8-2. Increase in survival time for 22 MeV neutrons

---

* Supported by grants CA 22431 and CA 18385 awarded by the National Cancer Institute, U.S. DHEW.

† Department of Radiology, University of Washington.

†† Department of Medicine, University of Washington.

7.9 Angular Correlation Measurements in the Decays of ^{147,147}Eu

K.S. Krane*

Cyclotron protons have been used to produce ^{147,149}Eu activities from separated ^{147,149}Sm by means of (p,n) reactions. Angular correlations of the decay gamma rays have been studied in order to determine spin assignments of ^{147,149}Sm levels and multipolarities of the emitted gamma rays.

---

* Oregon State University, Corvallis, Oregon.

7.10 Solar Cell Irradiations

C. Baze* and D. Russell*

The cyclotron has been used to conduct 11 MeV proton irradiations of 2 mil thick silicon solar cells in order to evaluate cell annealing techniques.

---

* Boeing Radiation Effects Laboratory.

7.11 Copper Foil Irradiation

J. Adamski,* J. Beymer,* R. Copeland,* and R. Guay*

Eleven MeV protons from the cyclotron were used to activate copper foil targets. The foil targets were used to calibrate a system for determining proton beam cross section profiles to aid in the analysis of beam transport and beam focusing techniques.

---

* Boeing Radiation Effects Laboratory.

7.12 Alpha-N Yield Neutron Measurements*

P.J. Grant,† D.L. Johnson†† and G.L. Woodruff†

The neutron yields produced by (α,n) reactions of importance to reactors are to be measured with incident alpha energies ranging from 4 MeV to 8 MeV. Initial experiments will focus on ^{18}O targets followed by others as interests dictate.

The spherical "long counter" to be used in these experiments is presently under construction on the zero degree beam line. The framework formerly used to support a magnet used for g-factor measurements was used to provide a

strong base on which to build the counter. The counter is composed of approximately 3,600 kgs of graphite stacked in an 130 cm diameter cylindrical matrix at right angles to the beam line. He^3 proportional counters, which are on loan from Q-1 Division, Los Alamos, are inserted on axis in the cylinder at even spacing around the circumference. A 15.2 cm diameter Be sphere has been machined to be placed in the center of the graphite cylinder to multiply the high energy neutrons from the targets in the center of the sphere, thereby extending the constant efficiency versus energy curve to higher energies.

---

* Work supported by Department of Energy Contract EY-650-5-06-2225, Basic Agreement No. 31, Mod A007.
† Department of Nuclear Engineering, University of Washington.
†† Westinghouse, Hanford.

7.13 Equilibrium Delayed Neutron Spectra*

P.J. Grant† and G.L. Woodruff†

Data reduction was completed for directly measured near-equilibrium delayed neutron energy spectra associated with fast neutron fission of ^{240}Pu.[1] The data were collected last year on the experimental apparatus developed by G.W. Eccleston[2] using a cyclical sequence consisting of 0.1 sec irradiation, 0.04 sec delay, 0.1 sec count and a 0.02 sec wait.

Comparison of this spectrum, which is contained in Fig. 7.13-1, with those measured by Eccleston of ^{232}Th, ^{233}U, ^{235}U, ^{235}U and ^{239}Pu show agreement in overall shape, with a large fraction of the neutrons at the low energies.

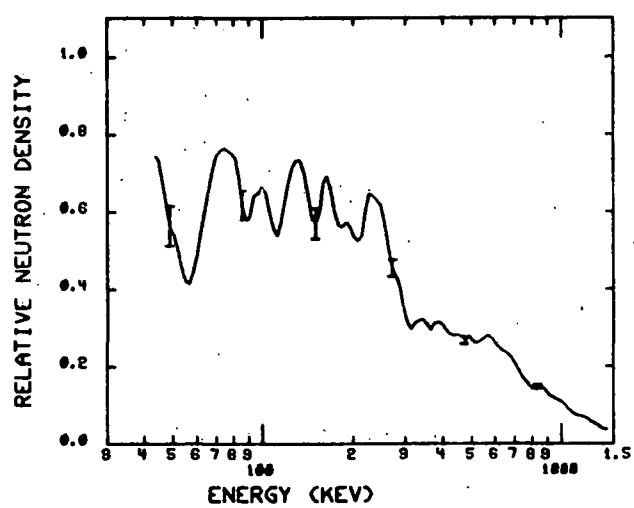

Fig. 7.13-1. ^{240}Pu Near-Equilibrium Delayed Neutron Spectrum

---

* Work supported by Department of Energy Contract EY-760-5-06-2225, Basic Agreement No. 31, Mod A007.
† Department of Nuclear Engineering, University of Washington.
1 Nuclear Physics Laboratory Annual Report, University of Washington (1978), p. 103.
2 Nuclear Physics Laboratory Annual Report, University of Washington (1977), p. 148.

---

8. ACCELERATOR AND ION SOURCE DEVELOPMENT

8.1 Van de Graaff Accelerator Operations and Development

H. Fauska, C. Linder, J. Rohrbaugh, G. Saling and W.G. Weitkamp

After more than 60,000 hours of operation, the beam tubes on the tandem refused to hold voltage satisfactorily and were replaced during the past year. As an aide to other tandem users, the symptoms of beam tube deterioration and the tests we used to diagnose the trouble will be described in some detail below. Other improvements to parts of the accelerator will also be described. Improvements to the polarized ion source, the new sputter ion source, and improvements to the accelerator related to the radiochronology project are described in Sections 8.2 through 8.4 of this report. Electronics built for the Van de Graaff accelerator are described in Section 9.4. Statistics of Van de Graaff accelerator operations are given in Table 8.1-1.

A) The Beam Tube Problem

During this past year the tandem Van de Graaff accelerator developed a severe problem holding high terminal voltage, which interferred with normal operations. The problem was eventually traced to the beam tubes and was eliminated by replacing the tubes. The problem caused a significant loss of research beam time because of poor accelerator performance, time required for diagnosis, and time required to replace the tubes.

The beam tubes which were replaced were aluminum electrode inclined field tubes built by High Voltage Engineering Corp. At replacement in December 1978, tube sections 1, 2, and 3 had been operated 60,900 hours and tube section 4 had been operated 76,800 hours.

The first observed and most obvious symptom of the problem with the tubes was abnormally large fluctuations of the terminal voltage. The corona regulator normally causes the corona current to fluctuate about 10 uA out of 50 in order to stabilize the terminal voltage, but when the symptoms were present, fluctuations might be larger than 200 uA, making terminal regulation impossible. The fluctuations were most pronounced at the highest terminal voltages, but would also appear as low as 5 MV. The fluctuations would persist even if the beam was stopped at the low energy end of the tandem and the terminal was stabilized by the GVM.

Intense X radiation was present whenever the fluctuations were and was observed whether beam was present or not. The intensity depended upon the terminal voltage. At 8 to 9 MV terminal voltage, up to 1 R was observed outside the pressure vessel, fluctuating by a factor of 5 or so. Fluctuations in x-ray intensity correlated with fluctuations in terminal voltage. The radiation was 8 times more intense on the beam tube side of the accelerator pressure vessel, indicating that the phenomenon was most likely associated with the beam tubes.

The fluctuations were also accompanied by a drop in terminal voltage, which required additional charging current to correct. Charging currents 25

Table 8.1-1. Statistics of Van de Graaff Operation
From April 16, 1978 to April 15, 1979

		Time (Hrs)	Percent
1.	Division of time among activities		
	Normal operations[a]	6280	72
	Scheduled maintenance and accelerator development	1036	12
	Unscheduled maintenance	613	7
	Unrequested time	831	9
	Total[b]	8760	100
2.	Division of beam time among particles		
	a. Two stage operation		
	Protons	1153	20
	Polarized protons	1332	24
	Deuterons	326	6
	^{4}He	69	1
	^{12}C	773	13
	^{14}N	34	1
	^{15}N	8	< 1
	^{16}O	1055	19
	^{18}O	26	< 1
	^{19}F	17	< 1
	^{9}Be	31	1
	^{28}Si	84	2
	^{32}S	512	9
	Subtotal	5420	96
	b. Three stage operation		
	Protons	44	1
	^{12}C	62	1
	^{14}N	129	2
	Subtotal	235	4
	TOTAL BEAM TIME	5655	100
3.	Division of normal operation among activities		
	University of Washington Nuclear Physics Laboratory	5848	93
	Battelle Northwest Laboratories	432	7
	TOTAL	6280	100

a) Includes all the time the accelerator was under the control of an experimenter.
b) This is the number of hours in a year.

percent above normal were typical under these conditions. There was never any clear indication as to where this additional current was going. The column currents for the high and low energy columns would change by different amounts, but the total column current, down charge current and corona current would not add up to the charging current. No evidence was observed that charge escaped by travelling down the beam tubes. The most reasonable explanation of this is that charge leaked directly from the terminal to the tank walls, possibly as a result of ionization caused by the intense X radiation in the tank.

During the early stages of the problem we had been trying to operate a titanium sublimation pump in the terminal of the tandem, and observed that symptoms appeared about 1/2 hour after the pump was heated up. We subsequently removed the pump, but the symptoms continued to appear from time to time. Except for this correlation between symptoms and terminal sublimation pump operation, the symptoms came and went without much relationship with other accelerator activities. The symptoms might last for several hours or a substantial fraction of a day. They did not seem to condition away, but simply disappeared.

The symptoms were not similar to normal beam tube conditioning because there was no visible light emitted from the beam tubes, nor did any activity show up at the high energy cup, as is the case with normal conditioning. The symptoms did not go away a few minutes after raising the terminal voltage either, as in normal conditioning.

A number of procedures were carried out to try to pin down the cause of the symptoms. The beam tube and column were carefully examined, but no external evidence of tube damage was obvious. Six radiation monitors were placed along the accelerator tank to try to localize the source of the radiation. Part of the time these monitors indicated the source was just upstream or downstream from the terminal. At other times, the indication was that a whole beam tube section was the source. We installed a 7 in long aluminum sled which could be remotely moved along the column to short out specific sections of the beam tube. During some runs, the radiation would drop when a sled was near the terminal. During other runs, no decrease in radiation would be observed, no matter where the sled was located.

It was suggested that the symptoms might result from tank gas leaking into the beam tube. During one refoiling operation, we observed a tank gas leak that only opened above a pressure of 170 psi, about 80% of maximum tank pressure. Since the symptoms appeared shortly after the tank was pressurized that time we were able to study the effect of a known tank gas leak on the symptoms. There was clearly no relationship between the amount of gas leaking into the beam tube and the X radiation intensity.

At the conclusion of this test with gas leaking into the tubes, we decided to see what effect a lot of gas in the beam tube might have. We flooded the beam tube by shutting off the pumps, with the terminal at high voltage. The pressure was allowed to rise to about 10^{-3} Torr. To our surprise, the symptoms disappeared, and did not return for several days. This cure proved effective for a period of several months and was used every time the symptoms appeared. However, the symptom eventually persisted even though the pressure in the beam tube was raised.

We also discovered that the symptoms could be suppressed by hanging small magnets on the beam tube. Magnets placed near the terminal were not effective, but when magnets were placed along most of the length of both tube sections 2 and 3, the symptoms were completely suppressed. The symptoms reappeared in several months, however.

In December, reconditioned aluminum electrode beam tubes were installed in the tandem. The voltage on these tubes was raised very carefully, and the symptoms have not reappeared in 1600 hours of operation since, 500 hours of which have been above 8.5 MV on the terminal. Within the first two weeks of operation with the new tubes, the terminal potential reached 9 MV and operation was exceptionally stable. In fact, long-time observers of the tandem operation claim that the machine operates more stably than ever before in history.

There has been a great deal of speculation about the cause of the symptoms. Contamination of the surfaces by residues from heavy ion beams, by small bits of carbon foils from the foil stripper, by pump oil, or by cesium from the ion sources is suspected. The fact that flooding the tubes with gas at high voltage would temporarily cure the symptoms supports this suspicion. A visual examination of the inside of the beam tubes after removal has shown that the electrodes are badly discolored, as might be expected after 60,000 hours of operation. There are several locations where a dull, dark grey deposit appears to have built up on the electrodes, corresponding to maxima in the excursion of the ion trajectories. These regions may possibly be loci of the discharge.

In any event, we feel that the tubes which were replaced served us well. Except for the few months prior to replacement, we never had any difficulty attaining high voltage attributable to tubes. The bottom line conclusion seems to be that tubes finally get old and die. Interestingly though, the parts can be recycled.

B) Other Accelerator Projects

Among the other accelerator development projects undertaken during the current year were the following:

1. The beam buncher was rebuilt.[1] In attempting to improve the vacuum in the beam tube at the low energy end of the machine, we decided to rebuild the buncher into a stainless steel tube with provision for auxilliary pumping. However, the Q of the buncher suffered greatly because the resistance of stainless is higher than the aluminum which was replaced. Copper plating the inside of the buncher and modifying the electrodes have now raised to Q to 211, about 50 percent higher than previously. With the rebuilt buncher we have seen helium ion bunches of 1.5 msec width, compared to about 6 msec seen previously. Testing has not been exhaustive, and part of the improvement is undoubtedly due to using the polarized ion source as a source of helium ions rather than a lithium charge exchange source.

2. The vacuum in the low energy end has been improved. As part of a continuing program to improve the low energy beam tube vacuum in order to increase heavy ion transmission of the accelerator, all the low energy components were overhauled to reduce virtual leaks. This was accomplished while the beam tubes in the tandem were being replaced. A liquid nitrogen trap was installed in the beam line to pump condensibles, and a new ion pump was placed between the two source magnets.

3. The radiation safety interlock system on the tandem has been redesigned to minimize even further the probability that experimenters could receive any radiation dose, yet permit maximum accessibility to the accelerator. The system is now operated by the accelerator programmable controller.[2]

---

1. H. Fauska, N.G. Ward, J. Lilley and C.F. Williamson, Nucl. Instr. and Meth. 63, 93 (1968).
2. Nuclear Physics Laboratory Annual Report, University of Washington (1978), p. 113.

8.2 Polarized Ion Source Development

W.B. Ingalls and T.A. Trainor

The failure of an electrical vacuum feedthrough on the duoplasmatron-cesium canal vacuum box diffusion pump was utilized as an opportunity to replace both the pump and the complicated Coolanol cooling system. These were replaced with an NRC 2000 l/s pump and a deionized water recirculating system which cools all three ion source diffusion pumps.

The closed loop recirculating system is, with the exception of the diffusion pump cooling lines, regenerative turbine recirculating pump,[1] and heat exchanger, constructed of PVC pipe. The system consists of two loops; a large loop containing the diffusion pumps, heat exchanger, recirculating pump and PVC insulating pipe, and a small bypass loop containing a commercial deionizer cartridge assembly.[2] The resistivity of the water is maintained at a minimum of 10 MΩ/cm by the deionizer. The system has operated continuously with occasional addition of fresh water for eight months.

The freon recirculating system suffered the disintegration of its plastic pump impellers twice this year. A pump identical to that utilized in the water system was purchased and adapted to the existing freon system.

Two well-regulated high voltage power supplies[3] have been installed this year. A 10 kV supply replaces the high maintenance, unregulated duoplasmatron extraction electrode supply. A 60 kV supply replaces the main frame voltage supply which suffered long-term drifts. A recent α-particle run benefitted from this replacement by achieving a time bunch of 1.5 nS FWHM, a factor of four better than the previous Laboratory milestone for an α beam.

The original recirculating cesium canal[4] designed for the hydrogen parity experiment has been installed in the polarized source. Experience with its use is still being gained, but it has, so far, provided beams of like quality to the old canal with a marked decrease in the amount of cesium accumulation in the duoplasmatron-cesium canal vacuum box.

---

1. Fairbanks-Morse Model 6801-8B.

2. Continental Water Conditioning Corporation Model A4000-H deionizer units with mixed bed cartridge #A-4050-4.
3. Spellman High-Voltage Electronics Corporation.
4. Nuclear Physics Laboratory Annual Report, University of Washington (1978), p. 11.

8.3 Sputter Ion Source Developments

J.F. Amsbaugh, G.W. Farwell, F.H. Schmidt, D.W. Storm, and W.G. Weitkamp

In the past year a sputter ion source has been built for development studies following the design considerations previously reported.[1] It has been installed on the Laboratory's ion source test stand and initial tests have lead to some redesign. In conjunction with this project, a device to measure ion beam emittance has been built to enable a comparison of various geometries and techniques which hopefully will improve transmission through the tandem. Finally, the Laboratory's Universal Negative Ion Source (UNIS) has undergone some revision.

A. The Development Sou

The development sputter ion source is currently installed on the ion source test stand.[2] Current base vacuum in the box is 6×10^{-7} Torr. The electrodes are mounted on an optical bench and are designed to facilitate alignment and geometry changes. This is shown in Fig. 8.3-1. The cesium beam is formed by extracting with a Pierce electrode at -20 to -50 kV the positive cesium ions from a porous ionizer, heated to 1100°C. Cesium currents are 1 to 2 ma. The cesium beam is then focused by a four sector einzel lens, modeled after the source at Bochum,[3] which enables beam steering before impingement on the sputter target. Six sputter targets or "cones" are fitted into a copper block which

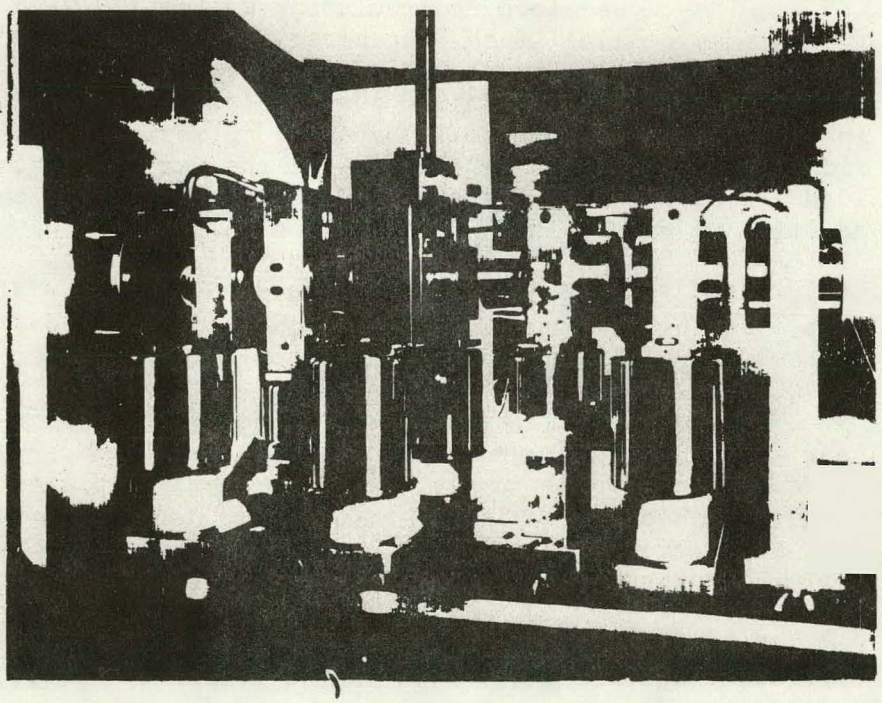

Fig. 8.3-1. Internal view of development sputter source. Ion beam exits right.

can be moved vertically without breaking vacuum. Next is the secondary beam extractor and after that two electrodes which form a decel-accel einzel lens.

Two major modes of operation are now possible. In the first mode the cesium beam sputters ions from the inside surface of a cone. In the second mode (called the reflected beam geometry) the cesium beam is steered through an off-axis hole and reflected by the secondary extraction electrode (normally grounded but in this case at a positive potential) to sputter ions from a small pellet. This is shown schematically in Fig. 8.3-2.

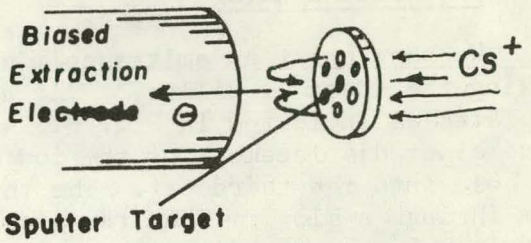

Fig. 8.3-2. Reflected Cs beam geometry

Visual observation is possible through a 30 x 15 cm lead glass view port of the cesium beam spot. The focus and steering of the cesium beam only partially determines where the reflected beam strikes, because the electrostatic field shape at the turning point of the cesium introduces both steering and focusing. A detailed study of this system is underway.

The vertical position of the copper sputter target block is selectable by a series of stops on the cooling line which feeds in through the top of the box and also provides electrical continuity. This feature is shown in Fig. 8.3-3, along with the cooling and electrical feed throughs (side plate) and cesium oven assembly (end plate). A new side plate is being designed to decrease corona losses and increase extraction voltage which is now limited to the 40 kV flash over rating of the ceramic feedthrough. A prototype of the new design feeds cooling and voltage through to the cesium extractor via 0.65 cm OD copper tubing. This has reduced corona losses from 1.0 ma to 0.1 ma at -35 kV potential and with cesium covered surfaces. The source has run over 100 hours while cooling only the cesium extractor and sputter target block. Typical source output has been 15 μA of ^{12}C and 1.2 μA of ^{63}Cu with beam energy of 35 keV and 1.2 ma of cesium beam.

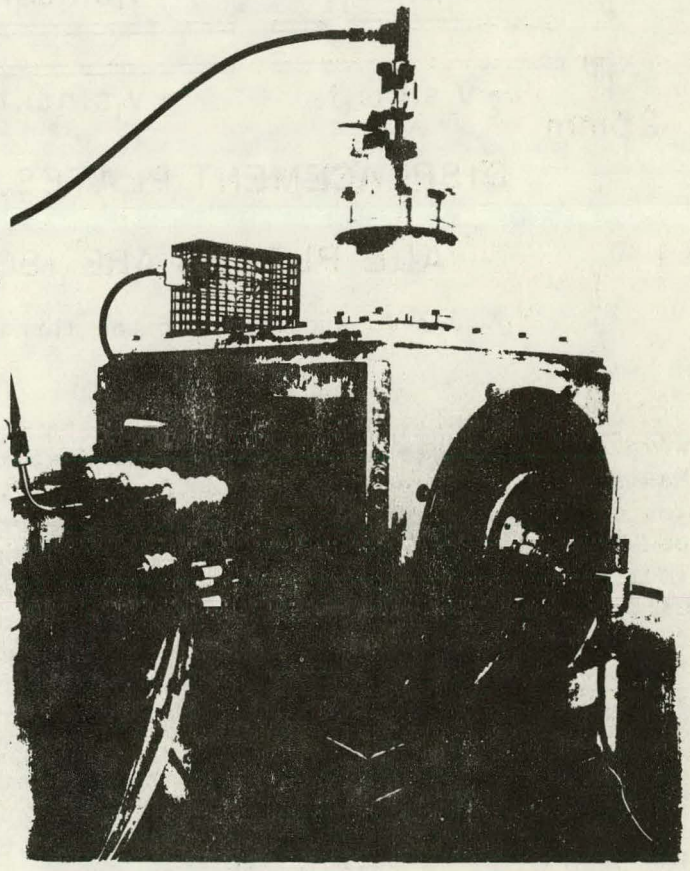

Fig. 8.3-3. External view of development source showing feed throughs, cesium oven, and sputter target positioner.

B. Emittance Monitor

We have built an emittance monitor for the test sputter ion source following the ideas of Billen.[4] The device uses three sets of electric deflection plates as indicated in Fig. 8.3-4. The first two sets are connected to produce a net displacement of the ion beam, which then passes through a small round hole into the third set. The third set deflects this beam which then passes through a slot. Thus the beam emerging from the slit corresponds to a certain value of the divergence angle (x') and a certain value of the displacement from the center (x) of the initial beam. This beam emerging from the slit is collected in a Faraday cup.

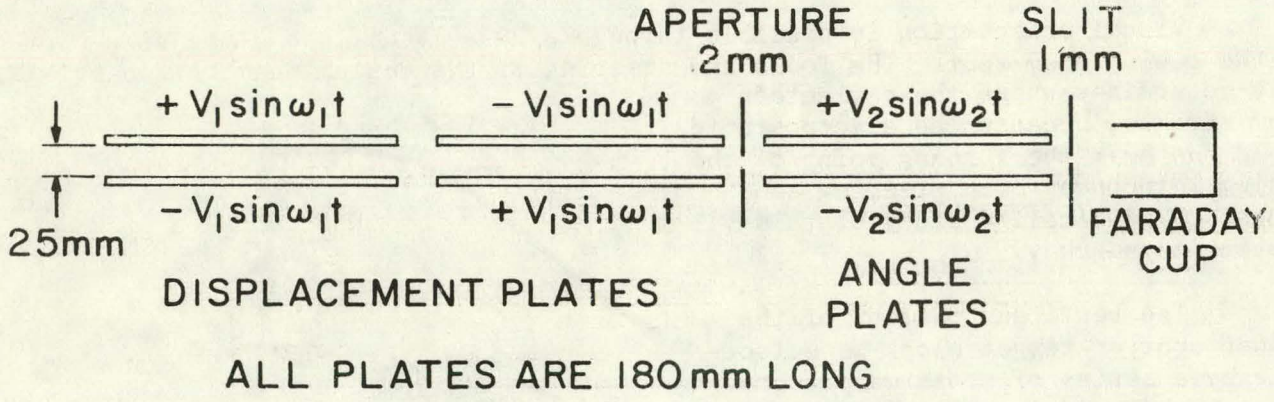

Fig. 8.3-4. A diagram of the three sets of deflection plates

The position displacing plates are presently excited with a 60 Hz sine wave and the angle bending plates are excited by a sine wave of about 800 Hz. Maximum voltage swing is from -700 to 700 V, and the amplitude is adjustable. The current from the Faraday cup is converted to a voltage and amplified by a preamp with a maximum useful gain of 1 V/nA, and a bandwidth of around 10 kHz. Thus the current from the Faraday cup has a modulation of 120 and 1600 Hz. (Some care had to be exercise in the construction of this amplifier to minimize 60 cycle pickup. Presently the pickup responds to substantially less than 1 nA.) The preamp output is run into a peak detector and a discriminator which fires at a preset fraction, f, of the peak amplitude.

Signals proportional to the deflecting plate voltages are connected to the X and Y inputs of an oscilloscope. Thus the coordinates of the spot on the screen at any instant are proportional to the (x,x') values of the part of the ion beam which is reaching the Faraday cup. The discriminator output is used to operate the oscilloscope intensity. It brightens the part of the screen cor-

responding to all values of (x,x') for which the ion current exceeds f times the peak intensity. Thus the border of the bright region is the contour of constant f in the (x,x') plane. By taking pictures at various values of f, the emittance figure I(x,x') may be determined. A block diagram of the system is given in Fig. 8.3-5 and a sample oscilloscope picture appears in Fig. 8.3-6. The intensified area corresponds to 60% of a 35 keV $^{12}C^-$ beam with a normalized emittance of 4.7 mm-mrad-MeV$^{1/2}$.

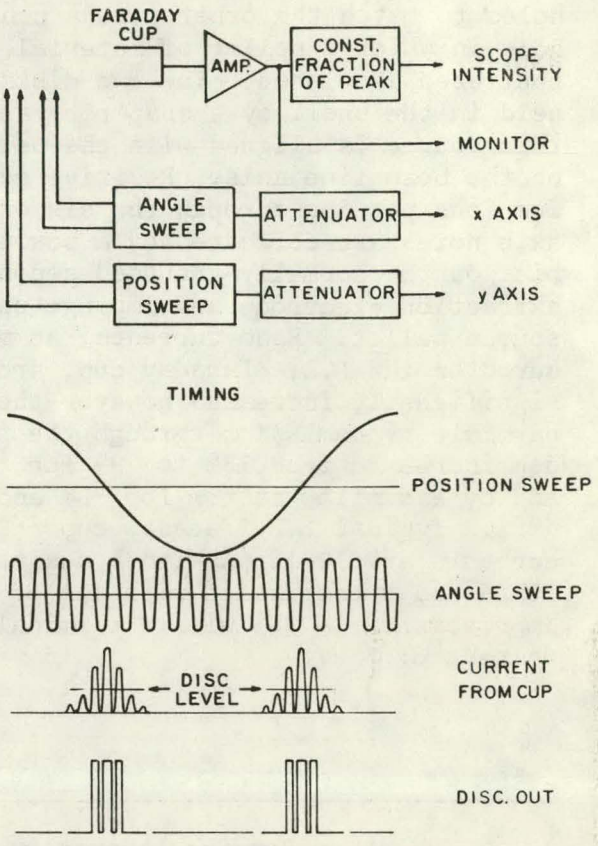

Fig. 8.3-5. Block diagram of detection and sweep electronics with timing diagram showing modulation of beam by sinusoidal sweep voltages

We expect this device to be particularly useful in testing various ion source modifications, because it will enable us to untangle the effects of different focusing fields on the shape of the emittance figure as well as on the emittance area or on the beam diameter.

C. UNIS Development

The UNIS sputter ion source, which is installed on the accelerator, has been modified in the past year to increase its performance and reliability.[5] Initially the source required maintenance every 120 hrs because of high decel electrode currents. The decel electrode provides a potential barrier to prevent negative ions formed at the sputter cone from being accelerated to the ionizer. These backstreaming ions sputter a hole in the ionizer causing the source to be inundated with cesium. A split ionizer mount was designed, built, and installed. It enables ready access to the decel insulator for cleaning without having to completely disassemble the source. Sputtered conducting materials was also found to be plated across the insulator surface. A shield was installed and the source has run 400 hours without maintenance.

A new extraction power supply has replaced the oil bath power supply. The new supply purchased from Spellman High-Voltage Electronics Corporation has a ripple of less than 0.01% measured during typical operation as compared to 0.2% of the old supply. The horizontal jitter previously observed on a beam profile scanner located near the tandem entrance is completely gone.

The finial improvement in the UNIS was the development of a reflected cesium beam. Two tantalum disks are fitted into a stainless steel shell whose dimensions match the standard cone shape. The upstream disk has six 2.4 mm diameter holes are placed on a 5.5 mm diameter. The downstream disk has six

holes to match the other plus a center hole in which a pellet of material to be sputtered is placed. The two disks are held in the shell by a snap ring and this source is aligned with the pellet on the beam line axis. Positive cesium ions passing through the six off axis holes are reflected by a positive bias on the normally grounded secondary extraction electrode and impinge upon the source pellet. Beam currents, as measured on the L.E. Faraday cup, are not significantly increased however the particle transmission through the tandem increased from 15% to 29% for ^{12}C and by a similar factor for ^{9}Be and ^{28}Si. Typical L.E. Faraday cup ^{12}C currents are 10-15 μA with a maximum of 20 μA and transmission with all of these improvements is 39% with a terminal voltage of 7 MV.

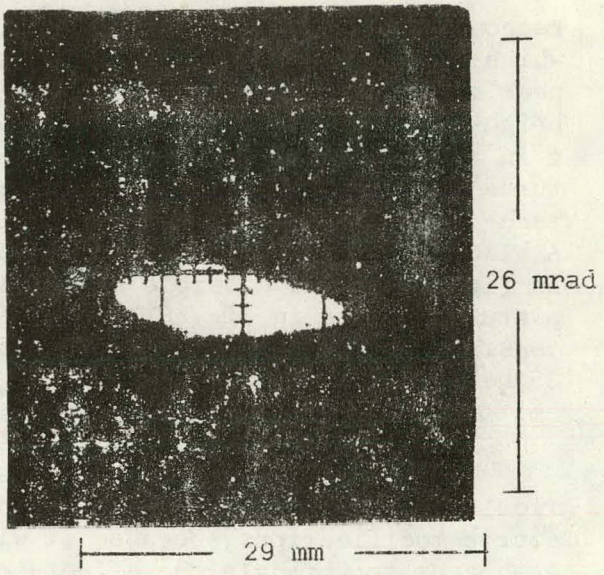

Fig. 8.3-6. Sample picture from oscilloscope showing region of (x,x') space where the beam intensity exceeds a selected fraction, 60% in this case, of the peak intensity with slits and Faraday cup.

1. Nuclear Physics Laboratory Annual Report, University of Washington (1978), p. 115.
2. Nuclear Physics Laboratory Annual Report, University of Washington (1975), p. 23.
3. K. Brand, Pevue de Physique Appliques 12, October 1977, p. 1453.
4. J.H. Billen, Rev. Sci. Instrum., 46, Jan. 1975, p. 33.
5. Nuclear Physics Laboratory Annual Report, University of Washington (1976), p. 26.

8.4 Accelerator Radiochronology

G.W. Farwell, T.P. Schaad, F.H. Schmidt, and M.-Y.B. Tsang, Nuclear Physics Laboratory, and P.M. Grootes, Geological Sciences Department and Quaternary Research Center

We began using our Van de Graaff accelerator for determination of small isotopic ratios of interest for purposes of dating in mid-1977. The work has continued at an accelerated pace. Funding for this program is derived partly from the D.O.E. contract, and partly from grants from the University of Washington Graduate School Research Fund ($16,000 to date).

The studies have concentrated so far on the technical problems associated with detection of ^{14}C and ^{10}Be. The isotopic ratios of interest for these radionuclides range from 10^{-16} to 10^{-12} for $^{14}C/^{12}C$, and from 10^{-12} to 10^{-8} (terrestial materials) or 10^{-7} (meteoritic and lunar materials) for $^{10}Be/^{9}Be$. These ratios encompass ages of approximately zero to 75 thousand years and zero to 20 million years for carbon and beryllium, respectively.

During the past year we have succeeded in stabilizing various components of the accelerator, and in detecting both ^{14}C and ^{10}Be within the isotopic ranges indicated. However, we have not yet achieved a wholly satisfactory means for normalizing the data to establish accurate ages. With improvements to be incorporated in a new sputter ion source and inflection system, we expect that this difficulty will be overcome.

The most serious problem encountered with this accelerator technique is unwanted background ions which are spuriously accelerated and find their way into the detector systems. We have identified the principal such background ions, and in most cases have found their origins. For both ^{14}C and ^{10}Be, we have developed adequate techniques either to eliminate these unwanted ions or to reduce their intensities to an acceptable level.

One very effective technique makes use of a (second) stripper foil placed approximately at the image slits of the 90° analyzing magnet, which serve also as the object slits for the switching magnet (30° deflection) which follows. In the case of ^{14}C, a thin carbon foil (20 $\mu g/cm^2$) strips the desired $^{14}C^{+4}$ ions largely to charge state +6; it also strips the contaminant ^{13}C and ^{12}C ions having the same magnetic rigidity. Analysis by the switching magnet, which is then set for $^{14}C^{+6}$, eliminates the ^{12}C and ^{13}C ion groups of highest intensity. In the case of ^{10}Be, a similar arrangement (though with a thicker second stripper foil: carbon, 1,000 $\mu g/cm^2$) entirely eliminates the very strong $^{10}B^{+3}$ contaminant in the $^{10}Be^{+3}$ ion beam. This is accomplished partly by stripping the ^{10}B largely to +5 and partly by differential energy degradation (^{10}B loses more energy in the stripper than ^{10}Be); the ^{10}B is removed by magnetic analysis in the switching magnet, which is set for $^{10}Be^{+4}$.

We have also very substantially reduced the ^{13}C and ^{12}C contaminants in the ^{14}C beam by improving the vacuum in both the sputter ion source and the accelerating tubes, and by developing improved sources for carbon ions; the consequent reduction in the mass-14 contaminants inflected and accelerated (CH_2^- for ^{12}C and CH^- for ^{13}C) has been an important accomplishment. Some related developments are reported in Sections 8.3 and 9.2 of this report.

$^{14}C/^{12}C$ ratios have been measured for contemporary and near-contemporary carbon and for graphite; measurements are continuing on various samples with ages known by tree-ring selection or by beta-counting in the Quaternary Isotope Laboratory, and on undated samples. The measurements on graphite yield an equivalent "age background" for the Van de Graaff system of at least forty-five thousand years. $^{10}Be/^{9}Be$ ratios in the range of 10^{-11} to 10^{-13} have been measured for commercially available beryllium; we are now working with materials

enriched in ^{10}Be, in order to provide a range of standards, and with unknowns from ocean sediments, sea water, and other sources in nature.

Contemplated future improvements include an intermediate-focus two-magnet inflection system, a velocity filter for final beam cleanup, and an automated multiple-ion switching device to facilitate continuous monitoring of ion-source yields. We expect to be able to resolve neighboring isotopic species up to mass 100 or greater.

At the University of Washington there are strong ongoing research programs in field such as atmospheric sciences, oceanography, geology, geophysics, and Quaternary studies. We are already working on radiometric dating problems with faculty in some of these fields and expect an even broader collaboration to develop during the next several years.

---

1. "Accelerator Dating and ^{14}C Enrichment Program at the University of Washington," by G.W. Farwell, T.P. Schaad, F.H. Schmidt, and M.-Y.B. Tsang (Nuclear Physics Laboratory) and P.M. Grootes and M. Stuiver (Quaternary Isotope Laboratory), University of Washington; accepted for presentation at the Tenth International Radiocarbon Conference, Bern and Heidelberg, August 19-26, 1979.
2. "An Effective Reflection-Type Geometry for Sputter Ion Sources," by F.H. Schmidt and G.W. Farwell, BAPS 24, 650 (1979).

8.5 Cyclotron Operations and Development

H. Fauska, B.L. Lewellen, G.E. Saling, P.W. Wiest, and W.G. Weitkamp

After a lull in cyclotron operations caused by the interruption of fast neutron cancer therapy patient treatment in August 1977, the cyclotron is again running on a relatively full schedule 40 hours per week. This is the result of the resumption of cancer therapy treatment. Articles describing the therapy program as well as other activities at the cyclotron are contained in Sections 7.4-7.11 of this Annual Report. Statistics of cyclotron operations are given in Table 8.5-1.

Table 8.5-1

STATISTICS OF CYCLOTRON OPERATIONS
From April 16, 1978 to April 15, 1979

		Time (hrs)	Percent
1.	Division of time among activities		
	Normal operation	603	75
	Scheduled maintenance	102	13
	Unscheduled maintenance	95	12
		800	100
2.	Division of beam time among projectiles		
	Deuterons	113	77
	Alpha particles	20	14
	Protons	14	9
		147	100
3.	Division of normal operating time among users		
	University of Washington Nuclear Medicine	383	63
	University of Washington Cancer Therapy Group	76	13
	University of Washington Radiation Biology	69	11
	University of Washington Nuclear Physics Laboratory	51	9
	Boeing Radiation Effects Laboratory	10	2
	University of Washington Nuclear Pharmacy	8	1
	Battelle Northwest Laboratory	4	1
	Oregon State University	3	1
		603	100

To support this renewed activity, several modifications to the cyclotron are underway. A 250 V - 200 A power supply to replace the aged (1950) motor generator set supplying current to the main magnet has been purchased and installation has begun. A programmable controller has been purchased to replace a substantial part of the wiring and relay networks controlling the cyclotron. This system will be installed as soon as the operating schedule permits.

9. INSTRUMENTATION AND EXPERIMENTAL TECHNIQUE

9.1 Design of a Momentum Filter/Spectrograph

K.J. Davis, D.W. Storm, and T.A. Trainor

A. Introduction

We have submitted a proposal for funds to build a new kind of magnet system which serves a dual function in particle detection. The design is isochronous and has a relatively large solid angle (20 msr) and energy acceptance ($E_{max}/E_{min} > 1.6$). Our main interest is to remove unwanted high-intensity particle groups which can cause pile up or otherwise impose rate limitations on singles or coincidence experiments. In this mode of operation we call the system a "momentum filter," and the overall energy resolution is determined by a charged particle detector. For example, in heavy ion reactions the device could remove elastically scattered particles or particles of some species that has a different momentum but similar kinetic energy to another species of interest. The system can also be used for studying reactions at 0°. This primary function would be accomplished by dispersing the particles entering the device across a system of blocking pins or slit jaws at an intermediate focus, and then recombining the transmitted particles at an achromatic focus on a solid state detector or detector telescope. This scheme has the great advantage of collecting particles using a large solid angle of acceptance, while transporting them a relatively large distance to a small high resolution detector. The device is particularly suited to time-of-flight measurements since, for a given rigidity, the orbits are isochronous. The solid angle for detecting background particles, especially neutrons or photons, is much smaller than that for detecting the particles of interest. In addition, because of the double bend system that we are proposing, substantial shielding can be introduced between the target and the detector to further suppress background counts. Also, because of the double imaging, a large rejection ratio can be achieved for 0° experiments. Finally, the fact that the particles are collected over a large solid angle but have a long flight path greatly enhances the sensitivity of time of flight measurements.

In its secondary function, the device becomes a magnetic spectrograph when a position sensitive detector (for example a multi-wire proportional chamber) is placed at the dispersed focus. The resolution is only moderate, because this is not intended as the primary function of the system (which is several times cheaper than a high resolution spectrograph). However, a momentum resolving power of better than 1100 would be achieved when the solid angle of acceptance is restricted to about 2 msr. With the maximum solid angle of 20 msr, a resolving power of about 150 would result. In a combined mode of operation one can use a polarimeter at the achromatic focus, taking advantage of the recombination of particles whose energy was selected at the dispersed focus by a slit. This permits use of a polarimeter optimized for efficiency at the expense of energy resolution.

In the following text we present our design criteria, followed by a description of a magnet system that meets those criteria. In the third section

we present construction plans, followed by a review of the present status of the project. We are greatly indebted to Professor Harold A. Enge, who has worked closely with us on the development of this system.

B. Design Criteria

The proposed momentum filter should have the following seven properties:

1) An achromatic focused spot is required at the final detector position, with small magnification, so the image of the target beam spot will appear within the area of an ordinary solid state detector. In the case of near unit magnification, with the typical one mm spot on target, the size of the spot at the detector will be primarily determined by the second order aberrations. The smaller the spot size the better, since the background rate is proportional to the detector size.

2) The device should be isochronous in the sense that, for a particular momentum, the time for a particle to traverse the apparatus should be independent (to first order) of the origin and angle of the particle trajectory. The transit time will depend on momentum because both the velocity and path length will.

3) The solid angle accepted by the system should be as large as possible. In particular, 10 to 20 msr appears to be a reasonable goal. Considerable deterioration of resolving power is expected when using maximum solid angle, and is acceptable. The phase space acceptance figure of the system should be such that solid angle acceptance is nearly constant over a target spot size of a few millimeters. The optics should permit the limiting trajectories to be removed by well designed baffles, in order to eliminate contamination of spectra by particles grazing the vacuum chamber walls.

4) The accepted energy range should be large. A ratio of Emax/Emin of about 2 is desirable.

5) The dispersion at the intermediate focal plane should be small enough that a broad range of momenta can be detected by a reasonable position-sensitive detector. At the same time reasonable momentum resolution is desired.

A resolving power of 1000 is acceptable for small solid angle acceptance and 100 would be tolerable with the maximum solid angle.

6) Correction for kinematic broadening should be possible by moving the dispersed focal plane.[1]

7) It is desirable to be able to operate at scattering angles of 0 to as near 180 degrees as possible, with the possibility of passing through 0 degrees. The device should be mechanically compact, while allowing room for shielding between the final achromatic focus and the target.

C. Design

In the beginning of this section we present the reasoning that led to the design that we have adopted. An outline of the mechanical details appears at the end.

In order to achieve a dispersed focus in the bending plane, followed by an achromatic double focus, at least two bends are required. Furthermore, if the system is symmetric about the dispersed focal plane, the final focus will necessarily be achromatic and, in addition, will have unit magnification (although the size of the image spot will exceed that of the target spot because of aberrations). However, in order for the symmetry to be complete, the dispersed focal plane must be perpendicular to central rays of all momenta, as indicated in Fig. 9.1-1. Otherwise chromatic aberrations at the final focus will be severe when the system is used to collect ions with a large momentum range. Finally, in a system with such symmetry, isochronism (as we have defined it) is automatic.[2]

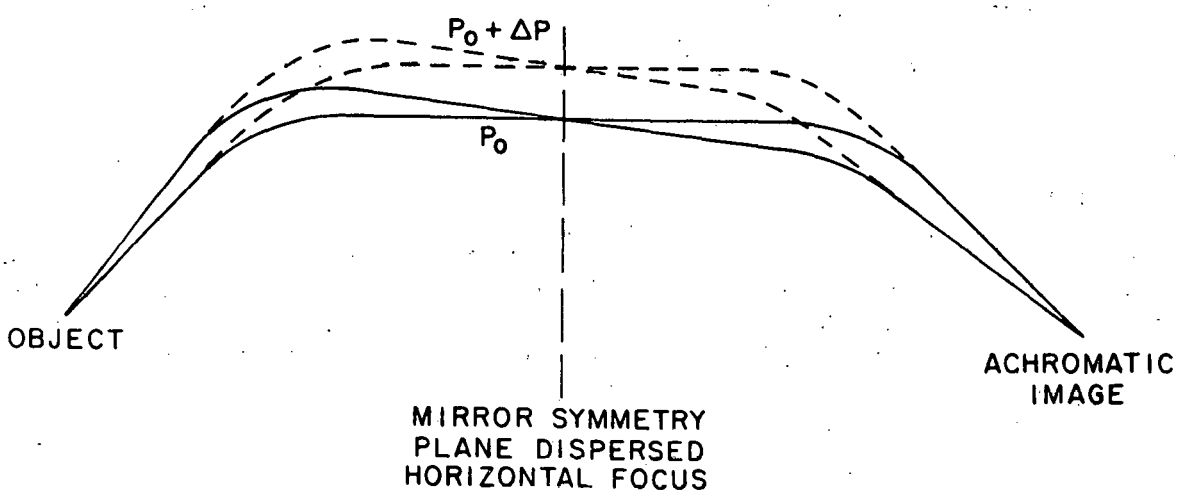

Fig. 9.1-1. A schematic indication of a symmetric two bend system, which has a dispersed focus at a plane perpendicular to the central ray. By symmetry, the second spot is achromatic and has unit magnification. If the dispersed focal plane is rotated, the final spot may be non-dispersed, but different momenta will be focused different distances from the final magnet.

In order to obtain a reasonable solid angle the first element should be a vertically focusing quadrupole singlet, followed by a dipole magnet supplying horizontal focusing and momentum dispersion in the horizontal plane.[1] This choice of bending in the horizontal plane permits adjustment of the focal plane slits or detector to correct for kinematic broadening, if the scattering plane is also horizontal. Such a pair of magnets alone generally has a large dispersion at the focal plane when used with small object distance (as required for large solid angle). Furthermore, it is generally impossible for the focal plane

to be perpendicular to central rays of all momenta, at least for ordinary dipole magnets. As suggested to us by Enge, addition of a horizontally focusing quadrupole after the dipole will bring the focal plane closer and decrease the dispersion. Its parameters can be chosen to make central rays of all momenta parallel to one another, since it bends toward the central momentum ray the off momentum rays that were initially on axis but were dispersed and are diverging after leaving the dipole (see Fig. 9.1-1). In general the focal plane will not be perpendicular to these central rays, so a sextupole element must be added to correct this chromatic aberration.[3] In the present system the sextupole will be incorporated in the second quadrupole. However the option remains of having a separate sextupole magnet near the second quadrupole.

The system is shown in Fig. 9.1-2 with a ray diagram from the target to the mirror symmetry plane, and the magnet parameters are listed in Table 9.1-1.

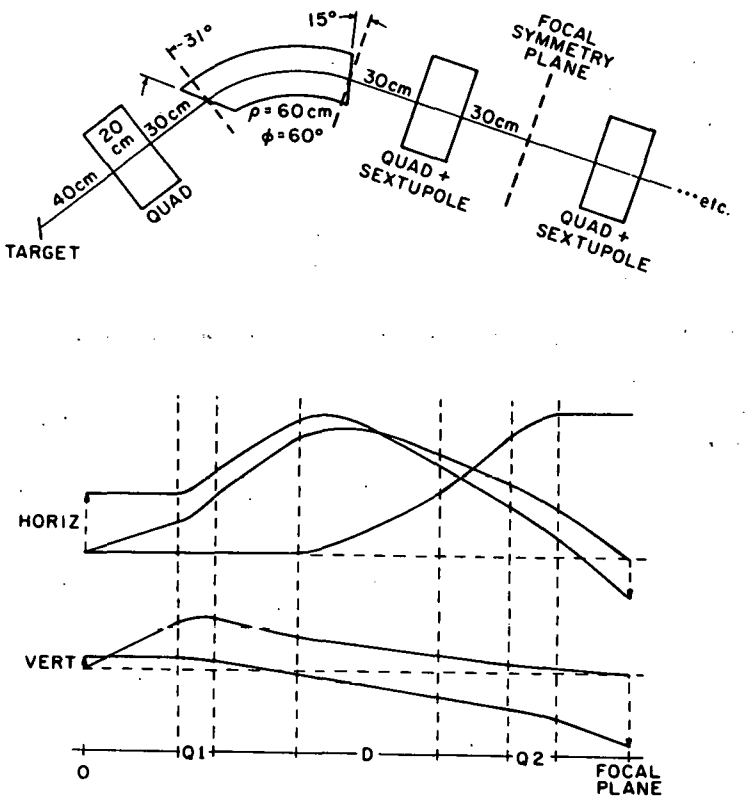

Fig. 9.1-2. Layout and ray diagram for half the proposed (symmetric) system. The layout is to scale. The ray diagram shows three principal rays with the following initial conditions:

x_o	x_o	p/p_o
0	1	0
0	0	1
1	0	0

The vertical scale is different from each ray, and the rays are not intended to indicate limiting rays.

Table 9.1-1. Magnet parameters for the system of Fig. 9.1-2
Fields are for K=25 MeV-Amu
(p/Z = 23 GeV/c)

Q1 and Q4:	
Length	20 cm
Bore	10 cm (diameter)
Gradient	1.2 kg/cm (vertical focusing)
D1 and D2:	
Gap Height	5 cm
Gap Width	25 cm
Edge Angles	31.1 deg
	-15.0 deg
Radius of Curvature	60.0 cm
Bending Angle	60.0 deg
Field	12.8 Kg
Q2 and Q3:	
Length	20 cm
Bore	20 cm (diameter)
Gradient	0.54 kg/cm (horizontal focusing)
Sextupole Admixture	22.2 g/cm^2

Table 9.1-2. Properties of beam when focused at the mirror symmetry plane as predicted to second order by TRANSPORT

Magnification, horizontal	0.395
vertical	6.13
Dispersion	7 mm/percent
First order resolving power (1.0 mm spot)	1750
Second order resolving power (1.0 mm spot)	
Solid angle 20 msr	150
2 msr	1100
Focal plane length for Emax//Emin = 2.0	25 cm
Maximum solid angle	20 msr

The second order beam optics program TRANSPORT[4] predicts a double focus at the mirror plane with the focal distance independent of momentum. The beam properties at this plane are summarized in Table 9.1-2. We conclude that this system meets the requirements set in the previous section satisfactorily.

From the first order ray trace (Fig. 9.1-2) we can determine the expected angular acceptance for various points on the target spot. The resulting values for the spot center are 65 mr in the horizontal plane and 100 mr in the vertical plane, at the central momentum (half angle values). The limits are at the exit and entrance of the first quadrupole respectively. For particles deviating from the central momentum by over 6.3% the second quadrupole becomes a limiting aperture. A 50% reduction in angular acceptance results for momenta 11% different from the central value. Thus, E_{max}/E_{min} is 1.6 for 50% transmission limits. Transmission vs. momentum deviation is given in Fig. 9.1-3.

The first order calculation indicates that correction for kinematic broadening can be accomplished by moving the intermediate focal plane detector by (30 cm)x(1/P)(dP/θ), where dP/θ is the momentum change per radian for a particle group from a particular nuclear energy level. (Kinematic broadening doesn't affect the final focus, of course, since it is achromatic.) Shifts of 20 cm are planned. If (1/P)(dP/θ) is 0.5, for example, the spot width at the symmetry plane would be 4.5 cm due to kinematic broadening with the full 20 msr acceptance. This figure can be compared to the monoenergetic spot width (to second order) of less than 1 cm.

The magnets involved are relatively simple to fabricate. The 10 cm bore quadrupoles (Q1 and Q4) can be purchased "off the shelf" with cylindrical pole tips. The dipoles have flat entrance and exit faces with a 5 cm uniform gap and about 4.2 x 103 square cm of uniform field. Final adjustment of these magnets is planned using field clamps mounted near the entrance and exit faces. The third magnet will be built like a quadrupole, but with two different pole radii used to produce a sextupole field component.[5] Since the vertical size of the beam is small at this magnet (about 5 mm) this field will be adequate for the vertical optics.

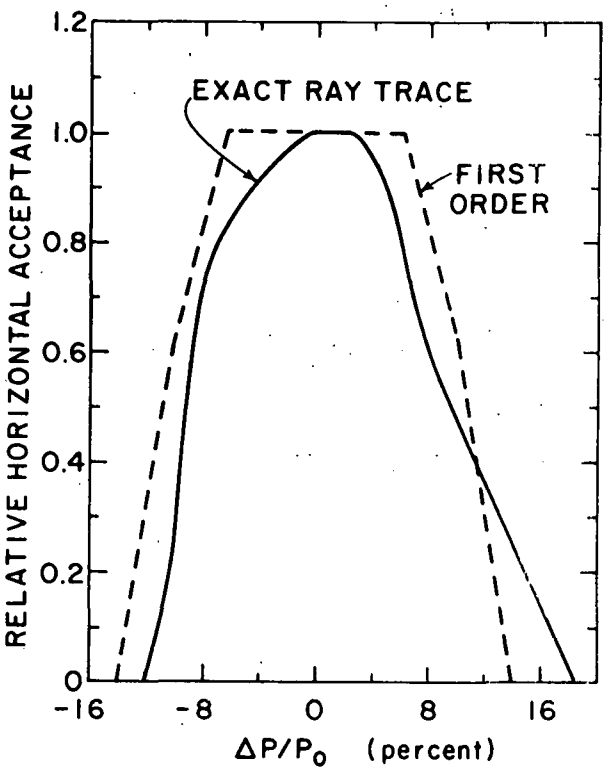

Fig. 9.1-3. Transmission of the ± 65 mr accepted by the first quadrupole through the remainder of the system, as a function of momentum. First order calculation and the results obtained using the M.I.T. ray tracing program are indicated.

The vacuum system should be clean and maintain a low pressure especially in the first half of the system. If charge changing collisions occur between residual gas atoms and ions of an intense group that is to be blocked at the focal plane, those ions will follow peculiar trajectories and may appear as background at the detector. We have chosen a cryopumping system, using two commercially manufactured cryopumps. One will be located at the target chamber and the other at the region of the dispersed focus. These pumps should yield pressures of 2×10^{-7} Torr in the region of the first dipole magnet and 5×10^{-7} Torr at the detector chamber. These vacuum figures are based on outgassing estimates and are mainly limited by the conductance of the system to the pumps. Oil diffusion pumps were the other candidates considered. With associated liquid nitrogen baffles they are about 3/4 as expensive as the cryopumps, and they would not produce as clean a vacuum. Ion pumps of smaller pumping speed are more expensive than cryopumps and are more difficult to operate with a system that will be opened often.

The scattering chamber that we plan for the initial installation will be extremely simple, with a small metal tape seal at the beam entrance permitting rotation of the chamber with the magnetic device through the polar angle about the beam.

D. Construction Plans

The magnets are to be purchased from commercial manufacturers. Estimated delivery times are 4 to 6 months. The table for rotating the system is already installed on a beam line in the experimental area, so the main construction to be done at the NPL will involve building vacuum apparatus and a support frame. This vacuum apparatus includes a very simple scattering chamber with sliding tape seal, as well as a box with motion feed throughs to adjust the slits. We plan to complete detailed design and construction of the vacuum system and support framework during the magnet construction period. Final assembly and testing should take 3 months. Thus we anticipate completion of the device in 9 months after placing orders.

E. Present Status

At the present time our efforts are directed toward detailed beam optics computations which we will use to determine the final configuration of the system before ordering magnets. To perform these studies we have obtained a ray-trace program[6,7] from M.I.T. which we have adapted to the PDP 11/60. This program carries out numerical integration of the particle trajectories through realistically parameterized magnetic fields. The results obtained so far give the final spot sizes in the horizontal plane direction from a point object at the target position as illustrated in Fig. 9.1-4. Since the actual object will be one mm diameter, with a first order image 0.4 mm (horizontal) by 6 mm (vertical) at the first focal plane, point object calculations give the main flavor of the system. The momentum resolving power at the central momentum is shown in Fig. 9.1-5, where the line shape is given for various solid angles. Finally in Fig. 9.1-6 the momentum resolving powers are illustrated as a function of momentum for large and small solid angles. These results are by no means intended as final, but are presented to illustrate the type of computations that we are

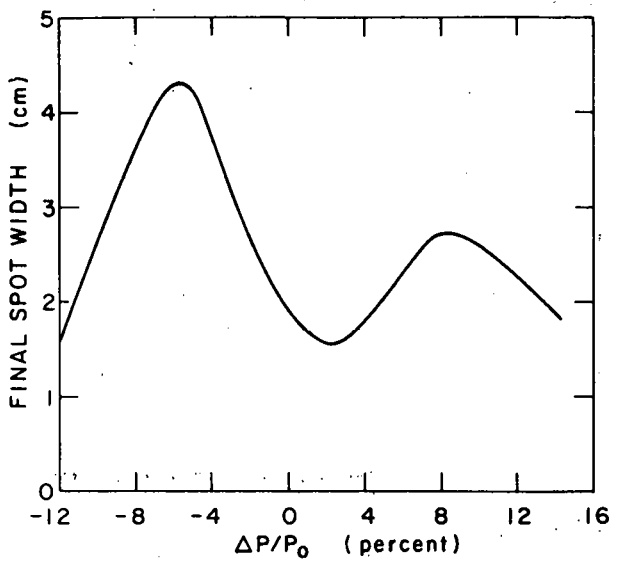

Fig. 9.1-4. Spot sizes in the horizontal direction at the final detector for maximum solid angle, assuming a point object. A perfect image of the 1 mm diameter object would also be one mm diameter.

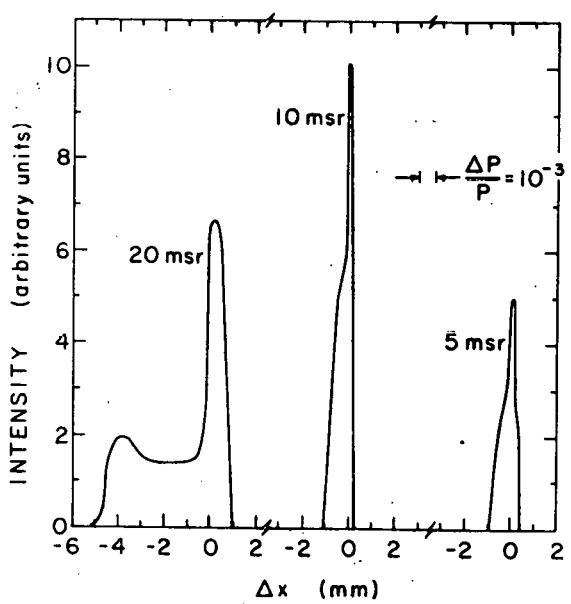

Fig. 9.1-5. Line shape of a monoenergetic group at the central momentum for various solid angles of acceptance. The dispersion, 7 mm/%, is illustrated.

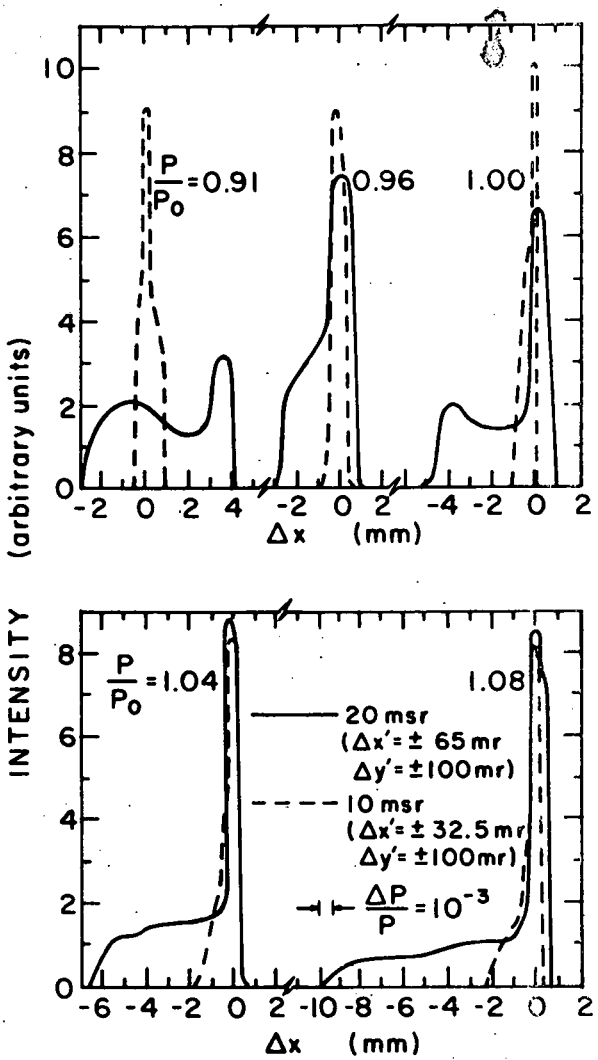

Fig. 9.1-6. Line shape of monoenergetic groups with various values of momentum P normalized to the central momentum Po. Two solid angles of acceptance are illustrated, 20 msr, the maximum and 10 msr, where the resolution is substantially higher. The dispersion, 7 mm/%, is illustrated.

carrying out. It is encouraging, however, that without yet making any changes from the parameters suggested by Enge, these detailed calculations support the results predicted by the second order TRANSPORT calculations.

1. H.A. Enge, Rev. Sci. Instru. 29, 885 (1958).
2. K.G. Steffen, High Energy Beam Optics, Interscience, 1965, p. 126. The third of Eq. 3-27 is not satisfied, but this merely means that trajectories with different momenta will have different path lengths.
3. N.M. King, CERN MPS/EP-26 (1962).
4. K.H. Brown, TRANSPORT, SLAC-75 (1967).
5. M.L. Good, Proc. LRL Instrum. Conf. (1960) p. 34; also Enge (private communication).
6. J.E. Spencer and H.A. Enge, Nucl. Instru. and Meth. 49, 181 (1967).
7. S. Kowalski, private communication.

9.2 Target Preparation

G.M. Hinn

This report covers the period from November 20, 1978 to April 1, 1979. Reconstruction of an "axial type electron gun" for making refractory material targets has been completed. Two are now in use, one in the beryllium evaporator in the hot lab and the other in the CVC evaporator in the target lab.

Targets from a few $\mu g/cm^2$ to several hundred $\mu g/cm^2$ have been produced so far and include ^{208}Pb, ^{39}K, ^{6}Li, $^{6}LiO_2$, $^{28}SiO_2$, ^{166}Er, and ^{24}Mg.

Beryllium has been evaporated onto tantalium buttons by the reduction of BeO with magnesium metal for accelerator dating purposes.

9.3 Large Solid Angle Gas Detector for the Magnetic Spectrograph

R.J. Puigh, Y-D. Chan, W. Lynch, and M.B. Tsang

In last year's annual report we described the results from testing a prototype position sensitive proportional counter for the magnetic spectrograph.[1] This prototype counter depended upon charge division for the position signal and we found the position resolution for ^{16}O ions to be 1.2 mm. The counter was not satisfactory since it had a relatively small solid angle and it only spanned a small range along the focal plane. We therefore built a larger version of this detector, shown schematically in Fig. 9.3-1. The vertical acceptance of this counter is 5 cm which is the largest vertical acceptance allowed by the pole tip separation (3 cm). Also the length of the detection region along the focal plane is 57 cm which now allows the possibility of detecting more than one charge state for a given heavy ion reaction at one time. These changes in the counter's design were made to reduce the experimental beam time needed to accumulate sufficient data.

The initial design of the electrode assembly for this counter is very similar to the design in Ref. 2. The differences in the design were a much larger separation of 7.3 cm between the cathode and anodes for our counter and only one resistive wire (980 Ω/m) was used to give position information. As in Ref. 2 the grid closest to the cathode was capacitively coupled to the cathode to yield total energy loss information and the top grid was held at ground potential and acted as a Frish grid.

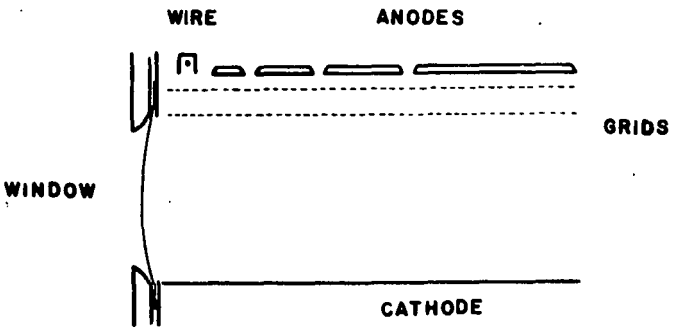

Fig. 9.3-1. Schematic of gas counter

In the initial testing of this counter we discovered a serious problem with the position information. Both the position and position resolution of the counter depended upon the distance of the ionizing particles' path above the cathode. In particular for any given heavy ion having a specific Bp value, the position resolution became worse as the particle's path came closer to the cathode. Also the centroid of the position peak shifted by 4 mm for 40 MeV ^{16}O elastic scattering from Au as a function of the ^{16}O ion path height above the cathode. We feel these results indicated that the position wire signal originated from different parts of the ionization track depending upon the track's vertical height above the cathode.

To minimize these effects we altered the electrode geometry in the manner shown schematically in Fig. 9.3-2. We placed the cathode along the median plane defined by the magnet pole tips and placed grids and collection anodes symmetrically above and below the cathode. This geometry reduces the effective solid angle by 2%, and the separation between the cathode and the anodes or wire has been reduced to 2.9 cm. This new geometry has eliminated the problems we had with the geometry shown in Fig. 9.3-1 and for 40 MeV ^{16}O ions elastically scattered from a 0.6 mm wide strip Au target the total position resolution was 1.75 mm (fwhm). This resolution was measured for the following operating voltages: +600 V on the wire, -100 V on the cathode, + 200 V on the anodes, and -15 V on the grid closest to the cathode.

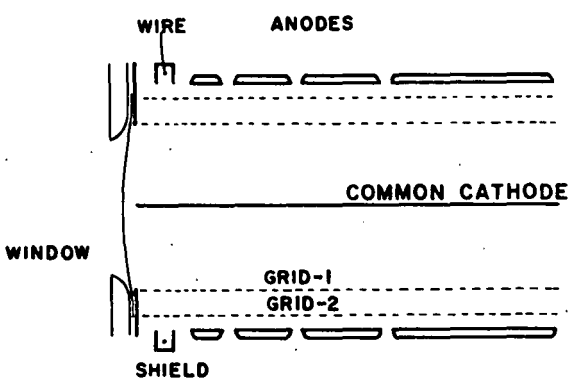

Reversely stacked gas focal plane counter

Fig. 9.3-2. Schematic of latest version of electrode assembly

At this point we are working to obtain signals from the anodes and cathode. We do observe signals from the cathode but the energy resolution is very poor. Because of the large size associated with the counter the noise due to capactive pick up was worse than in the prototype model, and

this counter is more sensitive to vibrations. We are currently working to resolve these problems which we feel are related to the electrode geometry.

---

1. Nuclear Physics Laboratory Annual Report, University of Washington (1978), p. 126.
2. J.R. Erskine, T.H. Braid, and J.C. Stoltzfus, Nucl. Instr. and Meth. 135, 67 (1976).

9.4 Design and Construction of Electronic Equipment

M. Bizak, H. Fauska, and R.E. Stowell

The frequent maintenance required by the old Victoreen analog-to-digital-converters on our on-line computer led us to build a simple interface to handle the new Northern Scientific analog-to-digital-converters, which are awaiting installation on our new on-line computer (see section 10.1 of this report). The interface allows the use of four ADC's in either single or multi-coincidence mode. Timing in the new interface permits multi-coincidence mode use in groups with two older Northern Scientific ADC's on the computer. As a result, we now have hardware facilities to provide up to six parameter multi-coincidence mode of operation. Sixteen-way routing of the individual ADC's has also been added.

The new scalers described in our 1978 Annual Report (p. 125) are in the final stages of construction. The prototype unit performed well within the specifications described. Difficulty in procurement of parts has resulted in construction delays. We will have 32 scalers of 10 digits each with computer readout or readin. All scalers can be sampled in one microsecond. The scalers have an upper count rate of 75 megahertz and will accept either fast or slow NIM logic level pulses.

The need for very reproducible switching magnet fields required us to install a nuclear magnetic resonance system in the magnetic field. The system uses a Cyclotron Corporation bridge type probe, which was purchased. We constructed the power supply, buffer amplifier, and field sweep circuit. The system also incorporates a stable signal generator and frequency meter.

The analyzing magnet nuclear magnetic resonance regulator system, which has been in use for several years, was in need of redesign to provide easier and more rapid setup. The new circuit has been designed and constructed. We hope to install the new chassis in the near future.

Work on the accelerator terminal regulator, which uses either slit derived error signals or generating voltmeter signals, has been continuing. The following items have been constructed. Optoisolated logarithmic preamplifiers, designed at Chalk River Laboratory which provide error signals from the image slits has been completed. Elimination of common ground loop problems is expected

to improve our regulation of the terminal voltage. The multiplex changing from slit regulation to generating voltmeter regulation has been designed and is nearing completion.

The new control handling provides either image slit control, generating voltmeter control, or the multiplexed operation described earlier. The control source selection provides signals to both corona regulator and the terminal derippler system.

A stepping motor control was designed and constructed to provide manual or computer control of stepping rate and direction for general Laboratory use. The design includes single stepping or stepping from an internal variable rate pulser.

The modification and installation of a continuous digital reading gaussmeter on our ion source bending magnet has been completed. The probe was purchased from Rawson; the digital readout is our design.

A new up-charge supply for the Van de Graaff charging belt has been installed and remote controls completed.

The design and construction of a diagnostic generator and gating device to speed up testing and repair of the Nuclear Data 2400 systems has been completed.

9.5 A Polarimeter for Measuring the Depolarization Parameter in Inelastic Scattering

W. Bartholet, H.C. Bhang, S.K. Lamoreaux, T.A. Trainor, and W.G. Weitkamp

A polarimeter has been designed, constructed and tested to measure the depolarization parameter for proton inelastic scattering to states in the continuum. This new polarimeter is based upon tests of a prototype described previously (ref. 1).

The depolarization parameter is measured by scattering a beam of polarized protons from a target and measuring the polarization of the outgoing protons with a second scattering. To be suitable for the measurements we plan, a polarimeter must meet the following specifications:

1) Detect and measure the polarization of protons with energies of 6 MeV or more in the presence of background produced by 18 MeV protons striking the target of interest.

2) Collect counts rapidly enough to permit statistically significant measurements to be made in a reasonable length of time.

3) Resolve particle groups well enough to prevent protons scattered from discrete states from interfering with measurements of protons scattered from states in the continuum.

A cross sectional view of the polarimeter is shown in Fig. 9.5-1. Elastic scattering from helium is used as a polarization analyzer. Up to 14.6 atm of helium can be contained by the 0.25 mil Havar windows of the gas cell. Left and right scattered protons are detected in telescopes comprised of an argon-filled proportional counter and a silicon detector. Background is caused primarily by neutrons; consequently the polarimeter is constructed entirely of iron to shield the detectors. The entrance and exit slits for the cell are tall and narrow so as to minimize the angular spread in the scattering and maximize the solid angle. The angular acceptance of the polarimeter is 5.6° FWHM, and the maximum angular spread in scattering from helium is 23.9° FWHM. The efficiency of the polarimeter is about 6×10^{-6} at 6 MeV.

The polarimeter has been tested with an unpolarized 18 MeV proton beam scattered from carbon, gold and copper targets. Scattering from the carbon target calibrated the energy spectrum of particles detected in the telescopes using the adequately resolved ground state, 4.43 and 9.6 MeV state particle groups. Carbon scattering also permitted comparison of the analyzing power of the polarimeter calculated from p + ^{4}He scattering values to the known polarization of protons elastically scattered from carbon. The agreement was reasonable in the two cases tested. The proton spectrum from a 27 mg/cm^2 gold target is shown in Fig. 9.5-2. This spectrum was used to examine slit scattering and foil-foil scattering in the polarimeter. The observed peak to valley ratio of 20:1 is adequate for the intended measurements.

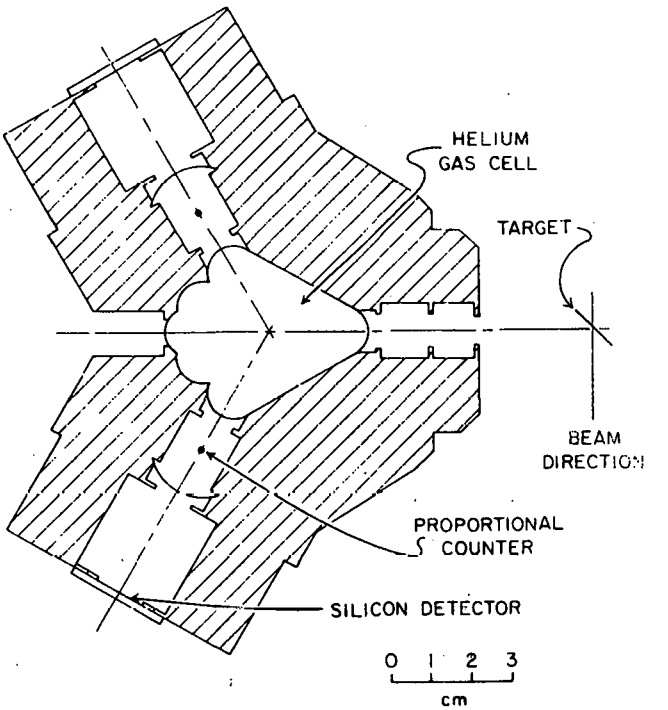

Fig. 9.5-1. Cross section through the midplane of the polarimeter.

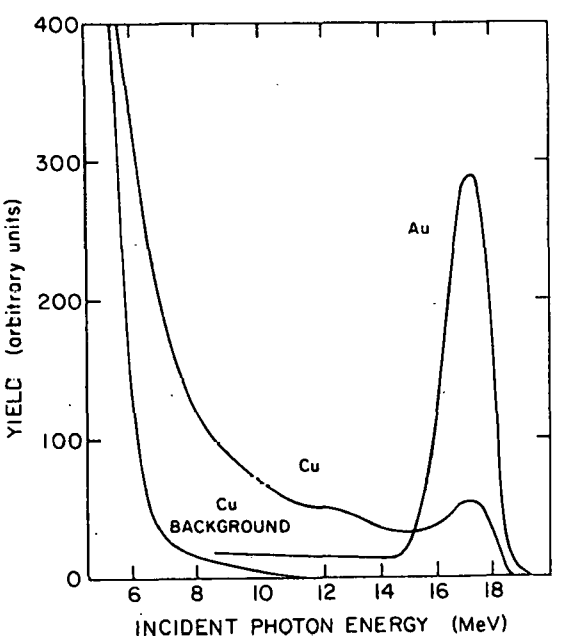

Fig. 9.5-2. Proton spectra from gold and copper targets observed in the polarimeter detectors. The copper background spectra was taken by stopping all charged particles at the entrance to the polarimeter

Copper is a possible target for measuring the depolarization, and a spectrum of protons from a 3 mg/cm^2 target is shown in Fig. 9.5-2 together with a background spectrum. The background was taken by inserting a thin sheet of aluminum in front of the polarimeter to stop all charged particles from entering. As is clear from the figure, protons with energies as low as 6 MeV can be detected satisfactorily. These spectra were taken with about 1 uA of beam current, and a substantial part of the background is due to accidental coincidences. These will vanish when data is taken with polarized beam with a maximum intensity of 0.1 uA.

9.6 A Chamber for In-Beam γ-γ Coincidence Spectroscopy

E.B. Norman

In order to achieve reasonable detection efficiencies during in-beam γ-γ coincidence experiments, it is necessary to position the two γ-ray detectors as close as possible to the target. Until now, the chambers available for the γ-ray spectroscopy at the Laboratory either did not allow close geometry or required the beam to be stopped in the target. For these reasons a new chamber was constructed which allows both detectors to be placed as close as 1.3 cm from the center of the target. The design of this chamber is based on that of a similar apparatus constructed at Argonne National Lab.[1]

The chamber consists of a block of stainless steel 14 cm x 9 cm x 2.5 cm. A 2-cm diameter hole was bored through the block lengthwise to permit the entrance and exit of the beam. A 3-cm diameter hole was bored through the block at 90° with respect to the beam direction. This hole is covered with Mylar windows 5 x 10^{-3} cm thick. The chamber has two flanges welded to it which allow the chamber to be inserted into a 10-cm diameter beam line. Because of the small size of the chamber, a new type of target rod and target frame was also constructed. The target and target rod are electrically isolated from the rest of the chamber and are inserted into the chamber through a 1.4-cm diameter hole in the top of the chamber. To date the chamber has been used in one experiment, and it performed very well.

---

1. C.N. Davids, private communication.

---

10. COMPUTERS AND COMPUTING

10.1 New On-Line and Off-Line Computer Systems

R. Seymour

Last year we reported the planned purchase of a DEC 11/60 computer. It was installed in May 1978 and has taken over the bulk of the Lab's number-crunching. The interface for high speed data acquisition was built and installed, and is currently being debugged. We have observed about an order of magnitude increase in computing throughput compared to the SDS 930s. The increased utility and availability of the 11/60 has brought about increased demand for its services. This plus the need to access large spectral arrays has caused us to reevaluate the requirements for the true off-line analysis computer. The two limits of the 11/60 are individual address space and total machine memory size. The individual address space limitation is overcome by choosing a computer with more than a 16 bit logical address space. The total memory limit can be overcome by buying lots of memory, or by buying a 'virtual' computer.

A 'virtual' computer allows users to write programs without practical concern for the memory space required. If the computer does not have enough memory, only the active part of a program is loaded into memory, with the rest left on a high-speed disk. When the in-core part is finished, it is swapped to the disk and the next segment is read into memory and executed. An additional requirement was some compatibility with the data-taking 11/60 to allow off-line program development and easy transfer of programs and data.

All of these requirements are met by the DEC VAX 11/780, which we have selected as our off-line computer. The VAX is a 32-bit computer with a 30-bit address limit for an individual user. It runs DEC's VMS (Virtual Monitor System) operating system, which can emulate the 11/60's RSX11M user environment. All of the user-written analysis programs written for the 11/60 may be transferred directly to the VAX without recompiling or relinking. Both machines run DEC's Fortran 4 Plus, although the VAX has some enhancements. Some of the peripherals purchased with the 11/60 will be transferred to the VAX. These include the 67 megabyte disk, an 8-line terminal multiplexer not required by a data-taking computer, and the 7-track tape drive. The 11/60 will receive a second 9-track drive for data collection. The VAX will have two 27 megabyte disks, two 9 track tapes, two graphics terminals, 16 terminal ports, 512K bytes of memory and a line printer/plotter. We expect delivery during the summer, followed by rapid changeover by the users of the 11/60 when we move the 67 megabyte disk.

In order to circumvent the 11/60's addressing limitation, we developed what we call a 'Bus Mirror'. It is a program-controlled hardware access to a 64K word data region. The user supplies an address, and the Bus Mirror performs a direct-memory-access fetch of the data, before the execution of the next 11/60 instruction. This is done beyond the user's 16 bit address limit. The user then reads the data from a local (to him) variable. To write to the remote data

zone, the user first supplies the address, and then writes into his local variable. The Mirror stuffs the number away before the next instruction. A transfer in either direction takes 600 nanoseconds more than if the user were accessing a single dimensioned array. The hardware allows operations such as X=f(X), and is being modified to provide auto-increment of the specified data word. The Mirror currently looks into the high end of the 11/60's main memory, but may be extended to other memory planes independent of the 11/60's 124K word address limit. The final configurations for the two DEC computers are listed below:

Real-Time Data Collection

DEC 11/60 computer
Floating Point Accelerator
2K byte cache memory
124K word MOS memory (60kw Plessey)
Two 5 megabyte RL01 disks
One 2.5 megabyte RK05 disk
Two 9 track 75 ips 1600 bpi tape drives (Pertec)
Printronix 300 lpm printer/plotter
IEEE bus interface
6 terminal ports
LA36 terminal
Tektronix 4006 terminal
Hazeltine 1500 terminals (shuffled from VAX as needed)
VT11 Graphic Display Processor
Bus Mirror
High speed DMA interface to 12 200 MHz Analog-to-Digital Converters

Off-Line Data Analysis

DEC VAX 11/780 computer
8K byte cache memory
512K byte main memory (Error-correcting MOS)
Two 28 megabyte RK07 disks
One 67 megabyte RM02 disk
Printronix 300 lpm printer/plotter
Two 9 track 75 ips 1600 bpi tape drives (vendor not selected yet)
One 7 track 75 ips 800 bpi tape drive (Pertec)
16 terminal ports
LA36 terminal
Qume 5/55 terminal
Ten Hazeltine 1500 terminals
Two Interactive Graphics display systems (vendor evaluation not finished)

In 1976 we purchased 12 Tracor Northern TN1213 200 MHz ADC's to replace the (then) 10 year old units which came with the first SDS computer. Over the next two years an interface was specified, designed and construction started. The interface was tailored to match the SDS input/output structure, with design decisions and compromises made in view of the SDS's 24-bit word. With the

decision to purchase the 11/60, the specifications for the interface were reevaluated and some changes were made. These included provision for 16-bit/32-bit channel precision, expanded coincidence functions and faster direct memory putaway. Among the decisions made was an attempt to utilize as much of the existing interface as possible.

Experimentor pressure for the new equipment, the threat and presence of intermittent SDS reliability, requirements for more functions from the final interface and numerous problems discovered during installation and debugging all combined to force reevaluation of the interface as it stood.

From that review came the construction of a "quicky" interface to directly replace the existing SDS ADC's. Thus 4 of the new ADC's began easing the equipment failure problem. Surveys of other labs showed an overwhelming acceptance of CAMAC-compatible systems. We had previously reviewed the CAMAC option, but had rejected it for reasons of data rate. We are now willing to sacrifice some of that data rate for ease and rapidity of implementation of a semi-standard data collection system. The flexibility and most of the speed we desire will be achieved through use of the microprogrammable branch driver concept developed at Los Alamos. Standard CAMAC modules will be bought to attach the TN1213's to the dataway. Programs using this equipment have been acquired and are being reviewed for use and modification. Projected impact upon the programs already developed for the original interface is minimal.

10.2 PDP 11/60 On-Line Data Acquisition Software

Kelly C. Green

A PDP 11/60 computer, purchased last year, is slated to replace our aging SDS 930 on-line system. Most of the software development necessary to perform singles acquisition has been completed. Multiparameter capability will be added to the system over the next year.

The multiprocessing ability of RXS 11M has been utilized to break the on-line software up into a family of programs, each of which is designed to perform a specific operation upon a centralized data base. The resulting modularity expedites the addition of specialized functions to the system. Programs can be developed off-line and then hooked into the on-line system with relatively minor modifications.

Access to the data base is regulated by a small monitor program termed the Real Time Monitor (RTM), which is the nucleus of the system. RTM manages the allocation and deallocation of data blocks for the tertiary tasks. It also maintains a directory of the data elements present, for rapid retrieval of a particular data block. Data blocks are organized into two parts. The first is a descriptor, the second an array. The descriptor is characterized by a unique name and type. It contains all information pertinent to the contents of the array. Only the first 13 words of the descriptor have fixed meaning and are used by RTM. The remainder (of arbitrary length) and the array (also arbitrary) are free to be defined as needed.

The acquisition system consists of programs to establish an experiment and initialize the monitor (RTM), create data blocks containing spectra, clear the spectra, print or plot the spectra, display spectra on a VT-11 CRT display, start or stop acquisition and read/write data tapes. These programs currently run in a conversational mode, leading a user step by step through any needed inputs. When installed as external MCR commands under RSX-11M, they are started by simply typing a three character mnemonic.

A. Existing Modules

EXPeriment — Initializes the monitor and its directories.

SPEctrum — Creates and establishes the characteristics of the spectra.

CLEar — Clears the spectra.

DISplay — Displays spectra on the VT-11. This display is very similar to that produced by MULTSING. This program is based upon a prior version by Norman Back.

PRInt — Produces a numeric printout of spectrum channels.

PLOt — Produces a high density histogram on the PRINTRONIX-300 plotter/printer, using the subroutine HISTO written by Jack Freeman.

OUTput — Writes data onto 7- or 9-track magtapes. The format will be discussed below.

INPut — Reads data in from magtapes produced by OUTPUT. This program is also capable of completely initializing the system, enabling one to set up by simply reading in a run from a previous experiment.

LISt — Makes a directory listing of the contents of a magtape.

STArt — Starts acquisition. Currently a dummy program, it places random data into all spectra.

STOp — Stops acquisition. Currently also a dummy program, terminating START.

B. To Be Written

CONnect — Identifies spectra with physical ADCs.

C. Magtape Format

Magtapes written by the program are structured similarly to the central database. A run is composed of descriptor-array pairs, followed by an end-of file mark. The end-of-volume is marked by two successive end-of-file marks. The tape is odd parity, and blocked into 1024 byte records. The first file of the tape is the only exception, consisting of 80 character ASCII records

documenting in detail the structure of the descriptors. A typical tape would resemble the following:

(BOT)	—	Beginning of tape mark
ASCII TEXT	—	Descriptive clear text 80 characters per record
(EOF)	—	End-of-file mark
DESCRIPTOR 1	—	This is always the experiment descriptor (1024 bytes)
ARRAY 1	—	The experiment directory (as many 1024 byte blocks as needed)
DESCRIPTOR 2	—	Any valid descriptor (1024 bytes)
ARRAY 2	—	(as many 1024 byte records as needed)
.		
.		
.		
(EOF)	—	End Of File
(repeat for next run)		
(EOF)	—	End Of File
(EOF)	—	End of Volume

The structure of the tape makes it unnecessary to read more than a single descriptor-array pair at any one time, yet still have sufficient information to analyze the data.

10.3 Off-Line Data Analysis with the DEC 11/60 Computer System

J. Freeman and A.J. Lazzarini

A large effort over the past several months by many individuals has made it possible to begin data analysis with the off-line DEC 11/60. The principle movers behind these developments have been members of the heavy ion group interested in reducing large volumes of multi-parameter data obtained both with the UW tandem Van de Graaff and at the LBL Hilac Facility. The decision to implement the software arose because the formerly available program, EDNA, used on the SDS computer was inadequate to analyze complex events taken with a large number of parameters as are currently being collected by the experimenters.

At present, reduction of multi-parameter data to spectra consists of several steps. By use of a generalized sorting program the experimenter may place a number of gating conditions—either one-dimensional gates or more complicated two-dimensional free-form gates—on any of the parameters recorded on the event tape. Further, the recorded parameters may themselves be used to generate any number—currently 20—of other quantities of interest. These "pseudo-parameters" may be, for example, mass, charge, momentum, particle angle, reaction Q-value, or any other physical quantity which may be defined from the measured parameters. These "pseudo-parameters" themselves may be used to define the gating conditions to which the data are subjected. The generation of the extra parameters occur via a user-written subroutine which is compiled and loaded with the main sorting program. This mode of operation was chosen to afford the most experimenters the greatest flexibility in the analysis of multi-parameter data.

With the sorting program, the gated spectra are accumulated on the disc. These spectra are eventually stored on disc as permanent and separate direct-access files. The spectra may then be retrieved and manipulated via several other programs which can read and alter the spectrum titles, dump the counts per channel content of the files to the terminal, or provide a directory of size, type, and title of all spectra in a user's area.

A generalized plotting package has been installed recently which can retrieve the spectra and plot them on a Printronix matrix line printer. The plots may be either histograms of one-dimensional spectra or density contour plots of two-dimensional spectra.

At present data reduction beyond this point is performed by hand. In the near future one or more display systems will be purchased that will allow the retrieval from disc of individual spectra to a scope. Integration of yields will then proceed by means of an interactive cursor or light pen.

The present system of programs is regarded as solely a temporary situation necessitated in large part by the need to analyze data. A more sophisticated system of software is presently being designed and written by Jack Freeman. The new, more powerful program should replace the present program and it is planned that it should eventually become interfaced with the future on-line data collection station here. This will then allow for the live display of gated data during the experiments themselves.

10.4 HOPREL: Relativistic Heavy Ion Optical Code

J.G. Cramer and W.G. Lynch

In Section 6.3 we discussed our experimental program to measure relativistic Coulomb effects using subcoulomb heavy ion elastic scattering. To make theoretical predictions of these effects we are adapting the heavy ion optical model program HOP-TWO.[1] Some of the adaptions have been made using portions of the pionic optical code RRFIPI.[2]

At the present time HOPREL differs from HOP-TWO in that it solves the Klein-Gordon equation instead of the Shroedinger equation. These equations differ in that the Klein-Gordon equation has an additional Coulomb term V'(r) where in the limit of a very large target mass:

$$V'(r) = - \frac{V^2_{coul}(r)}{2m_p c^2}$$

with

$m_p c^2$ = rest energy of projectile

V_{coul} = ordinary Coulomb potential between the two heavy ions.

At large distances V drops off as r^{-2}. This additional long range force requires that three basic changes be made in the optical model calculation. The first modification is that the numerically integrated wavefunction must be matched at the matching radius with Coulomb wavefunctions of complex angular momenta λ instead of ordinary Coulomb functions of angular momentum ℓ. Where:

$$\lambda = \sqrt{(\ell + 1/2)^2 - \gamma^2} - 1/2$$

with

$\gamma = z_t z_p \alpha$

z_t = target charge

z_p = projectile charge

α = fine structure constant

The second modification is that the standard Coulomb phase must be replaced by a complex phase shift:

$$e^{2i\delta_\lambda} = \frac{\Gamma(\lambda + 1 + i\eta)}{\Gamma(\lambda + 1 - i\eta)} e^{i\pi(\ell - \lambda)}$$

with

η = Sommerfeld parameter

The third modification is that the Rutherford scattering amplitude must be replaced by a Klein-Gordon scattering amplitude which includes the effects of V'(r). The Coulomb scattered Klein-Gordon amplitude can be written as:

$$f_{KG}(\theta) = f_R(\eta) + \frac{i\pi\gamma^2}{2} f_R(\eta + i/2) - \left(\frac{\pi^2\gamma^2}{8} + i\eta\gamma^2\right) f_R(\eta + i) +$$

$$i\pi\gamma^2(\gamma^2/8 - \frac{\pi^2\gamma^4}{48} - i\eta\gamma^2/2 + \eta^2/4 + i\eta/8) f_R(\eta + 3i/2) + f'(\theta)$$

with

$$f'(\theta) = \sum_\ell a_\ell P_\ell(\cos\theta)$$

$$f_R(\eta) = \eta/2k\left(\frac{2}{1-\cos\theta}\right)^{1+i\eta}\frac{\Gamma(i\eta)}{\Gamma(-i\eta)}$$

k = wavenumber

$f'(\theta)$ is evaluated separately in HOPREL. $f'(\theta)$ is added to the nuclear phase shifts and summed with the nuclear amplitude over 400 partial waves.

Since a_ℓ decreases as ℓ^{-3} errors due to truncating the partial wave expansion of $f'(\theta)$ can be important especially at backward angles. We eliminate the effect of these truncation errors by using the method of Yennie et al.[3]

We have tested HOPREL by turning off the relativistic effects and comparing the results with HOP-TWO. We have also calculated 8 MeV π^+ + ^{208}Pb with HOPREL and compared its prediction with the results calculated with the pion optical code RRFIPI. In both cases the agreement was excellent.

---

1. Nuclear Physics Laboratory Annual Report, University of Washington, p. 45 (1974), p. 26.
2. Written by Martin Cooper, MP-4, LAMPF.
3. D.R. Yennie, D.G. Ravenhall, and R.N. Wilson, Phys. Rev. 95, 500 (1954).

10.5 HEX-TWO: A Heavy Ion Optical Model Program for Excitation Functions

J.G. Cramer

In the past two years, our experimental program investigating the properties of heavy ion elastic scattering at tandem energies has increasingly involved the study of excitation functions at large angles, particularly at 180°.[1,2] While these measurements are now experimentally quite feasible, their theoretical analysis with the optical model has been fairly demanding because: 1) it is necessary to perform a time-consuming optical model calculation at each energy in the excitation function; 2) conventional optical model codes are oriented toward the analysis of angular distributions at a single energy, making comparisons between excitation function data and calculations unnecessarily complicated; and 3) there are no optical model search programs which are truly oriented toward the analysis of excitation functions.

The program described here, H(eavy ion) EX(citation function)-TWO, is based on HOP-TWO,[3-6] a heavy ion optical model program which has been in continual use and improvement at this Laboratory for the past five years. HEX-TWO is oriented toward excitation functions, and completely solves problem (2) mentioned above, and by providing the option of interpolating the optical-model S-matrix provides a partial solution to problem (1) by reducing the number of optical model calculations needed to analyze a particular excitation function. It is anticipated that when the new laboratory VAX-11/780 computer system is installed, a search version of HEX-TWO will be developed as a solution to problem (3).

The data input format of the program is very similar to that of HOP-TWO, including the optional input of experimental data. The latter is used to generate a chi-squared comparison of the data and fit and also to provide a high-density Printronix printer plot comparison of the data points (and error bars) with the calculated theoretical curve. A high-density Argand plot of the calculated S-matrix is also provided.

The program also includes an optional interpolation procedure by means of which the S-matrix is directly calculated only in coarse energy steps and is interpolated (using 4-point Lagrange interpolation) in the finer (and possibly irregular) energy steps of the experimental excitation function. The actual parameters interpolated are not the S-matrix elements themselves, but rather the parameters of local diffraction model fits to the calculated S-matrices, which should be relatively slowly varying and smooth with energy.

While the program is still evolving somewhat through the periodic addition of new options (constant *lab* angles, diffraction-model calculations, etc.) it is fully debugged and operational and has been in active use for the past six months.

---

1. See Chan *et al.*, this report, Section 6.1.
2. Nuclear Physics Laboratory Annual Report, University of Washington (1978), p. 79.
3. Nuclear Physics Laboratory Annual Report, University of Washington (1978), p. 133.
4. Nuclear Physics Laboratory Annual Report, University of Washington (1976), p. 40.
5. Nuclear Physics Laboratory Annual Report, University of Washington (1975), p. 45.
6. Nuclear Physics Laboratory Annual Report, University of Washington (1974), p. 26.

10.6 SMULTS—An Automatic Peak Summing Routine

C.D. Hoyle and P.G. Ikossi

The large volume of excitation function data accumulated in the $^{28}Si(\vec{p},p)$ experiment necessitated the development of an automatic peak summing program SMULTS for the PDP 11/60 computer.

SMULTS reads the spectra and associated information for each run from the "MULTSING" data tape. It obtains information from input file on the reactions to be considered, the angle, position (left or right to the beam direction) and beam polarization for each spectrum. Additional information on peak windows and associated reaction is also read from this input file. Up to 16 spectra can be analyzed and each spectrum may contain up to 6 peaks. The peaks for the first run are summed and the centroids are calculated. Then using kinematics a linear calibration of each spectrum is performed. For the following runs the program

uses the beam energy as read from the "MULTSING" tape to calculate the expected position of the centroid of each peak and shifts the windows appropriately. The energy calibration of the spectra is updated after 10 runs. A straight line background is calculated for each spectrum using two background regions defined by the operator in the input file. Each background window is allowed to move independently following a chosen peak in the spectrum. During the peak-sum calculation checks are made:

1) That background and peak windows do not overlap.

2) There is no appreciable deviation from linearity in background regions.

3) That the actual centroids of the peaks do not differ by an excessive amount from the predicted positions.

If any of these conditions are violated a message is written on the teletype and the operator is required to take an appropriate action. At this point the offending spectrum can be displayed on the VT11 and corrections, if necessary, can be made.

Detailed information on the peak sums, areas background and centroids and their associated errors are printed. A file containing a summary of these results is also written on the disk.

At the end of this procedure one can sort the summary file by angle and reaction, calculate print and plot cross sections and analyzing powers as a function of energy using the program "SORTIT". This allows easy inspection of all data on peaks of interest as well as contaminant peaks. Samples of excitation functions produced using these programs is shown elsewhere in this report (see, for example, Section 3.2).

11. APPENDIX

11.1 Nuclear Physics Laboratory Personnel

Faculty

Eric G. Adelberger, Professor
John S. Blair, Professor
David Bodansky, Professor, Chairman, Department of Physics
John G. Cramer, Professor
George W. Farwell, Professor
I. Halpern, Professor[1]
Fred H. Schmidt, Professor
Kurt A. Snover, Research Associate Professor
Thomas A. Trainor, Research Assistant Professor
Robert Vandenbosch, Professor
William G. Weitkamp, Research Professor,
Technical Director, Nuclear Physics Laboratory

Research Staff

Konrad Aniol, Research Associate
Hubert Doubre, Research Associate
Pitsa Ikossi, Research Associate
Albert J. Lazzarini, Research Associate
Eric B. Norman, Research Associate
Raymond J. Puigh, II, Research Associate
Ruedi Risler, Research Associate[2]

Senior Professional Staff

Harold Fauska, Research Electronics Supervisor; Assistant
Technical Director, Nuclear Physics Laboratory
Derek Storm, Senior Research Scientist

Predoctoral Research Associates

Norman L. Back
Hyoung C. Bhang
Yuen-dat Chan
David T.C. Chiang
Timothy E. Chupp
Katsuyaki Ebisawa[3]
Zafar Iqbal
William G. Lynch
Man-Yee B. Tsang
Richard Von Lintig

Research Assistants

Keith Davis
Charles D. Hoyle
Kevin T. Lesko
Robert Loveman

Full-Time Technical/Administrative Staff

Professional Staff

John F. Amsbaugh, Research Scientist
Michael Bizak, Research Scientist
Kelly C. Green, Research Scientist
Gervais M. Hinn, Research Scientist
Sally A. Hoffman, Research Scientist[5]
William B. Ingalls, Research Engineer
Alan G. Seamster, Research Engineer
Richard J. Seymour, Computer Systems Engineer
Rod E. Stowell, Electronics Engineer
H. Erik Swanson, Research Engineer

Technical

Peggy Douglass, Designer/Illustrator[5]
Louis Geissel, Student Shop Leadman
Norman E. Gilbertson, Instrument Maker[3]
Gustav E. Johnson, Instrument Maker
Barbara L. Lewellen, Accelerator Technician[5]
Carl E. Linder, Accelerator Technician
Lewis E. Page, Designer[5]
Georgia J. Rohrbaugh, Accelerator Technician
George E. Saling, Accelerator Technician
Hendrik Simons, Instrument Maker
Peter W. Wiest, Accelerator Operator
Allen L. Willman, Leadman

Administrative

Julie L. Anderson, Secretary
Dianne S. Hulford, Administrative Secretary
Dana L. Jones, Administrative Secretary[5]

Part-Time

William Bartholet[5]
Tim Bertram
Ambrose Chan
Linda Chapel[5]
Richard Eeymonaz
Alberto Ferreira
Eric Giessel
Daniel Giles
Barbara Hathaway[5]
Dale Hirt
William Hughey[5]
Mark Klebanoff
Steve Lamoreaux
Dong Lee[5]
Jim Martynovych
Kevin Mickelsen[5]
Shawn Pannell[5]
Leslie Pence
David Peterson
Duncan Prindle
Michael Rust
Theo Schaad
Byron Scott[5]
Loren Stokes[5]
Tim Van Wechel
Christopher Wagner
Richard Weisfield[5]
Stephen Weiss[5]

1. On leave, present address 61 Rue de Varenne, 75007 Paris, France.
2. No longer associated with the Nuclear Physics Laboratory; now at Siple Station, Antartica.
3. Completed Ph.D. Thesis, June 1978.
4. Retired October 31, 1978.
5. No longer associated with the Nuclear Physics Laboratory.

11.2 List of Publications

Published Papers:

"Isospin Nonconserving Proton Decays of $^{13}N(T=3/2)$ to Negative Parity States of ^{12}C," E.G. Adelberger, R.E. Marrs, and K.A. Snover, Phys. Rev. C 19, 1 (1979).

"On the Influence of Extra Neutrons Added to the $^{12}C + ^{16}O$ System: Cross Structures in γ-Ray Yields Following the $^{13}C + ^{16}O$ and $^{12}C + ^{18}O$ Reactions," Y.-d. Chan, H. Bohn, R. Vandenbosch, R. Sielemann, J.G. Cramer, K.G. Bernhardt, H.C. Bhang, and D.T.C. Chiang, Phys. Rev. Lett. 42, 687 (1979).

"Narrow $I^{\pi}=10^{+}$ Resonance for $^{12}C + ^{16}O$ in the Region of Strong Absorption," K.H. Eberhard, H. Bohn, and K.G. Bernhardt, Phys. Rev. Lett. 42, 432 (1979).

"Analyzing Power of $^{206}Pb(\vec{p},p_o)$ and $^{207}Pb(\vec{p},p_o)$ Near the $3_{p1/2}$ Isobaric Analog Resonance," N.L. Back. M.P. Baker, J.G. Cramer, and T.A. Trainor, Phys. Rev. C 17, 2053 (1978).

"Nuclear Time-Delay and X-Ray Proton Coincidences Near a Nuclear Scattering Resonance," J.S. Blair, P. Dyer, K.A. Snover, and T.A. Trainor, Phys. Rev. Lett. 41, 1712 (1978).

"Polarization Transfer Coefficients for $^{3}He(p,p)^{3}He$ Elastic Scattering Below 11 MeV," W.G. Weitkamp, W. Gruebler, V. Konig, P.A. Schmelzbach, R. Risler, and B. Jenny, Nucl. Phys. A311, 29 (1978).

"Gamma Decays of the First T=3/2 States in ^{9}Be and ^{9}B," P.A. Dickey, P.L. Dyer, K.A. Snover, and E.G. Adelberger, Phys. Rev. C 18, 1973 (1978).

"Electromagnetic Transitions Between the Low-Lying Levels of ^{21}Ne and Their Relation to Parity Mixing of the 2.80-MeV 1/2 Doublet," D.J. Millener, E.K. Warburton, K.A. Snover, R. Von Lintig, and P.G. Ikossi, Phys. Rev. C 18, 1878 (1978).

"A Search for Neutral Weak Current Effects in the Nucleus ^{18}F," M.M. Lowry, J.M. Davidson, R.E. Marrs; B.A. Barnes, F.M. Morinigo, B. Chang; E.G. Adelberger and H.E. Swanson, Phys. Rev. Lett. 40, 840 (1978).

"Isospin Forbidden Beta Decay of ^{28}Mg,: P.A. Dickey, J.E. Bussoletti, and E.G. Adelberger, Nucl. Phys. A303, 442 (1978).

"Total Width of the Lowest T=2 State in ^{24}Mg," J.L. Osborne, E.G. Adelberger, and K.A. Snover, Nucl. Phys. A305, 144 (1978).

"Decays of the Lowest T=2 State in ^{44}Ti," S.P. Freedman, C.A. Gagliardi, M.S. Oothoudt, A.V. Nero, R.G.H. Robertson, F.J. Zutavern, E.G. Adelberger, and A.B. McDonald, Phys. Rev. C 17, 2071 (1978).

"A Schematic Model for Isospin Mixing in Light Nuclei," A.B. McDonald and E.G. Adelberger, Phys. Rev. Lett. 40, 1692 (1978).

"Upper Limit on Parity Mixing in ^{21}Ne," K.A. Snover, R. Von Lintig, E.G. Adelberger, H.E. Swanson, T.A. Trainor, A.B. McDonald, E.D. Earle, and C.A. Barnes, Phys. Rev. Lett. 41, 145 (1978).

"Mass of the Lowest T=2 Level in ^{12}C," R.G.H. Robertson, T.L. Khoo, G.M. Crowley, A.B. McDonald, E.G. Adelberger, and S.J. Freedman, Phys. Rev. C 17, 1535 (1978).

"Effect of the Spin-Dependent Electromagnetic Forces on Low-Energy Proton-Proton Scattering," L.D. Knutson and D. Chiang, Phys. Rev. C 18, 1958 (1978).

"Heavy-Ion Elastic Scattering II: 142 MeV ^{16}O on ^{28}Si, ^{59}Co and ^{60}Ni," G.R. Satchler, M.L. Halbert, N.M. Clarke, E.E. Gross, C.B. Fulmer, A. Scott, D. Martin, M.D. Cohler, D.C. Hensley, C.A. Ludemann, J.G. Cramer, M.S. Zisman, and R.M. DeVries, Nuclear Physics A298, 313 (1978).

"Elastic and Deeply Inelastic Reactions in the ^{86}Kr + ^{139}La System at 505, 610 and 710 MeV," R. Vandenbosch, M.P. Webb, P. Dyer, R.J. Puigh, and R. Weisfield, Phys. Rev. C 17, 1672 (1978).

"Gross Structure in Gamma Ray Yields Following the ^{16}O + ^{12}C Reaction," Y. d Chan, H. Bohu, R. Vandenbosch, K.G. Bernhardt, J.G. Cramer, R. Sielemann, and L. Green, Nucl. Phys. A303, 500 (1978).

"Pion Cross Section Measurements on Aligned ^{165}Ho in the (3,3) Resonance Region," T.R. Fisher, J.A. Becker, B.A. Watson, H. Marshak, G.R. Burleson, M.D. Cooper, D.C. Hagerman, I. Halpern, M.J. Jakobson, R.H. Jeppeson, K.F. Johnson, L.D. Knutson, R.E. Marrs, H.O. Meyer, and R.P. Redwine, Phys. Rev. C 16, 2367 (1977).

Papers Submitted or in Press:

"A Simple Microscopic Model for Nuclear Alignment in Peripheral Nuclear Collisions," R. Vandenbosch, submitted to Phys. Rev. C.

"Magnitude and Alignment of Transferred Angular Momentum in Both Quasi and Deeply Inelastic Scattering," R.J. Puigh, P. Dyer, R. Vandenbosch, T.D. Thomas, L. Nunnelley, and M.S. Zisman, submitted to Phys. Rev. Lett.

"Q and Z Dependence of Angular Momentum Transfer in Deeply Inelastic Collisions of ^{86}Kr with ^{209}Bi," P. Dyer, R.J. Puigh, R. Vandenbosch, T.D. Thomas, M.S. Zisman, and L. Nunnelley, submitted to Nuclear Physics.

"Relative Yields of $^{26}Al^{g}$ and $^{26}Al^{m}$ from the $^{25}Mg(p,\gamma)$ Reaction," E.B. Norman, submitted to Astrophysical Journal.

"Alpha Width of the Lowest T=2 State in ^{28}Si," P.G. Ikossi, K.A. Snover, J.L. Osborne, E.G. Adelberger and A.B. McDonald, submitted to Nuclear Physics A.

"Decays of the Lowest T=2 States in A=4n Nuclei from ^{8}Be to ^{44}Ti," S.J. Freedman, C.A. Gagliardi, M.A. Outhoudt, A.V. Nero, R.G.H. Robertson, F.J. Zutavern, E.G. Adelberger, and A.B. McDonald, submitted to Phys. Rev. C.

Invited Papers and Talks and Conference Proceedings:

"Magnetic Dipole Strength in ^{16}O," K.A. Snover. Invited presentation at the Asilomar Meeting of the American Physical Society, November 1-3, 1978, BAPS 23, 957 (1978).

"Direct and Resonance Capture Reactions with Nucleons and Composite Particles," K.A. Snover. Invited talk at the Third International Symposium on Neutron Capture Gamma-Ray Spectroscopy and Related Topics, September 18-22, 1978 (to be published).

"Angular Momentum Transfer in Deeply Inelastic Collision," R. Vandenbosch. Invited talk for International Conference on the "Dynamical Properties of Heavy Ions," Johannesburg, August, 1978.

"Improvements to the University of Washington FN Belt Charge and GVM Control Systems," H. Fauska. Invited paper for the Symposium of Northeastern Accelerator Personnel, Holifield National Laboratory, Oak Ridge, Tenn., October 23, 1978.

"Forward Amplitudes for $\pi^{\pm}$ on Al, Ca, Cu, Sn, Ho and Pb in the Energy Range 65-215 MeV," R. H. Jeppesen et al. (collaboration of experiment #2). Submitted to the 2nd International Topical Conference on Meson-Nuclear Physics, Houston, March 5-9, 1979.

"The ^{11}C Production Yield Ratios from ^{12}C vs. ^{13}C and ^{12}C vs. ^{16}O for Incident π^{-} From 100 to 250 MeV," K. Aniol, D. Chiang, I. Halpern; D. Drake, and G. Haouat (collaboration of experiment #324). Submitted to the 2nd International Topical Conference on Meson-Nuclear Physics, Houston, March 5-9, 1979.

"A Review of the Physical Properties of Liquid Ionization Media," C.R. Gruhn and R. Loveman. Proceedings of the IEEE Nuclear Science Symposium, Washington, D.C., Nov. 18-20, 1978.

"Cross Sections Relevant to Gamma Ray Astronomy," P Dyer, D. Bodansky, and D.R. Maxson, in "Gamma Ray Spectroscopy in Astrophysics." Proceedings of Symposium at GSFC, April, 1978, T.L. Cline and R. Ramaty, ed., NASA Technical Memorandum 79619 (1978), p. 498.

"Alignment, Polarization, and Magnitude of Fragment Angular Momenta in Deeply Inelastic Collisions," R. Vandenbosch. Paper presented at Argonne Symposium on High Spin Phenomena in Nuclei, March 1979.

Contributed Abstracts:

"The E3/M2 Mixing Ratio of the ^{21}Ne $1/2^-(1.80) \rightarrow 5/2^+(0.35)$ Decay and its Role in Proposed Parity Mixing Measurements," K.A. Snover, R. Von Lintig, P.C. Ikossi, and E.K. Warburton, BAPS 23, 520 (1978).

"Nuclear Time-Delay and the Probability for K-shell Ionization," J.S. Blair, BAPS 23, 597 (1978).

"X-Ray Proton Coincidences in the Vicinity of the Narrow Nuclear Scattering Resonance at E_p = 3.15 MeV in ^{58}Ni + p," P. Dyer, K.A. Snover, T.A. Trainor, and J.S. Blair, BAPS 23, 597 (1978).

"The α-width of the Lowest 0^+, T=2 State in ^{28}Si," P.G. Ikossi, K.A. Snover, J.L. Osborne, E.G. Adelberger, and A.B. McDonald, BAPS 23, 521 (1978).

"An Accurate Value for the ^{20}Ne 2^+, T=1 (10.27) $\rightarrow$ 2^+, T=0 (1.63 MeV) Gamma-Decay Strength," K.A. Snover, K. Kim, and P.A. Dickey, BAPS 23, 501 (1978).

"Calculations of Hydrogen Metastable-State Populations for a Parity Nonconservation Experiment and 571G," T.A. Trainor, M.Z. Iqbal, E.G. Adelberger, and E.M. Henley, BAPS 23, 546 (1978).

"Principles of an Experiment to Detect Parity Nonconservation in n=2 Hydrogen Atoms," E.G. Adelberger, T.A. Trainor, and E.N. Fortson, BAPS 23, 546 (1978).

"Analyzing Powers for Particles Emitted to Continuum Excitations From ^{63}Cu in 18 MeV Proton Bombardment," T.A. Trainor, H.C. Bhang, I. Halpern, K-1 Liu, and W.G. Lynch, BAPS 23, 603 (1978).

"UW Parity Violation in Hydrogen: A progress report," T.A. Trainor, E.G. Adelberger, T. Chupp, K. Davis, D. Hoyle, M.Z. Iqbal, W.B. Ingalls, and H.E. Swanson, BAPS 24, 618 (1979).

"J^π Assignments in ^{29}P from Polarized Proton Scattering on ^{28}Si," P.G. Ikossi, K.A. Snover, E.G. Adelberger, and Y. Haque, BAPS 24, 613 (1979).

"The Role of the 6.3-s ^{26}Al^m in the Nucleosynthesis of ^{26}Al," E.B. Norman, BAPS 24, 63 (1979).

"Cross Sections for Possible Cosmic Gamma-ray Lines," P. Dyer, D. Bodansky, and D.R. Maxson, submitted for the Conference on Cosmic Ray Astrophysics of the American Physical Society, Durham, NC, Sept. 28-30, 1978.

"A Distance-Stabilized Recoil Doppler Apparatus," D.L. Clark and K.T. Lesko, BAPS 23, 937 (1978).

"Discrete Gamma Anistropies from the 600 MeV ^{86}Kr + ^{166}Er Reaction," R.J. Puigh, H. Doubre, A. Lazzarini, A. Seamster, R. Vandenbosch, D. Thomas, and M.S. Zisman, BAPS 24, 630 (1979).

"Gamma Ray Yields Following the ^{13}C + ^{16}O and ^{12}C + ^{18}O Reactions," Y-D Chan, H. Bohn, R. Vandenbosch, R. Sielemann, J.G. Cramer, D.T.C. Chiang, H. Bhang, and K.G. Bernhardt, BAPS 23, 933 (1978).

"180° Excitation Function for the Elastic Scattering of ^{32}S on ^{12}C," W.G. Lynch, Y D Chan, R.J. Puigh, J.G. Cramer, M-Y. Tsang, N. Back, and A. Lazzarini, BAPS 23, 941 (1978).

"Coincidence Study of the $^{27}Al(^{16}O,^{12}C)^{27}Al$ Reaction at 65 MeV," M.B. Tsang, W.G. Lynch, R.J. Puigh, A. Seamster, and R. Vandenbosch, BAPS 23, 934 (1978).

"Total Cross Sections for Inelastic Scattering of Very Energetic Heavy Ions," J.S. Blair, BAPS 23, 932 (1978).

"Fission Fragment Angular Correlations for the 720 MeV Kr + U Reaction," R.J. Puigh, P. Dyer, and R. Vandenbosch, BAPS 23, 958 (1978).

"Angular Momentum Transfer in Deeply Inelastic Scattering of ^{56}Fe + ^{209}Bi," M.S. Zisman, R.J. Puigh, R. Vandenbosch, T.D. Thomas, and L. Nunnelley, BAPS 23, 958 (1978).

"Van de Graaff Control Without Image Slits," F.H. Schmidt and H. Fauska, BAPS 23, 542 (1978).

"An Effective Reflection-Type Geometry for Sputter Ion Sources," F.H. Schmidt and G.W. Farwell, BAPS 24, 650 (1979).

"Inelastic Scattering of 67 MeV π^+ to the Continuum," D. Chiang, K. Aniol, I. Halpern, D. Barnes, N. Collela, M. Doss, S. Dytman, R. Eisenstein, C. Ellegard, S. Takeutchi, W. Wharton, L. Knutson, J. Amman, and M. Cooper, BAPS 23, 935 (1978).

Other Publications by Members of the Laboratory

"The $^{50,52,34}Cr(\alpha,p)^{53,55,57}Mn$ Reactions at E_α = 18 and 26 MeV," K.A. Aniol, D.W. Gebbie, C.L. Hollas and J. Nurzynski, Nucl. Phys. A303, 154 (1978).

"Population of Resonant ^{12}C + ^{12}C States Via the Reaction $^{12}C(^{16}O,\alpha)^{24}Mg$," A.J. Lazzarini, E.R. Cosman, A. Sperduto, S.G. Steadman, W. Thoms and G.R. Young, Phys. Rev. Lett. 40, 1426-1429 (1978).

"A Study of the $^{30}Si(\vec{d},\alpha)^{28}Al$ Reaction," P.G. Ikossi, A.B. McDonald and J.A. Kuehner, Nucl. Phys. A297 (1978).

"Spin-parity Combinations in ^{16}W from the $^{18}O(\vec{d},\alpha)^{16}N$ Reaction," A.M. Baxter, P.G. Ikossi, A.M. McDonald and J.A. Kuehner, Nucl. Phys. A297 (1978), 9.

"Elastic Scattering of Polarized Protons from ^{13}C for $9.1 < E_p < 18.4$ MeV," A.R. Weller, J. Szücs, P.G. Ikossi, J.A. Kuehner, P.T. Petty and R.G. Seyler, Phys. Rev. C18 (1978), 1120.

"Isospin-forbidden Particle Decays in Light Nuclei (IV) Total Width of the Lowest T=2 Level of ^{24}Mg," A.B. McDonald, E.D. Earl, W. McLatchie, H.B. Mak, D. Martin and P.G. Ikossi, Nucl. Phys. A305 (1978), 151.

"On the Conditions Required for the r-Process," E.B. Norman and D.N. Schramm, Astrophysical Journal 228, 881 (1979).

"Superallowed Fermi Decay of ^{62}Ga," C.N. Davids, C.A. Gagliardi, M.J. Murphy, and E.B. Norman, Phys. Rev. C19, 1463 (1979).

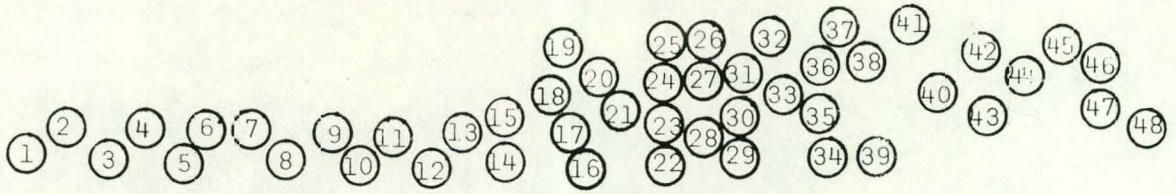

Employees by above numbers:

1) Chiang; 2) Blair; 3) Hinn; 4) Bhang; 5) Tsang; 6) Storm; 7) Chan; 8) Adelberger; 9) Holmgren; 10) Trainor; 11) Hoyle; 12) Ingalls; 13) Davis; 14) Von Lintig; 15) Linder; 16) Aniol; 17) Lesko; 18) Back; 19) Amsbaugh; 20) Green; 21) Murano; 22) Giessel; 23) Lazzarini; 24) Puigh; 25) Anderson; 26) Schmidt; 27) Metag; 28) Saling; 29) Stowell; 30) Swanson; 31) Seymour; 32) Fauska; 33) Lynch; 34) Loveman; 35) Farwell; 36) Leach; 37) Weitkamp; 38) Vandenbosch; 39) Rohrbaugh; 40) Grant; 41) Wiest; 42) Bizak; 43) Hulford; 44) Cramer; 45) Willman; 46) Simons, 47) Chupp; and 48) Iqbal